Constraining Fundamental Physics with Current Cosmological Data

University of Rome 'La Sapienza'

Dottorato di Ricerca in Fisica – XXVI Ciclo

Candidate

Eleonora Di Valentino

ID number 1042172

Thesis Advisor

Prof. Alessandro Melchiorri

A thesis submitted in partial fulfillment of the requirements
for the degree of Doctor of Philosophy in Physics

December 2014

Thesis not yet defended

This thesis has been typeset by LaTeX and the Sapthesis class.

Author's email: eleonora.divalentino@gmail.com

*Dedicated to
Tommaso and Kevin*

Ringraziamenti

La prima persona che voglio ringraziare e' sicuramente il mio supervisor, Prof. Alessandro Melchiorri, per aver creduto in me. Grazie dal lato professionale per avermi insegnato a cambiare punto di vista e spronato a fare sempre del mio meglio, e dal lato personale per avermi aiutata e sostenuta nei momenti difficili, pur non condividendo le mie scelte. Grazie per aver reso divertenti gli anni del mio dottorato ed aver reso possibile che il mio hobby diventasse il mio lavoro.

Un ringraziamento speciale va sicuramente ai miei bimbi Tommaso e Kevin per aver affrontato con me tutte le difficolta' ed aver riempito le mie giornate di colore e di felicita', anche quelle in cui tutto sembrava irrecuperabile. Grazie di essere cresciuti insieme a me ed avermi insegnato a diventare adulta. Grazie per i vostri mille sacrifici.

Un ringraziamento grandissimo va alla mia famiglia, i miei zii, i miei genitori, le mie nonne, Alessandra e Samantha per essere sempre presenti, aver colmato i miei vuoti ed essere arrivati li' dove io non riuscivo.

Grazie a Mirko per non avermi abbandonata nel momento del bisogno.

Ringrazio infine tutti gli amici del G31 e del dipartimento di fisica per avermi pazientemente sopportato durante tutti questi anni.

Contents

Introduction

In the past two decades the so-called ΛCDM model of cosmological structure formation has been spectacularly confirmed by a large amount of experimental data. In particular, the observations of the Cosmic Microwave Background anisotropies (both in temperature and polarization) from satellite experiments as WMAP, Ref. [1], and Planck, Ref. [2], as well from ground based experiment as Atacama Cosmology Telescope (ACT), Ref. [3], and South Pole Telescope (SPT), Ref. [4], have shown a perfect agreement with the simplest inflationary model based on primordial adiabatic and Gaussian perturbations.

Clearly the improving accuracy of the CMB measurements opens the window for testing extensions of the standard ΛCDM scenario. Between the possible extensions that we can consider, probably the most relevant are those connected with particle physics, as neutrino and dark matter. Indeed, we are close in testing the same neutrino and dark matter properties both with cosmological data and laboratory experiments. This overlap between cosmology and particle physics is extremely interesting since any conflict between the results could indicate the presence of new physics.

The research subject of this PhD thesis goes exactly in this direction: to identify possible hints for new physics in the most recent cosmological data. Hints that could also actually been tested in current and nearly future particle physics experiments.

My thesis is organized as follows: in the first three chapters I will briefly introduce the theory of cosmological structure formation and its main observables.

In particular, in Chapter 1 I will describe the Standard (unperturbed) Cosmological Model, based on the assumption of homogeneity and isotropy of the Universe (*Cosmological Principle*) at scale larger than $100 Mpc$. This assumption allow us to describe the evolution of the Universe through the Friedmann equations, introducing a set of cosmological parameters that we can constrain comparing theory with experimental data. I will then discuss the thermal history of the Universe from the Hot Big Bang to the production of the Cosmic Microwave Background (CMB) with a special emphasis on Big Bang Nucleosynthesis and the importance of the Cosmic Neutrino Background.

In Chapter 2 I will discuss cosmological structure formation and linear perturbation theory. I will follow the evolution of the primordial perturbations introducing small fluctuations at the first order in the homogeneous Universe. I will perturb the metric and the Einstein equations in order to study the growth of scalar and tensor perturbations and I will consider the Boltzmann equation in order to take into account the interactions between the several components of the Universe. Afterwards, I will describe the initial conditions of this set of differential equations considering a period

of exponential expansion of the Universe, introduced to solve the problems of the standard cosmological model: Inflation. Finally, I will define the scalar and tensor power spectra, as a function of the inflationary potential.

In Chapter 3 I will discuss the statistic of the perturbations, defining the correlation function and the power spectrum in Fourier space. I will expand the two-point correlation function of the temperature perturbations of the CMB in Legendre polynomials, introducing one of the main tools of research in cosmology: the CMB angular power spectrum of temperature and polarization. Afterwards, I will describe in detail the sources of temperature anisotropies, primary and secondary. Finally, I will discuss the matter power spectrum and the primordial CMB bispectrum.

In Chapter 4 I will discuss the damping tail of the CMB angular power spectrum of the temperature anisotropies, and which are the main parameters affecting it. In particular, I will focus on the current constraints on the neutrino effective number N_{eff} and the lensing amplitude A_{L} from ground based experiments as the South Pole Telescope, Ref. [4], and the Atacama Cosmology Telescope, Ref. [3], in tension between them, and satellite experiments, as WMAP9, Ref. [1], and Planck, Ref. [2]. Finally, I will try to explain the non-standard value of A_{L}, in tension with the standard value at 2-σ c.l., measured by the Planck satellite, see Ref. [5], considering non-standard neutrino properties, as the rest frame sound speed c_{eff}^2 and the viscosity parameter c_{vis}^2. This Chapter is based on the following published work:

- E. Di Valentino, S. Galli, M. Lattanzi, A. Melchiorri, P. Natoli, L. Pagano, N. Said, "Tickling the CMB damping tail: scrutinizing the tension between the ACT and SPT experiments", Phys. Rev. D88 (2013) 2, 023501 (2013);

- N. Said, E. Di Valentino, M. Gerbino, "Planck constraints on the effective neutrino number and the CMB power spectrum lensing amplitude", Phys. Rev. D88 (2013) 2, 023513;

- M. Gerbino, E. Di Valentino, N. Said, "Neutrino anisotropies after Planck", Phys. Rev. D88 (2013) 6, 063538.

In Chapter 5 I will place limits on models containing relativistic species at decoupling epoch, as the $(3 + 1)$ and $(3 + 2)$ sterile neutrino models and extended dark sectors with additional light species. I will present new constraints on the neutrino effective number N_{eff} and the effective mass of the sterile neutrino m_{eff}^s combining the Planck data, see Ref. [2], with both the HST measurements of H_0 from Ref. [6] and the full shape of the galaxy power spectrum from the Baryon Acoustic Oscillation Spectroscopic Survey BOSS Data Release 9 from Ref. [7]. This Chapter presents the work published in:

- E. Di Valentino, A. Melchiorri, O. Mena, "Dark radiation sterile neutrino candidates after Planck data", JCAP 1311 (2013) 018.

In Chapter 6 I will present up to date cosmological bounds on the sum of active neutrino masses as well as extended cosmological scenarios with additional thermal relics, as thermal axions or sterile neutrino species. I will include in the analyses the new Baryon Acoustic Oscillation Spectroscopic Survey BOSS Data Release 11 from

Ref. [8] finding that, when adding the constraints on σ_8 and Ω_m from the Planck Cluster catalog on galaxy number counts from Ref. [9], the total sum of the active neutrino masses $\sum m_\nu = 0.3 eV$ is favoured a 3-σ c.l.. Finally, when considering the detection of B mode polarization from BICEP2, Ref. [10], experiment, a combined analysis with CMB data in a $\Lambda CDM + r$ model favours $N_{\text{eff}} = 4.00 \pm 0.41$. However, this detection has been recently questioned by the Planck collaboration, see Ref. [?], since this signal could be completely explained by a polarization signal from galactic dust. This Chapter is based on the work published in:

- E. Giusarma, E. Di Valentino, M. Lattanzi, A. Melchiorri, O. Mena, "Relic Neutrinos, thermal axions and cosmology in early 2014", Phys. Rev. D90 (2014), 043507.

In Chapter 7 I will discuss the Curvaton scenario and the possible residual isocurvature perturbations that can be imprinted in the cosmic neutrino component after the decay of the Curvaton field. Firstly, I will discuss the forecasts obtained using the Fisher matrix techniques on constraining the amplitude of the neutrino isocurvature density α^{NID} and the neutrino effective number N_{eff} for a set of future CMB experiments. Secondly, I will translate these bounds in terms of the background neutrino degeneracy parameter ξ and the corresponding perturbation amplitude, and I will compare these with the bounds derived from Big Bang Nucleosynthesis. Finally, I will present the constraints obtained from the public Planck data, see Ref. [2], on these parameters α^{NID} and N_{eff} at the same time, also including the Hubble Space Telescope measurements on the Hubble constant H_0 from Ref. [6]. This Chapter explains the work presented in the following published papers:

- E. Di Valentino, M. Lattanzi, G. Mangano, A. Melchiorri, P. D. Serpico, "Future constraints on neutrino isocurvature perturbations in the Curvaton scenario", Phys. Rev. D85 (2012), 043511;

- E. Di Valentino, A. Melchiorri, "Planck constraints on neutrino isocurvature density perturbations", Phys. Rev. D90 (2014) 8, 083531.

In Chapter 8 I will discuss the possibility that axion particles account for the total amount of cold dark matter in the Universe, providing constraints on their masses given by Planck data, see Ref. [2], combined with BOSS DR11 from Ref. [8] and BICEP2 measurements, Ref. [10], in several extended cosmological scenarios. In this Chapter I follow the published work:

- E. Di Valentino, E. Giusarma, M. Lattanzi, A. Melchiorri, O. Mena, "Axion cold dark matter: status after Planck and BICEP2", Phys. Rev. D90 (2014), 043534.

In Chapter 9 I will discuss the possibility that the 2-σ tension between the abundance of primordial deuterium obtained from the Lyman-alpha absorption-line system, see Ref. [11], and that one computed using the Planck data, Ref. [5], is due to the uncertainty on the rate of the capture radiative reaction $d(p, \gamma)^3 He$ converting deuterium into helium. I will conclude that Planck data are able to constrain the rate of this process, providing a value closer to the theoretical one than the experimental one. This Chapter refers to the published work:

- E. Di Valentino, C. Gustavino, G. Lesgourgues, G. Mangano, A. Melchiorri, G. Miele, O. Pisanti, "Probing nuclear rates with Planck and BICEP2", Phys. Rev. D90 (2014), 023543.

In Chapter 10 I will constrain the spectral index of the tensor perturbations n_T considering the detection of B mode polarization from BICEP2, Ref. [10], experiment. Moreover, I will show the impact on this constraint of a possible unaccounted, dust component, finding that, while a dust component compatible with the dust template presented in Ref. [10] does not alter our conclusions, a component four times larger drastically change our results. In this chapter I will present the results of the works published before the results from the Planck collaboration, see Ref. [**?**], for which the BICEP2 detection could be completely due to a polarization signal from galactic dust. These works are:

- E. Di Valentino, A. Melchiorri, L. Pagano, "Testing the inflationary null energy condition with current and future cosmic microwave background data", Int.J.Mod.Phys. D20 (2011), 1183-1189,

- M. Gerbino, A. Marchini, L. Pagano, L. Salvati, E. Di Valentino, A. Melchiorri, "Blue Gravity Waves from BICEP2 ?", Phys. Rev. D90 (2014), 047301.

Finally, in Chapter 11 I will describe the Bispectrum, the three-point correlation function of the CMB temperature anisotropies, produced by a cross correlation between the Weak Lensing signal and the Integrated Sachs-Wolfe effect, and how this effect could be used to constrain parameters of modified gravity models, as well as cosmological parameters of the neutrino background. Although the constraining power of the Bispectrum is less than the one achievable by the CMB angular power spectrum, it provides, in any case, an independent way to bound the parameters, useful for a cross check the results. This Chapter is based on the published works:

- E. Di Valentino, A. Melchiorri, V. Salvatelli, A. Silvestri, "Parametrised modified gravity and the CMB Bispectrum", Phys. Rev. D86 (2012), 063517.

- E. Di Valentino, M. Gerbino, A. Melchiorri, "Dark radiation and the CMB bispectrum", Phys. Rev. D87 (2013) 10, 103523.

Chapter 1

The Standard Cosmological Model

1.1 Introduction

Modern cosmology was probably born between 1915, when Albert Einstein published his first paper on General Relativity, and 1927, when George Lemaître, making use of General Relativity, first derived what we now call the "Hubble law", proposing an expanding Universe to explain the recession velocity of the galaxies and suggesting an estimated value of the rate of expansion. Two years later Edwin Hubble confirmed the existence of that law and determined a value for the constant that now bears his name. Hubble and Lemaître inferred the recession velocity of the objects from their redshifts, many of which were earlier measured and related to velocity by Vesto Slipher in 1917.

In 1948 G. Gamow, R. Alpher and R. Herman theorized that the Universe originated from a hot "Big Bang", explaining the observed amount of light elements in the Universe with primordial nucleosynthesis (Big Bang Nucleosynthesis, BBN). The early Universe, in this theory, was mainly composed by ionized matter and electromagnetic radiation in thermodynamic equilibrium. This primordial plasma cooled with the expansion of the Universe, passing through a phase of recombination, when electrons and protons combined into neutral hydrogen atoms and decoupling, in which the Universe became subsequently trasparent to the motion of photons. One of the major prediction of this theory was therefore the existence of a Cosmic Microwave Background (CMB) radiation that permeates the entire observable Universe. After the discovery of the CMB radiation by Arno Penzias and Robert Wilson in 1964, a model of cosmological structure formation started to be developed that could explain the observed structure of the local Universe made of galaxies and cluster of galaxies, starting from a nearly isotropic and homogeneous universe as observed from the CMB. In this picture, developed by several scientists in the 1970s and 1980s, the present structure of the Universe, characterized by large voids and great concentrations of matter and filaments, formed starting from small fluctuations of the matter density in a nearly homogeneous state.

In this chapter we first introduce the homogeneous and isotropic cosmological model that provides a relatively good description of the Universe at early times (at

the epoch of BBN, for example) and/or on very large scales, approximately at more than $100Mpc$ (see e.g. Refs. [12, 13]) where density fluctuations are small. This assumption is called the '*Cosmological Principle*', that means that there are neither preferred places nor preferred directions in the Universe.

Cosmological observations such as the distribution of the galaxies clusters in the sky and the amplitude of the CMB anisotropies confirm that the *Cosmological Principle* is a very accurate zero-th order approximation. As we will see in the next chapters, the CMB anisotropies, roughly one part over 10^5, and density fluctuations on large scales can be treated as a first order perturbations of the homogeneous Universe.

Thanks the Cosmological Principle the evolution of the Universe can be described through the Friedmann equations, obtained using the Friedmann-Lemaître-Robertson-Walker's metric in the Einstein equation.

1.2 The Friedmann-Lemaître-Robertson-Walker metric of the Universe

In General Relativity a matter-energy distribution curves gravitationally the metric structure of the space-time.

Once we have fixed a four-dimensional coordinate system $\{x^\alpha\}$, with $\alpha = 0, 1, 2, 3$, the infinitesimal distance between two events is given by the invariant line elements ds^2:

$$ds^2 = g_{\mu\nu}dx^\mu dx^\nu \tag{1.1}$$

that can describe both a flat (Minkowsky's) and a curved space-time. Splitting the temporal, spatial and mix component, we obtain:

$$ds^2 = g_{00}c^2dt^2 + 2g_{0i}dx^i cdt + \sigma_{ij}dx^i dx^j \tag{1.2}$$

where dt is the infinitesimal time, dx the infinitesimal space and σ_{ij} the spatial metric. The spatial variables are called *comoving coordinates* because they are independent from time, and describe, for example, the position of an object in the expanding Universe reference frame.

We can introduce the Einstein equations:

$$G_{\mu\nu} = R_{\mu\nu} - \frac{1}{2}g_{\mu\nu}R = \frac{8\pi G}{c^2}T^{\mu\nu} + \Lambda g_{\mu\nu} \tag{1.3}$$

that connect the geometry of the space-time (left hand side), the *Einstein tensor* $G_{\mu\nu}$, with its energy content in the same point of the space-time (right hand side), the *energy-momentum tensor* $T_{\mu\nu}$. In these equations the *Einstein tensor* $G_{\mu\nu}$ depends on the *Ricci's tensor* $R_{\mu\nu}$, the *scalar curvature* R (i.e. from the first two derivatives of the tensor metric) and the *tensor metric* itself $g_{\mu\nu}$.

The Einstein equations are highly non linear, but introducing the *Cosmological Principle*, that means the homogeneity and the isotropy of the space-time, we can simplify the problem starting from a simpler metric. The isotropy, i.e. no preferred directions ($g_{0i} = 0$), and the homogeneity, i.e. that the density is independent

from the position but depends only on time, implies necessarily the rotational and translational symmetry. While the time synchronization, i.e. the assumption that the time is the same everywhere, implies that, in order to have $dt_1 = \sqrt{g_{00}}dt_2$, $g_{00} = 1$. In this way we obtain that the infinitesimal distance between two events in the space-time, considering the comoving polar coordinates (r, θ, ϕ), constant for any point at any time, is given by the Friedmann-Lemaître-Robertson-Walker (FLRW) metric:

$$ds^2 = c^2 dt^2 - a^2\left(t\right)\left[\frac{dr^2}{1 - kr^2} + r^2\left(d\theta^2 + sin^2\theta d\phi^2\right)\right]. \tag{1.4}$$

In the equation (1.4) we have introduced the adimensional *scale factor* $a(t)$, that describes the way in which the distances in the Universe contract or expand in function of time. It is usually normalized so that $a(t_0) = 1$ at present time. Only at scales much larger than $100Mpc$, or at very early times, the Universe expansion could be treated as the ideal, homogeneous and isotropic expansion described by the scale factor. In this way the physical distance between two points in the Universe is obtained taking the comoving distance times the corresponding scale factor:

$$\vec{x}(t) = a(t)\vec{r}. \tag{1.5}$$

The curvature of the Universe k introduced in (1.4), is proportional to the inverse of the curvature radius R squared ($k \propto R^{-2}$) and can be positive, null or negative. At these values corresponds an open (two lines that start moving parallel diverge), spatially flat (two lines moving parallel always keep the same distance) or closed (two lines that start moving parallel converge) Universe.

Using the change of coordinates $r \to \chi^{-1}(r)$ we can rewrite the spatial part of (1.4) in this way:

$$\frac{dr^2}{1 - kr^2} + r^2\left(d\theta^2 + sin^2\theta d\phi^2\right) = dr^2 + \chi^2(r)\left(d\theta^2 + sin^2\theta d\phi^2\right) \tag{1.6}$$

where

$$\chi(r) = \begin{cases} sin(x) & k > 0 \\ x & k = 0 \\ sinh(x) & k < 0 \end{cases} \tag{1.7}$$

Lastly we can introduce the new time quantity:

$$d\tau = \frac{dt}{a(t)} \tag{1.8}$$

called *conformal time*, that is the comoving distance traveled by light at the time t, along the geodetic $ds^2 = 0$. With τ the metric will be:

$$g_{\mu\nu}dx^\mu dx^\nu = a^2(t)\left(d\tau^2 - \sigma_{ij}dx^i dx^j\right). \tag{1.9}$$
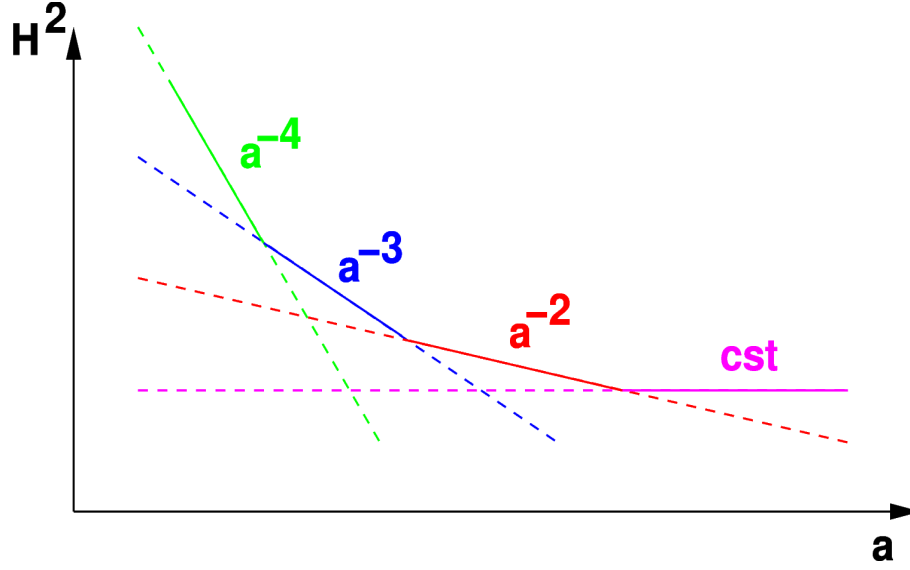
Figure 1.1. Evolution of the squared Hubble parameter to grow of a, in a Universe in which the expansion is given by the radiation (a^{-4}), the matter (a^{-3}), the curvature (a^{-2}) and the cosmological constant (cst), [14].

1.2.1   The Friedmann equations

The *scale factor* $a(t)$ evolves according to the Friedmann equations, obtained plugging the FLRW metric (1.4) in the Einsten's equations.

    The Ricci's tensor (1.3) is defined by the *Christoffel's symbol*:

$$R_{\mu\nu} = \Gamma^{\alpha}_{\mu\alpha,\nu} - \Gamma^{\alpha}_{\mu\nu,\alpha} + \Gamma^{\alpha}_{\mu\rho}\Gamma^{\rho}_{\mu\alpha} - \Gamma^{\rho}_{\mu\nu}\Gamma^{\alpha}_{\rho\alpha} \tag{1.10}$$

linked to the metric by:

$$\Gamma^{\alpha}_{\beta\gamma} = \frac{1}{2}g^{\alpha\rho}\left(g_{\rho\beta,\gamma} + g_{\rho\gamma,\beta} - g_{\beta\gamma,\rho}\right) \tag{1.11}$$

    Considering all the components of the Universe (radiation, matter, etc.) as perfect fluids, these can be described completely by the two parameters of density $\rho = \sum_i \rho_i$ and pressure $P = \sum_i P_i$: ρ and P are independent of time and the pressure is the same in all directions. So, the energy-momentum tensor has the simple diagonal shape:

$$T^{\mu\nu} = \begin{pmatrix} \rho & 0 & 0 & 0 \\ 0 & -P & 0 & 0 \\ 0 & 0 & -P & 0 \\ 0 & 0 & 0 & -P \end{pmatrix}. \tag{1.12}$$

    The formal approach to calculate the pressure and density of each component is, in general, to calculate its distribution function $f(\vec{x}, \vec{p}, t)$, that provides the fraction

of particles that has position $\vec{x}$ and momentum $\vec{p}$ at the time t, and then to compute pressure and density. So we can write:

$$\rho_i = g_i \int \frac{d^3p}{(2\pi\hbar)^3} f_i(\vec{x}, \vec{p}) \, E(p) \tag{1.13}$$

$$P_i = g_i \int \frac{d^3p}{(2\pi\hbar)^3} f_i(\vec{x}, \vec{p}) \, \frac{p^2}{3E(p)} \tag{1.14}$$

where g_i are the *degrees of freedom*, and where the distribution functions f are independent of time and equal to:

$$f = \frac{1}{e^{(E-\mu)/kT} \pm 1} \tag{1.15}$$

In these equation the sign $-$ is for bosons, i.e. for particles that have an integer spin, such as photons, and follow, in a homogeneous Universe, a Bose-Einstein distribution function, while the sign $+$ is for fermions, i.e. for particles with a half integer spin, such as neutrinos, that instead have a Dirac-Fermi distribution function. For almost all the particles at almost all times in the Universe, the chemical potential μ can be neglected because is much smaller than the temperature. So is sufficient to measure their temperature to compute their density.

The first Friedmann equation, with c=1, is obtained from the first component $(\mu, \nu) = (0, 0)$ of the eq. (1.3):

$$H^2 = \left(\frac{\dot{a}}{a}\right)^2 = \frac{8\pi G}{3}\rho - \frac{k}{a^2} + \frac{\Lambda}{3} \tag{1.16}$$

Here we have introduced a possible *cosmological constant* and defined the *Hubble constant* parameter H, that represents the rate of the expansion of the Universe at time t. The derivatives are respect to time. Conventionally H is parameterized in the following way:

$$H = \frac{da/dt}{a} = 100h\frac{km/s}{Mpc} \tag{1.17}$$

where h is the *reduced Hubble constant* that is dimensionless.

The second Friedmann equation can be obtained combining the eq. (1.16) with the trace of the eq. (1.3):

$$\frac{\ddot{a}}{a} = -\frac{4\pi G}{3}(\rho + 3P) + \frac{\Lambda}{3} \tag{1.18}$$

The first and second Friedmann equations provide the dependence on time of the expansion rate and acceleration of the Universe.

In order to solve the Friedmann equations respect to P, ρ and $a(t)$, we introduce the *equation of state* that links pressure and density. For a perfect fluid we have:

$$P = w\rho \tag{1.19}$$

where w is a constant that depends on the component considered. For the matter, radiation and cosmological constant components we have:

$$w = \begin{cases} 0, & \text{matter} \\ \frac{1}{3}, & \text{radiation} \\ -1, & \text{cosmological constant} \end{cases} \tag{1.20}$$

If we plug the FLRW metric, eq. (1.4), in the *conservation equation* of the energy-momentum tensor $T^{\mu\nu}_{;\nu} = 0$ (i.e. its covariant derivatives respect to ν are equal to zero), we have the *continuity equation*, that is not independent from the two Friedmann equations:

$$\dot{\rho} + 3H\left(\rho + P\right) = 0. \tag{1.21}$$

The latter, introducing the eq. (1.19), becomes

$$\frac{d\rho}{\rho} = -3\left(1+w\right)\frac{da}{a} \tag{1.22}$$

Integrating this last equation (we assume w as constant with time) we have the density ρ as a function of the scale factor $a(t)$:

$$\rho(a) = \rho_0 \frac{1}{a(t)^{3(1+w)}} \tag{1.23}$$

where with ρ_0 we denote the density today. Considering the different components of matter m, radiation r an cosmological constant Λ, we have:

$$\rho_m = \frac{\rho_m^0}{a^3}, \tag{1.24}$$

$$\rho_r = \frac{\rho_r^0}{a^4}, \tag{1.25}$$

$$\rho_\Lambda = \rho_\Lambda^0. \tag{1.26}$$

We can define the *critical density*, for every fixed value of the Hubble parameter, as follows:

$$\rho_c = \frac{3H^2}{8\pi G} = 10^{-29} h^2 g/cm^3 \tag{1.27}$$

and rewrite the eq. (1.16) as

$$\frac{\rho_m}{\rho_c} + \frac{\rho_r}{\rho_c} + \frac{\rho_\Lambda}{\rho_c} + \frac{\rho_k}{\rho_c} = 1 \tag{1.28}$$

where we introduced the quantities:

$$\rho_\Lambda = \frac{\Lambda}{8\pi G}, \tag{1.29}$$

and a *curvature density*

$$\rho_k = -\frac{3k}{8\pi G a^2} = \frac{\rho_k^0}{a^2}. \tag{1.30}$$

If we call the *density parameter* the ratio between the density of a physical component x today and the critical density:

$$\Omega_x = \frac{\rho_x^0}{\rho_c^0} \tag{1.31}$$

the eq. (1.28) becomes at present time:

$$\Omega_0 = \sum_i \Omega_i = \Omega_m + \Omega_\Lambda + \Omega_r = 1 - \Omega_k. \tag{1.32}$$

In this equation we denote with Ω_m the matter contribution, divided in (ordinary matter) baryonic Ω_b and Cold Dark Matter Ω_{CDM}, with Ω_Λ the cosmological constant, and with Ω_r the radiation, due to the relativistic components, photons and neutrinos in relativistic regime. Cosmological constant and Dark Matter are two phenomenological solutions to problem that cannot be explained with known physics, namely the accelerated expansion of the Universe and the problem of missing matter. We also introduced the *total density parameter* Ω_0, that provides an indipendent way to constrain the curvature of the Universe, via the parameter k in Ω_k:

$$\left\{ \begin{array}{lllll} \Omega_0 > 1, & \sum \rho > \rho_c, & \Omega_k < 0, & k > 0, & \text{closed} \\ \Omega_0 = 1, & \sum \rho = \rho_c, & \Omega_k = 0, & k = 0, & \text{flat} \\ \Omega_0 < 1, & \sum \rho < \rho_c, & \Omega_k > 0, & k < 0, & \text{open} \end{array} \right\} \tag{1.33}$$

Considering how the density parameter of the different component depends on the scale factor $a(t)$, we can write the eq. (1.16) as:

$$H^2 = \left(\frac{\dot{a}}{a} \right)^2 = H_0^2 \left(\frac{\Omega_r}{a^4} + \frac{\Omega_m}{a^3} + \frac{\Omega_k}{a^2} + \Omega_\Lambda \right) \tag{1.34}$$

So, while a is increasing with time, the different components will dominate the expansion of the Universe at different times. The H^2 as a function of a is shown in Figure 1.1. Primarily, for the smallest value of $a(t)$, the Universe expansion is driven by radiation, then it will be matter dominated, after curvature dominated and finally in the cosmological constant period[1].

The second Friedmann equation (1.18) becomes:

$$-\frac{1}{H_0^2} \left(\frac{\ddot{a}}{a} \right) = \frac{\Omega_r}{a^4} + \frac{1}{2} \frac{\Omega_m}{a^3} - \Omega_\Lambda \tag{1.35}$$

and we can define the *deceleration parameter* q_0 as

$$q_0 = -\frac{1}{H_0^2} \left(\frac{\ddot{a}}{a} \right)_{t=t_0}. \tag{1.36}$$

If q_0 is negative the Universe is accelerating, else decelerating. The presence of Ω_Λ gives a negative q_0.

Finally, solving the eq. (1.34) for the different epochs of the Universe, we obtain the evolution of the scale factor a with time. We can demonstrate that, considering

---

[1]This is true in general, also if the observations prefer a negligible curvature and the cosmological constant must be confirmed.

the initial condition $a(t=0) = 0$ and $a(t_0) = 1$ (where t_0 is 'today'), and fixing the curvature $k = 0$ (flat Universe), in the radiation epoch we have:

$$\left(\frac{\dot{a}}{a}\right)^2 = \Omega_r \frac{H_0^2}{a^4} \Rightarrow a(t) = \left(\sqrt{\Omega_r}H_0\right)^{1/2} t^{1/2}; \tag{1.37}$$

in the matter epoch:

$$\left(\frac{\dot{a}}{a}\right)^2 = \Omega_m \frac{H_0^2}{a^3} \Rightarrow a(t) = \left(\frac{3}{2}\sqrt{\Omega_m}H_0\right)^{2/3} t^{2/3}; \tag{1.38}$$

and in the cosmological constant epoch:

$$\left(\frac{\dot{a}}{a}\right)^2 = \Omega_\Lambda H_0^2 \Rightarrow a(t) = e^{\sqrt{\Omega_\Lambda}H_0(t-t_0)}. \tag{1.39}$$

As we will see in the next chapters, current observations provided from the Planck experiment, see Ref. [5], are in agreement with an Universe with parameters with values of about: $H_0 = 68 Km/s/Mpc$, $\Omega_m = 0.32$, $\Omega_\Lambda = 0.68$, $\Omega_r \sim 5 \times 10^{-5}$, and $k = 0$ (i.e. flat Universe). This model is now practically a "cosmological standard model" and is often referred in the literature as ΛCDM model. The ΛCDM model provides an accurate description of the Universe evolution from the primordial, hot, uniform era to now.

1.2.2 The cosmological redshift

In an expanding Universe we expect a stretching of the path of the travelling photons and consequently a red-shifting of their wavelength. There is an important relationship between the observed *cosmological redshift z* and the value of *scale factor a* at the time of photon emission.

The photon path in the space-time is described by a nil $ds = 0$ four-dimensional geodetic: $c^2 dt^2 = a^2(t)dr^2$. Given an electromagnetic wave, we define the emitted wavelength λ_e as the distance between two consecutive peaks in its (laboratory) rest frame, and the observed wavelength λ_o the distance between two consecutive peaks in the observer's rest frame, that is moving following the expansion of the Universe respect to the source.

The redshift is then defined as:

$$z = \frac{\lambda_o - \lambda_e}{\lambda_e}. \tag{1.40}$$

If we account that also the wavelength will follow the expansion of the Universe according to:

$$\lambda(t) = a(t)\lambda_0 \tag{1.41}$$

we arrive at:

$$\frac{a(t_o)}{a(t_e)} = \frac{\lambda_o}{\lambda_e} = 1 + z. \tag{1.42}$$

This means that, given a distant object, the redshift that we observe depends only on the ratio between the two scale factors and not on the manner in which the transition from $a(t_e)$ to $a(t_o)$ happened. Using the normalization $a(t_0) = 1$, we obtain:

$$1 + z = a^{-1}(t_e). \tag{1.43}$$

1.2.3 The Hubble law

As we discussed in the previous sections, our Universe is expanding and we have defined as H the rate of its expansion. Moreover, we have introduced the redshift z as the quantity with which we quantify the shift of the spectral lines of distant sources, such as galaxies.

Georges Lemaître and Edwin Hubble found that the redshift of objects increased with their distance. If we interpret this shift as a Doppler effect, we have that further objects appear to recede faster from us: the Universe is in expansion. In first approximation, for redshifts much smaller than one ($z \ll 1$), we can derive the Hubble law, that relate distance and redshift of an object, in this way:

$$cz = H_0 D_L \tag{1.44}$$

where H_0, the *Hubble constant*, is the expansion rate of the Universe today, and D_L the luminosity distance of the object. The *luminosity distance* is defined as:

$$D_L = \left(\frac{L}{4\pi f}\right)^{1/2} \tag{1.45}$$

where L is the known luminosity of the source, and f is the observed photons flux.

Indeed the true and general relationship between distance and redshift, valid also for larger redshifts, is more complicated. Moreover, the interpretation of the cosmological redshift as a Doppler effect is not correct, because is not due to peculiar velocities of the objects, but to the expansion of the space-time.

1.3 The hot Big Bang

The primordial Universe was made of a hot and homogeneous expanding plasma, with high energy density and temperature. Radiation, i.e. photons and neutrinos, and relativistic matter were kept in thermodynamic equilibrium through particle-antiparticle annihilation and pairs creation reactions, until the rate of these reactions $\Gamma = n\sigma <v>$, with n the particles density, σ the cross section and $<v>$ the average velocity, was greater than or equal to the rate of the Universe expansion H. When this condition was no longer verified, we have the *decoupling* between the particle species. In cosmology, two decoupling epochs are of particular interest since they provide observable consequences: the *neutrino decoupling*, with important implications for BBN and CMB, since it fixes the total relativistic energy content today, and the *photon decoupling*, observable today as the CMB.

1.3.1 The Universe cooling

From the *first law of thermodynamics* we know that:

$$dE = d(\rho V) = -pdV + TdS, \tag{1.46}$$

where E, V and S are, respectively, the energy, the volume and the entropy of the considered system. Therefore, we have:

$$S = \frac{E + PV}{T} = \frac{(\rho + P)V}{T}. \tag{1.47}$$

Defined the *entropy density* as follows:

$$s = \frac{S}{V} \tag{1.48}$$

we have:

$$s = \frac{\rho + P}{T}. \tag{1.49}$$

Using the distribution functions f_i defined in eq. (1.15), and considering the *energy density* introduced in the eq. (1.13) for relativistic particles with $m \ll T$:

$$\rho_i = g_i \int \frac{d^3 p}{(2\pi\hbar)^3} E(p) f_i(\vec{x}, \vec{p}) \tag{1.50}$$

we obtain in the two different cases:

$$\rho = \begin{cases} \rho_B = g_B \frac{\pi^2}{30} T^4, & bosons \\ \rho_F = \frac{7}{8} g_F \frac{\pi^2}{30} T^4, & fermions \end{cases} \tag{1.51}$$

Therefore the plasma total density will be:

$$\rho_r = g_{tot} \frac{\pi^2}{30} T^4 \tag{1.52}$$

with

$$g_{tot} = \sum_b g_B + \frac{7}{8} \sum_f g_F. \tag{1.53}$$

Remembering that a perfect fluid follows the equation of state 1.19, the plasma will have $P = (1/3)\rho$, and then

$$s = \frac{4}{3} \frac{\rho}{T} = \frac{2\pi^2}{45} g_{tot} T^3. \tag{1.54}$$

We remind that the pressure P_i can be expressed as an integral over the distribution function f_i defined in eq. (1.15) in the following way, eq. (1.14) :

$$P_i = g_i \int \frac{d^3 p}{(2\pi\hbar)^3} f_i(\vec{x}, \vec{p}) \frac{p^2}{3E(p)}. \tag{1.55}$$

We know that for almost all particles, the chemical potential μ is much smaller than the temperature, so, in good approximation, we can consider the distribution function only dependent on E/T. Therefore, we can write:

$$\frac{\partial P_i}{\partial T} = \frac{\rho_i + P_i}{T}. \tag{1.56}$$

We can demonstrate, using this relationship (see Ref. [13]), that the entropy density of the Universe scales as a^{-3}:

$$sa^3 = const. \tag{1.57}$$

Combining the eq. (1.54) with the eq. (1.57), we can conclude that

$$T \propto \frac{1}{a(t)\sqrt[3]{g_{tot}}}, \tag{1.58}$$

and, when $g_{tot} = const$, also the temperature scales as a^{-1}.

While expanding, the Universe cools, passing through several fundamental phases, as we will see in the following subsections.

1.3.2 The Planck Era

In the earliest moments of life of the Universe, the theories place the *quantum gravity*, in which we have the quantization of the gravity and the loss of validity of both General Relativity and quantum mechanics. In this phase, at about $t < 10^{-43}s$ after the Big Bang and $T \sim 10^{19} GeV$, starts the Planck era. All the fundamental forces (electromagnetic, weak and strong) are unified in a single one force, in which the particles are in thermal equilibrium.

From the *uncertainty principle* of Heisenberg $\Delta E \cdot \Delta t \geq \hbar$, we can compute the typical quantities of the Planck era. The most massive object that can be described by General Relativity is a black hole with radius R and mass $M = Rc^2/G$. Its energy is equal to $E = Rc^4/G$. Considering that the time traveled by light is $t = R/c$, we can define the Planck radius R_P:

$$R_P = \left(\frac{G\hbar}{c^3}\right)^{\frac{1}{2}} \sim 10^{-33} cm, \tag{1.59}$$

from which we derive the so called Planck mass:

$$M_P = \left(\frac{c\hbar}{G}\right)^{\frac{1}{2}} \sim 10^{-5} g; \tag{1.60}$$

and

$$t_P = \left(\frac{G\hbar}{c^5}\right)^{\frac{1}{2}} \sim 10^{-43} s, \tag{1.61}$$

$$E_P = \left(\frac{c^5\hbar}{G}\right)^{\frac{1}{2}} \sim 10^{19} GeV, \tag{1.62}$$

$$T_P = \sim 10^{32} K. \tag{1.63}$$

Using the natural units $c = \hbar = 1$, we can express everything in mass unit $G = M_P^{-2}$.

1.3.3 Inflation and baryogenesis

During inflation (in the first $\sim 10^{-30}s$), we have an exponential expansion of the Universe, driven by the Inflaton field (see Section 2.7). After the Inflaton decay, the released energy will produce particle-antiparticle pairs, that annihilate themselves istantaneously for the very high temperature and the relativistic velocities. For the symmetry of the creation and destruction processes, we expect that all the baryonic matter produced should disappear totally. Nevertheless in the Universe we observe the baryons, while the anti-baryons are almost totally absent. We need processes that provide an excess of particles respect to antiparticles: we call it *Baryogenesis Era* ($10^{17} GeV > T > 10^2 GeV$, $t \sim 10^{-33}s$). These physical processes are allowed in the *Grand Unified Theories* GUTs and break several symmetries: the baryonic number conservation, the charge conjugation (C) and this latter combined with the parity (CP). The simplest theory GUT has a symmetry $SU(5)$, that breaks spontaneously in $SU(3) \times SU(2) \times U(1)$ falling below the scale $E_{GUT} = 10^{15} GeV$, at $t_{GUT} = 10^{-37}s$. The direct result will be the separation between the *strong force* and the *electroweak force*, with the formation of gluons g, quark-antiquark ($q\bar{q}$) pairs and *magnetic monopoles*.

1.3.4 Electroweak transition

In the meantime the Universe continues to cool, and at a temperature of about $T_{EW} = 10^2 GeV$, i.e. $t_{EW} = 10^{-11}s$, we have the separation between the *electromagnetic force* and the *weak force*, due to breaking of the $SU(2) \times U(1)$ symmetry. In this phase the leptons acquire mass and the old bosons, intemediaries of the electroweak force, divide them between massive bosons, mediators of the weak interaction, i.e. Z_0 and $W^{\pm}$, and those massless of the electromagnetic force, i.e. the photons γ.

1.3.5 Quark-hadron transition

At a temperature of about $T_{QH} \simeq 200 - 300 MeV$, correspondig to $t_{QH} \simeq 10^{-5}s$, we have the last symmetry breaking, with the resulting confinement of quarks in hadrons: states qqq (baryons) and $q\bar{q}$ (mesons), held together thanks to the strong force.

1.3.6 The Cosmic Neutrino Background

Neutrinos are initially coupled to the rest of the primeval plasma through these weak interactions:

$$\nu + e^- \leftrightarrow \nu + e^-, \tag{1.64}$$

$$n + \nu_e \leftrightarrow p^+ + e^-, \tag{1.65}$$

$$n + e^+ \leftrightarrow p^+ + \bar{\nu}_e. \tag{1.66}$$

At that time, they have a momentum spectrum with an equilibrium Fermi-Dirac distribution at temperature T equal to:

$$f_{eq}(p) = \frac{1}{e^{(p-\mu_\nu)/T} + 1}, \tag{1.67}$$

where p is the momentum and μ_ν is the neutrino chemical potential, that is different from zero if there is a neutrino-antineutrino asymmmetry, see Ref. [15, 16, 17, 18]. Their weak interaction rate is

$$\Gamma_\nu = \langle \sigma_\nu n_\nu \rangle, \tag{1.68}$$

with $\sigma_\nu \propto G_F^2$ the cross section of the electron-neutrino process, G_F the Fermi constant and n_ν the neutrino number density. Neutrinos decouple from the rest of the plasma, when the rate of the interaction reactions, which keep them in thermodynamic equilibrium with the primeval plasma, becomes smaller than the expansion rate of the Universe

$$H = \sqrt{\frac{8\pi\rho}{3M_{Pl}^2}}, \tag{1.69}$$

where ρ is the total energy density and M_{Pl} the Planck mass. According to Ref. [15], if we consider $\Gamma_\nu \approx G_F^2 T^5$ and $H \approx T^2/M_{Pl}$, approximating the numerical factor to unity, we obtain a decoupling temperature of about $T_{dec} \approx 1 MeV$.

Therefore, in the standard cosmological model, a Cosmic Neutrino Background (CNB) is expected to be formed when the temperature falls below $T \sim 1 MeV$, and the Universe cannot transform anymore protons into neutrons, that have a difference of masses of $1.293 MeV$. From this moment neutrinos cease to interact and start to propagate freely (*free streaming*). Their distribution remains Fermi-Dirac, but their temperature falls as a^{-1}. After neutrinos decoupling, photons start to be heated by electrons-positrons annihilation:

$$e^- + e^+ \leftrightarrow \gamma + \gamma. \tag{1.70}$$

When the Universe temperature falls below $T \sim 0.5 MeV$, i.e. of order of electron mass, this reaction above proceeds only in the rightwards direction, producing the extra photons, that rapidly thermalize. From this moment the ratio between the temperatures of the backgrounds of neutrinos and photons will be fixed, despite the temperature decreases with the expansion of the Universe. If neutrinos decouple istantaneously, we can assume that the entropy transfer of this annihilation did not affect the decoupled neutrinos, and we can calculate the ratio between the temperature of relic photons and neutrinos, see Ref. [13].

Before the annihilation, at the scale factor a_1, to the total entropy density s contibute massless bosons, such as photons in 2 spin states, with $2\pi^2 T^3/45$ for each spin state; massless fermions, such as electrons in 2 spin states, positrons in 2 spin states, 3 generation of neutrinos and 3 of anti-neutrinos, each in 1 spin state, with

$(7/8) \times (2\pi^2 T^3/45)$ for each spin state; and massive fermions in negligible way. The total entropy density will be:

$$s(a_1) = \frac{2\pi^2}{45} T_1^3 \left[2 + \frac{7}{8}(2 + 2 + 3 + 3) \right] = \frac{43\pi^2}{90} T_1^3, \tag{1.71}$$

with T_1 the common temperature of the several components in a_1.

After annihilation, at the scale factor a_2, the electrons and positrons do no longer contribute to the total entropy density, and photons and neutrinos have temperatures no longer equal. Therefore we have:

$$s(a_2) = \frac{2\pi^2}{45} \left[2T_\gamma^3 + \frac{7}{8} 6 T_\nu^3 \right]. \tag{1.72}$$

We know that the total entropy density scales as a^{-3}, eq. (1.57), so we can equate (assuming that during the process the total entropy is approximately constant) :

$$s(a_1)a_1^3 = s(a_2)a_2^3 \tag{1.73}$$

obtaining

$$\frac{43}{2} (a_1 T_1)^3 = 4 \left[\left(\frac{T_\gamma}{T_\nu} \right)^3 + \frac{21}{8} \right] (T_\nu(a_2)a_2)^3. \tag{1.74}$$

Since neutrino temperature scales as a^{-1}, we have also

$$a_1 T_1 = a_2 T_\nu(a_2). \tag{1.75}$$

So, the ratio between the temperature of relic neutrinos and photons is:

$$\frac{T_\nu}{T_\gamma} = \left(\frac{4}{11} \right)^{1/3}, \tag{1.76}$$

that remains the same until now. Therefore we expect today a CNB at a temperature of about $T_\nu = T_\gamma \left(\frac{4}{11} \right)^{1/3} \simeq 1.945K$.

If the sum of the active neutrino masses is less than $1eV$, they are relativistic at the decoupling era. The relativistic neutrinos contributes to the present energy density of the Universe in this way:

$$\rho_{rad} = \rho_\gamma + \rho_\nu = g_\gamma \left(\frac{\pi^2}{30} \right) T_\gamma^4 + g_\nu \left(\frac{\pi^2}{30} \right) \left(\frac{7}{8} \right) T_\nu^4 \tag{1.77}$$

where we considered the different behavior of bosons and fermions, i.e. their different distribution functions, eq. (1.51). If we rewrite the latter equation (1.77) as a function of the photon energy density, that we know perfectly thanks to the CMB measurements, we obtain:

$$\rho_{rad} = \rho_\gamma \left(1 + \left(\frac{7}{8} \right) \left(\frac{4}{11} \right)^{4/3} \left(\frac{g_\nu}{g_\gamma} \right) \right) \tag{1.78}$$

using the eq. (1.76), that is valid only for instantaneous neutrino decoupling. In fact, in a more accurate analysis, the neutrino decoupling and the electrons-positrons

annihilation are sufficiently close in time to produce some residual interactions between $e^{\pm}$ and ν's. These interactions lead to a slightly smaller increase of the comoving photon temperature, than the case of istantaneous decoupling. We define *the effective number of relativistic degrees of freedom N_{eff}*, the ratio:

$$N_{\text{eff}} = \frac{g_\nu}{g_\gamma} \tag{1.79}$$

expected equal to 3.046, instead of 3 for the different neutrino flavours, to take into account effects for the non-instantaneous neutrino decoupling and neutrino flavour oscillations, see Ref. [19]. The relic active neutrinos density does not depend on the nature of neutrinos, either Dirac or Majorana particles. This is because in the computation of the degrees of freedom, we have to take into account only of those that are populated and brought into equilibrium before the time of neutrino decoupling, and are the same in both the cases. The value of N_{eff} is constrained at the BBN epoch, comparing experimental data with theoretical predictions on the primordial abundances of light elements, such as helium ^4He and deuterium D, which also depend on the baryon-to-photon ratio, $\eta = n_b/n_\gamma$. Moreover, independent constraints on this paramater N_{eff} at a later epoch, can be extracted from the power spectrum of CMB anisotropies. To find a $\Delta N_{\text{eff}} = N_{\text{eff}} - 3.046$ means to be able to constrain the *dark radiation*. This amount of dark radiation could be due to extra-relics relativistic non-standard particles present at the recombination epoch, such as hot axions or sterile neutrinos, see Refs. [20, 21]. Otherwise could be due to the bias given by other effects not considered in the standard scenario, such as a non-zero chemical potential in the neutrino distribution, like in the Curvaton model, see Refs. [22, 23]. Or also could be due to the degeneracies with parameters that mimic the same effect on the observables or systematics in the experiments. We will go through these several options in the following chapters.

Therefore, accounting for the different distribution function of bosons (photons) and fermions (neutrinos), see eq. (1.51), we have that the neutrino density is given by:

$$\rho_\nu = 3.046 \times \frac{7}{8} \left(\frac{4}{11}\right)^{4/3} \rho_\gamma \tag{1.80}$$

where the factor 3.046 is for the three neutrino (and antineutrino) flavours (electron, muon and tau), and the photon density is well measured by the CMB, providing $\Omega_\nu h^2 = 1.68 \times 10^{-5}$ for massless neutrinos. In the standard model of particle physics neutrinos are chargeless massless leptons. Indeed from neutrino oscillation experiments, we know that neutrinos are massive and the three masses of the mass-eigenstates are not totally degenerete, but at least, two neutrino states have mass enough for being non relativistic at present time. So in the non-relativistic regime, the massive neutrino energy density will be:

$$\Omega_\nu = \sum_i \frac{m_\nu^i}{92.5 h^2 eV} \tag{1.81}$$

with $i = e, \mu, \tau$.

1.3.7   Big Bang Nucleosynthesis

With *Big Bang Nucleosynthesis* we indicate the epoch between $10 MeV > T > 0.1 MeV$ and $10^{-2} < t < 10^2 s$.

Nuclei may be formed when the temperature is no longer so high to break the chemical bonds. This happens, in an efficient way, when the temperature is significantly lower than the binding energy, due to the very high density of photons, that have a black body spectrum, respect to the baryons. We introduce η the ratio between the number density of baryons and photons:

$$\eta = \frac{n_b}{n_\gamma} \simeq 2.68 \cdot 10^{-8} \Omega_b h^2, \tag{1.82}$$

and the mass fraction X_a of the nucleus a:

$$X_a = \frac{A n_a}{n_b} \tag{1.83}$$

as the ratio between the mass number A times the number density n_a of the nucleus a, and the baryon number density n_b. At thermal equilibrium, the non-relativistic proton number density is:

$$n_p = g_p \left(\frac{m_p T}{2\pi} \right)^{\frac{3}{2}} exp \left(-\frac{(m_p - \mu_p)}{T} \right), \tag{1.84}$$

with μ the chemical potential, and the neutron number density is:

$$n_n = g_n \left(\frac{m_n T}{2\pi} \right)^{\frac{3}{2}} exp \left(-\frac{(m_n - \mu_n)}{T} \right), \tag{1.85}$$

with $g_p = g_n = 2$ degrees of freedom.

Moreover, is valid the *Saha equation*:

$$\mu_a = (A - Z)\mu_n + Z\mu_p, \tag{1.86}$$

with Z the atomic number. Combining all the equations from the [1.82-1.86] we obtain:

$$X_a = g_a A^{\frac{5}{2}} 2^{\frac{3A-5}{2}} \zeta_3^{A-1} \pi^{\frac{1-A}{2}} \left(\frac{T}{m_b} \right)^{\frac{3(A-1)}{2}} \eta^{A-1} X_p^Z X_n^{A-Z} e^{\left(\frac{B_a}{T} \right)} \tag{1.87}$$

where $B_a = (A - Z)m_n + Zm_p - m_a$ is the binding energy of the nucleus a. In order to have $X_a \approx 1$, we need $(B_a/T) \gg 1$, to compensate for a η^{A-1} very small.

Until the thermal equilibrium is kept, we have the conversion of protons in neutrons and viceversa, via the processes:

$$\nu + n \leftrightarrow p + e \tag{1.88}$$

$$\bar{e} + n \leftrightarrow p + \bar{\nu} \tag{1.89}$$

and the Saha equation (1.86) becomes

$$\mu_n = \mu_p. \tag{1.90}$$

Defined $Q = m_n - m_p \approx 1.29 MeV$ as the difference between neutron and proton masses, the ratio between the number densities (1.84) and (1.85) is equal to:

$$\frac{n_n}{n_p} = \frac{X_n}{X_p} = exp\left(-\frac{Q}{T}\right) \tag{1.91}$$

which is valid until the rate of the reactions (1.88) and (1.89) is greater than H, the rate of the Universe expansion. When the expansion becomes too fast, neutrons and protons are no longer in equilibrium and we have the *freeze-out* of the ratio (1.91) at the value of 1/6. Only the beta decay of the neutron continues to have place, with a lifetime $\tau_n \sim 880s$:

$$n \to p + e + \bar{\nu} \tag{1.92}$$

leading the ratio (1.91) at the value of 1/7. At this point starts the *primordial nucleosynthesis*, i.e. the formation of the first light nuclei, at the temperature of about $T = 0.8 MeV$, via the synthesis reactions of Deuterium D, of Helium ^3He and ^4He, and in small percentages also of Litium ^7Li:

$$n + p \leftrightarrow D + \gamma \tag{1.93}$$

$$D + p \leftrightarrow^3 He + \gamma \tag{1.94}$$

$$D + D \leftrightarrow^4 He + \gamma. \tag{1.95}$$

The heavier elements are produced, instead, subsequently in the synthesis reactions during the stellar evolution.

The nucleosynthesis allows to discriminate between the several theories of the standard model, comparing the expected abundances of the different elements with those observed. For example, assuming that all the free neutrons form ^4He, i.e. $n_{He} = (n_n/2)$, we can compute its primordial abundance, with $(n_n/n_p) = (1/7)$:

$$Y_{\mathrm{p}} = \frac{4n_{^4He}}{n_n + n_p} = \frac{n_n}{n_n} \frac{4 \cdot \frac{1}{2}}{\left(1 + \frac{n_p}{n_n}\right)} = 0.25. \tag{1.96}$$

Comparing the deuterium measurements, we can also estimate the baryon density $\Omega_b h^2$ and then η.

1.3.8   Recombination

The Universe, thanks to cooling due to the expansion, passes through the phase of recombination, in which electrons and protons combine into hydrogen atoms (the first neutral atoms $t \sim 10^6 s$), and the phase of decoupling, in which becomes trasparent to the motion of photons. The Hydrogen has a binding energy of $B_H = 13.6 eV$, but as explained previously, it will be formed at a temperature smaller than B_H

for the very high density of photons respect to the baryons. We can compute this temperature T_{rec} using the Saha equation for the reaction:

$$p + e^- \rightarrow H + \gamma. \tag{1.97}$$

Considering the Boltzmann statistics for no longer relativistic particles, we have that the number density of the $i - th$ particle is:

$$n_i \simeq g_i \frac{(m_i k_B T)^{\frac{3}{2}}}{\hbar^3} exp\left(\frac{\mu_i - m_i c^2}{K_B T}\right). \tag{1.98}$$

Using the chemical potentials equilibrium $\mu_e + \mu_p = \mu_H$, and defining the ionization fraction for the electron $x_e = \frac{n_e}{n_e + n_H}$ (with $n_e = n_p$) and the binding energy $B_H = (m_p + m_e - m_H)c^2$, we obtain the Saha equation:

$$\frac{1 - x_e}{x_e} = n_\gamma \eta \left(\frac{\hbar^2}{2\pi m_e k T}\right)^{\frac{3}{2}} exp\left(\frac{B}{kT}\right). \tag{1.99}$$

Replacing the values, we get $T_{rec} \simeq 3000K$, corresponding to a redshif $z_{rec} = 1300$.

The recombination of electrons and protons into neutral hydrogen atoms coincides with the trasparency of the Universe. Before the recombination, all the ordinary matter in the Universe was under the form of a completely ionized plasma, and the free electrons caused the opacity of the Universe. The photons interact mainly with the free electrons via Thomson and Compton scatterings, and with the atoms via Rayleigh scattering. At the T_{rec} the Thomson scattering

$$\gamma + e^- \rightarrow \gamma + e^- \tag{1.100}$$

is the predominant reaction and hinders the photons propagation, because their free mean path is much smaller than the current dimension of the Universe. Its rate is equal to $\Gamma = n_e \sigma_e c$, where $\sigma_e \simeq 6.65 \cdot 10^{-25} cm^2$ is its cross section, and n_e is the free electron number density. The characteristic time of this reaction is $\gamma = 1/\Gamma$ and in order to have the thermal equilibrium it must be smaller than the time scale of the Universe expansion: $\gamma < H^{-1}$. When is the radiation to dominate the Universe expansion, the coupling condition is verified, because $H^{-1} = 2t$ and $\gamma \sim t^{3/2}$. Instead, after the matter-to-radiation equality at $z \sim 3570$, during the matter epoch, $H^{-1} = 3t/2$ and $\gamma \sim t^2$: in this case we obtain that the Thomson scattering ceased to be efficient just after the decoupling time, at a redshift $z \sim 1100$. At this epoch Γ falls below the expansion rate H and the Universe becomes trasparent to the motion of the photons. Therefore, the radiation decouples from the plasma, with which was in thermodynamics equilibrium, and hereinafter the photons at a $T \simeq 3000K$ propagate freely until us (*free streaming*), keeping the shape of the black body spectrum of the primordial plasma, but cooling with the expansion of the Universe. At the recombination, each CMB photon had the last scattering and we can observe this *Last Scattering Surface* through its emission of light, the CMB.

1.4   The Cosmic Microwave Background

The Cosmic Microwave Background, predicted for the first time in 1948 by Gamow, Alpher and Herman as a direct consequence of the *hot Big Bang theory*, was discovered accidentally in 1964 by Arno Penzias and Robert Wilson, like a background thermal noise of a transmission antenna, isotropic and coming from all the directions with the same intensity. However, was Robert Dicke whom explained this signal as a radiation coming from the recombination era, and was the FIRAS (Far Infrared Absolute Spectrophotometer, see Ref. [24]) experiment, of the COBE (Cosmic Background Explorer, see Ref. [25]) satellite in 1992 to demonstrate its black body spectrum at a temperature of about $T_\gamma = 2.726K$.

Until the recombination epoch, as already discussed, we have the thermodynamics equilibrium of the primordial plasma: a dense, hot, opaque body produces a black body radiation, given by the Planck distribution. This means that, when photons decouple, have, in the frequency range $[\nu, \nu + d\nu]$ at the temperature T, an energy density given by the Planck distribution:

$$P\left(\nu, T\right) d\nu = 8\pi h \left(\frac{\nu}{c}\right)^3 \left(e^{\frac{h\nu}{k_B T}} - 1\right)^{-1} d\nu. \qquad (1.101)$$

The energy density of a photons fluid, with $c = 1$, is:

$$\rho_\gamma = \sigma T^4. \qquad (1.102)$$

where σ is the Stephan constant. Due to the Universe expansion, the wavelengths are redshifted, so the frequencies are reduced as a^{-1}, while the volume $V \propto a^{-3}$. The result is that the energy density, that is proportional to T^4, eq. (1.102), scales as a^{-4}. The consequence will be that the shape of the black body spectrum remains the same, but its temperature decreases with a^{-1}.

Today the CMB is a black body with a temperature of about $T_\gamma = (2.7255 \pm 0.0006)K$, see Ref. [5], then going back in time, when the scale factor a was very small, the temperature and the density of the Universe were so high to allow the complete thermalization of the matter and the thermodynamics equilibrium of the plasma (hot Big Bang). The energy density, given by the eq. (1.102), of the CMB is $\rho_\gamma \simeq 4^{-14} Jm^{-3}$, and the photons number density in the Universe is $n_\gamma \simeq 411 cm^{-3}$.

Defining as τ the *optical depth* (dimensionless), we obtain that the photons flux intensity, to cross a given thickness, has an attenuation according to the law:

$$I(t_0, z) = I(t)e^{-\tau(z)}. \qquad (1.103)$$

Though in first approximation the CMB is extremely isotropic, to mimic the temperature homogeneity of the primordial plasma, without small anisotropies the structure in the Universe that we observe couldn't exist. The temperature fluctuations, given a direction of observation (θ, ϕ), are described by the ratio:

$$\frac{\Delta T}{T}(\theta, \phi) = \frac{T(\theta, \phi) - <T>}{<T>} \qquad (1.104)$$

and can be due to the primary, at the recombination, and secondary, along the way, processes. The root mean square of the temperature fluctuations are of order to, see Ref. [25]:

$$\left\langle \left(\frac{\Delta T}{T}\right)^2 \right\rangle^{1/2} \simeq 10^{-5}. \tag{1.105}$$

Moreover, the CMB shows a dipole anisotropy, due to the motion of the Earth respect to the radiation isotropy rest frame. If θ is the angle between the directions of the Earth's and photons motions, we obtain:

$$T = T_0 \left[1 + \frac{v}{c}cos\theta + \frac{1}{2}\left(\frac{v}{c}\right)^2 cos(2\theta) + O(v^3)\right]. \tag{1.106}$$

This local effect is of order to:

$$\left\langle \left(\frac{\Delta T}{T}\right)^2_{dipole} \right\rangle^{1/2} \simeq 10^{-3}. \tag{1.107}$$

To study the CMB anisotropies allow us to bound the parameters that describe the standard cosmological model, through several tools of research, such as the angular and the matter power spectra, the bispesctrum signal and the Barionic Acoustic Oscillation (BAO), how we will see in the next chapter.

Chapter 2

The Perturbed Universe

2.1 Introduction

In the previous chapter we anticipated that the current structures of the Universe started to form from small fluctuations of the matter density. The linear perturbation theory, see Ref. [26], is extremely powerful in describing the formation of structures that we see in the Universe today at scales larger than $\sim 10 Mpc$.

We start in perturbing the metric tensor, through generic functions of time and space, as, for example, the scalar fields ϕ and ψ, which will evolve following perturbed Einstein equations. Then we consider the proper Boltzmann equations, that, accounting for the interactions between the several elements, describe how the energy density perturbations depend on ϕ and ψ. We will work mainly in Fourier space since in this case, in linear perturbation theory, each mode evolves in an independent way.

2.2 The perturbed metric

As we have seen, the metric can be described by the eq. (1.4):

$$ds^2 = g_{\mu\nu}\left(\tau, x\right) dx^\mu dx^\nu \tag{2.1}$$

where in the $g_{\mu\nu}\left(\tau, x\right)$ we made esplicit the space dependence.

We can develop the latter as the sum of an unperturbed component (of background) of a flat, homogeneous and isotropic Universe $g_{\mu\nu}^0\left(\tau\right)$, and perturbations of increasing orders. We consider only the first order term obtaining:

$$g_{\mu\nu}\left(\tau, x\right) = g_{\mu\nu}^0\left(\tau\right) + \delta g_{\mu\nu}\left(\tau, x\right) \tag{2.2}$$

with $|\delta g_{\mu\nu}| \ll 1$. In general we can decompose a symmetric tensor as the sum of a scalar, a vector and a tensor component. The $\delta g_{\mu\nu}\left(\tau, x\right)$ can be therefore written:

$$\delta g_{\mu\nu}\left(\tau, x\right) = \begin{pmatrix} 2\psi & w_i \\ w_i & 2\phi\delta_{ij} + h_{ij} \end{pmatrix}. \tag{2.3}$$

The quantities ψ and ϕ are scalar fields, the $w(\tau, x)$ is a vector with three components w_i, and $h(\tau, x)$ is a symmetric 3×3 tensor with null trace, with components h_{ij}:

- the scalar component, corresponding to the quantum fluctuations of the Inflaton field, describes the density perturbations, that, growing with time, produce the large scale structures;

- the vector component, corresponding to the vector perturbations due to the generalization of a rotational fluid, is not predicted in the standard cosmological model [1] during inflation, but anyway produces vortex motion that rapidly decays;

- the tensor component describes tensor fluctuations created, for example, by primordial gravitational waves.

To determine the evolution of the metric, we have to perturb at the first order the Einstein equations (1.3). The theory must be independent by the reference frame, i.e. covariant for coordinate transformations. We want first to obtain the FLRW metric in presence of perturbations. We can rewrite the metric (2.1), using the eq. (2.3), as:

$$ds^2 = a^2 (\tau) \left\{ - (1 + 2\psi) \, d\tau^2 + 2w_i d\tau dx^i + \left[(1 - 2\phi) \, g^{(3)}_{ij} + 2h_{ij} \right] dx^i dx^j \right\} \quad (2.4)$$

with τ the conformal time and $g^{(3)}_{ij}$ the spatial component of the unperturbed FLRW metric, for which $g^{(3)}_{ij} h^{ij} = 0$. In this way we decompose the metric, and therefore the perturbations, in three indipendent components with different transformation properties: scalar $d\tau^2$ term; vector $d\tau dx^i$ term; and tensor $dx^i dx^j$ term. Overall we have 10 fields, but only 6 are independent physical degrees of freedom of the system, because for General Relativity, we can transform the 4 coordinates of the space-time without modifying the physics.

We can decompose the vector field w in a longitudinal component $w^{\parallel}$ and a transverse component $w^{\perp}$ respect to the wave vector $\vec{k}$:

$$w = w^{\parallel} + w^{\perp}. \quad (2.5)$$

The longitudinal component can be written as the gradient of a scalar function $w^{\parallel} = \nabla w_s$, because it satisfies the condition

$$\nabla \times w^{\parallel} = 0, \quad (2.6)$$

i.e. is irrotational; while the transverse component is divergenceless:

$$\nabla \cdot w^{\perp} = 0. \quad (2.7)$$

---

[1]Vector perturbations are anyway expected in models with topological defects or inhomogeneous magnetic fields.

We find both the longitudinal and transverse terms of the Einstein equations, G_{0i} and T_{0i}, when we derive the $0i$ components. The divergence of these equations selects only longitudinal terms, while the curl only transverse terms. So the two components can be treated separately, because are completely decoupled.

Similarly we can decompose the tensor field h in three terms with null trace: a longitudinal component $h^{\parallel}$, a solenoidal component $h^{\perp}$ and a transverse component h^T:

$$h = h^{\parallel} + h^{\perp} + h^T, \tag{2.8}$$

that transform respectively as a scalar term, a vector term and a tensor term. These components satisfy the relationships:

$$\epsilon_{ijk}\partial_i\partial_k h^{\parallel}_{ij} = 0, \tag{2.9}$$

$$\partial_i\partial_j h^{\perp}_{ij} = 0, \tag{2.10}$$

$$\partial_i h^T_{ij} = 0. \tag{2.11}$$

Since $\partial_i h^{\parallel}_{ij}$ is irrotational, we can define:

$$h^{\parallel}_{ij} = \left(\partial_i\partial_j - \frac{1}{3}\delta_{ij}\nabla^2\right) B, \tag{2.12}$$

where B is a scalar function. In each point, the perturbation can be described by four scalar quantities $(\phi, \psi, w^{\parallel}, h^{\parallel})$, two vector fields $(w^{\perp}, h^{\perp})$ and one tensor component of two dimensions (h^T). The perturbations of each type evolve independently from each other. The vector terms correspond to the rotational velocity perturbations, that are damped in all the known theories, while the tensor term is due to gravitational waves, and is totally decoupled from the scalar term, so we can treat them separately. Considering only the scalar quantities that derive from w_i and h_{ij}, we can build from the two scalar quantities E and B, the vector $\vec{E}$ and the traceless tensor $D_{ij}B \equiv B_{ij} - \frac{1}{3}\delta_{ij}B^{,k}_{,k}$. The eq. (2.3) becomes

$$\delta g_{\mu\nu}(\tau, x) = \begin{pmatrix} 2\psi & E_{,i} \\ E_{,i} & 2\phi\delta_{ij} + D_{ij}B \end{pmatrix}. \tag{2.13}$$

The metric (2.4) is gauge invariant: the gauge transformations leave unmodified the background metric, changing the perturbed metric. To choose a gauge means to choose a coordinate system in which we could represent the physics, that obviously remains the same. But changing gauge varies also the difficulty to calculate and to understand the physical meaning of the different quantities. Defined a comoving coordinates frame for the unperturbed system, we can, for example, choose between:

- the *newtonian gauge*;

- the *synchronous gauge*;

that we are now both going to describe.

The metric in the *conformal newtonian gauge* corresponds to the choice $w_i = h_{ij} = 0$ (or $E = B = 0$), i.e. the vector and tensor degrees of freedom are eliminated from the beginning:

$$ds^2 = a^2(\tau) \left[-(1 + 2\psi) \, d\tau^2 + (1 - 2\phi) \, dx^i dx_i \right]. \tag{2.14}$$

In this gauge the metric tensor $g_{\mu\nu}$ is diagonal, and ψ and ϕ have the clear physical meaning of, respectively, the Newton's gravitational potential and the space curvature. Only when the energy-momentum tensor T_ν^μ has longitudinal components, the two scalar potentials ψ and ϕ are different.

In the *synchronous gauge* we have both $g_{00} = -1$ and $g_{0i} = 0$ unperturbed, and $\psi = w_i = 0$:

$$ds^2 = a^2(\tau) \left[-d\tau^2 + (\delta_{ij} + h_{ij}) \, dx^i dx^j \right]. \tag{2.15}$$

and this implies the possibility of synchronizing the clocks in the whole space-time. At this choice of gauge are associated the appearance of coordinates singularities, due to the definition of the coordinates frame by a freely falling observer that can intersect each other in a point of the spacetime. This point will have two coordinates label, and spurious gauge modes, because the synchronous gauge doesn't fix the gauge degrees of freedom completely. This gauge is preferred in codes (see for example CAMB, Ref. [27]) that compute the anisotropies and inhomogeneities in the Universe, because has a better numerical behaviour.

Another possible choice one could consider is the gauge invariant formalism with the *Bardeen* variables Φ_A and Φ_B) such that $\Phi_A = \psi$ and $\Phi_B = -\phi$. This possibility removes completely the ambiguities of the choice of gauge, to the detriment of the simplicity of the formalism.

2.3   Scalar perturbation

We now consider scalar perturbations in the conformal newtonian gauge, and, in order to determine their evolution, we consider the first-order perturbed Einstein equations (see Ref. [26]). For a perfect fluid the energy-momentum tensor is given by:

$$T_\nu^\mu = P g_\nu^\mu + (\rho + P) \, U^\mu U_\nu \tag{2.16}$$

where ρ is the energy density, P is the pressure and $U_\nu^\mu = dx^\mu / \sqrt{-ds^2}$ is the four-velocity of the fluid. The four-velocity has components (considering only the first order perturbations):

$$U^0 = \frac{1}{a \, (1 + 2\psi)^{1/2}} \simeq \frac{1}{a \, (1 + \psi)} \tag{2.17}$$

$$U^i = \frac{1}{a \, (1 + 2\psi)^{1/2}} \frac{dx^i}{d\tau} \simeq \frac{v^i}{a} \tag{2.18}$$

$$U_0 = a \, (1 + 2\psi)^{1/2} \simeq a \, (1 + \psi) \tag{2.19}$$

$$U_i = -\frac{a\,(2\phi)}{(1+2\psi)^{1/2}}\delta_{ij}\frac{dx^j}{d\tau} \simeq -av_i, \tag{2.20}$$

where $v^i \equiv \frac{dx^i}{d\tau}$ is a small coordinate velocity with which the fluid moves. This can be considered as a perturbation of the same order as $\delta\rho = \rho - \bar{\rho}$ and $\delta P = P - \bar{P}$.

The components of the perturbed energy-momentum tensor, at first order, are:

$$T_0^0 = -\left(\bar{\rho} + \delta\rho\right) \tag{2.21}$$

$$T_i^0 = \left(\bar{\rho} + \bar{P}\right)v_i \tag{2.22}$$

$$T_i^j = \left(\bar{P} + \delta P\right)\delta_i^j. \tag{2.23}$$

Considering a perfect fluid the non-diagonal terms with $i \neq j$ are zero, otherwise we should have an anisotropic shear perturbation Σ_j^i in $T_j^i = \left(\bar{P} + \delta P\right)\delta_i^j + \Sigma_j^i$. This happens only to the neutrinos before recombination, because photons and baryons are tightly coupled in a single perfect fluid. This anisotropic perturbation tensor is defined as the traceless component of T_j^i:

$$\Sigma_j^i \equiv T_j^i - \frac{\delta_j^i T_k^k}{3}. \tag{2.24}$$

We can introduce two perturbation quantities, that are the dimensionless density perturbation δ, i.e. the fractional variation of the energy density respect to the mean background density $\bar{\rho}$, and the velocity divergence θ, in this way:

$$\delta = \frac{\rho(x) - \bar{\rho}}{\bar{\rho}}, \tag{2.25}$$

$$\theta = \nabla^i v_i. \tag{2.26}$$

Of course, we have a δ and θ for each fluid component. We have that δ will be negative in the sub-dense regions, its minimum value is $\delta = -1$ when $\rho = 0$, and positive in over-dense regions, without upper limits. We can use the linear perturbation theory when $|\delta|$ remains much smaller than one.

It is useful to expand all the perturbations in Fourier space, assuming that they are the sum of plane waves e^{ikr}, with $kr \equiv \vec{k} \cdot \vec{r}$:

$$\phi = \int e^{ikr}\phi_k d^3k, \tag{2.27}$$

$$\psi = \int e^{ikr}\psi_k d^3k, \tag{2.28}$$

$$\delta = \int e^{ikr}\delta_k d^3k, \tag{2.29}$$

$$\theta = \int e^{ikr}\theta_k d^3k = ik\int e^{ikr}v_k d^3k, \tag{2.30}$$

where we have omitted the tilde to indicate the Fourier transforms, and, since we work always in Fourier space, we will omit also the index k of the perturbations mode. In the linear perturbation theory, we have the same set of equations for each wave, but for different wave numbers k, that evolve independently.

The first order perturbed Einstein equations in Fourier space will be (see Ref. [26]):

$$k^2\phi + 3\frac{\dot{a}}{a}\left(\dot{\phi} + \frac{\dot{a}}{a}\psi\right) = 4\pi G a^2 \rho\delta, \tag{2.31}$$

$$k^2\left(\dot{\phi} + \frac{\dot{a}}{a}\psi\right) = 4\pi G a^2\left(\bar{\rho} + \bar{P}\right)\theta, \tag{2.32}$$

$$\ddot{\phi} + \frac{\dot{a}}{a}\left(\dot{\psi} + 2\dot{\phi}\right) + \left(2\frac{\ddot{a}}{a} - \frac{\dot{a}^2}{a^2}\right)\psi + \frac{k^2}{3}\left(\phi - \psi\right) = \frac{4\pi}{3}G a^2\delta P, \tag{2.33}$$

$$k^2\left(\phi - \psi\right) = 12\pi G a^2\left(\bar{\rho} + \bar{P}\right)\sigma, \tag{2.34}$$

where all the derivatives are respect to the conformal time τ, that is related to t as $d\tau = dt/a$, and σ is given by $\left(\bar{\rho} + \bar{P}\right)\sigma \equiv -\left(\hat{k}_i\hat{k}_j - \frac{1}{3}\delta_{ij}\right)\Sigma^i_j$. We can note that the first equation (2.31) is the relativistic generalization of the Poisson equation, and the latter equation (2.34) demonstrates that the space curvature ϕ and Newton's potential ψ are different only if the components of the Universe own an anisotropic stress σ, depending on the quadrupole moment of the perturbations.

It is possible to obtain the Euler equation:

$$\dot{\theta} = \frac{\dot{a}}{a}\left(3w - 1\right)\theta - \frac{\dot{w}}{1+w}\theta + k^2\psi - k^2\sigma - \frac{c_s^2}{1+w}k^2\delta \tag{2.35}$$

with $w = P/\rho$ and $c_s^2 = \delta P/\delta\rho$ is the adiabatic sound speed squared.

We have four independent variables for the perturbations (ϕ, ψ, δ and θ), then we need only four linear independent perturbation equations to determine their evolution, that can be obtained combining the previous equations. For example, considering a single perfect decoupled fluid, i.e. $\Sigma^i_j = 0$ and $\phi = \psi$, these could be:

$$\dot{\delta} = (1+w)\left(3\dot{\phi} - \theta\right) - 3\frac{\dot{a}}{a}\left(c_s^2 - w\right)\delta, \tag{2.36}$$

$$\dot{\theta} = -\frac{\dot{a}}{a}\left(1 - 3w\right)\theta + k^2\left(\frac{c_s^2}{1+w}\delta + \phi\right), \tag{2.37}$$

$$k^2\left(\dot{\phi} + \frac{\dot{a}}{a}\phi\right) = 4\pi G a^2\left(1 + w\right)\rho\theta, \tag{2.38}$$

$$k^2\phi + 3\frac{\dot{a}}{a}\left(\dot{\phi} + \frac{\dot{a}}{a}\phi\right) = 4\pi G a^2\rho\delta. \tag{2.39}$$

Finally, we can write the last two equations in a quasi-Poissonian form:

$$k^2\phi = 4\pi G a^2\rho\left[\delta + 3\frac{\dot{a}}{a}\left(1 + w\right)\frac{\theta}{k^2}\right]. \tag{2.40}$$

2.4 Tensor perturbation

In order to study the tensor perturbations we consider the *synchronous gauge*, see eq. (2.15):

$$ds^2 = a^2(\tau) \left[-d\tau^2 + \left(\delta_{ij} + h_{ij} \right) dx^i dx^j \right]. \tag{2.41}$$

and in order to determine their evolution, we have to perturb the Einstein equations without sources, i.e. $T_{\mu\nu} = G_{\mu\nu} = 0$.

The first order perturbed Christoffel symbols, eq. (1.11), are:

$$\delta\Gamma^0_{00} = 0, \tag{2.42}$$

$$\delta\Gamma^i_{00} = 0, \tag{2.43}$$

$$\delta\Gamma^0_{0i} = 0, \tag{2.44}$$

$$\delta\Gamma^k_{k\mu} = 0, \tag{2.45}$$

$$\delta\Gamma^j_{0i} = \dot{h}^j_i, \tag{2.46}$$

$$\delta\Gamma^0_{ij} = 2\frac{\dot{a}}{a}h_{ij} + \dot{h}_{ij}, \tag{2.47}$$

$$\delta\Gamma^j_{ki} = \partial h^j_k + \partial_k h^j_i - \partial^j h_{ki}. \tag{2.48}$$

where always the greek letters run from 0 to 3, and the roman from 1 to 3.

We can compute the perturbed Ricci's tensor components, see eq. (1.10):

$$\delta R_{00} = 0, \tag{2.49}$$

$$\delta R_{0i} = 0, \tag{2.50}$$

$$\delta R_{ij} = \ddot{h}_{ij} + 2\frac{\dot{a}}{a}\dot{h}_{ij} + 2\frac{\ddot{a}}{a}h_{ij} + 2\left(\frac{\dot{a}}{a}\right)^2 h_{ij}. \tag{2.51}$$

Finally, the perturbed Einstein equations (1.3) will be:

$$\delta G^i_j = \frac{1}{a^2}\left(\ddot{h}^i_j + 2\frac{\dot{a}}{a}\dot{h}^i_j - \partial_k \partial^k h^i_j \right) = 0. \tag{2.52}$$

Expanding the tensor perturbation in Fourier space:

$$h_{ij}\left(\tau, x\right) = \int h_{ij}\left(\tau, x\right) e^{-ikr} d^3k \tag{2.53}$$

the eq. (2.52) becomes:

$$\ddot{h} + 2\frac{\dot{a}}{a}\dot{h} + k^2 h = 0 \tag{2.54}$$

that has an analytical solution of damped harmonic oscillator, called gravitational wave, if we know the evolution of the scale factor $a(t)$. In fact, without the damping term, that depends on the expansion of the Universe $H = \dot{a}/a$, this should be a steady wave, propagating with light speed.

We saw that h_{ij} satisfies the relationships (2.9) and (2.11), that in Fourier space become:

$$h_i^i = 0 \tag{2.55}$$

$$h_i^j k_j = 0 \tag{2.56}$$

that reduce the independent components of the simmetric tensor to two degrees of freedom. These are the two polarization states of the gravitational wave. If the wave vector has the components $\vec{k} = (0, 0, k)$, the previous relationships become:

$$h_{11} = -h_{22} \tag{2.57}$$

$$h_{i3} = h_{3i} = 0. \tag{2.58}$$

Therefore, we can rewrite the equation (2.2) as:

$$g_{\mu\nu} = g_{\mu\nu}^0 + 2a^2(\tau)h_{\mu\nu}, \tag{2.59}$$

with $h_{\mu\nu}$ given by:

$$h_{\mu\nu} = \begin{pmatrix} 0, & 0, & 0, & 0 \\ 0, & h_+, & h_x, & 0 \\ 0, & h_x, & h_+, & 0 \\ 0, & 0, & 0, & 0 \end{pmatrix} \tag{2.60}$$

where h_+ and h_x are simmetric tensors, respectively, divergenceless and traceless. A result of its divergenceless is that, if the reference frame has the z axis parallel to the wave vector $\vec{k}$, that corresponds to the propagation direction of the wave, it will perturb the space time in the orthogonally (x, y) plane.

As we will see, several inflationary models predict tensor perturbations, with their amplitude being a sizable fraction of the amplitude of the scalar perturbations. An imprint of the gravitational waves is expected in the temperature and polarization anisotropies of the Cosmic Microwave Background.

2.5   The Boltzmann equation

The Boltzmann equation allows us to study the evolution of each energy density perturbations component, taking into account the interactions with other components and the metric perturbations.

In general, the Boltzmann equation describes how a thermodynamic system not in thermodynamic equilibrium statistically evolves. For each component the general form of this equation (see Ref. [28]) gives the total derivative of the distribution function $f(t)$ respect to the time. This can be written as:

$$\frac{df}{dt} = \left(\frac{\partial f}{\partial t}\right)_{force} + \left(\frac{\partial f}{\partial t}\right)_{diff} + \left(\frac{\partial f}{\partial t}\right)_{coll} \tag{2.61}$$

with the *force* term corresponding to the forces exerted by an external source on the particles, the *diff* term taking into account for the particles diffusion, and *coll* term describing all the interactions between a specific component and all the other components, such as the scattering processes. In absence of collisions, the distribution function of each component f needs to satisfy:

$$f\left(\vec{r} + \frac{\vec{p}}{m}\Delta t, \vec{p} + \vec{F}\Delta t, t + \Delta t\right) d^3\vec{r} d^3\vec{p} = f\left(\vec{r}, \vec{p}, t\right) d^3\vec{r} d^3\vec{p} \tag{2.62}$$

which shows that the number of particles, in a given portion of the phase space volume element $d^3\vec{r}d^3\vec{p}$, does not change, when a force $\vec{F}$ instantly acts on each particle, that passes from the position $\vec{r}$ and the momentum $\vec{p}$ at time t, to the position $\vec{r} + \Delta\vec{r} = \vec{r} + \vec{p}\Delta t/m$ and the momentum $\vec{p} + \Delta\vec{p} = \vec{p} + \vec{F}\Delta t$ at time $t + \Delta t$. But we have the collisions, so the particle number density will change in the following way:

$$dN = f\left(\vec{r} + \frac{\vec{p}}{m}\Delta t, \vec{p} + \vec{F}\Delta t, t + \Delta t\right) d^3\vec{r} d^3\vec{p} - f\left(\vec{r}, \vec{p}, t\right)) d^3\vec{r} d^3\vec{p}, \tag{2.63}$$

then

$$dN = \left(\frac{\partial f}{\partial t}\right)_{coll} \Delta t d^3\vec{r} d^3\vec{p} = \Delta f d^3\vec{r} d^3\vec{p}. \tag{2.64}$$

with Δf the change in the total distribution function. Taking the limits for $\Delta t \to 0$, we obtain that the total derivative of f of each component depends only on the collisional term:

$$\frac{df}{dt} = \left(\frac{\partial f}{\partial t}\right)_{coll}, \tag{2.65}$$

that in general depends on the distribution functions of all the other components.

In the Universe the phase space volume element expands, so we have to take into account also the metric perturbations. In the four-dimension space-time the total derivative of the distribution function of a component of the Universe can be written as:

$$\frac{df}{dt} = \frac{\partial f}{\partial t} + \frac{\partial f}{\partial x^i}\frac{\partial x^i}{\partial t} + \frac{\partial f}{\partial P^\mu}\frac{\partial P^\mu}{\partial t}. \tag{2.66}$$

where x^i are the components of the position $\vec{r}$ and P^μ is the four-momentum. Considering an interaction $A + B \leftrightarrow C + D$, we can write the collisional term for the component A in this way:

$$\left(\frac{\partial f\left(\vec{p}_A\right)}{\partial t} \right)_{coll} = \frac{1}{p_A} \int \frac{d^3 p_B}{\left(2\pi\right)^3 2E\left(p_B\right)} \int \frac{d^3 p_C}{\left(2\pi\right)^3 2E\left(p_C\right)} \int \frac{d^3 p_D}{\left(2\pi\right)^3 2E\left(p_D\right)}$$

$$\times |M|^2 \left(2\pi\right)^4 \delta^{(4)} \left(P_{A+B}^{\mu} - P_{C+D}^{\mu} \right) \left\{ f\left(\vec{p}_C\right) f\left(\vec{p}_D\right) - f\left(\vec{p}_A\right) f\left(\vec{p}_B\right) \right\} \tag{2.67}$$

where $|M|$ is the invariant amplitude of the considered process, and the Dirac's $\delta^{(4)}$ guarantees the conservation of the four-momentum.

2.6   The growth of linear perturbations

Linear cosmological perturbation theory is based on gravitational instability of a no longer relativistic gas, compressed by its own gravity countered by a gradient of pressure. We have that in over-dense regions, respect to the density mean of the Universe ($\delta > 0$), the gravity is stronger than the pressure of the particles and attracts more matter in the same region by making it denser; while in under-dense regions ($\delta < 0$) happens the contrary and the pressure produces random thermal motions of the particles, causing a loss of mass of that region that becomes even less dense. We can describe this process with the following equation:

$$\ddot{\delta} + \left(Pressure - Gravity\right)\delta = 0. \tag{2.68}$$

From the latter equation we can infer that when the gravity wins, the density perturbation δ grows exponentially, otherwise oscillates in time. In general, the rate of growth of the perturbations depends on the different cosmological conditions of the environments. When the Universe is matter dominated, δ grows in function of time as a power law, while when is radiation dominated grows only logarithmically. In order to create structures, the over-dense region has to be both greater than the *Jeans Length*, necessary condition to collapse under its own gravity instead of to oscillate making stable sound wave (hydrostatic equilibrium), and faster in the collapse (t_{dyn}) than the characteristic time of expansion of the Universe. The Jeans Length is defined as:

$$\lambda_J \equiv c_s \left(\frac{c^2 \pi}{G\bar{\rho}} \right)^{1/2} = 2\pi c_s t_{dyn} \tag{2.69}$$

with the sound speed

$$c_s = c \left(\frac{dP}{d\rho} \right)^{1/2} = c\sqrt{w} \tag{2.70}$$

where $w > 0$ is the parameter of the equation of state of a non relativistic gas. This is approximately

$$w \approx \frac{kT}{\mu c^2} \tag{2.71}$$

with T the temperature and μ the mean mass of the particles of the gas. So the pressure of the gas increases with the temperature, and the pressure gradient

propagates with the sound speed c_s, with the characteristic time $t_{pres} \sim R/c_s$, in a region of radius R. The hydrostatic equilibrium is reached when $t_{pres} < t_{dyn}$, i.e. when predominates the pressure on the gravity.

In a flat expanding Universe, the Jeans length is:

$$\lambda_J = 2\pi \left(\frac{2}{3}\right)^{1/2} \frac{c\sqrt{w}}{H(t)}. \tag{2.72}$$

Depending on the value of the w, different for the different components, the density fluctuation will be supported or not by pressure, collapsing or not under its own gravity. For example, in the radiation dominated Universe, when $w = 1/3$, the fluctuations don't collapse, but produce stable wavelengths: the density fluctuations are supported by pressure, if are approximately smaller than three times the Hubble radius cH^{-1}. We need a component with $w \sim 0$ to have collapsed structures. To produce the observed structures of the Universe the baryons are not enough, because until they are coupled to the photons they have $w \sim 1/3$, and so they could start to produce structures only after decoupling, when their equation of state w becomes approximately zero. Therefore, we have to introduce a dark matter component that does not have pressure gradients, for which the Jeans length is approximately always negligible, that starts to collapse well before decoupling, and makes gravitational potential wells into which the ordinary matter falls after its decoupling.

If we move to Fourier space, all the modes evolve in an independent way. In the beginning they are outside the causal horizon and their behaviour depends on the chosen gauge. The causal horizon is defined as $d_h(t) = a(t) \int_0^t dx = a(t) \int_0^t \frac{cdt'}{a(t')}$ and represents the maximum physical distance on which the photon can propagate at time t. Then the modes enter into the causal horizon, but their evolution, the same in either the gauges, depends whether the Universe is radiation or matter dominated, i.e. if the causal horizon crossing of the wavelengths happens before or after the equivalence epoch.

To have an idea of the evolution of the perturbations in these different epochs, we can use a Newtonian approch. The perturbation equations (2.36), (2.37) and (2.40), in the Newtonian limit, for small scales $k \gg \dot{a}/a$, become (see Ref. [29]):

$$\dot{\delta} = -\theta, \tag{2.73}$$

$$\dot{\theta} = -\frac{\dot{a}}{a}\theta + c_s^2 k^2 \delta + k^2 \phi, \tag{2.74}$$

$$k^2 \phi = -4\pi G a^2 \rho \delta, \tag{2.75}$$

where the latter equation is the Fourier version of the Poisson equation. Deriving the first equation (2.73), and substituting the other equations (2.74) and (2.75), we obtain:

$$\ddot{\delta} + \frac{\dot{a}}{a}\dot{\delta} + \left(k^2 c_s^2 - 4\pi G a^2 \rho\right)\delta = 0. \tag{2.76}$$

Now, considering $c_s^2 = 0$ and δ for the matter density fluctuations, we have:

$$\ddot{\delta} + \frac{\dot{a}}{a}\dot{\delta} - 4\pi G a^2 \rho_m \delta = 0, \tag{2.77}$$

We can rewrite the latter equation in terms of the density paramater $\Omega_m = \rho_m/\rho_c$. Moreover, we replace the derivatives respect to the conformal time τ, denoted with $\dot{-}$, with the derivatives respect to time t, denoted with $-'$, remembering that $d\tau = dt/a$. We obtain:

$$\delta'' + 2H\delta' - \frac{3}{2}\Omega_m H^2 \delta = 0. \tag{2.78}$$

where $H = a'/a$. During the epoch of radiation, we can approximate $\Omega_m \approx 0$ and $H = a'/a = 1/2t$. The eq. (2.78) becomes in this case:

$$\delta' + \frac{1}{t}\delta' = 0, \tag{2.79}$$

which has a solution of logarithmic growth for the perturbations:

$$\delta(t) = B_1 + B_2 lnt. \tag{2.80}$$

During the epoch of matter, we can approximate $\Omega_m = 1$ and $H = 2/3t$. The eq. (2.78) becomes:

$$\delta'' + \frac{4}{3t}\delta' - \frac{2}{3t^2}\delta = 0, \tag{2.81}$$

which has a solution as power law for the perturbations:

$$\delta(t) = C_1 t^{2/3} + C_2 t^{-1}. \tag{2.82}$$

All the constants values (B_1, B_2, C_1, C_2) are determined imposing initial condition for $\delta(t)$. The decaying solution t^{-1} is not observed, otherwise we should have a large amount of structures in the primordial Universe, contrary to our assumptions of small linear perturbations. Moreover, putting the growing solution in the Poisson equation (2.75) we have:

$$k^2\phi = -4\pi G a^2 \delta = -\frac{3}{2}H^2 a^2 \delta. \tag{2.83}$$

So, we obtain:

$$k^2\phi = -\frac{3}{2}\frac{4}{9t^2}t^{4/3}C_1 t^{2/3} = const, \tag{2.84}$$

i.e. the gravitational potential is constant in a Universe matter dominated.

Summarizing, we can consider different scales of the perturbations: when smaller scales cross the causal horizon, the Universe is radiation dominated and their growth is slower (logarithmic); instead, when larger scales enter into the causal horizon, we have the matter dominated epoch and the growth is faster (power law). So we expect that the large scales will grow more than the small scales.

2.7 Initial conditions: Inflation

In order to solve the set of differential equations driving the evolution of the first order perturbations, we have to know their initial conditions, that are thought to be due to the *Inflation process*. The inflationary paradigm has been introduced to solve some problems of the standard cosmological model, based on the Hot Big Bang. Inflation was initially conceived by Alan Guth in 1981, see Ref. [30], to solve in particular the *monopole*, the *flatness* and the *horizon* problems, and today represents an entire class of theories without a defined and detailed model. Inflation needs then to be verified through the general characteristics common to all models: the evolution of the Inflaton scalar field towards the minimum of the potential produces an exponentially accelerated expansion of the Universe immediately after its beginning. Inflation drives the Universe towards an homogeneous and spatially flat configuration, producing the initial condition for the standard Hot Big Bang. Simultaneously it expands the quantum fluctuations presents in the matter and in the space time, providing the small inhomogeneities that will eventually grow into galaxies and clusters of galaxies.

2.7.1 The flatness problem

While General Relativity allows the possibility of a curved Universe, observations show that it is nearly flat. This means, from equation (1.33), a total density parameter today $\Omega_0 = 1$, i.e. $\sum \rho = \rho_c$ and $k = 0$, but, in the standard Big Bang model, it is a highly unstable solution that implies an extreme fine tuning of the initial condition with an Universe with curvature exactly zero. A slight deviation from $\Omega = 1$ in the early Universe would produce today a totally different Universe, because the difference from the unity would rapidly grow.

From the second Friedmann equation (1.18) we know that the components of the Universe for which $\rho + 3P > 0$ produce a decelerated expansion of the Universe ($\ddot{a} < 0$). Imposing the equation of state (1.19), this condition is achieved with $w < -1/3$. If $k = 0$, combining the first Friedmann equation (1.16) with the equation (1.23), we have:

$$\frac{\dot{a}}{a} = \sqrt{\frac{8\pi G}{3}} a^{-\frac{3(1+w)}{2}}, \tag{2.85}$$

that integrated gives

$$a \propto t^{\frac{2}{3(1+w)}}. \tag{2.86}$$

We can define the curvature or the flatness deviation $C(a)$ as:

$$C(a) = \frac{|\Omega - 1|a^{-2}}{\Omega a^{-3(w+1)}} = C_0 a^{(1+3w)}, \tag{2.87}$$

where C_0 is the value today. We can see that for $a \ll 1$, in the early Universe, $C \to 0$: the Universe was very much flatter than today. We can rewrite the above equation as a funcion of the temperature:

$$C(T) = C_0 \left(\frac{T_0}{T}\right)^{1+3w}. \tag{2.88}$$

Thus, if today $T_0 \sim 3K \sim 10^{-12} GeV$ and we assume $T = T_P \sim 10^{19} GeV$, considering that the last observations give $|\Omega_0 - 1| < 0.1$, we have $C_P < 0.1 \cdot 10^{-31(1+3w)}$. Remembering that the Universe is initially radiation dominated, i.e. $w = 1/3$, the result is that the difference from $\Omega = 1$ at the Planck era was about 10^{-62}. We obtain a similar result when we consider a matter dominated era with $w = 0$ or any other components with equation of state $w > -1/3$. In conclusion, an initial deviation from the flatness, would have produced an immediate collapse of the Universe or its very rapid cooling. In order to have the initial condition $\Omega = 1$, we consider the inflationary solution of the Einstein equations that provides a period in which the Universe is dominated by an equation of state with $w < -1/3$, that implies a phase of accelerated expansion $\ddot{a} > 0$.

If we consider, for example, an exponential accelerated expansion, i.e. $w = -1$, we have $C_P = C_0 10^{62}$: even if the initial curvature was $C_P = 10^{50}$, today we would get $\Omega_0 = 1 \pm 10^{-12}$, an extremely flat Universe. With a phase of exponential acceleration, the solution $\Omega = 1$ is stable: whatever primordial geometrical curvature was present, it has been diluted during the expansion. In this case the flat Universe is an attractor of the inflationary solution.

For this solution with $w = -1$, we can define the expansion ratio:

$$log\frac{a_e}{a_i} = \Delta N \tag{2.89}$$

where a_i and a_e are the scale factors immediately before and after the inflationary period, and ΔN is the number of *e-folding*[2], the time interval in which the exponential growth increases by a factor of *e*. We can rewrite the above equation in this way:

$$\left(\frac{T_e}{T_i}\right)^2 = e^{-2\Delta N}, \tag{2.90}$$

where T_i and T_e are the temperatures immediately before and after the inflationary period. At the end of the inflation, the Universe is radiation dominated with $w = 1/3$ and a temperature $T_{GUT} = 10^{15} GeV$. Repeating the previous calculations, the curvature today will be $C_0 = e^{-2\Delta N} 10^{54} = 10^{54-0.87\Delta N}$. Comparing with the observed curvature $C_0 \sim 1$, the duration of the inflationary period has to be at least of $\Delta N = 62$ e-folding.

2.7.2 The horizon problem

The CMB observations show a correlation between different areas of the sky, on scales larger than the causal horizon size at the time of recombination, when the radiation was emitted. The causally connected regions at the recombination epoch would correspond at about $1°$ degree in the sky. But the CMB has the same temperature,

---

[2]The definition (2.89) is indeed the totally number N_T of e-folding, from the beginning to the end of the inflation. A stricter definition could be $\Delta N = N_T - N$, where $\Delta N = log(a/a_i)$ and $N = log(a_e/a)$. Then we have that $\Delta N = N_T$, if $a = a_e$.

and in general the Universe has the same characteristics, in all the directions of the sky.

We can determine if two areas are causally connected by calculating the causal horizon d_h, a region of finite size due to the finite velocity c at which light propagates, since the information travel at the speed of light. The causal horizon, as stated before, is defined as the maximum physical distance on which the photon can propagate between the time $t = 0$, the beginning of the Universe, and t, that corresponds to the maximum physical distance between two points that could have exchanged informations. Using the condition for the light propagation $ds^2 = 0$, and assuming that the propagation is radial, i.e. $d\theta = d\phi = 0$, from the metric (1.4) we obtain

$$dt^2 = a^2(t)\frac{dr^2}{1 - kr^2} \tag{2.91}$$

with $c = 1$. For a flat Universe the causal horizon will be:

$$d_h = \int_0^t dt = a(t)\int_0^r \frac{dr}{\sqrt{1 - kr^2}} = a(t)\int_0^t \frac{dt'}{a(t')} = a(t)\int_0^\infty \frac{da'}{Ha'^2}. \tag{2.92}$$

Assuming $a(t) \sim t^n$ and $H = H_0 a^{-1/n}$, the causal horizon can be written as

$$d_h = \frac{na^{\frac{1}{n}}}{(1 - n)H_0}. \tag{2.93}$$

Today, with $a_0 = 1$ and $n = 2/3$, becomes:

$$d_h = \frac{2c}{H_0} = 6000h^{-1}Mpc. \tag{2.94}$$

This is the size of the observable Universe, in a matter dominated Universe. Instead, if we consider the best fit to the observational data (see Ref. [5]), we have a finite horizon distance of about:

$$d_h \sim \frac{3.24c}{H_0} \sim 14000Mpc. \tag{2.95}$$

Moreover, we can define the *Hubble horizon*:

$$R_h = \frac{c}{H(t)} \tag{2.96}$$

as the maximum distance that the photon could travel during one expansion time $t = H^{-1}(t)$, considering the expansion rate of the Universe fixed at the constant value $H(t)$. Today we have:

$$R_0 = H_0^{-1} = 3000h^{-1}Mpc. \tag{2.97}$$

The difference between the causal horizon and the Hubble horizon is that, while d_h can only grow, R_h could be both larger or smaller in the past, depending on the behaviour of $H(t)$. Then if two points are separated by a distance greater than d_h but smaller than R_h, they could be in causal contact in the past, though today

cannot communicate to each other. Only if their distance is also greater than R_h we can say that these two points could have never spoken with each other.

We can define the *horizon crossing* the relationship $\lambda = 1/aH$, that is the time in which a comoving scale perturbation λ, i.e. a physical scale perturbation $a\lambda$, cross the Hubble horizon H^{-1}.

We want to know what is the distance today of a scale that was in horizon crossing at the scale factor a. We have to consider the Hubble horizon evolution together with the scale expansion and to solve the following system of equations imposing $\lambda = R_h$:

$$\begin{cases} R_h = H^{-1} = H_0^{-1} \left(\frac{a}{a_0}\right)^{\frac{3(1+w)}{2}} = R_0 \left(\frac{a}{a_0}\right)^{\frac{3(1+w)}{2}} \\ \lambda = \lambda_0 \left(\frac{a}{a_0}\right) \end{cases} \tag{2.98}$$

We obtain:

$$\lambda_0 = R_0 \left(\frac{a}{a_0}\right)^{\frac{3(1+w)}{2} - 1} \tag{2.99}$$

that is the maximum distance of two points today that were in causal contact at the scale factor a. Considering $a/a_0 = z^{-1}$ and a Universe matter dominated with $w = 0$, we can compute what are the sizes today of some scales that were in horizon crossing at known epochs, such as the decoupling era and the matter-to-radiation equivalence:

$$\lambda(z_{dec} = 1100) = 95h^{-1}Mpc \tag{2.100}$$

$$\lambda(z_{eq} = 2.4 \cdot 10^4) = 19h^{-1}Mpc \tag{2.101}$$

neglecting, for the last one, the radiation contribution to the evolution[3].

We can calculate roughly the angular dimension of the causal horizon at the recombination epoch $\Delta\theta_{sky}$, from the ratio between the values today of the scale that was in horizon crossing at the decoupling epoch, about $100h^{-1}Mpc$, and the causal horizon, about $6000h^{-1}Mpc$. We obtain:

$$\Delta\theta_{sky} = \frac{100}{6000} \cdot \frac{180}{\pi} \simeq 0.95°. \tag{2.102}$$

This means that if two points of the cosmic background have an angular separation on the sky greater than about $1°$, they have to be causally disconnected because haven't never communicate to each other. The result should be the identification of separate structures of fixed sizes on the fluctuations of the CMB, because those regions of dimension greater than the horizon haven't never interact between them. The paradox is the isotropy over all the sky of the temperature of the CMB, i.e. of the photons coming from the last scattering surface, also in causally uncorrelated regions. The problem is that if these regions have never been in causal contact before the recombination epoch, there is no way to establish the thermal equilibrium.

---

[3]If we integrate numerically the cosmological equations at two components we obtain $\lambda_{eq} = 13h^{-1}Mpc$.

We can solve the horizon problem with the inflationary process. In simple words, we have to consider that the physical distance of particles initially in causal contact grows exponentially, while the Hubble horizon remains almost constant. We suppose to have an inflationary epoch, up to the time t_e, in which the expansion is driven by $w_i < -1/3$, and at the end of the inflation by $w_f > -1/3$. We can rewrite the system of equations (2.98) as:

$$
\begin{cases}
R_h = R_0 \left(\frac{a}{a_e}\right)^{\frac{3(1+w_i)}{2}} \left(\frac{a_e}{a_0}\right)^{\frac{3(1+w_f)}{2}} \\
\lambda = \lambda_0 \left(\frac{a}{a_e}\right) \left(\frac{a_e}{a_0}\right)
\end{cases}
\tag{2.103}
$$

Let's now look for the value $a < a_e$, during inflation, when the Hubble radius today R_0 crossed the horizon, that implies that all the Universe was in causal contact in a time earlier than t_e. In this way we have two horizon crossing for all the scales $\lambda < R_0$, as we can see in Fig. 2.1. First of all we have a comoving inflationary expansion, faster than the linear growth of the causal horizon: all the scales are stretched outside the horizon at $t < t_e$ from the largest one to the smallest one. Afterwards, at the end of the inflation, is the causal horizon to grow faster and the several scales re-enter from the smallest one to the largest one (*last out $\rightarrow$ first in*). In this way we can explain the isotropy of the CMB, because the scales that are outside the horizon at the decoupling epoch, were all contained inside the horizon before the inflation.

In order to solve the system of equations (2.103), we impose again $\lambda_0 = R_0$. If we introduce the e-folding number $N = log(a_e/a)$, as the minimum number of e-folding needed to have R_0 inside the horizon, and then all the observable Universe in causal contact, we obtain:

$$
e^{-N+N\frac{3(1+w_i)}{2}} = \left(\frac{a_0}{a_e}\right)^{\frac{3(1+w_f)}{2}}.
\tag{2.104}
$$

Assuming $T_e = 10^{15} GeV$, the temperature nedeed to have at the end of the inflation the baryogenesis and the nucleosynthesis processes, considering a radiation dominated Universe $w_f = 1/3$, and the temperature of the cosmic background $T_0 = 10^{-12} GeV$, we have

$$
N_T \approx 62 \left(\frac{1}{\frac{3(1+w_i)}{2} - 1}\right) log\left(\frac{T_e}{10^{15} GeV}\right).
\tag{2.105}
$$

If we take $w_i = -1$, we find that $N_T = 60$ solves both the horizon and the curvature problems. Obviously we can have also $N > N_T$, but the previous scales, expanded beyond our horizon are forgotten because unobservable. Finally, if we impose that the scale $R_0 = 3000h^{-1} Mpc$ has always been inside the causal horizon, we obtain the same number of e-folding of the previous resolutions ($N_T = 60$).

2.7.3 The magnetic monopoles problem

The magnetic monopoles problem is due to the apparent absence of them in the Universe: these have never been observed, therefore they should be present in negligible quantities, while are predicted many more. In fact, magnetic monopoles are
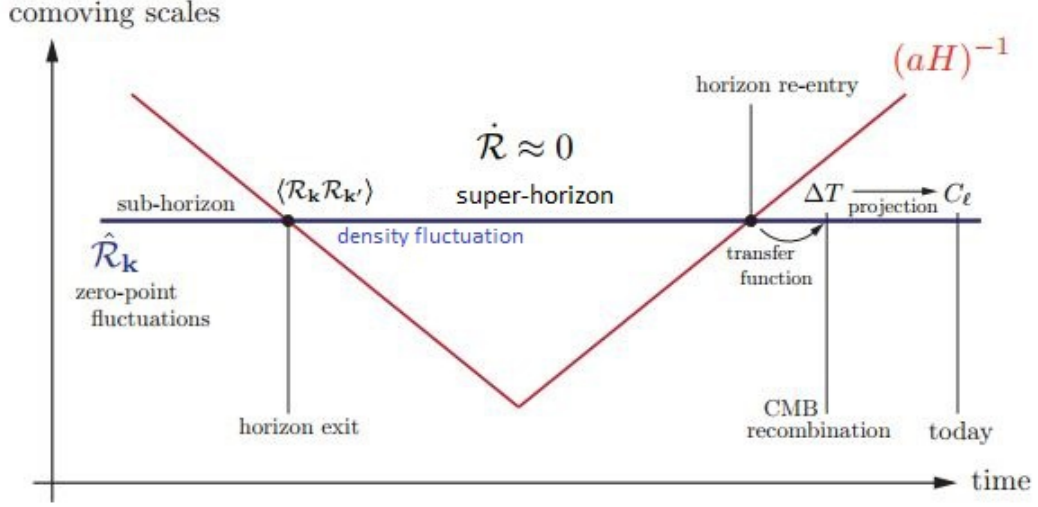
Figure 2.1. The inflation solves the horizon problem. All scales observables today, at sufficiently early times, were smaller than the causal horizon and therefore causally connected. With the inflation all scales are stretched outside the Hubble horizon and re-enter at relatively recent times, [31].

topological defects, that form when a spherical symmetry is broken. These particles are zero-dimensional (point-like) objects, and, first introduced in order to explain the quantization of the electric charge in 1931 by Dirac, are important in cosmology because are an unavoidable prediction of the Grand Unified Theories (GUT), due to the spontaneous symmetry breaking of the $SU(5) \rightarrow SU(3) \times SU(2) \times U(1)$.

The existence of these particles is cosmologically catastrophic: they are expected to be supermassive

$$m_M c^2 \sim E_{GUT} \sim 10^{12} TeV, \tag{2.106}$$

because are created in the GUT phase transition. Moreover, their number density and energy density would be, respectively:

$$n_M(t_{GUT}) \sim \frac{1}{(2ct_{GUT})^3} \sim 10^{82} m^{-3}, \tag{2.107}$$

and

$$\epsilon_M(t_{GUT}) \sim (m_M c^2) n_M \sim 10^{94} TeV m^{-3}. \tag{2.108}$$

Therefore, their presence would produce an evolution of the Universe that contradicts the observational data that we have, anticipating the matter-to-radiation equality. Inflation could solve this puzzle diluting the monopoles during the accelerated expansion phase, at a point that they cannot be observed today, because are expected roughly one per horizon volume.

2.7.4 The Inflaton dynamics

As we have seen, the problem of the standard cosmological model can be solved in a simple and elegant way, taking an exponentially accelerated expansion of the Universe, driven by a physical component with an equation of state (1.19) with $w < -1/3$. We have to explain what is this physical component and how after $N_T = 60$ e-foldings we can come back to the radiation dominated evolution, i.e. if the mathematical solution corresponds to a physical process.

Particle physics showed the existence of scalar fields, such as the Higgs boson, see Ref. [32, 33]. Inflation postulates the presence of one scalar field, the *Inflaton* ϕ_I, that leads an exponential growth of the Universe in an epoch in which its vacuum energy was the dominant component. The potential energy $V(\phi_I, T)$ of ϕ_I is assumed to vary with the temperature, as in the Figure 2.2. For the temperature $T > T_c$ the absolute minimum of the energy will be stable and in $\phi_I = 0$, while when the temperature falls below $T < T_c$ two minima degenerate are formed in $\phi_I \neq 0$. The result is that the point $\phi_I = 0$ becomes unstable, or of *false vacuum*, while these new minima are of *true vacuum*. When the field ϕ_I rolls down towards a new minimum, produces a spontaneous symmetry breaking, causing the accelerated expansion of the Universe.
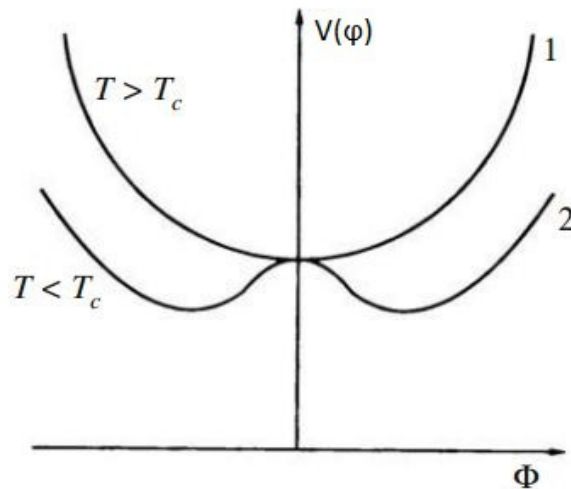
Figure 2.2. Example of a potential energy $V(\phi_I, T)$ as a function of ϕ_I. For temperature $T > T_c$ the absolute minimum of the energy will be stable and in $\phi_I = 0$, when the temperature falls below $T < T_c$ we have a spontaneous symmetry breaking and two minima degenerate are formed in $\phi_I \neq 0$, [34].

The dynamics of inflation, with a scalar field minimally coupled to the gravity, is described by the following action, see Ref. [31]:

$$S = \int d^4x \sqrt{-g} L_{\phi_I}, \tag{2.109}$$

with $g \equiv Det(g_{\mu\nu})$ and L_{ϕ_I} the Lagrangian:

$$L_{\phi_I} = \frac{1}{2} g^{\mu\nu} \partial_\mu \phi_I \partial_\nu \phi_I - V(\phi_I, T). \tag{2.110}$$

The energy-momentum tensor will be:

$$T_{\mu\nu} = \partial_\mu \partial_\nu \phi_I - g_{\mu\nu} \left(\frac{1}{2} \partial^\sigma \phi_I \partial_\sigma \phi_I + V(\phi_I, T) \right), \tag{2.111}$$

that for a homogeneous and isotropic geometry, takes the perfect fluid form, with energy density ρ and pressure P:

$$\rho_{\phi_I} = \frac{1}{2} \dot{\phi}_I^2 + V(\phi_I, T) \tag{2.112}$$

$$P_{\phi_I} = \frac{1}{2} \dot{\phi}_I^2 - V(\phi_I, T). \tag{2.113}$$

The resulting equation of state will be:

$$w_{\phi_I} \equiv \frac{P_{\phi_I}}{\rho_{\phi_I}} = \frac{\frac{1}{2} \dot{\phi}_I^2 - V(\phi_I, T)}{\frac{1}{2} \dot{\phi}_I^2 + V(\phi_I, T)} \tag{2.114}$$

which shows that a scalar field can lead to accelerated expansion with $w_{\phi_I} < -1/3$ if the potential energy $V(\phi_I, T)$ dominates over the kinetic terms $\dot{\phi}_I^2$.

We can derive the equation of the motion of the scalar field ϕ_I:

$$\frac{d}{dt} \frac{\partial \left(L_{\phi_I} a^3 \right)}{\partial \dot{\phi}_I} - \frac{\partial \left(L_{\phi_I} a^3 \right)}{\partial \phi_I} = 0, \tag{2.115}$$

$$\ddot{\phi}_I + 3H \dot{\phi}_I + \frac{\partial V(\phi_I)}{\partial \phi_I} = 0. \tag{2.116}$$

In this equation the second term $3H$ is a term of viscosity due to the expansion of the Universe and the third $-\partial V(\phi_I)/\partial \phi_I$ is a forcing term.

If we consider a potential $V(\phi_I, T) \sim const$ during the inflationary epoch, see Fig. 2.3, we obtain the *slow-roll* conditions, that are necessary but not sufficient for inflation:

$$\dot{\phi}_I^2 \ll V(\phi_I), \tag{2.117}$$

$$\left| \ddot{\phi}_I \right| \ll \left| \frac{\partial V}{\partial \phi_I} \right|, 3H \dot{\phi}_I. \tag{2.118}$$

We can rewrite the first (1.16) and the second (1.18) Friedmann equations, using the ρ_{ϕ_I} and the P_{ϕ_I} given by the eq. (2.112) and (2.113):

$$H^2 = \frac{8\pi}{3m_{Pl}^2} \left[\frac{1}{2} \dot{\phi}_I^2 + V(\phi_I) \right], \tag{2.119}$$

$$\left(\frac{\ddot{a}}{a} \right) = \frac{8\pi}{3m_{Pl}^2} \left[-\dot{\phi}_I^2 + V(\phi_I) \right], \tag{2.120}$$

where we used $m_{Pl} = G^{-1/2}$. In order to compute the scale factor evolution, we consider the slow-rolling approximation in the eq. (2.119):

$$\left(\frac{\dot{a}}{a} \right)^2 = \frac{8\pi}{3m_{Pl}^2} V(\phi_I), \tag{2.121}$$
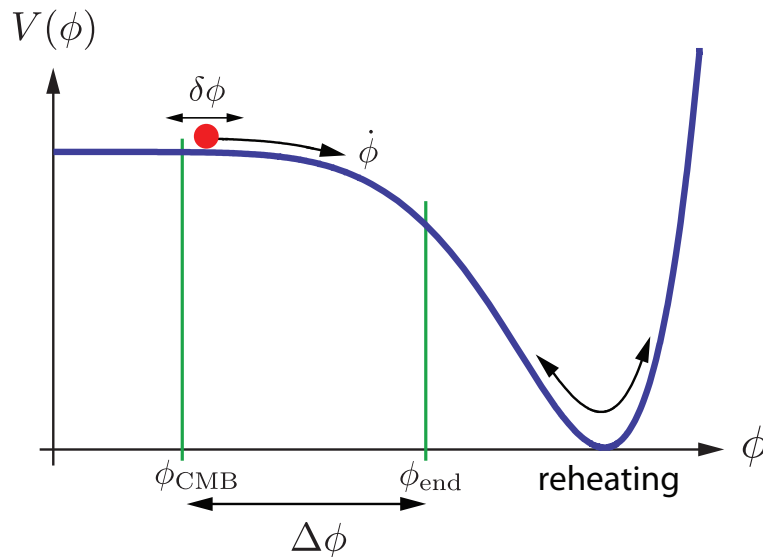
Figure 2.3. Example of a possible Inflaton potential energy $V(\phi_I, T)$ as a function of the field ϕ_I. The accelerated expansion occurs when the potential energy $V(\phi_I, T)$, that is maintained constant during the inflation, dominates over its kinetic energy $\dot{\phi}_I^2$, and ends when this condition is no longer valid, because the kinetic terms grows. At reheating phase, the energy density of the Inflaton is converted into radiation and allows to create the Standard Model particles, [31].

from which we obtain the exponentially accelerated expansion:

$$a \propto e^{t/\tau}, \tag{2.122}$$

where τ is equal to:

$$\tau = \left(\frac{3m_{Pl}^2}{8\pi V(\phi_I)} \right)^{1/2} \sim 10^{-34}s, \tag{2.123}$$

in the typical model. We have that $\tau \sim H^{-1} \sim const$ with time during all the inflationary period. Moreover, we can calculate the number of e-folding (2.89) in the range (t_i, t_f) in the following way:

$$N = log\frac{a\left(t_f\right)}{a\left(t_i\right)} \simeq -\frac{8\pi}{m_{Pl}^2} \int_{\phi_{i,i}}^{\phi_{i,f}} \left(\frac{dlogV(\phi_I)}{d\phi_I} \right)^{-1} d\phi_I. \tag{2.124}$$

Finally, we can rewrite the eq. (2.115) under these slow-rolling assumptions:

$$\dot{\phi}_I \simeq -\frac{1}{3H}\frac{\partial V}{\partial \phi_I}. \tag{2.125}$$

We introduce the slow-roll parameters ϵ and η to quantify the inflationary dynamics:

$$\epsilon \equiv -\frac{\dot{H}}{H^2} \simeq \frac{m_{Pl}^2}{16\pi} \left(\frac{V'}{V} \right)^2, \tag{2.126}$$

$$\eta \equiv -\frac{\ddot{\phi}_I}{H\dot{\phi}_I} \simeq \frac{m_{Pl}^2}{8\pi}\left[\left(\frac{V''}{V}\right) - \frac{1}{2}\left(\frac{V'}{V}\right)^2\right], \tag{2.127}$$

that have to satisfy the conditions:

$$\epsilon \ll 1 \tag{2.128}$$

$$|\eta| \ll 1 \tag{2.129}$$

that are equivalent to the previous conditions (2.117) and (2.118). In particular they guarantee that inflation occurs when the potential energy $V(\phi_I, T)$, that is nearly constant, dominates over its kinetic energy $\dot{\phi}_I^2$. Inflation ends when the Inflaton field ϕ_I reaches the true vacuum, in the minimum of the potential energy. In fact at this point, a very large quantity of energy is converted from potential into kinetic, which grows until the slow-roll conditions are no longer valid. At this point ϕ_I starts to oscillate around the minimum, and the energy density of the Inflaton is converted into radiation through its decay, allowing particles creation (see Ref. [35]). This phase is called *reheating*, since the interactions between the decay products of the Inflaton heat the temperature of the Universe, after the supercooling of the inflationary epoch. At the end of Inflation the epoch of radiation domination starts.

In order to solve the standard cosmological model problems, the plateau of the potential energy $V(\phi_I, T)$ in the Fig. 2.3 has to be enough long to guarantee the right number of e-folding:

$$N \sim H_i \frac{\phi_{i,0}}{\dot{\phi}_I} \sim \left(\frac{V'}{V_0}\right)^{-1}\phi_{i,0} \geq 60, \tag{2.130}$$

where we defined $V(\phi_I = 0) = V_0$ the value of the potential on the plateau, different from the $V_{min} = 0$ that is the value of the potential at the true vacuum $\phi_{i,0}$.

2.8 Primordial perturbations

The homogeneous scalar field ϕ_I considered so far, can have, for the Heisenberg uncertainty principle, random Gaussian quantum-mechanical fluctuations, with zero mean and a variance different from zero, that are stretched on cosmological scales by the inflationary process. The same behaviour have the quantum fluctuations of the metric that can be both tensor and scalar[4]. Those scalar fluctuations will be the seeds of the inhomogeneities and the structures we see today in the Universe, while those tensor fluctuations will generate a primordial background of gravitational waves. During the superluminal expansion of the Universe the quantum fluctuations on small scales are amplified on scales much larger than the horizon size, where are then frozen. The evolution of the fluctuation of a given scale depends wheter its re-entry in the causal horizon happens before or after the equivalence epoch, i.e. if the Universe is matter or radiation dominated. In any way, while the density

---

[4]The vector perturbations are not predicted in the standard cosmological model.

fluctuations start to oscillate or grow depending on their nature entering into the horizon, the tensor perturbations dissipate.

The scalar field ϕ_I, so far only function of time, in case of perturbations depends also on the position:

$$\phi_I(x,t) = \phi_I^{(0)}(t) + \delta\phi_I(x,t). \tag{2.131}$$

In the linear perturbation theory, every scale of a physical perturbation λ corresponds to a mode $k = a/\lambda$ of the Fourier expansion of the inhomogeneous field $\delta\phi_I$:

$$\delta\phi_{I,k} = \int \delta\phi_I e^{-i\vec{k}\cdot\vec{x}} d^3\vec{x}. \tag{2.132}$$

The perturbation has to be compared with the Hubble horizon H^{-1}. We have that the scale $k < aH$ is out of the horizon, $k > aH$ is inside the horizon and $k \sim aH$ is at horizon crossing.

For the statistics of the perturbations, as we will see in the next section 3.1, we can define the power spectrum $P_{\delta a}$ of any perturbed quantity $a = a_0 + \delta a$ using the eq. (3.6). Here, in order to define a *dimensionless* power spectrum $P_{\delta\phi_I}$, we use the following relationship:

$$\left\langle \delta\phi_I^*\left(\vec{k}\right) \delta\phi_I\left(\vec{k}'\right) \right\rangle = \left(\frac{2\pi}{k}\right)^3 \delta^3_{Dirac}(\vec{k} - \vec{k}') P_{\delta\phi_I}(k), \tag{2.133}$$

where the δ^3_{Dirac} guarantees the independence of the several modes, and the k^{-3} to be dimensionless instead of to have the dimension of a $[length]^3$. We can demonstrate that the initial conditions of the metric scalar perturbations are related to the perturbations of the scalar field ϕ_I, when coming out from the horizon are frozen. The relationship converting the power spectrum of the scalar field fluctuations $\delta\phi_I$, at horizon crossing, in the final scalar power spectrum of the metric perturbations P_S is given by (see Ref. [13]):

$$P_S(k) = \left[\frac{4}{9}\left(\frac{aH}{\dot{\phi}_I^{(0)}}\right)^2 P_{\delta\phi_I}(k)\right]_{k=aH}. \tag{2.134}$$

We can calculate, following Ref. [13], the power spectra, P_T and P_S, using quantum field theory for the tensor and the scalar perturbations, that we express as a function of the slow-roll parameter ϵ, obtaining:

$$P_S(k) = \left[\frac{8\pi}{9}\frac{H^2}{\epsilon m_{Pl}^2}\right]_{k=aH}, \tag{2.135}$$

$$P_T(k) = \left[8\pi\frac{H^2}{m_{Pl}^2}\right]_{k=aH}. \tag{2.136}$$

The power spectra are not calculated for a fixed time, but for the time of horizon crossing, that is different for each scale k. We can define the scalar n_S and the tensor n_T *spectral indices* as:

$$P_S(k) = A_S\left(\frac{k}{k_{S0}}\right)^{n_S-1}, \tag{2.137}$$

$$P_T(k) = A_T \left(\frac{k}{k_{T0}} \right)^{n_T}, \tag{2.138}$$

(with $k_{S0} = k_{T0} = aH$) to quantify the deviations from scale-invariance. The power spectrum is defined *scale invariant* if each mode k has the same amplitude in horizon crossing, i.e. if the different scales have the same power. We have *Harrison-Zel'dovich-Peebles* scale invariant spectra[5] when $n_S = 1$ and $n_T = 0$. These are the appropriate values, if $H = const$ during all the inflationary period. However, since Inflation is a dynamical process that ends at certain point, we expect spectra to be "nearly" scale-invariant. It is possible to demonstrate that we can rewrite the spectral indices as a function of the slow-roll parameters in this way:

$$n_S = 1 - 4\epsilon + 2\eta, \tag{2.139}$$

$$n_T = -2\epsilon. \tag{2.140}$$

Moreover, if H is not totally constant, because $V(\phi)$ slowly varies, then n_S is not perfectly one. We can introduce the running of the spectral indices $\alpha_{S,T}$:

$$\alpha_{S,T} = \frac{dn_{S,T}}{dlogk}, \tag{2.141}$$

that express the variation of the spectral indices with the scale k.

Another observable quantity is r, the ratio between the tensor and the scalar spectra, that can be expressed as a function of the slow-roll parameters:

$$r \equiv \frac{P_T}{P_S} = 16\epsilon, \tag{2.142}$$

Using the eq. (2.140), we can then derive the consistency relation of Inflation:

$$n_T \simeq -2\epsilon = -\frac{r}{8}, \tag{2.143}$$

that needs to be satisfied if the slow-roll condition is valid.

Finally, we can rewrite the inflationary potential through its Taylor expansion, obtaining the following relationships:

$$P_S(k) \sim \left(\frac{V^3}{m_{Pl}^6 (V')^2} \right)_{k=aH}, \tag{2.144}$$

$$P_T(k) \sim \left(\frac{V}{m_{Pl}^4} \right)_{k=aH}. \tag{2.145}$$

We can therefore see that by constraining the inflationary parameters n_S, n_T, r, α_S and α_T, we can reconstruct the inflationary potential: $P_T \to V$, $P_S \to V'$, $n_S \to V''$ and $\alpha_S \to V'''$.

---

[5]By defining the power spectrum using the eq. (3.6), the scale-invariance condition will be reached when $k^3 P$ is constant, i.e. does not depend on k.

Chapter 3

The Cosmic Microwave Background

3.1 The statistic of perturbations

Taken the density field $\rho(\vec{x}, \tau)$, we can separate the homogeneous term $\rho(\tau)$ from the perturbed term $\delta(\vec{x}, \tau) = \delta\rho/\rho$:

$$\rho(\vec{x}, \tau) = \rho(\tau) \left(1 + \delta(\vec{x}, \tau)\right), \tag{3.1}$$

where the $\delta\rho$ is the difference respect to the homogeneous term.

To study the inhomogeneities of a given field means to study the functions $\delta(\vec{x}, \tau)$ that are random fields. Since is not possible to find a specific measurement of random variables in infinite-dimensional vector spaces, the fields are defined specifying the joint probability distribution for n points. If the random fields are homogeneous and isotropic, we will have that the one-point distribution doesn't depend on the position, while two-points distribution depends only on the scalar quantity $x \equiv |\vec{x}_1 - \vec{x}_2|$, where x_1 and x_2 are the coordinates of the two points. The ergodic theorem for a Gaussian stochastic field guarantees that the average of ensemble can be regarded as a spatial average, see Ref. [36], so:

$$\langle \delta\left(\vec{x}_1\right) \rangle = \lim_{R \to \infty} \frac{3}{4\pi R^3} \int_{|\vec{x}| < R} \delta(\vec{x}) d^3 \vec{x}, \tag{3.2}$$

where R is the radius of the sphere. Moreover, Gaussianity plus ergodicity implies that the mean value is $\langle \delta\left(\vec{x}\right) \rangle = 0$. In this case, in order to totally define the field distribution function, is sufficient to know the covariance matrix C_{mn} of the perturbation field taken in two different directions.

If we define the correlation function:

$$\xi(x) = \langle \delta\left(\vec{x}_1\right) \delta\left(\vec{x}_2\right) \rangle, \tag{3.3}$$

this specifies completely the Gaussian random field, because we have:

$$C_{mn} \equiv \langle \delta\left(\vec{x}_m\right) \delta\left(\vec{x}_n\right) \rangle = \xi\left(|\vec{x}_m - \vec{x}_n|\right). \tag{3.4}$$

We have seen that in Fourier space the several modes evolve in an indipendent way. Thus, given the Fourier transform of the field $\delta(\vec{x})$

$$\delta(\vec{k}) = \int \delta(\vec{x}) e^{-i\vec{k}\cdot\vec{x}} d^3\vec{x} \tag{3.5}$$

we can define the power spectrum of the perturbation $P(k)$ as

$$\left\langle \delta^*\left(\vec{k}\right) \delta\left(\vec{k}'\right) \right\rangle = (2\pi)^3 \delta^3_{Dirac}(\vec{k} - \vec{k}') P(k), \tag{3.6}$$

with $\delta^*(\vec{k})$ the complex conjugate. The Wiener-Khintchine theorem states that the autocorrelation function of a random variable and the power spectrum are Fourier transform pair:

$$\xi(x) = \frac{1}{(2\pi)^3} \int P(k) e^{-i\vec{k}\cdot\vec{x}} d^3\vec{k} \tag{3.7}$$

In order to study the CMB anisotropies in the next section, we introduce a system of spherical coordinates in which we are in the origin, and we project the δ of the three-dimensional space R^3 into the Δ of the two-dimensional surface of the sphere S^2. We then expand the $\Delta(\theta, \phi)$ in spherical harmonics $Y_{lm}(\theta, \phi)$:

$$\Delta(\theta, \phi) = \sum_{l=0}^{\infty} \sum_{m=-l}^{l} a_{lm} Y_{lm}(\theta, \phi), \tag{3.8}$$

with

$$Y_{lm}(\theta, \phi) = \sqrt{\frac{(2l+1)(l-m)!}{4\pi(l+m)!}} P_l^m(cos\theta) e^{i\phi}, \tag{3.9}$$

where P_l are the Legendre polynomials. The coefficients a_{lm} are given by:

$$a_{lm} = \int Y_{lm}^*(\theta, \phi) \Delta(\theta, \phi) d\Omega. \tag{3.10}$$

In analogy with the three-dimensional case, we define the angular correlation function $c(\theta)$ between two direction in the sky $\hat{n}$ an $\hat{n}'$:

$$c(\theta) = \left\langle \Delta(\hat{n})\Delta(\hat{n}') \right\rangle, \tag{3.11}$$

and $\hat{n} \cdot \hat{n}' = cos\theta$, and the angular power spectrum C_l:

$$\langle a_{lm}^* a_{l'm'} \rangle = \delta_{ll'} \delta_{mm'} C_l, \tag{3.12}$$

that are a Legendre transform pair:

$$c(\theta) = \frac{1}{4\pi} \sum_{l=0}^{\infty} (2l+1) C_l P_l(cos\theta). \tag{3.13}$$

We can rewrite the coefficients C_l as:

$$C_l = \frac{1}{(-1)^l} \int_{-1}^{1} \frac{dcos\theta}{2} P_l(cos\theta) \Delta(cos\theta) \tag{3.14}$$

that can be measured experimentally. Given a theoretical model, we can always compare the theoretically computed C_l with those observed. Considering that in a two-dimensional space the field is not ergodic, the average of ensemble is not equal to the spatial average, then the mean value measured is not exact: we can quantify the statistical error ΔC_l through the *cosmic variance*:

$$\Delta C_l^2 = \frac{2}{2l+1} C_l^2. \tag{3.15}$$

The cosmic variance is an intrinsic limit, un unavoidable source of uncertainty, to the accurate estimate of the power spectrum, and consequently of the cosmological parameters, due to the stochastic nature of the problem. Observing only one realization of the Universe, we have not sufficient samples to the very large scales. This sampling uncertainty takes into account that each C_l is χ^2 distributed with $(2l+1)$ degrees of freedom for our observable volume of Universe. Also an ideal experiment is subjected to this limit. Moreover, considered a possible partial sky coverage, the cosmic variance is increased by a factor $1/f_{sky}$, where f_{sky} is the fraction of the sky sampled:

$$\Delta C_l^2 = \frac{2}{f_{sky}(2l+1)} C_l^2, \tag{3.16}$$

and, in this case, the modes become partially correlated.

3.2 The CMB angular power spectrum

The temperature anisotropies of the CMB can be studied through the linear perturbation theory. Assuming that is the inflation the physical process that generates the fluctuations, we can consider them adiabatic and Gaussian. The field of the temperature fluctuations on the celestial sphere can be studied through the expansion in spherical harmonics, as explained in the previous section. We have:

$$\frac{\Delta T}{T}(\theta, \phi) = \sum_{l=1}^{\infty} \sum_{m=-l}^{l} a_{lm} Y_{lm}(\theta, \phi), \tag{3.17}$$

with the coefficients

$$a_{lm} = \int Y_{lm}^*(\theta, \phi) \frac{\Delta T}{T}(\theta, \phi) d\Omega \tag{3.18}$$

statistically independent and Gaussian distributed that, containing all the information about the temperature fluctuations, weighting the contributions of each spherical harmonic. The expected value for the mean is

$$\langle a_{lm} \rangle = 0, \tag{3.19}$$

while the variance is given by

$$\langle a_{lm}^* a_{l'm'} \rangle = \delta_{ll'} \delta_{mm'} C_l, \tag{3.20}$$

where the ensemble average is over infinite realizations of the Universe, or thanks to the ergodic principle, over the directions of the sky. In multipole space the average will be done over m, because in an isotropic Universe we expect that a_{lm} have the same variance for each fixed value of l. The latter equation (3.20) defines the angular power spectrum C_l for the Cosmic Microwave Background. The C_l's no longer depend on m, again because there are not preferred directions of the observation in the sky. Moreover, the angular power spectrum and the two-point correlation function are Legendre's transform pair:

$$\left\langle \frac{\Delta T}{T}(\hat{\gamma}_1)\frac{\Delta T}{T}(\hat{\gamma}_2) \right\rangle = \frac{1}{4\pi}\sum_{l=0}^{\infty}(2l+1)C_l P_l(\hat{\gamma}_1 \cdot \hat{\gamma}_2), \qquad (3.21)$$

where $\hat{\gamma}$ is the direction of the observation.

We have that an estimator for C_l is:

$$\hat{C}_l = \left\langle |a_{lm}^2| \right\rangle = \frac{1}{2l+1}\sum_m a_{lm}^2, \qquad (3.22)$$

and its variance is the cosmic variance:

$$\Delta\hat{C}_l^2 = \frac{2}{2l+1}C_l^2, \qquad (3.23)$$

higher at large scales, small l, than at small ones, and always increased by a factor $1/f_{sky}$ when we have a partial sky coverage.

In fact the decomposition in multipoles l of the temperature field provides the contribution of the temperature anisotropies to the CMB temperature fluctuations on angular scales $\theta = 180°/l$. We have that the coefficient $a_{00} = 0$ because the monopole $l = 0$ is the average deviation $(T - T_0)/T_0$ all over the sky T_0, that vanishes. We have the dipole for $l = 1$, but the primordial dipole is obscured by the dipole term due to the peculiar motion of the Earth respect to the reference framework where the CMB is isotropic . In fact we observe a Doppler effect on the CMB photon, due to the resulting movement of the Earth around the Sun, added to that of the Sun around the Galactic Center, that moves around the center of mass of the Local Group, which goes towards the Virgo cluster. The result will be that in the direction towards which we move, at about $371 km/s$, we have hotter photons than in the opposite direction. Usually the dipole is removed from the CMB studies. Finally for $l = 2$ we have the quadrupole term, from which we start to study the CMB (Figure 3.1).

3.3 Polarization

The temperature anisotropies that originate from the primordial fluctuations, are polarized by the Thomson scattering off free electrons. A combined analysis of the polarization signal and of the temperature anisotropies allows to evaluate the consinstency of the standard cosmological model: measuring the CMB polarization increases the accuracy with which the cosmological parameters are measured. An important characteristic is the possibility to discriminate, studying the shape of the
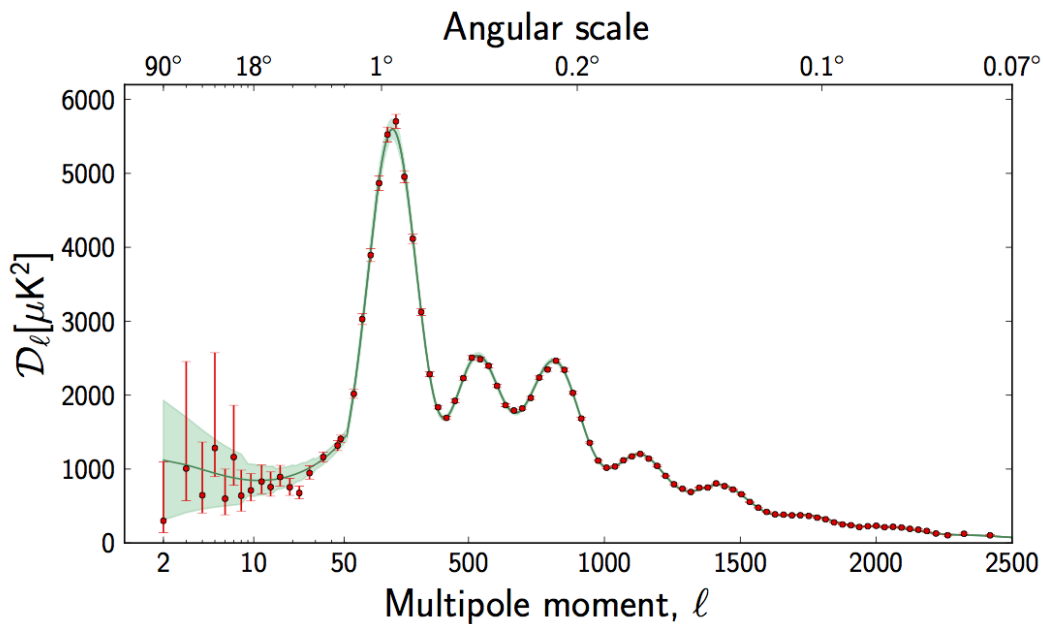
Figure 3.1. The angular power spectrum of the Cosmic Microwave Background, where $D_l = l(l+1)C_l/2\pi$, [5] .

polarization, between the several sources of the temperature anisotropies: scalar, vector or tensor.

3.3.1   The Stokes parameters

We remind here some basic notion of electromagnetism. Given a electromagnetic wave with frequency ω_0, the electric field propagating parallel to the axis $\hat{z}$ has components:

$$E_x = a_x(t)cos\left[\omega_0 t + \theta_x(t)\right],\qquad(3.24)$$

$$E_y = a_y(t)sin\left[\omega_0 t + \theta_y(t)\right],\qquad(3.25)$$

that are plane waves oscillating in the plane (x, y), with amplitudes $a_{x,y}(t)$ and phases $\theta_{x,y}(t)$ slowly varying with time[1]. We introduce the Stokes parameters through the following time averages:

$$I \equiv \left\langle a_x^2 \right\rangle + \left\langle a_y^2 \right\rangle,\qquad(3.26)$$

$$Q \equiv \left\langle a_x^2 \right\rangle - \left\langle a_y^2 \right\rangle,\qquad(3.27)$$

$$U \equiv \left\langle 2a_x a_y cos\left(\theta_x - \theta_y\right)\right\rangle,\qquad(3.28)$$

---

[1]A pure monochromatic and purely polarized wave has amplitude and phase constant with time.

$$V \equiv \langle 2a_x a_y sin\left(\theta_x - \theta_y\right)\rangle. \tag{3.29}$$

where I is the wave's intensity, Q is the difference of intensity between the directions $\hat{x}$ and $\hat{y}$, U is the difference of intensity in a reference frame rotated of $45°$ (i.e. Q and U are related to the linear polarization) and V is the difference of intensity between left and right circular polarization.

While I and V are invariant under a change of coordinates, Q and U transform in the following way under rotation of the reference frame of an angle ϕ:

$$Q' = Qcos(2\phi) + Usin(2\phi) \tag{3.30}$$

$$U' = -Qsin(2\phi) + Ucos(2\phi) \tag{3.31}$$

i.e. as the components of the polarization vector[2]:

$$V_P = Q\hat{x} + U\hat{y}. \tag{3.32}$$

We can introduce the polarization matrix, that is a tensor of rank 2 on the sphere, as:

$$M_P = \frac{1}{2}\left(\sigma_0 I + \sigma_x Q + \sigma_y U + \sigma_z V\right) = \frac{1}{2}\begin{pmatrix} I-Q & U-iV \\ U+iV & I+Q \end{pmatrix} \tag{3.33}$$

with $\sigma_\mu \equiv (1, \sigma_i)$, where the σ_i are the Pauli matrices. This matrix has the right property of transformation, which summarize the previous.

Moreover, we can introduce the polarization parameter P as:

$$P = \frac{\sqrt{Q^2 + U^2 + V^2}}{I} \tag{3.34}$$

that represents the percentage of polarized light respect to the total intentity, and vary in the range $[0, 1]$.

3.3.2 Thomson Scattering

The main process of interaction between matter and radiation is quantistically the Compton scattering, when $\hbar\omega \gg mc^2$, or classically the Thomson scattering, when $\hbar\omega \ll mc^2$. This latter correlates the temperature anisotropies and the polarization.

If the incident radiation is isotropic, then the outgoing radiation is non-polarized, because for the symmetry of the process, the orthogonal directions of polarization cancel each other. Otherwise, if the incident radiation shows a quadrupole component, the Thomson scattering produce a linear polarization. The quadrupole moment of the CMB originates between the photons-electrons decoupling and the recombination.

We consider a classical model in order to demonstrate that a quadrupole term in the incident radiation produces an outcoming polarized light, as we can see in Ref. [37]. The cross section of the Thomson scattering between an electromagnetic wave and an electron is given by:

---

[2]This is not a proper vector because has not a versus.

$$\frac{d\sigma}{d\Omega} = \frac{3\sigma_T}{8\pi}|\hat{\epsilon}' \cdot \hat{\epsilon}|^2, \tag{3.35}$$

with σ_T the Thomson cross section and $\hat{\epsilon}'$ and $\hat{\epsilon}$ the versors of the polarization vectors (defined in the eq. (3.32)) of the incident and of the scattered waves in the rest reference frame of the electron, as in the Fig. 3.2.
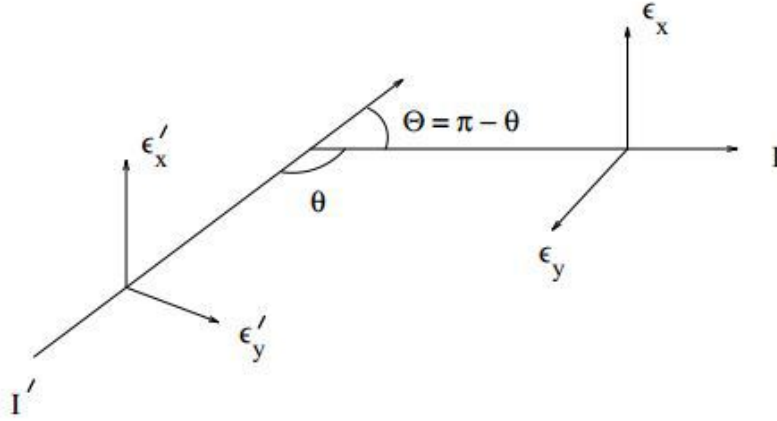
Figure 3.2. Thomson scattering between a photon and an electron, [37].

Named I' and I the intensities of the incident and scattered (along $\hat{z}$) waves, we have $I'_x = I'_y = I'/2$. We introduce:

$$I_x = \frac{I + Q}{2}, \tag{3.36}$$

$$I_y = \frac{I - Q}{2}. \tag{3.37}$$

We have:

$$I_x = \frac{3\sigma_T}{8\pi}\left[I'_x\left(\hat{\epsilon}'_x \cdot \hat{\epsilon}_x\right)^2 + I'_y\left(\hat{\epsilon}'_y \cdot \hat{\epsilon}_x\right)^2\right] = \frac{3\sigma_T}{16\pi}I' \tag{3.38}$$

$$I_y = \frac{3\sigma_T}{8\pi}\left[I'_x\left(\hat{\epsilon}'_x \cdot \hat{\epsilon}_y\right)^2 + I'_y\left(\hat{\epsilon}'_y \cdot \hat{\epsilon}_y\right)^2\right] = \frac{3\sigma_T}{16\pi}I'cos^2\theta, \tag{3.39}$$

where θ is the angle between the propagation directions of the incident and the scattered waves (see Figure 3.2). We can rewrite the Stokes parameters for the scattered wave as:

$$I = I_x + I_y = \frac{3\sigma_T}{16\pi}I'\left(1 + cos^2\theta\right), \tag{3.40}$$

$$Q = I_x - I_y = \frac{3\sigma_T}{16\pi}sin^2\theta, \tag{3.41}$$

while in order to calculate U we use eq. (3.30) rotating the reference frame of an angle $\pi/4$, and considering the $Q' = U$ and $U' = -Q$. Then we have to integrate over all the possible directions for the incident radiation:

$$I = \frac{3\sigma_T}{16\pi} \int d\Omega \left(1 + cos^2\theta\right) I'(\theta, \phi) \tag{3.42}$$

$$Q = \frac{3\sigma_T}{16\pi} \int d\Omega \, sin^2\theta cos\left(2\phi\right) I'(\theta, \phi) \tag{3.43}$$

$$U = \frac{3\sigma_T}{16\pi} \int d\Omega \, sin^2\theta sin\left(2\phi\right) I'(\theta, \phi) \tag{3.44}$$

while V is homogeneous and decoupled from other parameters. In fact solving correctly the equations, we see that, if initially the incident wave is not circularly polarized, it remains the same after the Thomson scattering. However can be produced through other processes, such as the Bremsstrahlung.

The polarization of the outgoing radiation depends only on the intensity distribution of the incident one. We can expand this quantity in spherical harmonics

$$I'(\theta, \phi) = \sum_{l,m} a_{lm} Y_{lm}(\theta, \phi), \tag{3.45}$$

obtaining

$$I = \frac{3\sigma_T}{16\pi} \left[\frac{8}{3}\sqrt{\pi}a_{00} + \frac{4}{3}\sqrt{\frac{\pi}{5}}a_{20} \right] \tag{3.46}$$

$$Q = \frac{3\sigma_T}{4\pi} \sqrt{\frac{2\pi}{15}} Re(a_{22}) \tag{3.47}$$

$$U = -\frac{3\sigma_T}{4\pi} \sqrt{\frac{2\pi}{15}} Im(a_{22}). \tag{3.48}$$

As we can see, there is polarization if we have a quadrupole term ($Y_{22} \neq 0$) in the incident radiation intensity. Also considering a more complex model, with Compton cross section and Boltzmann equations, we obtain the same conclusions.

3.3.3   E and B modes

Being Q and U dependent on the reference frame, these are not useful to study the symmetries of the system. We follow Ref. [38] in order to derive the polarization power spectra of the CMB. We introduce two independent combinations:

$$(Q \pm iU)'(\hat{n}) = e^{\mp 2i\psi}(Q \pm iU)(\hat{n}) \tag{3.49}$$

that transform as spinors of spin ± 2 under the rotation of an angle ψ of the plane orthogonal to $\hat{n}$, that is the direction of observation. The expansion in the usual spherical harmonics is valid for the spin 0. We can generalize the expansion in terms of the spin s spherical harmonics $_sY_{lm}(\hat{n})$ in this way:

$$(Q \pm iU)(\hat{n}) = \sum_{l,m} a_{lm}^{(\pm 2)} \left[_{\pm 2}Y_{lm}(\hat{n}) \right]. \tag{3.50}$$

The spin s spherical harmonics satisfy the same conditions of orthonormality and completeness of the spherical harmonics, but have the spin raising and lowering operators $\eth$ and $\bar{\eth}$:

$$(\tilde{\eth}f)' = e^{-i(s+1)\psi}\eth_s f \tag{3.51}$$

$$(\bar{\tilde{\eth}}f)' = e^{-i(s+1)\psi}\bar{\eth}_s f. \tag{3.52}$$

Are valid these relationships:

$$\begin{cases} {}_sY_{lm} = \left[\frac{(l-s)!}{(l+s)!}\right]^{1/2}\eth^s Y_{lm}, & 0 \le s \le l \\ {}_sY_{lm} = \left[\frac{(l+s)!}{(l-s)!}\right]^{1/2}\bar{\eth}^{-s}Y_{lm}, & -l \le s \le 0. \end{cases} \tag{3.53}$$

Then, by applying twice these operators to the eq. (3.50), we obtain

$$\bar{\eth}^2(Q+iU)(\hat{n}) = \sum_{l,m}\left[\frac{(l+s)!}{(l-s)!}\right]^{1/2} a_{lm}^{(2)}Y_{lm}(\hat{n}) \tag{3.54}$$

$$\eth^2(Q-iU)(\hat{n}) = \sum_{l,m}\left[\frac{(l+s)!}{(l-s)!}\right]^{1/2} a_{lm}^{(-2)}Y_{lm}(\hat{n}) \tag{3.55}$$

that have spin 0, with coefficients of expansion equal to

$$a_{lm}^{(2)} = \left[\frac{(l+s)!}{(l-s)!}\right]^{-1/2}\int d\Omega Y_{lm}^*(\hat{n})\bar{\eth}^2(Q+iU)(\hat{n}) \tag{3.56}$$

$$a_{lm}^{(-2)} = \left[\frac{(l+s)!}{(l-s)!}\right]^{-1/2}\int d\Omega Y_{lm}^*(\hat{n})\eth^2(Q-iU)(\hat{n}). \tag{3.57}$$

It is convenient to introduce their linear combinations $a_{(E,B),lm}$:

$$a_{E,lm} = -\frac{\left[a_{lm}^{(2)} + a_{lm}^{(-2)}\right]}{2} \tag{3.58}$$

$$a_{B,lm} = i\frac{\left[a_{lm}^{(2)} - a_{lm}^{(-2)}\right]}{2} \tag{3.59}$$

and to name $\hat{a}_{(E,B),lm}$:

$$\hat{a}_{(E,B),lm} = \left[\frac{(l+s)!}{(l-s)!}\right]^{1/2} a_{(E,B),lm}. \tag{3.60}$$

Finally we consider the two scalar and pseudoscalar quantities that describe the polarization:

$$E(\hat{n}) = -\frac{1}{2}\left[\bar{\eth}^2(Q+iU) + \eth^2(Q-iU)\right] = \sum_{l,m}\hat{a}_{E,lm}Y_{lm}(\hat{n}) \tag{3.61}$$

$$B(\hat{n}) = \frac{i}{2}\left[\bar{\eth}^2(Q+iU) - \eth^2(Q-iU)\right] = \sum_{l,m}\hat{a}_{B,lm}Y_{lm}(\hat{n}) \tag{3.62}$$

that are invariant under rotations, but while E remains the same under parity, B changes sign.

These represent the decomposition of the polarization tensor in a *divergence free* term B and a *curl free* term E. In the Figure 3.3 we can see the patterns formed by the polarization field around cold (blue) and hot (red) spots in the sky: the E mode is invariant under reflexion, while the B mode changes pattern.
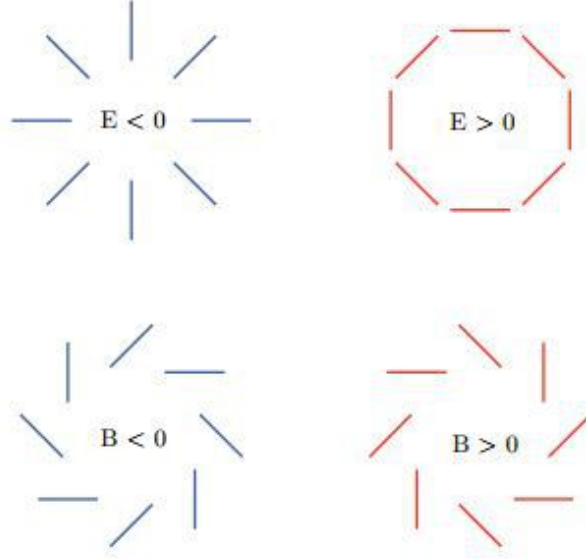
Figure 3.3. E and B modes polarization patterns, [39].

3.3.4 The polarization power spectra

For symmetry reasons, between temperature and polarization anisotropies we have 4 types of two-points correlation functions: the autocorrelations of the temperature fluctuations and the E and B modes, named TT, EE and BB, and the cross-correlation TE between the temperature fluctuations and the E mode, because TB and EB are zero (opposite parity). The angular power spectra are defined as:

$$C_l^{XY} \equiv \frac{1}{2l+1} \sum_m \left\langle a_{lm}^X a_{lm}^Y \right\rangle, \tag{3.63}$$

with $X, Y = T, E, B$. We can build the 3×3 matrix of the spectra:

$$\begin{pmatrix} C_l^{TT} & C_l^{TE} & 0 \\ C_l^{ET} & C_l^{EE} & 0 \\ 0 & 0 & C_l^{BB} \end{pmatrix}. \tag{3.64}$$

Each of these spectra (Figure 3.4) has a different dependence on the cosmological parameters: by combining the measurements of the several spectra we can better constrain the parameters, disciminating between the several cosmological models.

A CMB fluctuations map is a possible realization of a statistical ensemble, then we can extract all the informations at the first order with the power spectrum.
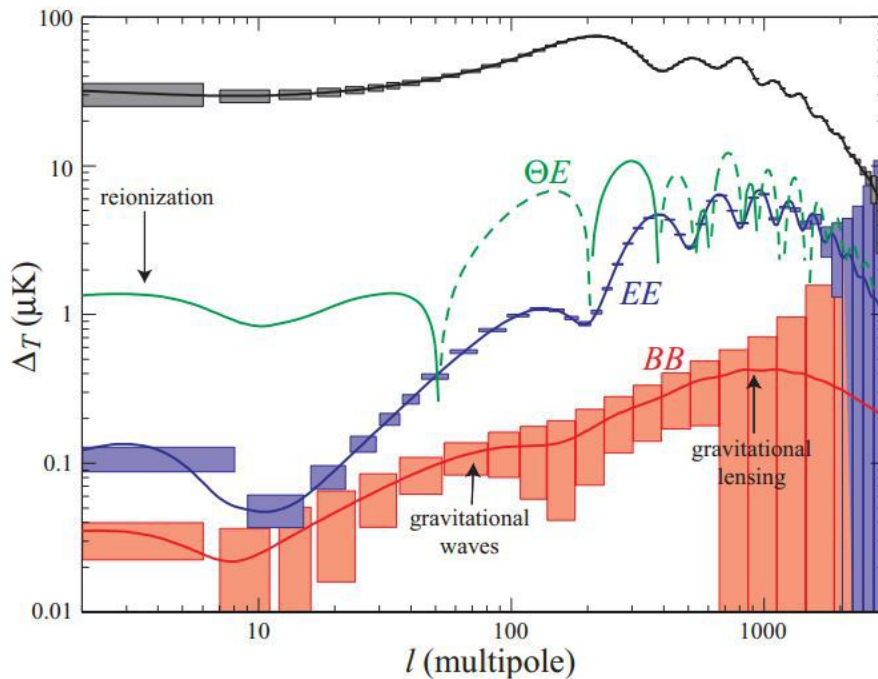
Figure 3.4. Temperature and polarization spectra, [40].

Indeed, in order to have a more detailed description, we can consider tools of higher orders, such as the bispectrum (the three-points correlation functions that we will see in the Section 3.7), that, however, are zero supposing total Gaussianity. The power spectrum provides the anisotropies amplitude to the several angular resolution. Temperature quadrupole, i.e. multipole $l = 2$, can be produced both by scalar perturbations and by tensor perturbations. We have that:

- Scalar perturbations (density) produce only E modes;

- Vector perturbations (vorticity) produce only B modes;

- Tensor perturbations (gravitational waves) produce both E and B modes.

About the 10% of the CMB radiation is polarized. In order to study the CMB polarization we have to note that the B mode has two different contributions: the first one is due to the gravitational waves produced in the primordial Universe, the second one is due to the gravitational lensing that mix the E modes and the B modes, converting the E modes in the B modes. To detect the primordial B modes allows to study the tensor modes, so the inflationary models. The primordial contribution can be dominant for angular scales smaller than $2°$, as we can see in Figure 3.4, but its amplitude depends on the unknown energy scale with which are generated the gravitational waves in a primordial phase, and could be too small to be detected. Instead, the B modes due to the gravitational lensing are detectable at smaller angular scales and contain informations related to the other cosmological parameters, such as dark matter, dark energy or spatial curvature.

In the Figure 3.4 we can see, moreover, that the peaks of the temperature power spectrum and EE polarization are out of phase of $\pi/2$. Moreover, the EE and BB spectra are dominated to the large scales, i.e. $l \leq 10$, from the reionization signal. It is important to note that the position and the height of the reionization peak in the CMB polarization spectra are fundamental to determine the optical depth to reionization τ, as defined in the eq. (3.76). This parameter suppress the peaks amplitude in the polarization and temperature spectra, but in the latter its effect is completely degenerate with other parameters.

3.4   Primary anisotropies

The CMB photons temperature is affected by the imprints of the previous coupling of the photons with other fields, such as gravity, density and velocity. The anisotropies that originate on the last scattering surface, are called primary and are from three processes independent of the frequency:

- The Sachs-Wolfe effect, due to the gravitational potential fluctuations present on the last scattering surface, for which photons are redshifted coming out from a potential well ($\Psi < 0$), and viceversa (Sachs and Wolfe 1967 in Ref. [41]);

- The effect due to the intrinsic adiabatic fluctuations of the photon plus baryon fluid, for which photons diffusing from over-dense regions ($\delta_b > 0$) are hotter, and viceversa (Silk 1968 in Ref. [42]);

- The Doppler effect, due to the bulk motion, i.e. the peculiar velocity, during decoupling of the different regions of the last scattering surface, for which photons emerging from regions that move in opposite direction to the observer ($v_b > 0$) are redshifted, and viceversa (Sunyaev and Zel'dovich 1970 in Ref. [43]).

Primary temperature fluctuation is simply given by the linear sum of the previous three contributions:

$$\frac{\Delta T}{T}(\hat{n}) = [\Psi + \Theta + \hat{n} \cdot \vec{v}_b]_{t=t_{LS}} \tag{3.65}$$

where $\Theta \equiv \Delta T/T = \delta_b/3$, t_{LS} is the time of the last scattering, and $\hat{n}$ the direction of observation. So, the measured mean squared temperature fluctuations is:

$$\left\langle \left(\frac{\Delta T}{T}\right)^2 \right\rangle = (\Psi + \Theta)^2 + (\hat{n} \cdot \vec{v}_b)^2. \tag{3.66}$$

We can identify three different regions on the angular power spectrum (Figure 3.5), that refer to the temperature fluctuations behavior as a function of the different scales, or multipoles l:

- $2 \leq l < 100$, the Sachs-Wolfe plateau;

- $100 \leq l < 800$, the acoustic waves or the Doppler peaks;

- $l \geq 800$, the damping tail.
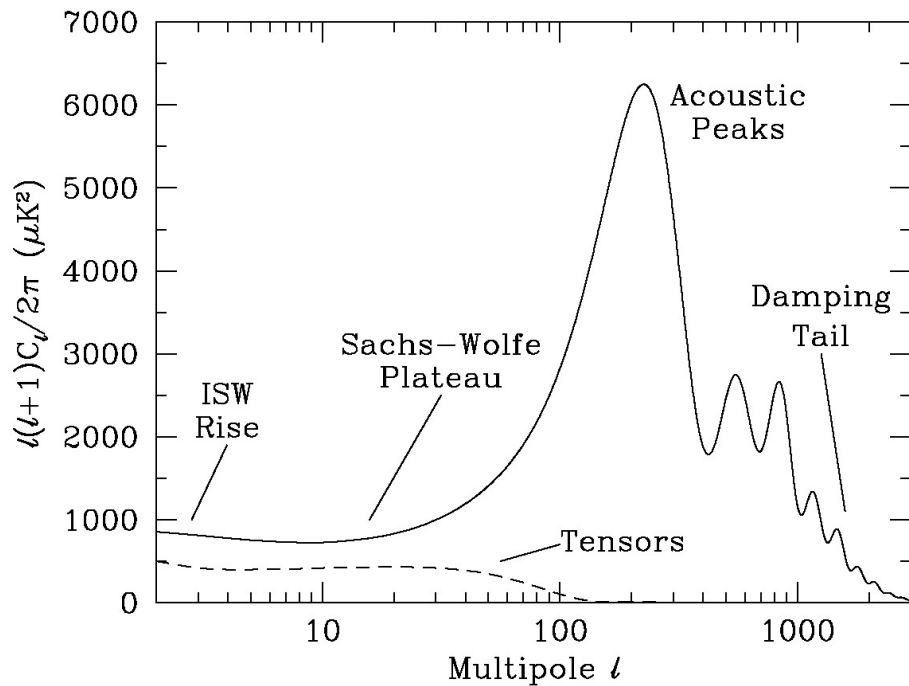
Figure 3.5. The regions of the angular power spectrum: the ISW Rise (secondary effect); Sachs-Wolfe Plateau; Acoustic Peaks; and Damping Tail, [44].

3.4.1 The Sachs-Wolfe plateau

We have the Sachs-Wolfe plateau on scales greater than the horizon at decoupling, that correspond to the angular scales greater than 2°, and is due to the combined effect of gravity and density fluctuations.

As we said, photons coming out from the potential wells are redshifted, while those from the potential peaks blueshifted. Named ψ the fluctuation of the gravitational potential Ψ, we have

$$\left(\frac{\delta T}{T}\right)_g = \frac{\delta \Psi}{\Psi} = -\frac{|\psi|}{c^2}. \tag{3.67}$$

On the contrary, photons diffusing from over-dense regions, that are hotter, will be blueshifted and from sub-dense regions redshifted. Remembering that $\rho \propto \lambda^{-3}$ and $T \propto \lambda^{-1}$, we have

$$\left(\frac{\delta T}{T}\right)_d = \frac{1}{3}\frac{\delta \rho_b}{\rho_b} = \frac{1}{3}\delta_b. \tag{3.68}$$

From the Newtonian limit of the metric in General Relativity, we know that

$$\delta_b = 2\frac{|\psi|}{c^2}, \tag{3.69}$$

then

$$\left(\frac{\delta T}{T}\right)_d = \frac{2}{3}\frac{|\psi|}{c^2}. \tag{3.70}$$

Being the over-dense regions also potential wells, thanks to the adiabaticity of the perturbation, the total temperature fluctuation will be

$$\frac{\delta T}{T} = \left(\frac{\delta T}{T}\right)_d + \left(\frac{\delta T}{T}\right)_g = -\frac{1}{3}\frac{|\psi|}{c^2}, \tag{3.71}$$

in favor of the gravity.

3.4.2 The Doppler peaks

We have acoustic waves, or Doppler peaks, on angular scales between $0.1°$ and $2°$, for the combined effect of the $(\Psi + \Theta)$ and the Doppler terms.

The coupled fluid of baryons and photons falls into the potential wells of the dark matter, that, thanks a negligible Jeans length, are formed before. However in the falling, the fluid becomes over-dense and the radiation pressure grows until rejects it out. This process can be well described by a harmonic oscillator, see the Figure 3.6.
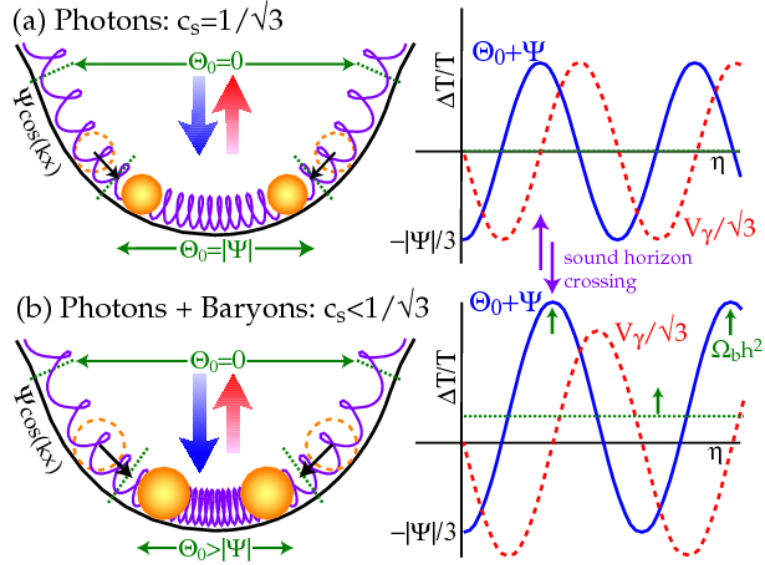
Figure 3.6. The fluid of baryons and photons coupled adiabatically falls into the potential wells of the dark matter, supported by the radiation pressure that reject it out. This process can be well described from a harmonic oscillator. Without baryons (a), we do not have the acoustic wave because the two contribution of density and velocity of the fluid cancel each other. Otherwise the baryon-drag (b) produce the acoustic peaks, [45].

The dynamics of a fluid of density ρ, velocity $\vec{v}$ and pressure P, is governed by the continuity equation (2.73), the Euler equation (2.74) and the Poisson equation (2.75). In tight-coupling approximation, i.e. for the simultaneity of decoupling and recombination, the dynamics of the fluid depends on the only variable $\Theta \equiv \Delta T/T = \delta_b/3$. We can write the solution for a single mode k in Fourier space of the previous equations, as a harmonic oscillator with a forcing term independent of time:

$$\Theta(t) = -(1+R)\Psi + B_1 cos(kc_s t) + B_2 sin(kc_s t), \tag{3.72}$$

where $R \equiv (3\rho_b)/(4\rho_\gamma)$ is time independent, B_1 and B_2 are coefficients fixed by the initial condition and $c_s = c/\sqrt{3(1+R)}^{1/2}$ is the sound speed in the medium. All the scales into the horizon, represented by the several Fourier modes, are described as acoustic waves that propagate with the same velocity c_s: at the recombination epoch the smallest scales have done the higher number of oscillations.

If in the harmonic oscillator model, eq. (3.72), we take $R = 0$ (and $c_s = c/\sqrt{3}$), i.e. we ignore the baryonic contribution, and we assume an adiabatic perturbation, we can separate the contribution due to the δ field from the one due to the Doppler effect. Initially, neglecting the Doppler effect, we obtain:

$$\Theta(t) = -\Psi + \frac{1}{3}\Psi cos(kc_s t). \tag{3.73}$$

The $(\Theta + \Psi)$ term has a cosinusoidal oscillation with peaks for $kc_s t_{LS}$ integer multiple of π. This means that a single scale which has done half-oscillation at recombination, is in the maximum compression when is in the potential wells, and in the maximum rarefaction on the peaks. This scale produce the highest $\Delta T/T$, and the first peak of the CMB power spectrum, due to the δ contribution. Moreover, the scale corresponding to the half of the previous scale, has done a complete oscillation at recombination, and is in the maximum compression on the potential peaks, and in the maximum rarefaction in the wells. This latter scale corresponds to the second acoustic peak of the CMB power spectrum, due to the δ contribution. In conclusion, the odd acoustic peaks, of the CMB power spectrum, correspond to the maximum compression in the potential wells, and the even acoustic peaks to the maximum compression on the potential peaks.

Instead, if we consider only the Doppler effect, we have:

$$\left[\frac{\Delta T}{T}\right]_{Doppler} = \frac{i}{3}\Psi sin(kc_s t), \tag{3.74}$$

out of phase by $\pi/2$ respect to the contribution due to the δ field. Ignoring the baryonic contribution ($R = 0$), the two effects, that have the same amplitude and are summed in quadrature, cancel each other producing the cancellation of the acoustic waves (upper right plot of the Figure 3.6). In other words, is constant the sum of the kinetic energy, due to the velocity of the fluid, and the potential energy, due to the compression. Indeed, thanks to the $R > 0$ (and $c_s < c/\sqrt{3}$) the cosinusoidal oscillations, due to the density and gravity terms, are larger than those sinusoidal, due to the Doppler effect, because baryons contribute in a non-negligible way to the deep of the potential wells. We have:

$$\Theta(t) = \frac{1}{3}(1+3R)\Psi cos(kc_s t) - (1+R)\Psi. \tag{3.75}$$

In this case, since the amplitude of the peaks depends on the baryon density, increasing R corresponds to increasing the odd peaks respect to the even. Therefore, the sum in quadrature of the temperature fluctuations is no longer constant, producing the acoustic peaks (lower right plot of the Figure 3.6). The *baryon-drag* moves the energy balance in favor of the energy potential.

3.5   Secondary anisotropies

The secondary anisotropies originate after recombination, during the travel of the photons from the last scattering surface to the observer ($0 \leq z \leq 10^3$). The physical processes producing these secondary anisotropies are of two kind. The first ones we have are those due to the interactions with the gravitational potential between recombination and today (Figure 3.7):

- Integrated Sachs-Wolfe effect (ISW), early and late;

- Rees-Sciama effect (RS);

- Gravitational Weak Lensing (WL).

The second ones we have are those due to the scattering with the free electrons (Figure 3.8). In fact, the Universe between $6 < z < 100$ passes through the phase of reionization and the photons of the CMB will be again affected from the baryons velocity and overdensity, erasing the old or producing new temperature anisotropies. These are:

- Sunyaev-Zel'dovich effect (SZ), thermal and kinetic;

- Ostriker-Vishniac effect (OV);

- Reionization.
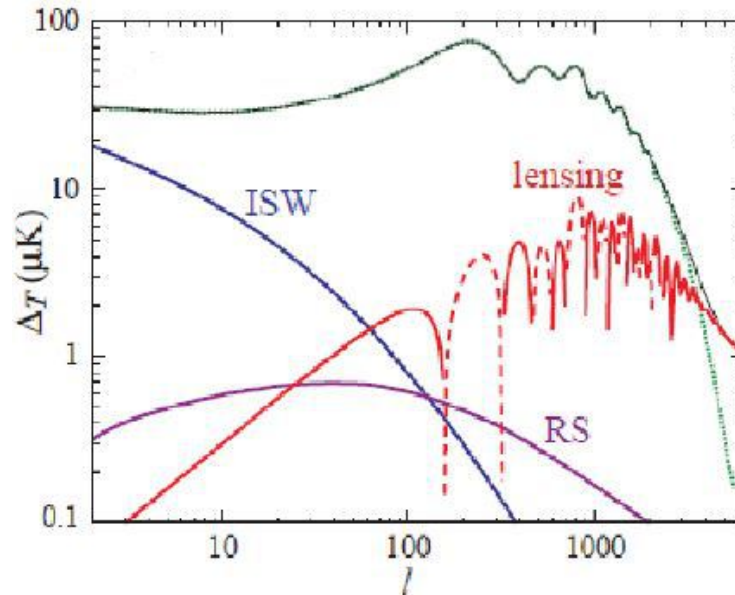
Figure 3.7. Power spectrum of the secondary anisotropies due to the interactions with the gravitational potential, [46].
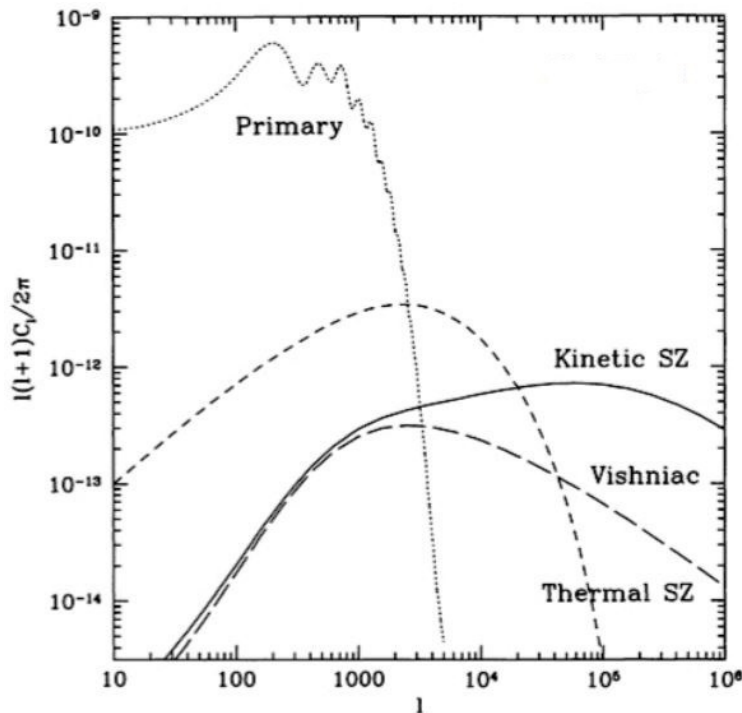
Figure 3.8. Power spectrum of the secondary anisotropies due to the scattering with the free electrons, [47].

3.5.1   Integrated Sachs-Wolfe effect

The Integrated Sachs-Wolfe, see Ref. [41], is the effect for which photons are gravitationally redshifted, or blueshifted, crossing a varying with time gravitational potential ($\dot{\psi} \neq 0$). The difference respect to the primary SW effect is that, instead of occurring at the last scattering surface, is integrated along the photon's path between the last scattering surface and the observer.

If in the time between the photon falling in and coming out from a potential well, this latter changes with time, the difference between the photon blueshift and redshift, crossing the potential well, can produce a net change of its energy. If the Universe is matter dominated, the spatial curvature is negligible, and the linear perturbation theory is valid, the ISW effect is zero, because in this case ψ is constant with time. In a realistic cosmological model the matter radiation equality occurs no long before the last scattering, so, during this and shortly afterwards, the matter dominated approximation is not completely correct. Then, we can distinguish (Figure 3.9) the *Early ISW*, that occurs immediately after the photons decoupling, when matter does not completely dominate over radiation, and the *Late ISW*, that arise quite recently, when the dark energy, or the cosmological constant, starts to dominate the Universe expansion, changing the gravitational potential. The gravitational potential produces anisotropies only if the scale k^{-1} of the perturbation is comparable to the time scale of its decay. Otherwise, if the wavelength is much shorter, it crosses many overdensities and underdensities, and the contributions of the different ISW terms cancel with each other. The ISW affects the CMB angular

power spectrum for $l \leq 200$, being the time scale for the potential decay about of order of the horizon size at last scattering.
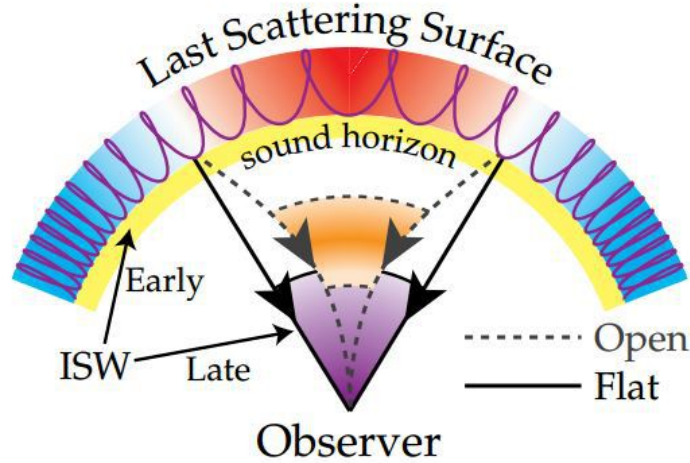
Figure 3.9. Secondary anisotropies: difference between Early ISW and Late ISW, [45].

3.5.2 Rees-Sciama effect

The Rees-Sciama effect, see Ref. [48], is a ISW effect due to the non-linear growth with time of the gravitational potential from the collapse of structures at very late times. This effect is smaller than the primary anisotropies of about two order of magnitude, as we can see in Figure 3.7, and its relevant angular scale is of $5 - 10$ arcminutes, i.e. that one of galaxy clusters and superclusters.

3.5.3 Gravitational Weak Lensing

The structures present a large scales, beside producing secondary anisotropies, distort the primary through gravitational lensing. If a pair of photons moves towards the observer, forming initially an angle θ between their directions of propagation, for the lensing effect the observer will see an angle $\theta + \delta\theta$, where $\delta\theta$ is the distorsion of light (few arcmin). This distorsion is called Weak Lensing effect, see Ref. [49], and the result is the smearing of the oscillations of the CMB angular power spectrum at small scale.

3.5.4 Sunyaev-Zel'dovich effect

The Sunyaev-Zel'dovich effect, see Ref. [43], is due to the inverse Compton[3] scattering of the low energy CMB photons with the high energy free electrons of the hot ionized gas in a cluster of galaxies. This effect affects the small angular scales, is frequency dependent and can be divided in:

---

[3]In the rest reference frame of the relativistic particle, we can see the inverse Compton scattering as Thomson scattering.

- Thermal: photons, crossing the cluster, are scattered by the random motion of free electrons, from which receive energy, deforming the black body spectrum: we have a temperature reduction for the lowest frequencies (Rayleigh-Jeans part) and an increase for the highest (Wien part);

- Kinetic: photons have a preferred direction of Thomson scattering, due to the bulk motion with a peculiar velocity of the hot ionized gas with a cluster at low redshift, and they will be redshifted or blueshifted for the Doppler effect, without to distort the power spectrum.

3.5.5 Ostriker-Vishniac effect

The Ostriker-Vishniac effect, see Ref. [50], is a kinetic SZ effect, due to the photons scattering off ionized regions or clouds with bulk peculiar velocities at high redshift. This effect generate temperature fluctuations on angular scale of order of 1 arcmin, when we consider the second order perturbation theory for small inhomogeneities, while at the first order vanishes.

3.5.6 Reionization

The Universe at late time reionized and again CMB photons scattered off free electrons, reaching the observer from a different direction respect to the initial one. Reionization is demonstrated by the absorption spectra of high redshift quasar, but the sources that produce it are still discussed. This CMB photons mixing occurs at angular scale smaller than the horizon size at the time of reionization, then the angular scales increases as the redshift of the scattering decreases. However this process is contrasted by the free electrons density reduction that corresponds to the decrease of the probability that this scattering happens. The final effect is a decrease of the power in the spectra for $l > 10$, while the power at large scales remains unchanged. The power spectrum is suppressed by a factor $e^{2\tau}$, where τ is

$$\tau = \int_{\eta_{reion}}^{\eta_0} d\eta n_e \sigma_T a \tag{3.76}$$

the optical depth to reionization, η_{reion} is the conformal time at reionization, n_e the electrons number density and σ_T the cross section of the Thomson scattering.

The parameter τ suppress the peaks amplitude in the temperature power spectrum, but its effect is completely degenerate with other cosmological parameters. On the contrary, the reionization signal dominates the position and the height of the peaks in the polarization spectra to the large scale $l \leq 10$, allowing to better constrain τ.

3.5.7 The visibility function

So far we considered an istantaneous last scattering surface at $z = 1100$, that means the contemporaneity of recombination and decoupling. Indeed this has a thickness, that we can describe through a *visibility function* $g(z)$, which depends on the probability of having the last scattering increasing the fraction of free electrons X_e with time. We can write:

$$g(z) = e^{-\kappa} \frac{\sigma_T X_e n_e}{1+z}, \tag{3.77}$$

with κ the optical depth of the last scattering surface:

$$\kappa = \int_{\eta}^{\eta_0} d\eta' n_e \sigma_T a. \tag{3.78}$$

The temperature fluctuations will be modulated from the visibility function in this way:

$$\frac{\Delta T}{T}(\hat{n}) = \int_0^{\infty} \left[g(z) \left(\Psi + \Theta + \hat{n} \cdot \vec{v}_b \right) + e^{-\tau} H^{-1} \dot{\Psi} \right] dz, \tag{3.79}$$

where $\int_0^{\infty} \left(e^{-\tau} H^{-1} \dot{\Psi} \right) dz$ is the ISW effect.

In conclusion, we can calculate the CMB angular power spectrum fixing a model of Universe through the values of its parameters, and following in this scenario the evolution of the photons distribution function, obtained integrating the Boltzmann equations (2.61). Changing the model, the shape of the theoretical spectrum is modified (Figure 3.10).
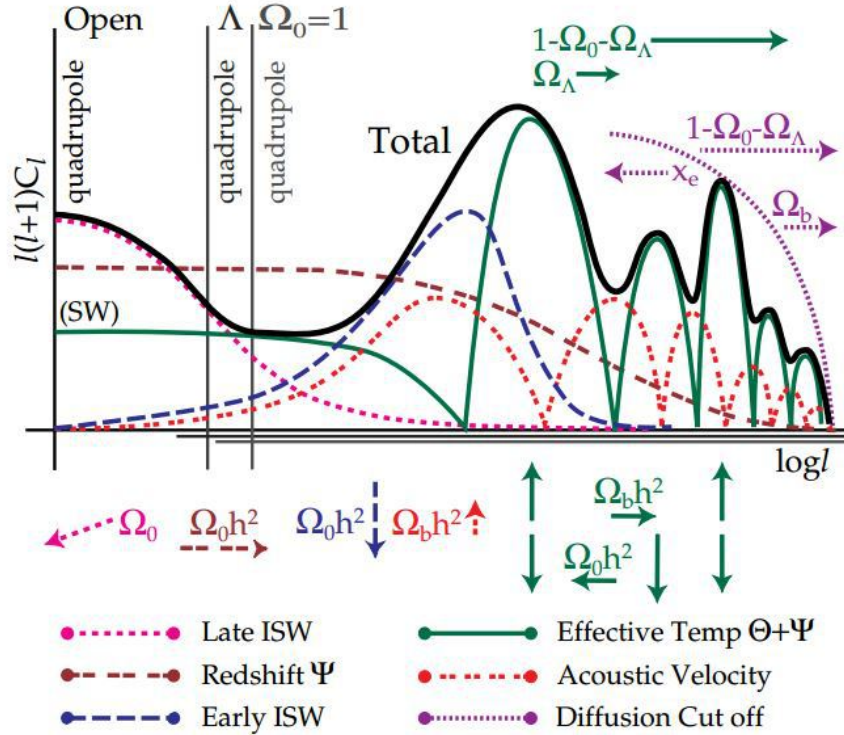
Figure 3.10. Parameter sensitivity of the CMB angular power spectrum, to vary of perturbations, [45].

The angular power spectrum depends mainly on some cosmological parameters, see Ref. [51]:

- Ω_0, because, decreasing, reduces the angular scale of a given physical scale, changing the curvature of the Universe, and shifts the peaks towards higher l;

- H_0, that, decreasing, increases the last scattering surface distance, delaying the matter to radiation equivalence, and shifts the peaks towards higher l;

- $\Omega_b h^2$, that is $\propto R$: if $\Omega_b = 0$ there is not baryon-drag and acoustic peaks, but growing $\Omega_b \neq 0$ increases the gravitational potential, enhancing the amplitude of the odd peaks respect to the even;

- Λ, that, growing, increases the last scattering surface distance, accelerating the Universe expansion, so the Late ISW effect enhances the power of the spectrum for $l \to 0$;

- n_S, the tilt of the primordial power spectrum that, increasing, enhances the slope, therefore the power, of the angular power spectrum at smaller angular scales (higher l).

3.6 The matter power spectrum

As discussed, the large scale modes evolve very much differently than the small scale modes, depending on the time of the horizon crossing, before or after the matter-to-radiation equivalence. We have that the amplitude of the matter perturbation is constant out of the horizon, and, within the horizon, grows logarithmically during the radiation domination and linearly with the scale factor a during the matter domination. However, all the modes evolve in the same way at the late time, and in this epoch we can study the distribution of the matter.

When perturbations evolve in the matter dominated Universe within the horizon, we can factorize their dependences on the scale k and the scale factor a, see Ref. [13]. We name these two factors, independent each other, respectively *Transfer function* $T(k)$, which describes the evolution of perturbations depending on their dimension:

$$T(k) \equiv \frac{\phi(k, a_{late})}{\phi_{Large-Scale}(k, a_{late})}, \tag{3.80}$$

valid for $a \gg a_{late}$ that is taken in a very late time, and *Growth function* $D(a)$:

$$D(a) = a \frac{\phi(a)}{\phi(a_{late})}. \tag{3.81}$$

The primordial potential decreased by a small amount on large scales, as we can see in Ref. [13], then we have $\phi_{Large-Scale}(k, a_{late}) = (9/10)\phi_P(\vec{k})$, where ϕ_P is the value of the potential during the inflation. Moreover, we have the $T(k) = 1$ on large scales and $D(a) = a$ in the matter dominated Universe. In conclusion we can write the evolution of the perturbation as:

$$\phi(\vec{k}, a) = \frac{9}{10}\phi_P(\vec{k})T(k)\frac{D(a)}{a}, \tag{3.82}$$

always valid for $a \gg a_{late}$. Using the Poisson equation in Fourier space:

$$k^2\phi = 4\pi G\rho a^2 \delta_m, \tag{3.83}$$

we can write the matter overdensity today as:

$$\delta(\vec{k}, a) = \frac{3}{5}\frac{k^2}{\Omega_m H_0^2}\phi_P(\vec{k})T(k)D(a). \tag{3.84}$$

We can derive the matter power spectrum, see eq. (3.6), in terms of the primordial power spectrum of the scalar fluctuations $P_S(k)$, eq. (2.137):

$$P_{dm}(k, a) = \frac{9}{25}\frac{k^4}{\Omega_m^2 H_0^4}P_S(k)T^2(k)D^2(a). \tag{3.85}$$

Considering $P_S(k) \propto k^{-3}k^{n_S-1}$ we obtain:

$$P_{dm}(k, a) \propto k^{n_S}T^2(k)D^2(a). \tag{3.86}$$

In Figure 3.11 we can see the behavior of the matter power spectrum, fixing Ω_m as a function of Ω_b: $P_{dm} \propto k$ on large scales, because $n_S \simeq 1$ and $T(k) = 1$, while on small scales P_{dm} is a decreasing function of k, because the smallest scales, by entering into the horizon before the matter domination, will be more suppressed when the metric perturbation decay. The point of turnover in the power spectrum corresponds at the scale that is in horizon crossing at the matter-to-radiation equality.
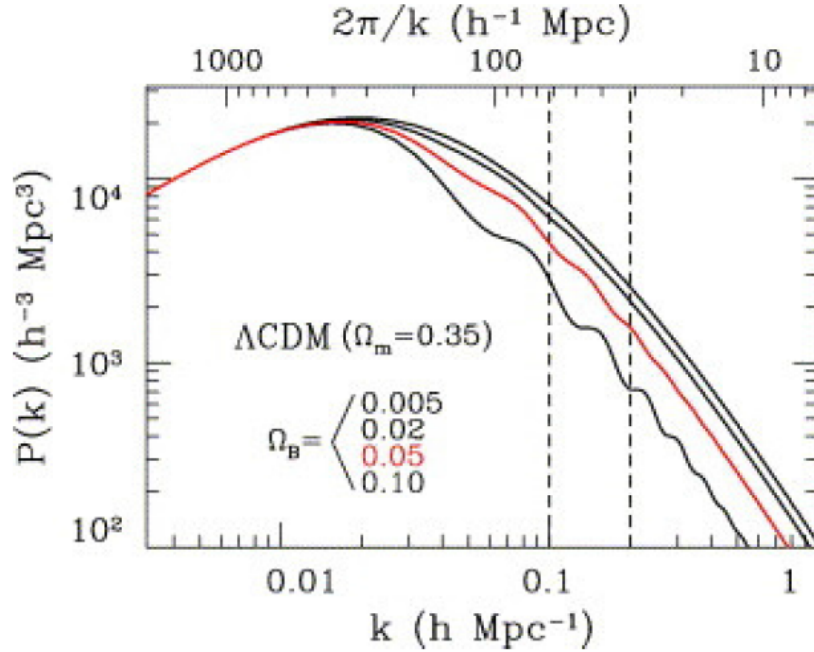
Figure 3.11. An example of the matter power spectrum in the ΛCDM model for a fixed value of Ω_m. By increasing the amount of baryons, we increase the amplitudes of the acoustic oscillations (BAO) and the suppression of the power at the small scales, [52].

However, this perturbations power spectrum is not that one observed in the visible matter with the galaxies surveys P^*, but the two spectra are proportional through a bias factor b:

$$P^* = b^2 P_{dm}. \tag{3.87}$$

Moreover, we have to introduce a window function W which takes into account that only a sample of the galaxy distribution is observed, then we will have a convolution of P_{dm} with this one. W is equal to V^-1 inside a sphere of radius R and volume V, and zero outside, while in Fourier space is:

$$W_k = 3\frac{sin(kr) - krcos(kr)}{(kr)^3}. \tag{3.88}$$

Obviously, we can derive only the statistical properties of the observed spectrum, therefore we introduce the variance of the field:

$$\sigma_R^2 = \int P_{dm}(k)W_k(kr)d^3k. \tag{3.89}$$

Very important in the matter power spectrum measurements is σ_8, the root mean squared of the fluctuations over a volume of radius $8h^{-1}Mpc$. This is constrained with the detection of the Baryon Acoustic Oscillations (BAO) that, due to the effect of the oscillations of baryons, which are tightly coupled to photons before decoupling and then oscillate with them, are imprinted at small scales in the matter power spectrum.

3.7 Primordial non Gaussianities and the CMB Bispectrum

As discussed in the previous section, primordial perturbations are expected to be Gaussian and all the CMB statistics should be mostly described by the angular power spectrum (i.e. the two point correlation function). However it is interesting to also consider the possibility of non-Gaussianities, either primordial, either produced lately and the three point correlation function. Given, for example, a primordial non-Gaussian density fluctuation of the gravitational potential $\psi(\mathbf{k})$, we have

$$\langle\psi(\mathbf{k}_1)\psi(\mathbf{k}_2)\psi(\mathbf{k}_3)\rangle = P_\psi^{(3)}(k_1, k_2, k_3)\delta_{Dirac}(\mathbf{k}_1 + \mathbf{k}_2 + \mathbf{k}_3), \tag{3.90}$$

where $P_\psi^{(3)}(k_1, k_2, k_3)$ is the spatial bispectrum of the gravitational potential. The angular three point correlation function used to investigate the possible non-Gaussian features of the CMB can be written as:

$$\left\langle\frac{\Delta T}{T}(\hat{n}_1)\frac{\Delta T}{T}(\hat{n}_2)\frac{\Delta T}{T}(\hat{n}_3)\right\rangle = \sum_{l_i,m_i} \langle a_{l_1m_1}a_{l_2m_2}a_{l_3m_3}\rangle Y_{l_1m_1}(\hat{n}_1)Y_{l_2m_2}(\hat{n}_2)Y_{l_3m_3}(\hat{n}_3),$$

$$\tag{3.91}$$

where, as usual, we consider the expansion of the CMB temperature anisotropies in spherical harmonics $Y_{lm}(\hat{n})$ with multipoles

$$a_{lm} = \int d^2\hat{n} Y_{lm}^*(\hat{n}) \frac{\Delta T}{T}(\hat{n}). \tag{3.92}$$

We can split the multipoles a_{lm} into two parts:

$$a_{lm} = a_{lm}^L + a_{lm}^{NL}, \tag{3.93}$$

where a_{lm}^L is that one Gaussian and a_{lm}^{NL} is that one non-Gaussian. We define the angular CMB bispectrum as the harmonic conjugate of the three point correlation function:

$$\langle a_{l_1 m_1} a_{l_2 m_2} a_{l_3 m_3} \rangle = B_{l_1 l_2 l_3}^{m_1 m_2 m_3}, \tag{3.94}$$

that, ignoring the second order terms in a_{lm}^{NL}, can be written as:

$$B_{l_1 l_2 l_3}^{m_1 m_2 m_3} = \left\langle a_{l_1 m_1}^L a_{l_2 m_2}^L a_{l_3 m_3}^{NL} \right\rangle + \begin{pmatrix} l_3 \leftrightarrow l_1 \\ l_2 \leftrightarrow l_3 \end{pmatrix} + \begin{pmatrix} l_3 \leftrightarrow l_2 \\ l_1 \leftrightarrow l_3 \end{pmatrix}. \tag{3.95}$$

The rotational invariance of the CMB sky implies that we can decompose $B_{l_1 l_2 l_3}^{m_1 m_2 m_3}$ in this way:

$$B_{l_1 l_2 l_3}^{m_1 m_2 m_3} = \begin{pmatrix} l_1 & l_2 & l \\ m_1 & m_2 & m \end{pmatrix} B_{l_1 l_2 l_3}, \tag{3.96}$$

where we have that the matrix is the Wigner 3j symbol and $B_{l_1 l_2 l_3}$ is the angle averaged bispectrum, i.e. the observational quantity. The Wigner 3j symbol ensures that the bispectrum satisfies the triangle conditions $|l_i - l_j| \le l_k \le l_i + l_j$ for all permutation of indices i, j, k, and the selection rules $m_1 + m_2 + m_3 = 0$ and $l_1 + l_2 + l_3 = even$.

Obviously, in order to calculate the correct bispectrum signal we have to take into account the proper initial conditions after the end of the inflation in the Universe radiation dominated. These initial condition reflect the nature of the cosmological perturbations, that can be adiabatic or isocurvature or mixed if there are extra degrees of freedom (for example the Curvaton field) other than the Inflaton field ϕ_I (see Ref. [53]), depending on the scenario considered.

It is possible to describe the contribution of non-linear effects to the curvature perturbations, introducing a phenomenological parameter that we can compare with the experimental measurements. Therefore, in order to study the amplitude and angular structure of the non-Gaussian signal, we define the kernel $f_{NL}(\mathbf{k}_1, \mathbf{k}_2, \mathbf{k}_3)$ writing the non-Gaussian part of the primordial gravitational potential as a double convolution in Fourier space:

$$\phi_{NL}(\mathbf{k}_3) = \frac{1}{(2\pi)^3} \int d^3 k_1 d^3 k_2 \delta^{(3)}(\mathbf{k}_1 + \mathbf{k}_2 + \mathbf{k}_3) \phi_L(\mathbf{k}_1) \phi_L(\mathbf{k}_2) f_{NL}(\mathbf{k}_1, \mathbf{k}_2, \mathbf{k}_3), \tag{3.97}$$

where $\phi_L(\mathbf{k})$ is the Gaussian part of the primordial gravitational potential. The simplest choise, widely used in the literature, is to take $f_{NL}(\mathbf{k}_1, \mathbf{k}_2, \mathbf{k}_3) = f_{NL}$, where the constant f_{NL} is a phenomenological parameter introduced to parameterize the

level of non-Gaussianity. In this model, in real space, we can write the curvature perturbations as:

$$\phi(x) = \phi_L(x) + f_{NL} \left[\phi_L^2(x) - \left\langle \phi_L^2(x) \right\rangle \right]. \tag{3.98}$$

where the first term is the linear contribution and the second one the quadratic correction. Taking $f_{NL} = 0$ we obtain again the linear approximaxion, i.e. Gaussian perturbations. The CMB angular bispectrum for a constant kernel has been calculated by Ref. [54], but it is possible to demonstrate that is important to include the momentum dependence in the data analysis (see Ref. [55]), because the non-Gaussian signal in standard slow-roll inflation scenario comes from the momentum-dependent part of $f_{NL}(\mathbf{k}_1, \mathbf{k}_2, \mathbf{k}_3)$. However, being $\phi \sim 10^{-5}$, the second term at right of the equation (3.98) is $\phi \sim 10^{-5} f_{NL}$, smaller than the first one, and a constant parameterization is enough to provide the non-Gaussianity level.

The non-Gaussianity, or non-linearity, parameter f_{NL} can also be expressed in terms of the standard slow-roll parameters ϵ and η as (see Ref. [56, 57, 58]):

$$f_{NL} \sim 3\epsilon - 2\eta. \tag{3.99}$$

It is important to note that the parameterization (3.98) is valid only for local non-Gaussianity (*squezeed*), $k_1 \ll k_2 \sim k_3$, predicted, for example, from the standard inflationary models, and is not valid for equilateral configurations, $k_1 \sim k_2 \sim k_3$. Moreover, sources of non-Gaussian signals are also the secondary anisotropies of the CMB, that have to be removed in order to detect the primordial non-Gaussian anisotropies, as the bispectrum resulting from the 2nd order Rees-Sciama effect (see for example Ref. [59, 60]), or the cross correlation between the gravitational lensing and the Integrated Sachs-Wolfe (ISW) effect, and the cross-correlation between the gravitational lensing with the Sunyaev-Zel'dovich (SZ) effect (see for example Ref. [61]).

Chapter 4

Constraining Cosmological Parameters from recent observations of the Damping Tail of the CMB angular spectrum

The measurements of the CMB damping tail, corresponding to the multipole range going from $l \sim 700$ up to $l \sim 3000$ of the anisotropies power spectra, play a key role in the determination of crucial parameters as the relativistic number of degrees of freedom N_{eff}, the primordial Helium abundance Y_{p} and the running $dn_S/d\ln k$ of the scalar spectral index.

While Y_{p} does not represent a free parameter of the theory, because can be determined unambigously assuming standard BBN, $dn_S/d\ln k$ is expected to be negligible in most inflationary models. On the other hand, we saw that the effective number of relativistic degrees of freedom N_{eff} practically parametrizes the energy density of relativistic particles in the early Universe. Deviations from the standard value due to a non-vanishing neutrino chemical potential are possible but bound to be small. A detection of $N_{\mathrm{eff}} \neq 3.046$ could indicate the presence of physics beyond the standard model of particle physics, like the existence of a yet unknown particle, e.g., a sterile neutrino or an axion (see next chapters).

In general, the small-scale CMB anisotropies are sensitive to the ionisation and expansion history at the time of recombination. In fact, a great effort has been put towards taking into account all processes relevant to the standard recombination picture, and assessing how the corresponding uncertainties propagate to the C_ℓ's and to the parameter estimates, see Refs. [62, 63, 64, 65, 66, 67, 68, 69, 70, 71, 72, 73]. Currently, standard recombination physics is believed to be under control, with a consensus emerging between the two recombination codes HyRec, see Ref. [72], and CosmoRec, see Ref. [70], whose results on the ionisation history agree at a level of 10^{-3} at $z \sim 1100$. On the other hand, a non-standard recombination history is a possibility from the theoretical point of view. This includes delayed recombination scenarios, see Ref. [74], related, for example, to the presence of

decaying or annihilating particles, see Refs. [75, 76, 77, 78, 79, 80, 81, 82], or to the variation of fundamental constants, see Refs. [83, 84, 85]. Model-independent constraints on the allowed deviations from the standard reionization history from recent CMB data have been discussed in Refs. [86, 87].

Moreover, the damping tail is also affected by other physical effects generally taking place at a much later epoch respect to the recombination. These include the extragalactic foreground emission of point sources, radio galaxies, the Sunyaev-Zel'dovich effect and similar unresolved backgrounds, that are well identified by their spectral and angular dependence and have in general a minimal correlation with the cosmological parameters.

Furthermore, the CMB damping tail is affected by the lensing of CMB photons by dark matter clumps along the line of sight. This effect is linear and depends on cosmological parameters that also affect the primary CMB spectrum. However, the lensing amplitude is strictly dependent on the growth of perturbations, and can be significant different if, for example, general relativity is not the correct theory to describe gravity at the very large scales, but the accelerated expansion of our Universe is indeed provided by modified gravity. We can introduce a calibration parameter A_L to test the correct amplitude of the lensing signal, as in Ref. [88], in such a way that $A_L = 0$ corresponds to the complete absence of lensing, while $A_L = 1$ is the expected value assuming general relativity. In fact, this parameter simply rescales the lensing potential:

$$C_l^{\phi\phi} \rightarrow A_L C_l^{\phi\phi} \tag{4.1}$$

where $C_l^{\phi\phi}$ is the power spectrum of the lensing field. A detection of A_L very different from unity would hint that general relativity is not the correct theory to describe gravity at the cosmological scales.

4.1 The state-of-the-art

While the WMAP satellite hasn't measured accurately the CMB damping tail, observing just up to multipole $l \sim 1200$, the Atacama Cosmology Telescope (ACT), see Ref. [89], and the South Pole Telescope (SPT), see Refs. [90, 91], have both provided exquisitely precise observations of them, hinting for deviations from the simplest ΛCDM model when combined with the results from 7 years of observations from the WMAP satellite (WMAP7, Ref. [92]). Instead the newest Planck satellite measured alone the whole CMB damping tail without the possible problems of calibration that we could have when combining the high-l experiments with the WMAP data.

WMAP alone was unable to constrain the effective neutrino number, providing 7 years of observations $N_{eff} > 2.7$ at 95% c.l. (see Table 8 in Ref. [92]) and 9 years of observations $N_{eff} > 1.7$ at 95% c.l. (see Table 7 in Ref. [1]). The SPT experiment confirmed an indication for a value for $N_{eff} > 3.046$, more marginal when considering only the WMAP7+SPT data with $N_{eff} = 3.62 \pm 0.48$ at 68% c.l., but more significant when combining the SPT data with the measurement of the Hubble constant $H_0 = 73.8 \pm 2.4 \mathrm{km\,s^{-1}\,Mpc^{-1}}$ from the Hubble Space Telescope (HST), see Ref. [6], and with information from Baryonic Acoustic Oscillation (BAO) data

(see Table 4 in Ref. [90]), yielding a final value of $N_{\mathrm{eff}} = 3.71 \pm 0.35$. Meanwhile, the ACT collaboration presented a similar analysis obtaining different results. The WMAP7+ACT data alone constrained $N_{\mathrm{eff}} = 2.78 \pm 0.55$, i.e. perfectly consistent with the standard expectations 3.046, and also combining the ACT data with HST and BAO measurements $N_{\mathrm{eff}} = 3.52 \pm 0.39$ (see Table III in Ref. [89]). Finally, the Planck data, combined with the polarization of WMAP9, provided $N_{\mathrm{eff}} = 3.51 \pm 0.39$ at 68% c.l., suggesting the presence of a dark radiation component at 91.1% c.l.

Interestingly, the two datasets ACT and SPT were in tension also for the bounds on the lensing amplitude parameter. While the SPT dataset was fully compatible with the standard expectation, with $A_{\mathrm{L}} = 0.86^{+0.15}_{-0.13}$ at 68% c.l. (see Ref. [91]), the ACT data suggested a 2-σ deviation from the standard value, with $A_{\mathrm{L}} = 1.70 \pm 0.38$ at 68% c.l.. At that time, the most recent bound on this parameter from WMAP alone was for 5 years of observations (WMAP5), see Ref. [93], and equal to $A_{\mathrm{L}} = 2.5^{+1.3}_{-1.2}$ at 68% c.l. (see Table II in Ref. [88]). Planck data, combined with the polarization of WMAP9, have instead provided the constraint $A_{\mathrm{L}} = 1.22^{+0.11}_{-0.13}$ at 68% c.l., hinting for a value greater than the standard at about 94.3% c.l..

In this chapter (but see also Ref. [94]) we further investigate these discrepancies between the two high-l experiments ACT and SPT by improving their analyses in three ways. First of all, we perform our analyses allowing both N_{eff} and A_{L} parameters to vary at the same time, allowing to better identify the tension between the two experiments. Secondly, we add the latest dataset from nine years of observations coming from the WMAP satellite (WMAP9) as in Ref. [1], while both ACT and SPT teams used the previous 7-year WMAP dataset in their papers. Thirdly, (see also Ref. [95]), we perform again the same analysis, varying both N_{eff} and A_{L} parameters at the same time, but considering in this case the more recent Planck dataset combined with the polarization of WMAP9.

Finally, (see Ref. [96]), we present new constraints on the rest-frame sound speed, c_{eff}^2, and the viscosity parameter, c_{vis}^2, of the Cosmic Neutrino Background from the measurements of the Planck satellite, finding a correlation between these neutrino parameters and A_{L}. We conclude that the anomalous large value of A_{L} measured by Planck could also be connected to non-standard neutrino properties.

4.2 SPT and ACT combined with WMAP9

Our first analysis (see Ref. [94] for more details) is based on a modified version of the public CosmoMC, see Ref. [97], Monte Carlo Markov Chain code, considering the following CMB data: WMAP9, Ref. [1], SPT, Ref. [90], and ACT, Ref. [89], including measurements up to a maximum multipole number of $l_{\mathrm{max}} = 3750$. Since ACT and SPT dataset provided different results on N_{eff} and A_{L}, we consider them separately: i.e. we split the analysis in two: WMAP9+ACT and WMAP9+SPT. We also consider the effect of including additional dataset, like the measurements of the HST, Ref. [6], i.e. a Gaussian prior on the Hubble constant $H_0 = 73.8 \pm 2.4 \, \mathrm{km \, s^{-1} \, Mpc^{-1}}$, and information from measurements of BAO from galaxy surveys, i.e. combining 6dFGRS from Ref. [98], SDSS-DR7 from Ref. [99], SDSS-DR9 from Ref. [7] and WiggleZ from Ref. [100].

We sample the standard six-dimensional set of cosmological parameters, adopting

flat priors on them: the baryon and cold dark matter densities $\Omega_{\rm b}h^2$ and $\Omega_{\rm c}h^2$, the ratio of the sound horizon to the angular diameter distance at decoupling θ, the optical depth to reionization τ, the scalar spectral index n_s and the overall normalization of the spectrum A_s at $k = 0.05Mpc^{-1}$. As discussed, we also consider variations in the effective number of relativistic degrees of freedom $N_{\rm eff}$ and in the lensing amplitude parameter $A_{\rm L}$, taking the flat priors $1 < N_{\rm eff} < 10$ and $0 < A_L < 4$. In our basic runs, we don't consider the effect of massive neutrinos, but we performed additional runs in which we allowed for a non-vanishing neutrino mass, parametrized by means of the neutrino fraction $f_\nu \equiv \Omega_\nu/\Omega_c$. We always assume standard BBN, so that the Helium abundance $Y_{\rm p}$ is uniquely determined by the values of $\Omega_b h^2$ and $N_{\rm eff}$. Then, in order to assess the convergence of our MCMC chains, we compute the Gelman and Rubin $R - 1$ parameter demanding that $R - 1 < 0.03$.

In Table 4.1 we report the constraints on the considered parameters from each run WMAP9+SPT, WMAP9+ACT, WMAP9+SPT+HST+BAO and WMAP9+ACT+HST+BAO. As we can see, the ACT and SPT provide significantly different constraints on the $N_{\rm eff}$ and $A_{\rm L}$ parameters. We plot in figure 4.1 and 4.2 the 2-D constraints on the $N_{\rm eff}$ vs $A_{\rm L}$ plane respectively for the CMB only case and for the CMB+HST+BAO analysis.
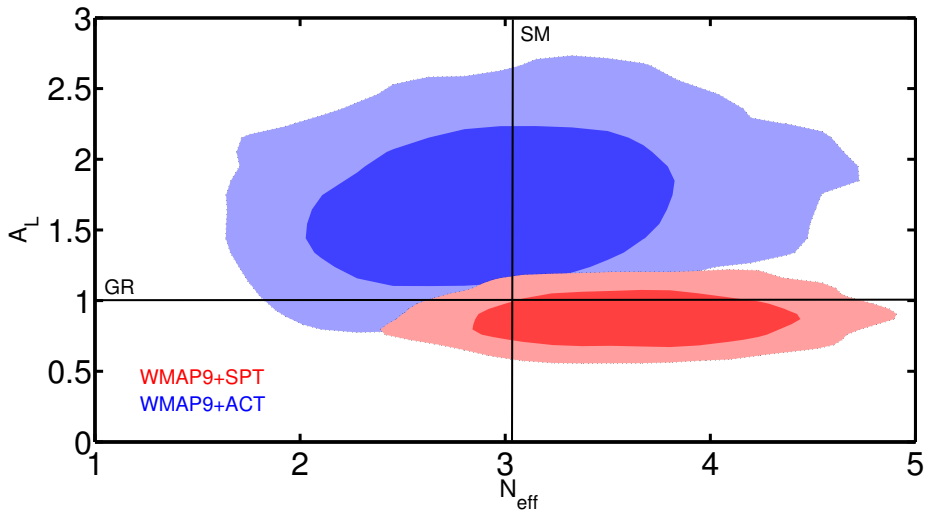
Figure 4.1. Constraints in the $A_{\rm L}$ - $N_{\rm eff}$ plane from a CMB only analysis. The blue contour includes the ACT data while the red contour refers to the SPT data. The line at $A_{\rm L} = 1$ indicates the standard expectations based on General Relativity. The line at $N_{\rm eff} = 3.046$ indicates the prediction from the standard model with three neutrino flavours, [94].

As we can see, the central values for $N_{\rm eff}$ and $A_{\rm L}$ obtained from WMAP9+ACT analysis are outside the 95% confidence level of the WMAP9+SPT and vice-versa. In particular, the ACT dataset point towards a value of $N_{\rm eff}$ consistent with $N_{\rm eff} = 3.046$, while (as it can be seen from Table 4.1 and Figure 4.2), preferring at the same time an exotic high value for the lensing potential, with $A_{\rm L}$ larger than unity at more than 95% c.l. when we includ the BAO and HST datasets. We found $A_{\rm L} = 1.70^{+0.77}_{-0.67}$ at 95% c.l. for the WMAP+ACT analysis and $A_{\rm L} = 1.64^{+0.67}_{-0.63}$ at

Parameters	SPT+WMAP9	ACT+WMAP9	SPT+WMAP9+HST+BAO	ACT+WMAP9+HST+BAO
$\Omega_b h^2$	0.02264 ± 0.00051	0.02295 ± 0.00052	0.02250 ± 0.00034	0.02301 ± 0.00036
$\Omega_c h^2$	0.1232 ± 0.0080	0.112 ± 0.011	0.1308 ± 0.0067	0.1250 ± 0.0078
θ	1.0415 ± 0.0012	1.0410 ± 0.0025	1.0409 ± 0.0010	1.0388 ± 0.0021
τ	0.088 ± 0.014	0.090 ± 0.015	0.084 ± 0.013	0.087 ± 0.013
n_s	0.982 ± 0.018	0.975 ± 0.019	0.978 ± 0.011	0.983 ± 0.012
N_{eff}	3.72 ± 0.46	3.00 ± 0.61	3.78 ± 0.33	3.54 ± 0.41
A_L	0.85 ± 0.13	1.70 ± 0.37	0.79 ± 0.11	1.64 ± 0.32
$H_0 [\mathrm{km/s/Mpc}]$	74.6 ± 3.7	70.9 ± 3.9	72.7 ± 1.7	71.7 ± 1.9
$\log(10^{10} A_s)$	3.169 ± 0.048	3.083 ± 0.044	3.198 ± 0.032	3.115 ± 0.034
Ω_Λ	0.736 ± 0.023	0.731 ± 0.025	0.710 ± 0.010	0.712 ± 0.011
Ω_m	0.264 ± 0.023	0.269 ± 0.025	0.290 ± 0.010	0.288 ± 0.011
Age/Gyr	13.14 ± 0.43	13.74 ± 0.57	13.10 ± 0.27	13.3 ± 0.34
D^{SZ}_{3000}	5.8 ± 2.4	—	6.0 ± 2.4	—
D^{CL}_{3000}	5.2 ± 2.1	—	5.3 ± 2.1	—
D^{PS}_{3000}	19.6 ± 2.5	—	19.5 ± 2.4	—
A_{SZ}	—	0.98 ± 0.57	—	0.89 ± 0.56
$\chi^2_\mathrm{min}/2$	3806.25	3798.79	3808.96	3801.92

Table 4.1. Cosmological parameter values and 68% confidence level errors. The SPT and ACT datasets produce different values for some of the parameters, most notably N_eff and A_L, [94].
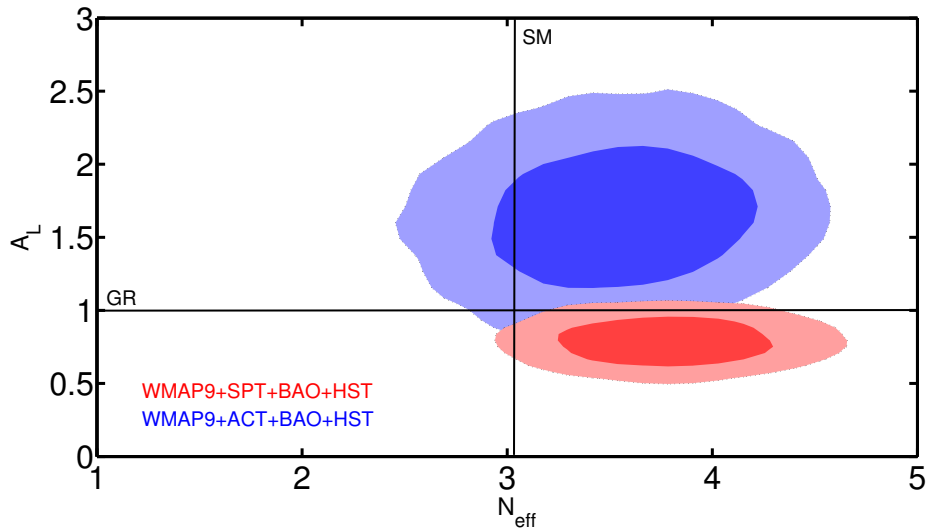
Figure 4.2. Constraints in the A_L - N_{eff} plane from a CMB analysis including the HST prior and BAO. The blue contour includes the ACT data while the red contour refers to the SPT data. The lines at $A_L = 1$ and $N_{eff} = 3.046$ indicate the expected values for the parameters, [94].

95% c.l. for the WMAP+ACT+BAO+HST. We have the opposite for the SPT data: while SPT is consistent with $A_L = 1$, it constrains N_{eff} to a larger value than the standard expectation. When we include the HST and BAO data, we found that not only data suggest a value of $N_{eff} > 3.04$ at more than 95% c.l., but also a value of A_L smaller than one at about 68% c.l.. Namely, we obtain that $A_L < 1.00$ at 95% c.l. from WMAP9+SPT+BAO+HST while $A_L > 1.03$ at 95% c.l. from WMAP9+ACT+BAO+HST, i.e. for the lensing parameter the SPT and ACT datasets provide constraints in disagreement at more than 95% c.l..

We note that the tension between the ACT and SPT datasets is not limited to the A_L or N_{eff} parameters, but also the constraints on H_0, n_s, $\Omega_b h^2$ and $\Omega_c h^2$ are quite different, although the discrepancy is less significant (see Figures 4.3 and 4.4). We note however that these discrepancies could also be explained by varying the recombination history, see e.g. Ref. [87].

So far, all neutrinos were considered as relativistic and massless. Since the SPT dataset provided a detection at 95% c.l. for a neutrino mass with $\Sigma m_\nu = 0.48 \pm 0.21$ in a WMAP7+SPT+BAO+HST analysis (see Ref. [90]), we now also consider massive neutrinos.

In table 4.2 we report the constraints on cosmological parameters from the WMAP9+SPT+HST+BAO and WMAP9+ACT+HST+BAO datasets respectively when we included a variation in the neutrino masses in two cases: varying A_L and fixing $A_L = 1$.

As we can see, while the ACT dataset does not favour the presence of neutrino masses, the SPT dataset gives $\Sigma m_\nu = 0.43 \pm 0.19$ at 68% c.l. in the case of $A_L = 1$. This is consistent with the results reported in Ref. [90] considering the different WMAP and BAO datasets. However, by varying A_L, the evidence for a neutrino mass vanishes, as also clearly seen in Figure 4.5.
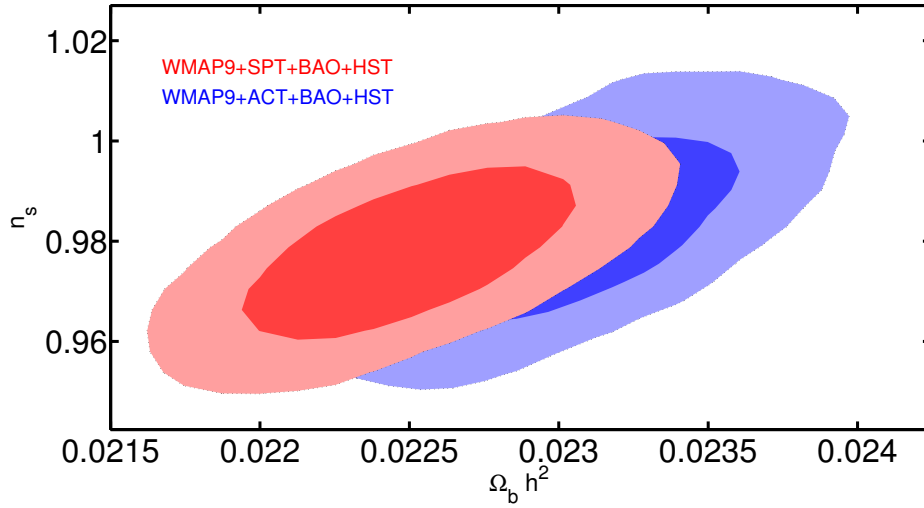
Figure 4.3. Constraints in the $\Omega_b h^2$ - n_s plane from ACT (blue contours) and SPT (red contours) including WMAP9, HST and BAO data. The ACT-SPT tension is less pronounced for these parameters, [94].
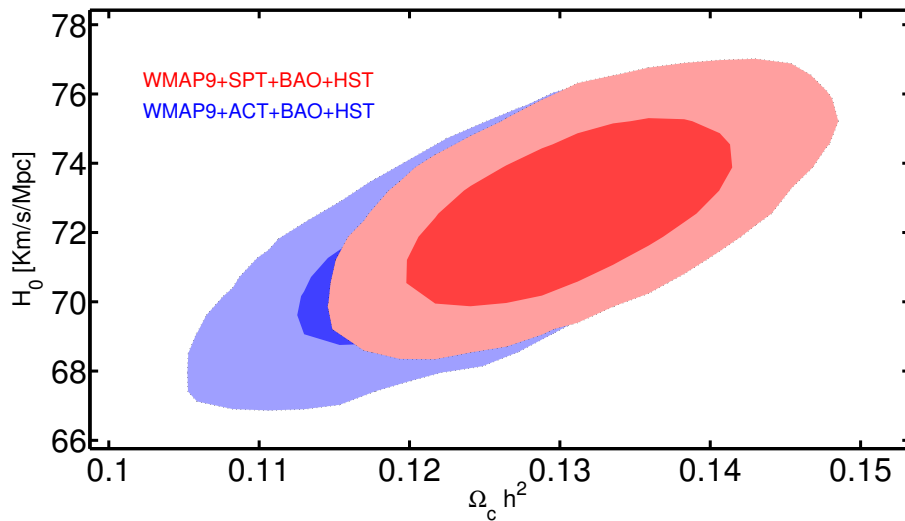
Figure 4.4. Constraints in the $\Omega_c h^2$-H_0 plane from ACT (blue contours) and SPT (red contours) including WMAP9, HST and BAO data, [94].

Parameters	SPT +WMAP9+HST+BAO	SPT +WMAP9+HST+BAO	ACT +WMAP9+HST+BAO	ACT +WMAP9+HST+BAO
$\Omega_b h^2$	0.02279 ± 0.00036	0.02271 ± 0.00039	0.02305 ± 0.00038	0.02317 ± 0.00038
$\Omega_c h^2$	0.1325 ± 0.0074	0.1323 ± 0.0074	0.1224 ± 0.0076	0.1248 ± 0.0077
θ	1.0410 ± 0.0011	1.0410 ± 0.0011	1.0393 ± 0.0021	1.0393 ± 0.0021
τ	0.088 ± 0.013	0.089 ± 0.014	0.094 ± 0.015	0.091 ± 0.014
n_s	0.989 ± 0.012	0.987 ± 0.013	0.985 ± 0.012	0.988 ± 0.013
N_{eff}	3.94 ± 0.37	3.92 ± 0.37	3.40 ± 0.39	3.56 ± 0.40
Σm_ν	0.43 ± 0.19	$< 0.74 \ (95\% \ c.l.)$	$< 0.41 \ (95\% \ c.l.)$	$< 0.53 \ (95\% \ c.l.)$
A_L	1.00	0.90 ± 0.14	1.00	1.82 ± 0.38
$H_0[\mathrm{km/s/Mpc}]$	72.2 ± 1.9	72.2 ± 1.9	70.5 ± 1.9	71.1 ± 1.8
$\log(10^{10} A_s)$	3.157 ± 0.034	3.168 ± 0.037	3.117 ± 0.038	3.115 ± 0.034
Ω_Λ	0.702 ± 0.012	0.702 ± 0.012	0.708 ± 0.011	0.707 ± 0.011
Ω_m	0.298 ± 0.012	0.298 ± 0.012	0.292 ± 0.011	0.293 ± 0.011
Age/Gyr	13.12 ± 0.29	13.09 ± 0.31	13.47 ± 0.33	13.36 ± 0.33
D^{SZ}_{3000}	5.9 ± 2.3	6.2 ± 2.4	—	—
D^{CL}_{3000}	5.3 ± 2.2	5.2 ± 2.1	—	—
D^{PS}_{3000}	19.2 ± 2.5	19.2 ± 2.5	—	—
A_{SZ}	—	—	0.96 ± 0.56	0.96 ± 0.57
$\chi^2_{\min}$	3809.03	3808.71	3804.32	3801.92

Table 4.2. Cosmological parameter values and 68% confidence level errors for the analysis that considers massive neutrinos. As we can see, varying A_L strongly affects the constraints on the total neutrino mass. Vice-versa, allowing for a neutrino mass renders the SPT value for A_L more compatible with the standard value while exacerbates the problem for the ACT dataset, [94].

We can better understand what is happening by looking at the constraints in the A_L vs Σm_ν plane in Figure 4.7, in which we have a degeneracy between A_L and Σm_ν: a larger value of Σm_ν decreases the lensing signal and can be compensated with a larger A_L. Since the SPT dataset prefers smaller values of the lensing parameter, by taking $A_L = 1$ forces the neutrino mass to be more consistent with the data.

Fynally, the inclusion of a neutrino mass exacerbate the lensing problem for ACT, indeed the lensing parameter A_L is even higher when we consider massive neutrinos (see Table 4.2).
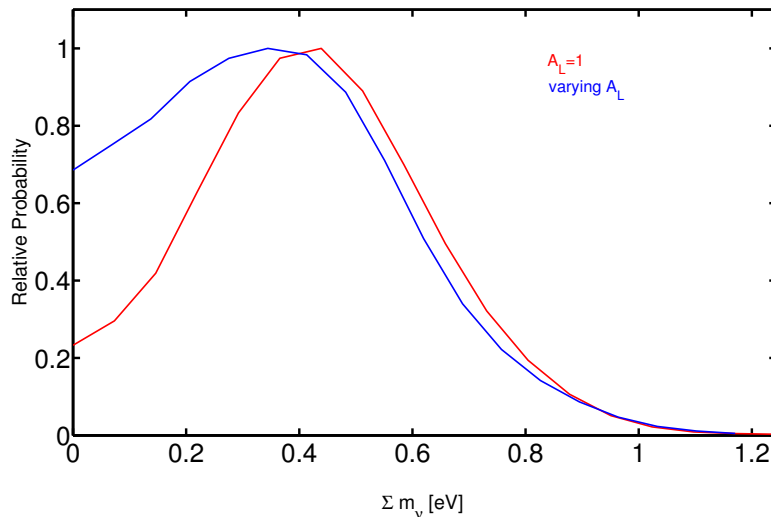
Figure 4.5. Posterior distribution function for the total neutrino mass parameter Σm_ν from a SPT+WMAP+BAO+HST analysis in the case of fixing lensing to $A_L = 1$ and letting it to vary. As we can see, if we let the A_L parameter to vary the small indication for a neutrino mass from the SPT analysis vanishes, [94].

In conclusion, the discrepancy between the ACT and SPT datasets is not significantly at more than the 95% confidence level. The SPT experiment confirms the previous indications for a "dark radiation" component with $N_{eff} = 3.78 \pm 0.33$ at 68% c.l.; in particular we have found that $N_{eff} > 3.16$ at more than 95% c.l., while the ACT experiment is fully consistent with $N_{eff} = 3.046$ even when we include the HST and BAO datasets. Moreover, ACT presents a value for the lensing parameter that is off by more than 95% from the expected value $A_L = 1$. This deviation is more difficult to explain from a physical point of view, calling for more drastic changes in the cosmological model: for example assuming a modification to General Relativity. On the contrary, the SPT experiment is compatible with $A_L = 1$ but suggests a value $A_L < 1$ at about 68% c.l. especially when we include the BAO and HST data.

4.3   Constraints from the Planck 2013 dataset

The precise measurements of the CMB temperature anisotropies released by the Planck collaboration, see Ref. [2], are providing the tightest constraints on cosmological parameters to date (see Ref. [5]).

In this section (see also Ref. [95]), we use this dataset to constrain the neutrino
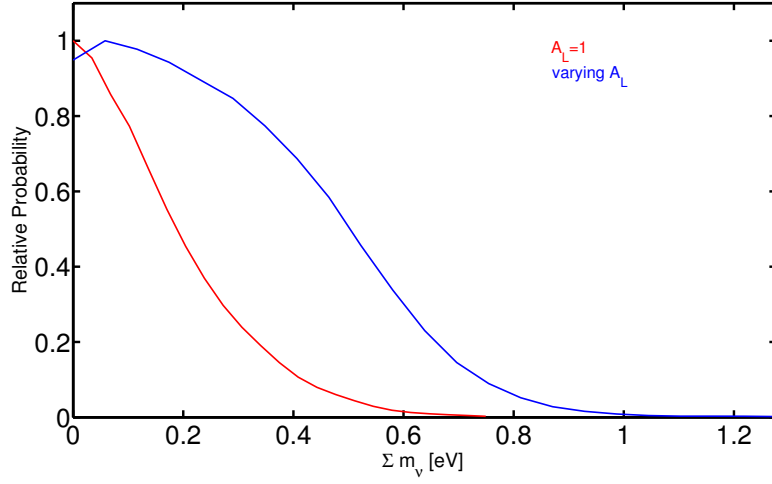
Figure 4.6. Posterior distribution function for the total neutrino mass parameter Σm_ν from a ACT+WMAP+BAO+HST analysis in the case of fixing lensing to $A_L = 1$ and letting it to vary. As we can see, to let the A_L parameter to vary weakens the constraints from ACT, [94].
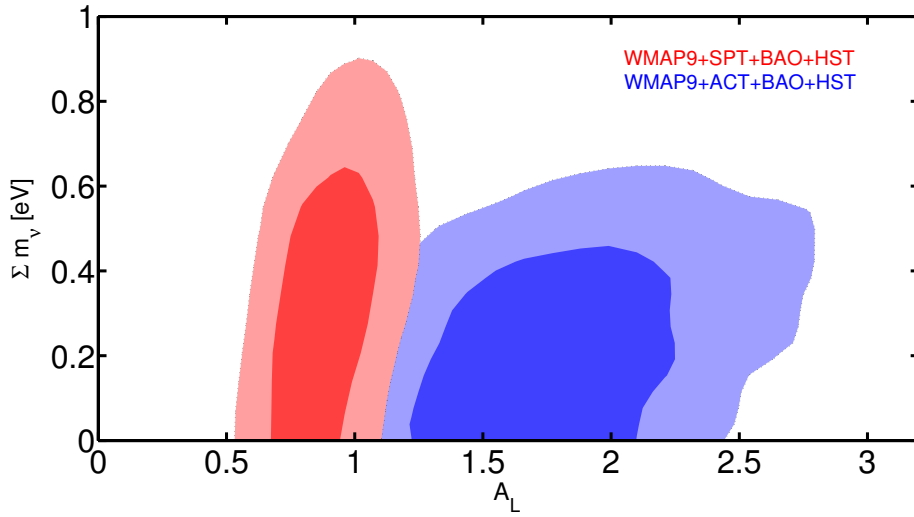
Figure 4.7. Constraints in the A_L vs Σm_ν plane for the SPT+WMAP+BAO+HST and ACT+WMAP+BAO+HST datasets. A degeneracy is present between the two parameters: larger values for A_L let larger neutrino masses to be more consistent with the data. The SPT indication for a neutrino mass is driven by the low value of A_L obtained in the neutrino massless case, [94].

effective number N_{eff} and the lensing amplitude A_{L} simultaneously, while the Planck collaboration presented results in Ref. [5] on N_{eff} and A_{L} separately.

Our main CMB dataset consists in the Planck public data release of March 2013, see Ref. [2]. We compare this dataset with the theoretical models using the `CAMspec` likelihood version 6.2 for high multipoles and the `commander` version 4.1 likelihood for low multipoles, see Ref. [101]. We also consider the WMAP low-l likelihood for polarization, see Ref. [102], and we name this combination of data as "PLANCK+WP". For BAO surveys we include SDSS-DR7 from Ref. [99] at redshift $z = 0.35$, SDSS-DR9 from Ref. [7] at $z = 0.57$ and WiggleZ from Ref. [103] at $z = 0.44, 0.60$, and 0.73. Finally, we include the measurements for the Hubble constant H_0 from the analysis of Ref. [6] and we refer to this dataset as HST.

For the analysis method we use the version March 2013 of the publicly available Monte Carlo Markov Chain package `cosmomc`, Ref. [97], which include the support for the Planck Likelihood Code v1.0 (see http://cosmologist.info/cosmomc/) and implements an efficient sampling of the space using the fast/slow parameters decorrelation, see Ref. [104]. The plots shown are obtained via the `python` codes included in the `cosmomc` package.

We run again over the six-dimensional space of standard cosmological parameters, considering purely adiabatic initial conditions and imposing spatial flatness: the baryon and cold dark matter densities Ω_{b} and Ω_{c}, the ratio of the sound horizon to the angular diameter distance at decoupling θ, the reionization optical depth τ, the scalar spectral index n_S, and the overall normalization of the spectrum A_S at $k = 0.05 Mpc^{-1}$. In addiction we consider the number of neutrinos species (assumed massless) N_{eff} and the lensing amplitude parameter A_{L}, assuming the flat priors: $1.047 \leq N_{\text{eff}} \leq 10$ and $0.0 \leq A_{\text{L}} \leq 4.0$. We choose to work with massless neutrinos, but it is worth to remember that the inclusion of a neutrino mass (fix or variable) could change significantly the results. As shown in Fig. 26 in Ref. [5] the massive neutrinos can have strong impact on the lensing amplitude. In the previous section we showed how allowing the neutrino mass to vary leads to higher values of A_{L}, as well depicted by the WMAP9+ACT+BAO+HST dataset, for which we have $A_{\text{L}} = 1.64 \pm 0.32$ in the case of massless neutrinos, and $A_{\text{L}} = 1.82 \pm 0.38$ when their mass is allowed to vary. In our runs, we also marginalize over the foreground parameters as in Refs. [101, 5].

We show the posteriors on the cosmological parameters obtained using the Planck+WP dataset in Table 4.3.

As we can see, the Planck+WP dataset provide an indication for a larger value of both N_{eff} and A_{L}: $N_{\text{eff}} = 3.71 \pm 0.40$ and $A_{\text{L}} = 1.25 \pm 0.13$ at 68% c.l.. The constraint on N_{eff} reported by the Planck collaboration for the same dataset is $N_{\text{eff}} = 3.51 \pm 0.39$ at 68% c.l., but it is obtained fixing $A_{\text{L}} = 1$: the slightly larger value obtained in our analysis clearly shows that there is a small correlation between these two parameters.

We can compare these results with the ones obtained in the previous section for the ACT and SPT dataset. The Planck+WP result on N_{eff} is perfectly consistent with the WMAP9+SPT constraint, while there is a tension with the WMAP9+SPT result on A_{L}. Vice-versa, the WMAP9+ACT constraint on N_{eff} is clearly in tension with the Planck+WP result, while there is a better agreement with the bound on the lensing parameter A_{L}. We plot in Figures 4.8 and 4.9 the 1-D posterior distribution

Parameter	Planck+WP
$\Omega_b h^2$	0.02306 ± 0.00051
$\Omega_c h^2$	0.1239 ± 0.0054
θ	1.04124 ± 0.00077
τ	0.095 ± 0.015
n_s	0.996 ± 0.018
$log[10^{10}A_s]$	3.111 ± 0.034
N_{eff}	3.71 ± 0.40
A_{L}	1.25 ± 0.13
Ω_Λ	0.736 ± 0.022
$t_0[\mathrm{Gyr}]$	13.08 ± 0.38
Ω_m	0.264 ± 0.022
$H_0[\mathrm{km/s/Mpc}]$	74.9 ± 3.7

Table 4.3. Constraints at 68% confidence level on cosmological parameters from our analysis using Planck+WP, [95].

functions respectively for N_{eff} and A_{L} coming from these three analyses, while in Figure 4.10 we report the constraints in the 2-D $N_{\mathrm{eff}} - A_{\mathrm{L}}$ plane.

In general we obtain that the Planck+WP dataset is in better agreement with the WMAP9+SPT dataset than the WMAP9+ACT on most of the parameters, as the Hubble constant H_0, the matter density Ω_m and the scalar spectral index n_S. A similar conclusion was reached by the SPT collaboration, see Ref. [105]. However, when fixing $A_{\mathrm{L}} = 1$, we have that Plank+WP was in better agreement with the WMAP9+ACT dataset, as reported in Ref. [5] .

In Table 4.4 we show how, allowing the lensing parameter to vary, can lead to changes in the constraints on the number of relativistic species, while the variation of N_{eff} has minor consequences on the value of A_{L}.

Moreover, we report the results obtained from the Planck+WP+HST, Planck+WP+BAO and Planck+WP+HST+BAO analyses in the three columns of Table 4.5, respectively, where we named Planck+WP as "CMB". We show the 1-D posterior probability distributions for N_{eff} and A_{L} in Figures 4.11, 4.12, 4.13 and 4.14, and the 2-D confidence regions for N_{eff} and A_{L} in Figures 4.15 and 4.16 for all the dataset combinations discussed: CMB, CMB+HST, CMB+BAO and CMB+BAO+HST.

Our results are in perfect agreement with those already presented in Ref. [5]. In fact, the introduction of the BAO dataset shifts the values of N_{eff} and A_{L} in a better consistency with the standard expectation, while the inclusion of the HST dataset mantains the Planck+WP mean values of the parameters, reducing the error bars and therefore increasing the hints for new physics. In particular, for the CMB+HST case, both N_{eff} and A_{L} have larger values than expected at more than 95% confidence level. Combining both BAO and HST, the final effect is to lower the value of $A_{\mathrm{L}} = 1.17 \pm 0.10$, still not in full agreement with the expected value of unity, and to lower the number of neutrinos species as well, giving $N_{\mathrm{eff}} = 3.56 \pm 0.27$, at almost $2 - \sigma$ away from the standard value.

In conclusion, the hints for new physics from the Planck+WP dataset are

Parameter	WMAP7+SPT[90]	WMAP9+SPT[94]	WMAP7+ACT[89]	WMAP9+ACT[94]	Planck+WP[5]	PLANCK+WP
N_{eff}	3.62 ± 0.48	3.72 ± 0.46	2.78 ± 0.55	3.00 ± 0.61	3.51 ± 0.39	3.71 ± 0.40
A_{L}	1.00	0.85 ± 0.13	1.00	1.70 ± 0.37	1.00	1.25 ± 0.13

Parameter	WMAP7+SPT[91]	WMAP9+SPT[94]	WMAP7+ACT[89]	WMAP9+ACT[94]	Planck+WP[5]	PLANCK+WP
N_{eff}	3.046	3.72 ± 0.46	3.046	3.00 ± 0.61	3.046	3.71 ± 0.40
A_{L}	$0.86^{+0.15}_{-0.13}$	0.85 ± 0.13	1.70 ± 0.38	1.70 ± 0.37	$1.22^{+0.11}_{-0.13}$	1.25 ± 0.13

Table 4.4. In this table we compare the results of our analysis with N_{eff} and A_{L} varied simultaneously with the results obtained by SPT, ACT and Planck collaborations with just one of those parameters variable. The constraints are at 68% confidence level.
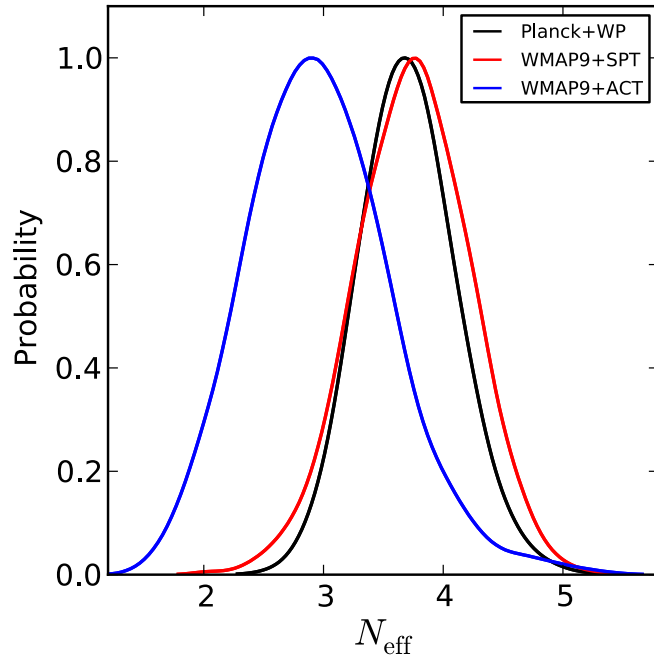
Figure 4.8. Comparison of the results for Planck+WP, WMAP9+SPT and WMAP9+ACT datasets in terms of the 1-D posterior distribution functions for N_{eff}, [95].
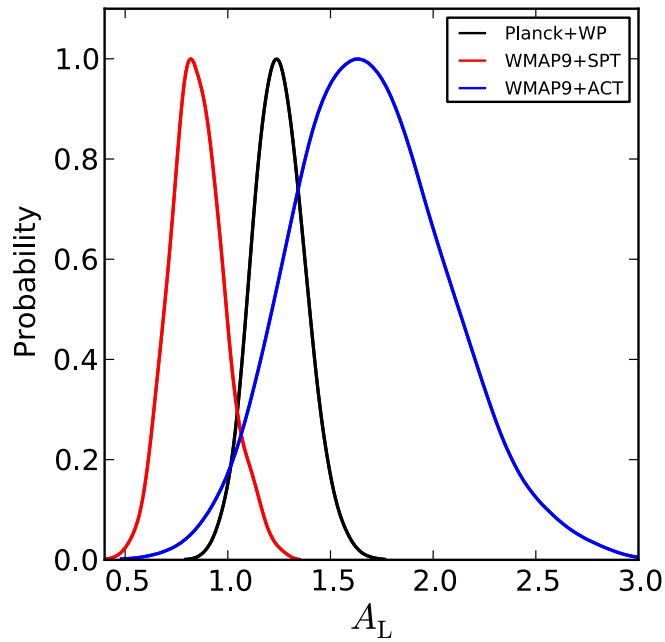
Figure 4.9. Comparison of the results for Planck+WP, WMAP9+SPT and WMAP9+ACT datasets in terms of the 1-D posterior distribution functions for A_{L}, [95].
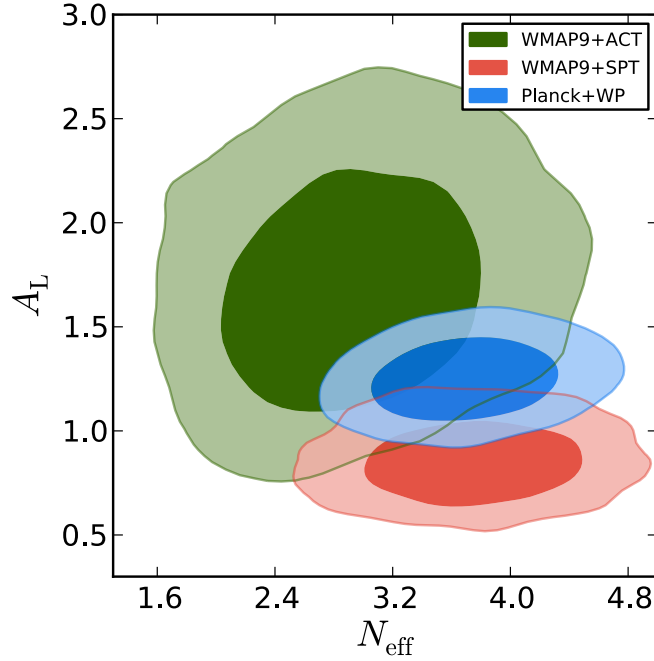
Figure 4.10. Comparison of the 2-D posterior distribution function from the Planck+WP, WMAP9+ACT and WMAP9+SPT datasets in the $N_{\text{eff}} - A_{\text{L}}$ plane. We show contours for 68% and 95% confidence level, [95].

Parameter	CMB+HST	CMB+BAO	CMB+BAO+HST
$\Omega_b h^2$	0.022953 ± 0.00035	0.02246 ± 0.00031	0.02262 ± 0.00028
$\Omega_c h^2$	0.1234 ± 0.0050	0.1232 ± 0.0053	0.1260 ± 0.0049
θ	1.04123 ± 0.00077	1.04112 ± 0.00078	1.04085 ± 0.00075
τ	0.094 ± 0.014	0.087 ± 0.013	0.089 ± 0.013
n_s	0.992 ± 0.011	0.974 ± 0.011	0.9815 ± 0.0088
$log[10^{10} A_s]$	3.108 ± 0.030	3.093 ± 0.030	3.103 ± 0.029
N_{eff}	3.63 ± 0.27	3.35 ± 0.31	3.56 ± 0.27
A_{L}	1.24 ± 0.12	1.16 ± 0.10	1.17 ± 0.10
Ω_Λ	0.733 ± 0.014	0.706 ± 0.011	0.7119 ± 0.0094
$t_0[\text{Gyr}]$	13.15 ± 0.23	13.47 ± 0.28	13.27 ± 0.23
Ω_m	0.267 ± 0.014	0.294 ± 0.011	0.2881 ± 0.0094
$H_0[\text{km/s/Mpc}]$	74.0 ± 2.0	70.4 ± 1.9	71.8 ± 1.6

Table 4.5. Constraints at 68% confidence level on cosmological parameters from our analysis using CMB+HST, CMB+BAO and CMB+BAO+HST, [95].
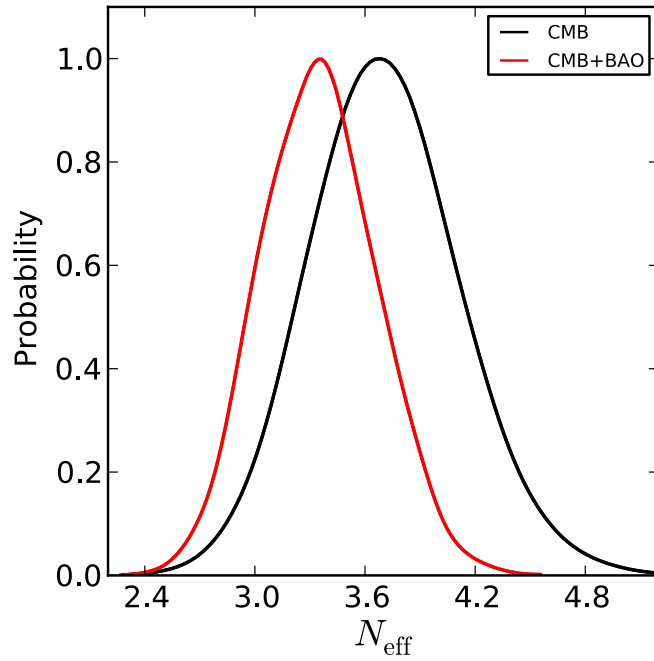
Figure 4.11. Comparison of the 1-D posterior distribution functions from the CMB-only
(Planck+WP) and CMB+BAO datasets for N_{eff}, [95].
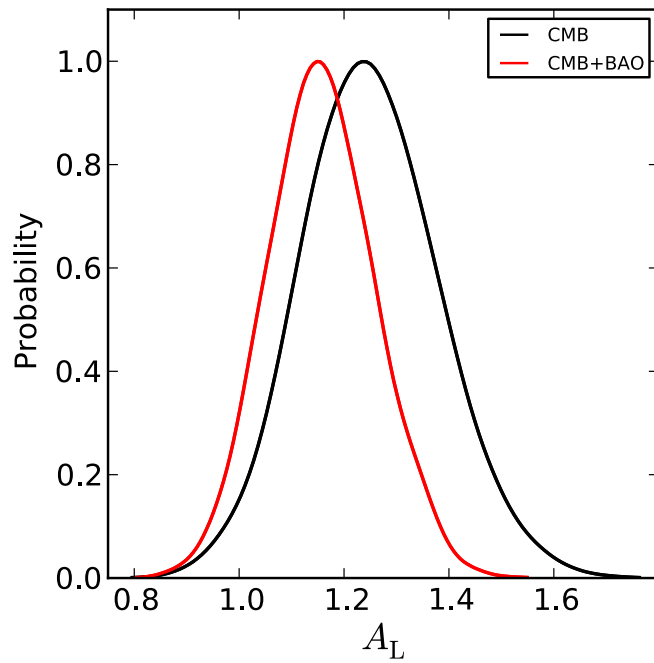
Figure 4.12. Comparison of the 1-D posterior distribution functions from the CMB-only
(Planck+WP) and CMB+BAO datasets for A_{L}, [95].
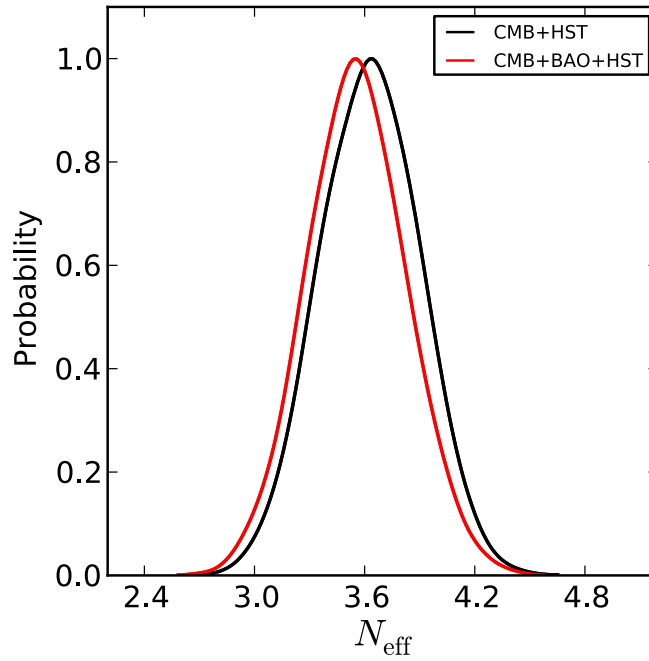
Figure 4.13. Comparison of the 1-D posterior distribution functions from the CMB+HST (Planck+WP) and CMB+BAO+HST datasets for N_{eff}, [95].
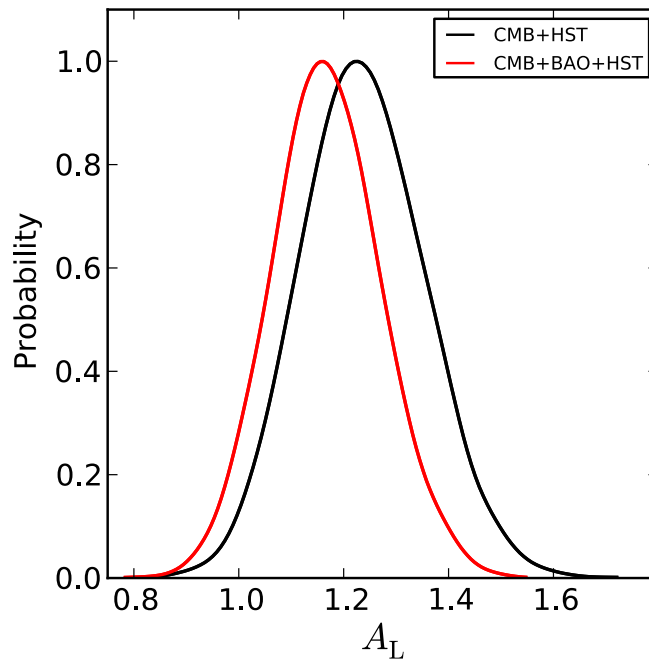
Figure 4.14. Comparison of the 1-D posterior distribution functions from the CMB+HST (Planck+WP) and CMB+BAO+HST datasets for A_{L}, [95].
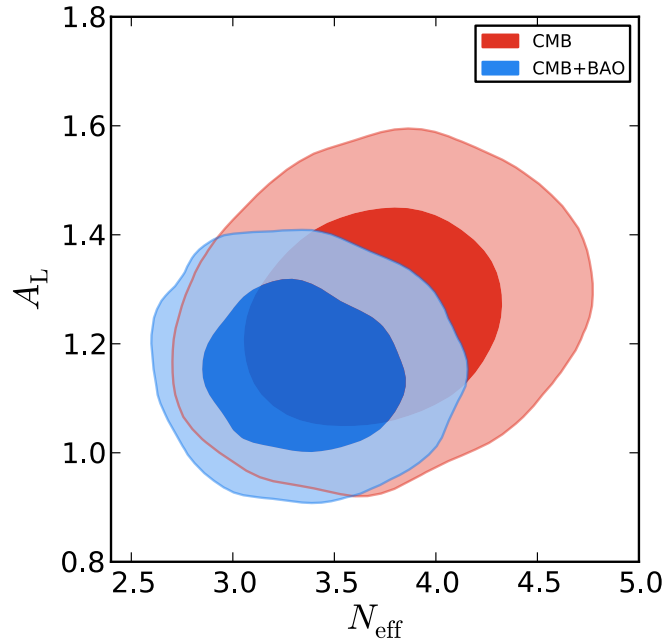
Figure 4.15. Comparison of the 2-D posterior distribution functions from the CMB-only and CMB+BAO datasets in the $N_{\text{eff}} - A_{\text{L}}$ parameters plane. The contours shown are at 68% and at 95% confidence level, [95].
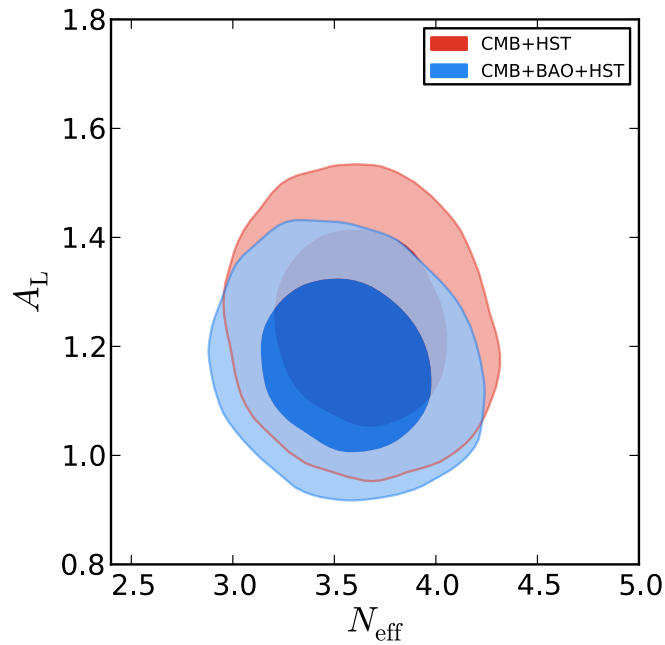
Figure 4.16. Comparison of the 2-D posterior distribution functions from the CMB+HST and CMB+BAO+HST datasets in the $N_{\text{eff}} - A_{\text{L}}$ parameters plane. The contours shown are at 68% and at 95% confidence level, [95].

confirmed and reinforced when the HST measurements are included and are weakened when the BAO dataset is considered. Instead, the CMB+HST+BAO analysis also suggests the presence of anomalous values but at smaller statistical significance.

The next Planck data release, expected around the end of 2014, with the full mission and polarization data, will provide more precise, CMB only, constraints on the neutrino number and the lensing amplitude and will certainly confirm or falsify these current hints for new physics.

4.4 Planck Constraints on Anisotropies of the Cosmic Neutrino Background
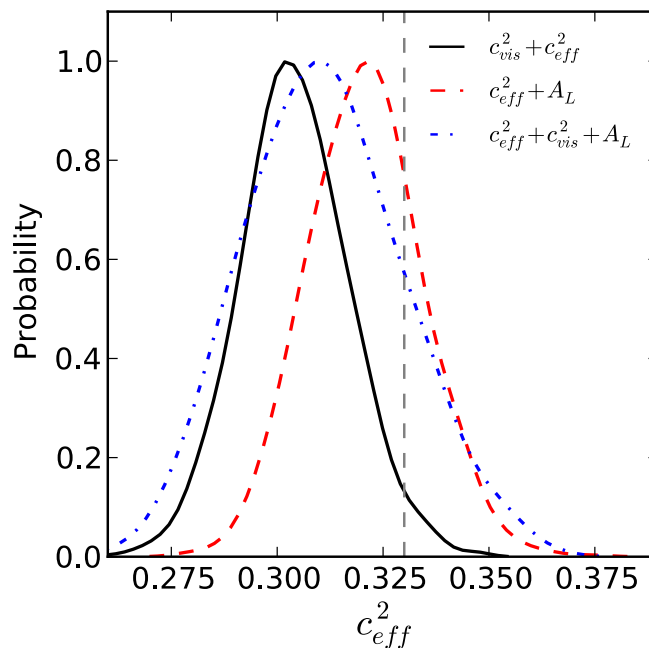
Figure 4.17. One-dimensional posterior probabilities of the parameter c_{eff}^2 for the indicated models for Planck+WP. The vertical dashed line indicates the expected value in the standard model, [96].

The Planck satellite, see Refs. [2, 5, 101] measurements, although in excellent agreement with expectations of the standard ΛCDM cosmological model, clearly opens the opportunity to further test some of its assumptions and to possibly identify the presence of new physics.

Following recent analyses (see e.g. Refs. [95, 106, 107, 108, 109]), in this section (but see also Ref. [96]) we test some properties of the Cosmic Neutrino Background (CNB).

The Planck experiment, see Ref. [5], reporting the bound $N_{\text{eff}} = 3.51 \pm 0.39$ at 68% c.l., provided evidence for the neutrino background at the level of about nine standard deviations. However, the slightly higher value for N_{eff} suggests that we can have new physics in the neutrino sector. Moreover, the Planck data suggest an
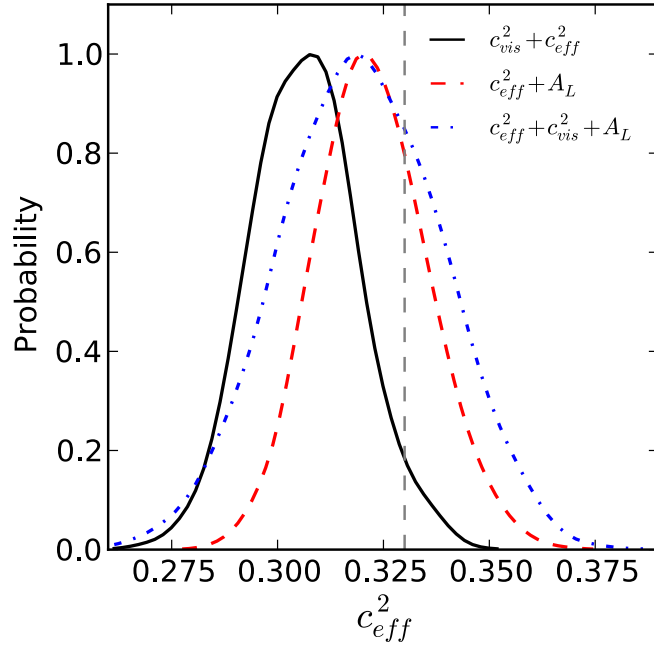
Figure 4.18. One-dimensional posterior probabilities of the parameter c_{eff}^2 for the indicated models for Planck+EX. The vertical dashed line indicates the expected value in the standard model, [96].
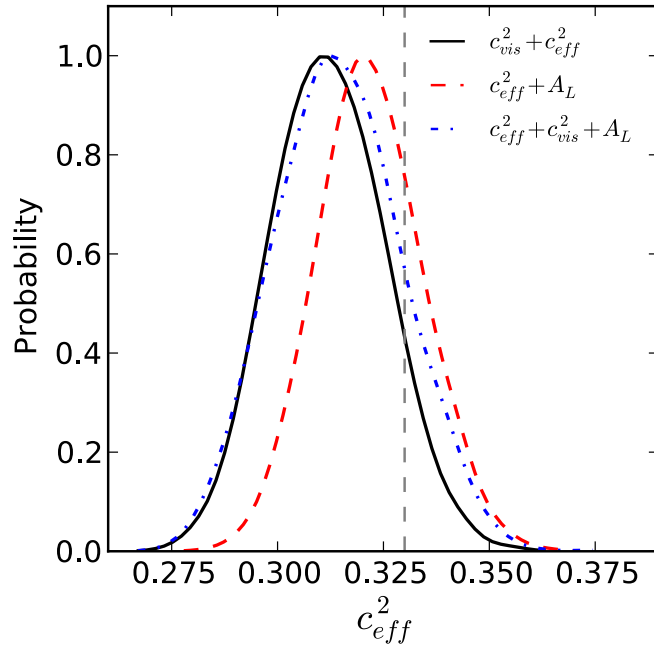
Figure 4.19. One-dimensional posterior probabilities of the parameter c_{eff}^2 for the indicated models for Planck+L. The vertical dashed line indicates the expected value in the standard model. We have a different range in the x axes for this dataset respect to the others, [96].
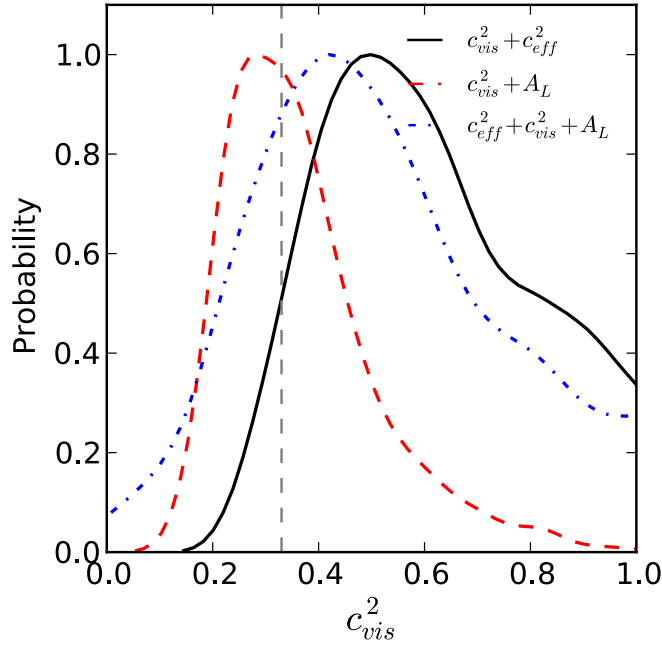
Figure 4.20. One-dimensional posterior probabilities of the parameter c_{vis}^2 for the indicated models for Planck+WP. The vertical dashed line indicates the expected value in the standard model, [96].
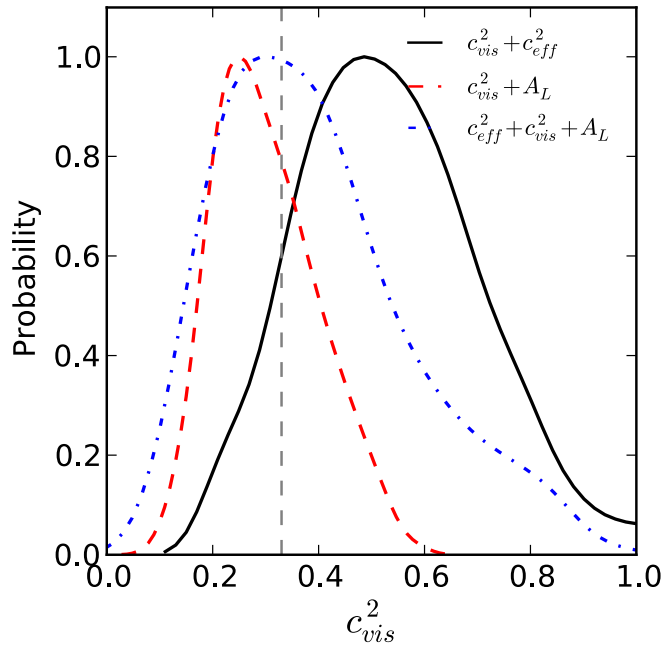
Figure 4.21. One-dimensional posterior probabilities of the parameter c_{vis}^2 for the indicated models for Planck+EX. The vertical dashed line indicates the expected value in the standard model, [96].
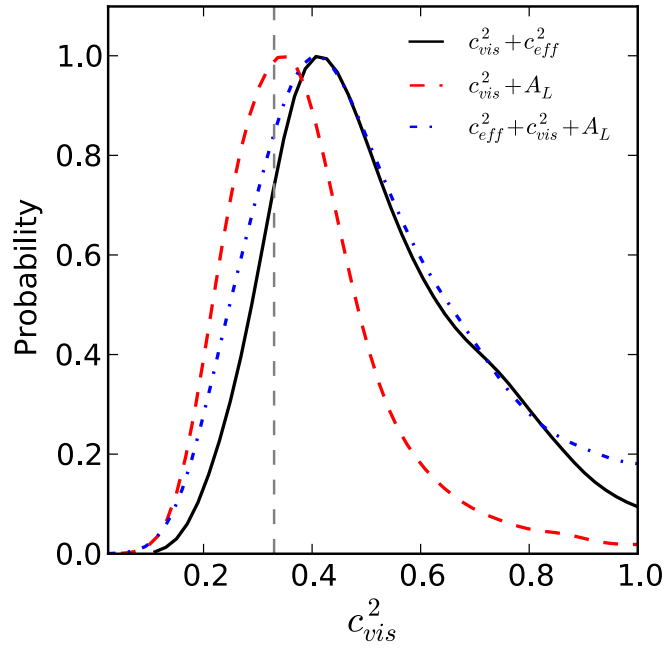
Figure 4.22. One-dimensional posterior probabilities of the parameter $c^2_{\rm vis}$ for the indicated models for Planck+L. The vertical dashed line indicates the expected value in the standard model, [96].
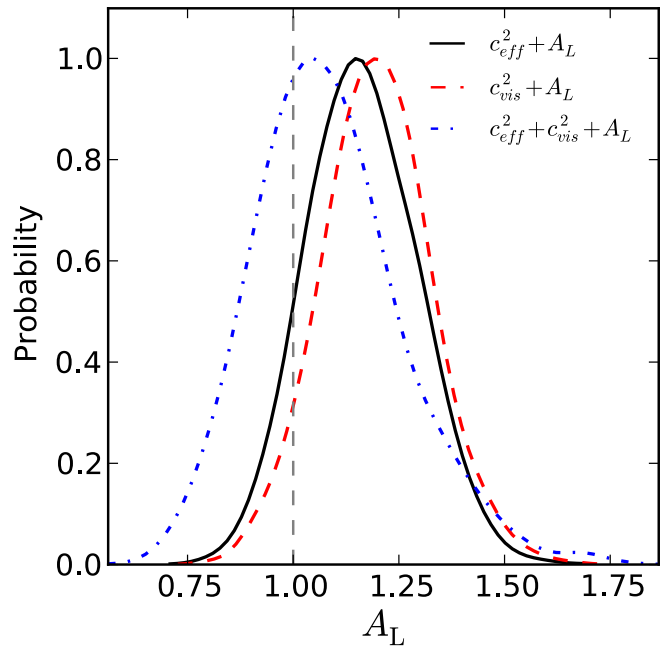
Figure 4.23. One-dimensional posterior probabilities of the parameter $A_{\rm L}$ for the indicated models for Planck+WP. The vertical dashed line indicates the expected value in the standard model, [96].
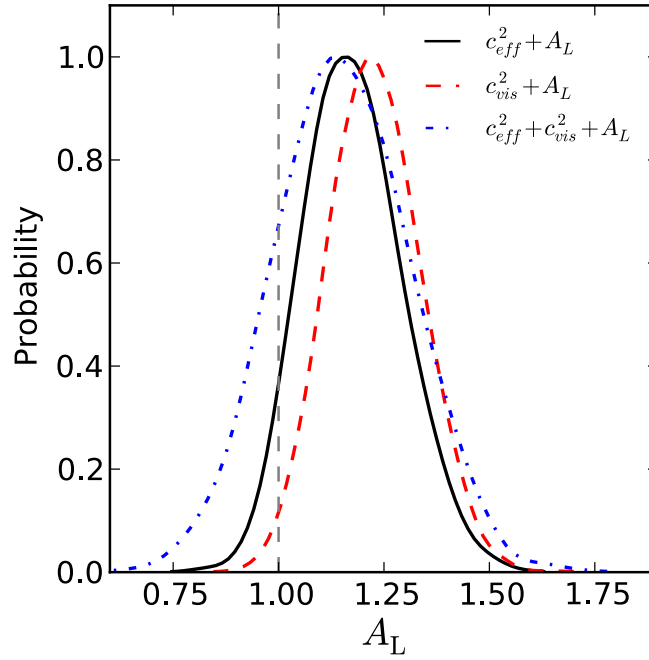
Figure 4.24. One-dimensional posterior probabilities of the parameter A_L for the indicated models for Planck+EX. The vertical dashed line indicates the expected value in the standard model, [96].
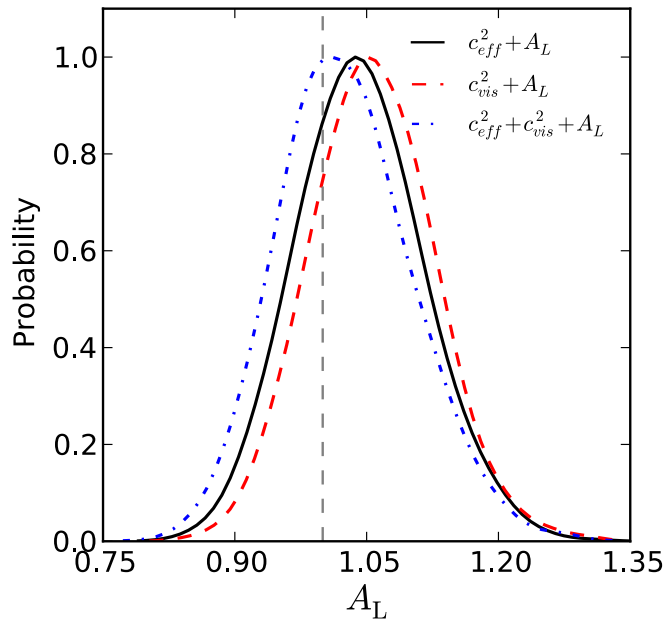
Figure 4.25. One-dimensional posterior probabilities of the parameter A_L for the indicated models for Planck+L. The vertical dashed line indicates the expected value in the standard model. We have a different range in the x axes for this dataset respect to the others, [96].

anomalous value for the lensing amplitude of $A_{\mathrm{L}} = 1.22^{+0.11}_{-0.13}$ at 68% c.l.. Finally, as we saw in the previous section, allowing a simultaneous variation in N_{eff} and A_{L} in the analysis provides $N_{\mathrm{eff}} = 3.71 \pm 0.40$ and $A_{\mathrm{L}} = 1.25 \pm 0.13$ at 68% c.l., suggesting the presence of some anomalies at higher significance.

Here we consider a different modification to the CNB: we fix $N_{\mathrm{eff}} = 3.046$ but we modify the CNB clustering properties as first proposed in Ref. [110]. By following Ref. [111], the CNB can be modelled as a Generalized Dark Matter (GDM) component with a set of equations, describing the evolution of perturbations, given by (see Refs. [107, 111, 112]):

$$\dot{\delta}_\nu = \frac{\dot{a}}{a}\left(1 - 3c^2_{\mathrm{eff}}\right)\left(\delta_\nu + 3\frac{\dot{a}}{a}\frac{q_\nu}{k}\right) - k\left(q_\nu + \frac{2}{3k}\dot{h}\right) \tag{4.2}$$

$$\dot{q}_\nu = k\,c^2_{\mathrm{eff}}\left(\delta_\nu + 3\frac{\dot{a}}{a}\frac{q_\nu}{k}\right) - \frac{\dot{a}}{a}q_\nu - \frac{2}{3}k\pi_\nu \tag{4.3}$$

$$\dot{\pi}_\nu = 3\,c^2_{\mathrm{vis}}\left(\frac{2}{5}q_\nu + \frac{8}{15}\sigma\right) - \frac{3}{5}kF_{\nu,3} \tag{4.4}$$

$$\frac{2l+1}{k}\dot{F}_{\nu,l} - lF_{\nu,l-1} = -\left(l+1\right)F_{\nu,l+1}\ l \geq 3 \tag{4.5}$$

where c^2_{eff} is the sound speed in the CNB rest frame and describes pressure fluctuations respect to density perturbations, and c^2_{vis} is the "viscosity" parameter which parametrizes the anisotropic stress. Standard neutrinos have $c^2_{\mathrm{eff}} = c^2_{\mathrm{vis}} = 1/3$, and the observation of deviations from the standard values could hint for non-standard physics. Constraints on these parameters have been set by several authors (see e.g. Refs. [106, 107, 113]), using cosmological data previous to Planck.

In Ref. [108] the authors found that, assuming $N_{\mathrm{eff}} = 3.046$, the case $c^2_{\mathrm{eff}} = c^2_{\mathrm{vis}} = 1/3$ was ruled out at the level of two standard deviation, and in Ref. [107] the authors found that current cosmological data from the South Pole Telescope SPT, Refs. [90, 91], excluded the standard value of $c^2_{\mathrm{vis}} = 1/3$ at $2 - \sigma$ level, pointing towards a lower value.

Here we bound the values of the neutrino perturbation parameters using the Planck data, also considering the possible degeneracies between c^2_{eff}, c^2_{vis} and the temperature power spectrum lensing amplitude A_{L}.

We sample a six-dimensional set of standard cosmological parameters, imposing flat priors: the baryon and cold dark matter densities Ω_b and Ω_c, the angular size of the sound horizon at decoupling θ, and the optical depth to reionization τ, the scalar spectral index n_S and the overall normalization of the spectrum A_S at $k = 0.05 Mpc^{-1}$, always considering purely adiabatic initial conditions spatial flatness. We vary the Helium abundance Y_{p} assuming a Big Bang Nucleosynthesis (BBN) consistency (given N_{eff} and Ω_b, Y_{p} is a determined function of them). Moreover, we vary the effective sound speed c^2_{eff}, the viscosity parameter c^2_{vis} and the lensing amplitude parameter A_{L}, adopting the following flat priors: $0 \leq c^2_{\mathrm{vis}}, c^2_{\mathrm{eff}} \leq 1$ and $0 \leq A_{\mathrm{L}} \leq 4$. Firstly, we consider them in pair ($c^2_{\mathrm{eff}} - c^2_{\mathrm{vis}}$, $c^2_{\mathrm{eff}} - A_{\mathrm{L}}$, $c^2_{\mathrm{vis}} - A_{\mathrm{L}}$), fixing the third parameter at its standard value ($A_{\mathrm{L}} = 1$, $c^2_{\mathrm{vis}} = 1/3$, $c^2_{\mathrm{eff}} = 1/3$). Finally, we analyze the three parameters all together.

Concerning the datasets, we use the Planck temperature power spectrum in combination with the WMAP low-l likelihood for polarization, Ref. [102]. We refer

to this combination as Planck+WP.

We also consider the inclusion of additional datasets: a Gaussian prior on the Hubble constant $H_0 = 73.8 \pm 2.4 \, \mathrm{km \, s^{-1} \, Mpc^{-1}}$ from the HST measurements in Ref. [6], measurements of Baryon Acoustic Oscillations (BAO) from galaxy surveys, combining three datasets: SDSS-DR7 freo Ref. [99], SDSS-DR9 from Ref. [114] and 6dF Galaxy Survey from Ref. [115]. We refer to this combination as Planck+EX.

Since the information on the lensing amplitude derived from the trispectrum does not hint at the high value of the lensing parameter allowed by the temperature power spectrum (see discussion in Ref. [5]), we also investigate the impact of the addition of the Planck lensing likelihood from Ref. [9] to the Planck+WP dataset, and we refer to this combination as Planck+L.

Our analysis method is based on the publicly available Monte Carlo Markov Chain package, Refs. [97, 104] (version released in March 2013), using the Gelman and Rubin statistic as convergence diagnostic.

We show our results in Table 4.6, Table 4.7 and Table 4.8 in the form of the 68% confidence level, i.e. the interval containing 68% of the total posterior probability centered on the mean.

Firstly, by allowing both c_{eff}^2 and c_{vis}^2 to vary, we obtain posterior values in disagreement with the standard model (see Table 4.6 or Figures 4.17 and 4.20): $c_{\mathrm{vis}}^2 = 0.60 \pm 0.18$ at 68% c.l., greater than the standard value at about 1.5 standard deviations, $c_{\mathrm{eff}}^2 = 0.304 \pm 0.013$ at 68% c.l., smaller than the standard value at more than 95% c.l.. The addition of BAO and HST datasets only improves the constraining power (see Table 4.7 and Figures 4.18 and 4.21). The addition of the lensing power spectrum (see Table 4.8) alleviates the disagreement respect to the standard values for the neutrino parameters (see Figures 4.19, 4.22 and 4.25).

Secondly, when we allow the lensing amplitude parameter to vary (see Table 4.6 and Figures 4.17, 4.20 and 4.23), in the $c_{\mathrm{vis}}^2 + A_{\mathrm{L}}$ case, we recover the standard value of the viscosity parameter $c_{\mathrm{vis}}^2 = 0.35 \pm 0.12$, and similarly, in the $c_{\mathrm{eff}}^2 + A_{\mathrm{L}}$ case, c_{eff}^2 is in agreement with the expected value $c_{\mathrm{eff}}^2 = 0.321 \pm 0.014$. However, A_{L} is still in disagreement with the standard value at more than 1-σ level (respectively, $A_{\mathrm{L}} = 1.20 \pm 0.12$ and $A_{\mathrm{L}} = 1.16 \pm 0.13$), showing a degeneracy with the clustering parameters c_{vis}^2 and c_{eff}^2 (see Figures 4.26, 4.27, 4.28 and 4.29). Also in these cases, the addition of BAO and HST allows to get tighter constraints (see Table 4.7 and Figures 4.18 and 4.21). The addition of the lensing power spectrum (see Table 4.8), allowing the lensing amplitude to vary, produces a further shift of parameters towards the expected values in the standard scenario, within 1-σ.

Finally, when we allow all the three parameters to vary, their posteriors are in good agreement with the standard model, considering all the three combinations of datasets. For example, we get $c_{\mathrm{eff}}^2 = 0.311 \pm 0.019$, $c_{\mathrm{vis}}^2 = 0.51 \pm 0.22$ and $A_{\mathrm{L}} = 1.08 \pm 0.18$ for the Planck+WP case (see Table 4.6 or Figures 4.17 and 4.20).

As we can see from Tables 4.6, 4.7 and 4.8, varying the neutrino parameters results in pronounced variations in other cosmological parameters, in particular the scalar spectral index n_S and the scalar amplitude A_S. A similar analysis has been performed in Ref. [112] considering the viscosity c_{vis}^2. We can see in Figures 4.30 and 4.32 a negative correlation between c_{eff}^2 and the inflationary parameters, and in Figures 4.31 and 4.33 a positive between c_{vis}^2 and these ones.

In conclusion, in this section we presented constraints on the clustering properties

Parameter	ΛCDM	$+c^2_{\mathrm{vis}} + c^2_{\mathrm{eff}}$	$+c^2_{\mathrm{eff}} + A_{\mathrm{L}}$	$+c^2_{\mathrm{vis}} + A_{\mathrm{L}}$	$+c^2_{\mathrm{eff}} + c^2_{\mathrm{vis}} + A_{\mathrm{L}}$
$100\,\Omega_b h^2$	2.206 ± 0.028	2.118 ± 0.047	2.219 ± 0.045	2.236 ± 0.053	2.162 ± 0.095
$\Omega_c h^2$	0.1199 ± 0.0027	0.1157 ± 0.0038	0.1177 ± 0.0032	0.1170 ± 0.0034	0.1159 ± 0.0036
$100\,\theta$	1.0413 ± 0.0006	1.0412 ± 0.0014	1.0428 ± 0.0012	1.0421 ± 0.0019	1.0420 ± 0.0020
$\log[10^{10} A_S]$	3.089 ± 0.025	3.173 ± 0.052	3.086 ± 0.028	3.08 ± 0.05	3.141 ± 0.078
τ	0.090 ± 0.013	0.089 ± 0.013	0.088 ± 0.013	0.087 ± 0.013	0.089 ± 0.014
n_S	0.9606 ± 0.0073	0.998 ± 0.018	0.9732 ± 0.0099	0.970 ± 0.014	0.989 ± 0.023
A_{L}	$\equiv 1$	$\equiv 1$	1.16 ± 0.13	1.20 ± 0.12	1.08 ± 0.18
c^2_{vis}	$\equiv 0.33$	0.60 ± 0.18	$\equiv 0.33$	0.35 ± 0.12	0.51 ± 0.22
c^2_{eff}	$\equiv 0.33$	0.304 ± 0.013	0.321 ± 0.014	$\equiv 0.33$	0.311 ± 0.019
$H_0[\mathrm{km/s/Mpc}]$ (a)	67.3 ± 1.2	68.0 ± 1.3	68.7 ± 1.5	68.9 ± 1.5	68.6 ± 1.7

Table 4.6. Comparison between extended cosmological models and the standard ΛCDM for the Planck+WP dataset, [96].

Parameter	ΛCDM	$+c_{\text{vis}}^2 + c_{\text{eff}}^2$	$+c_{\text{eff}}^2 + A_{\text{L}}$	$+c_{\text{vis}}^2 + A_{\text{L}}$	$+c_{\text{eff}}^2 + c_{\text{vis}}^2 + A_{\text{L}}$
$100\,\Omega_b h^2$	2.236 ± 0.026	2.142 ± 0.048	2.228 ± 0.037	2.258 ± 0.043	2.209 ± 0.091
$\Omega_c h^2$	0.1180 ± 0.0016	0.1160 ± 0.0025	0.1171 ± 0.0018	0.1173 ± 0.0023	0.1167 ± 0.0024
$100\,\theta$	1.0417 ± 0.0006	1.0417 ± 0.0016	1.0427 ± 0.0011	1.0429 ± 0.0018	1.0426 ± 0.0018
$\log[10^{10} A_S]$	3.111 ± 0.032	3.158 ± 0.050	3.084 ± 0.028	3.065 ± 0.043	3.104 ± 0.075
τ	0.101 ± 0.015	0.091 ± 0.013	0.088 ± 0.013	0.087 ± 0.013	0.088 ± 0.013
n_S	0.9621 ± 0.0061	0.993 ± 0.016	0.9737 ± 0.0080	0.967 ± 0.012	0.978 ± 0.023
A_{L}	$\equiv 1$	$\equiv 1$	1.18 ± 0.12	1.23 ± 0.11	1.15 ± 0.17
c_{vis}^2	$\equiv 0.33$	0.53 ± 0.16	$\equiv 0.33$	0.302 ± 0.097	0.40 ± 0.19
c_{eff}^2	$\equiv 0.33$	0.306 ± 0.013	0.322 ± 0.013	$\equiv 0.33$	0.319 ± 0.019
$H_0[\text{km/s/Mpc}]$ [a]	68.31 ± 0.73	68.29 ± 0.74	68.93 ± 0.80	69.16 ± 0.87	68.88 ± 0.99

Table 4.7. Comparison between extended cosmological models and the standard ΛCDM for the Planck+EX dataset, [96].

Parameter	ΛCDM	$+c_{\mathrm{vis}}^2 + c_{\mathrm{eff}}^2$	$+c_{\mathrm{eff}}^2 + \mathrm{A_L}$	$+c_{\mathrm{vis}}^2 + \mathrm{A_L}$	$+c_{\mathrm{eff}}^2 + c_{\mathrm{vis}}^2 + \mathrm{A_L}$
$100\,\Omega_b h^2$	2.206 ± 0.028	2.155 ± 0.049	2.214 ± 0.038	2.217 ± 0.046	2.166 ± 0.063
$\Omega_c h^2$	0.1199 ± 0.0027	0.1151 ± 0.0034	0.1171 ± 0.0030	0.1159 ± 0.0034	0.1151 ± 0.0037
$100\,\theta$	1.0413 ± 0.0006	1.0414 ± 0.0015	1.0426 ± 0.0012	1.0415 ± 0.0018	1.0415 ± 0.0017
$\log[10^{10} A_S]$	3.089 ± 0.025	3.146 ± 0.054	3.084 ± 0.027	3.094 ± 0.051	3.137 ± 0.064
τ	0.090 ± 0.013	0.090 ± 0.013	0.088 ± 0.013	0.088 ± 0.013	0.088 ± 0.013
n_S	0.9606 ± 0.0073	0.990 ± 0.019	0.9726 ± 0.0098	0.974 ± 0.015	0.989 ± 0.021
$\mathrm{A_L}$	$\equiv 1$	$\equiv 1$	1.042 ± 0.072	1.057 ± 0.070	1.025 ± 0.076
c_{vis}^2	$\equiv 0.33$	0.52 ± 0.18	$\equiv 0.33$	0.39 ± 0.14	0.50 ± 0.19
c_{eff}^2	$\equiv 0.33$	0.312 ± 0.013	0.322 ± 0.012	$\equiv 0.33$	0.314 ± 0.015
$H_0[\mathrm{km/s/Mpc}]$ (a)	67.3 ± 1.2	68.5 ± 1.1	68.8 ± 1.4	68.9 ± 1.4	68.8 ± 1.5

Table 4.8. Comparison between extended cosmological models and the standard ΛCDM for the Planck+L dataset, [96].
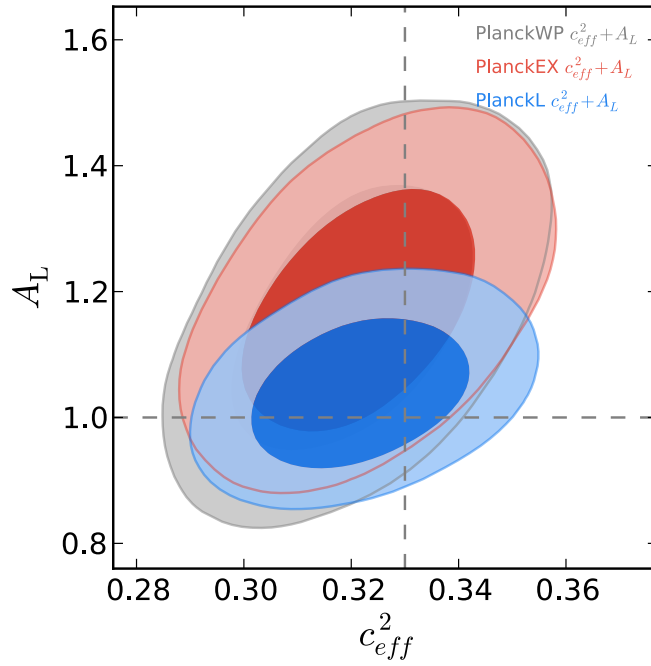
Figure 4.26. Two-dimensional posterior probabilities in the $c_{vis}^2 - A_L$ plane for the indicated datasets and models. The dashed lines indicate the expected values in the standard model, [96].
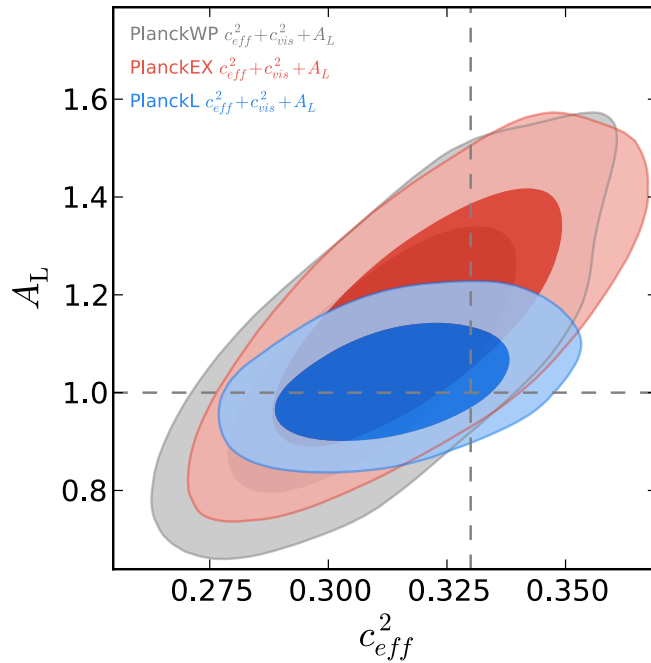
Figure 4.27. Two-dimensional posterior probabilities in the $c_{eff}^2 - A_L$ plane for the indicated datasets and models. The dashed lines indicate the expected values in the standard model, [96].
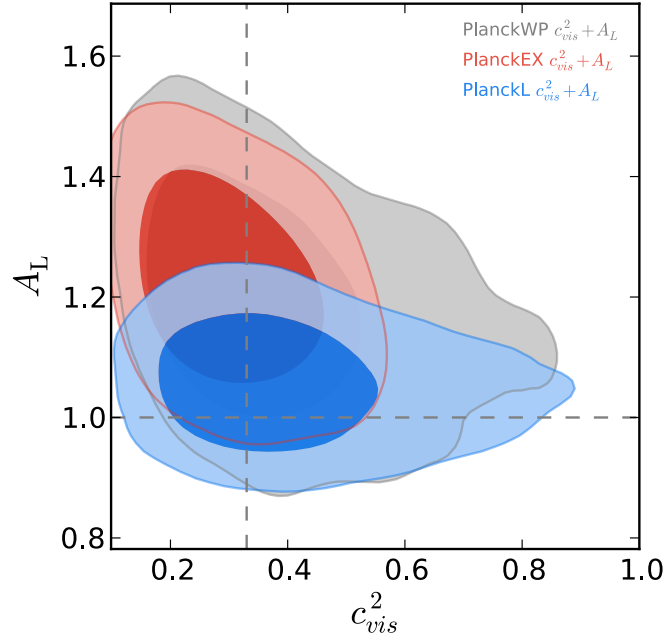
Figure 4.28. Two-dimensional posterior probabilities in the $c_{\mathrm{vis}}^2 - A_{\mathrm{L}}$ plane for the indicated datasets and models. The dashed lines indicate the expected values in the standard model, [96].
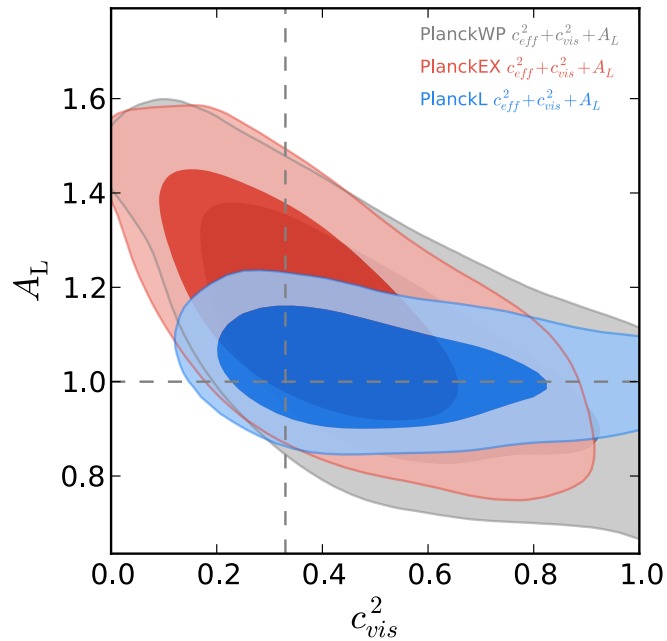
Figure 4.29. Two-dimensional posterior probabilities in the $c_{\mathrm{vis}}^2 - A_{\mathrm{L}}$ plane for the indicated datasets and models. The dashed lines indicate the expected values in the standard model, [96].
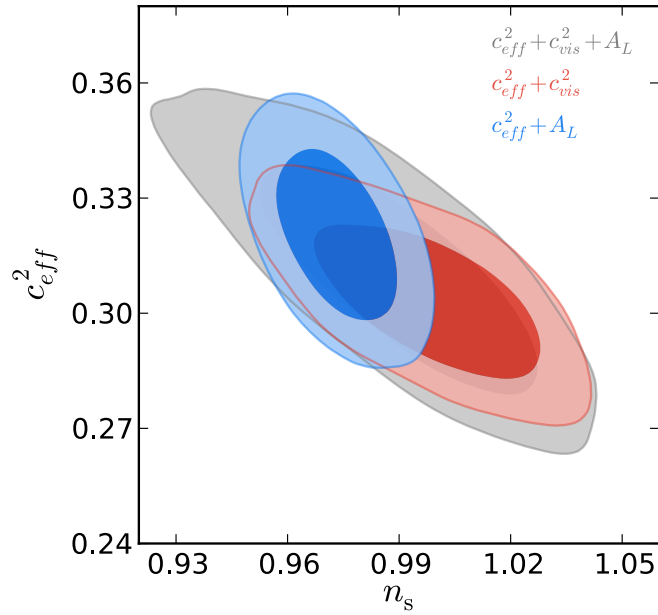
Figure 4.30. Degeneracy between the clustering parameters c_{eff}^2 and the scalar spectral index n_S for the Planck+WP dataset and the indicated models, [96].
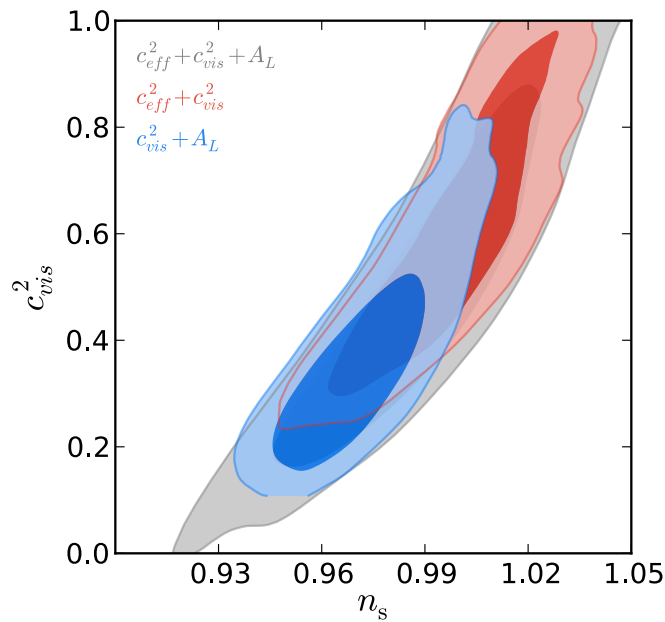
Figure 4.31. Degeneracy between the clustering parameters c_{vis}^2 and the scalar spectral index n_S for the Planck+WP dataset and the indicated models, [96].
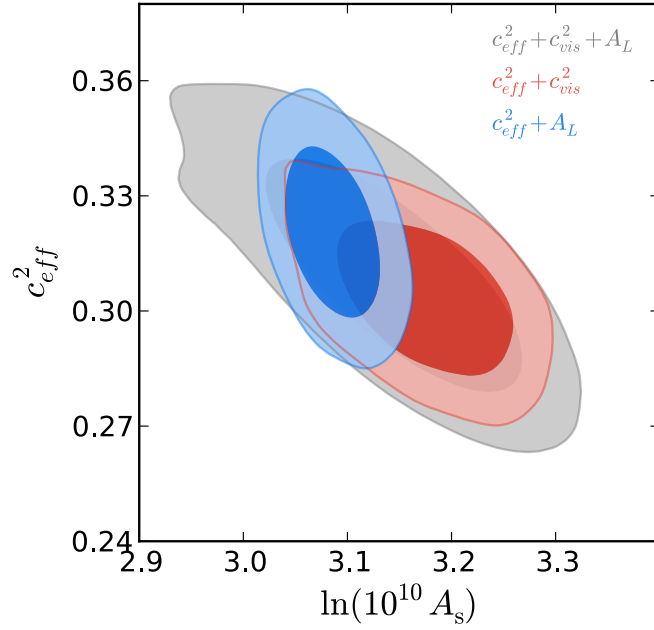
Figure 4.32. Degeneracy between the clustering parameters c_{eff}^2 and the scalar amplitude A_S for the Planck+WP dataset and the indicated models, [96].
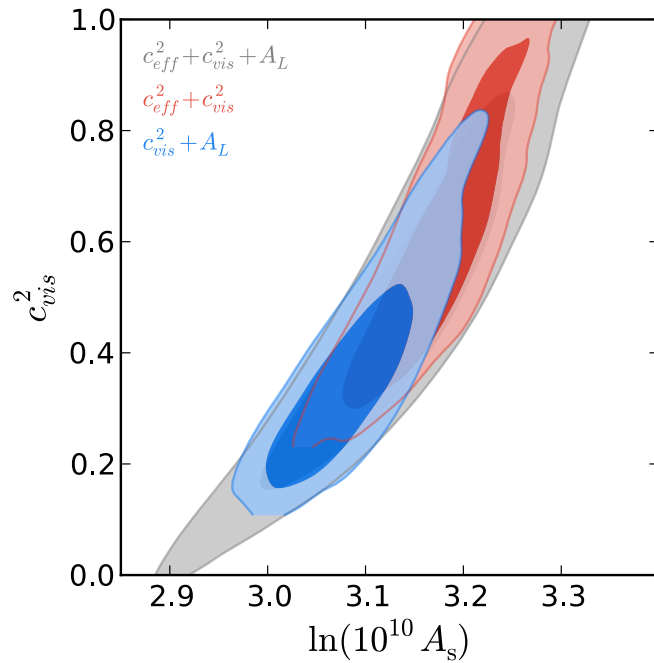
Figure 4.33. Degeneracy between the clustering parameters c_{vis}^2 and the scalar amplitude A_S for the Planck+WP dataset and the indicated models, [96].
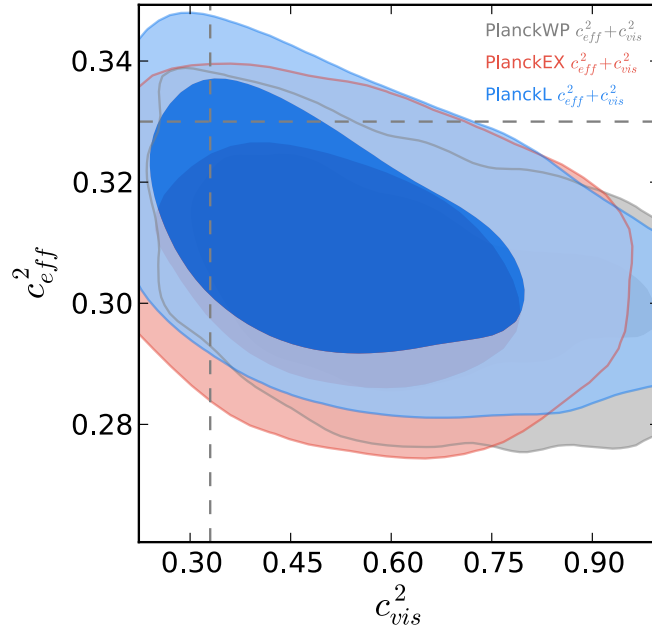
Figure 4.34. Two-dimensional posterior probabilities in the $c_{\mathrm{vis}}^2 - c_{\mathrm{eff}}^2$ plane for the indicated datasets and models. The dashed lines indicate the expected values in the standard model, [96].
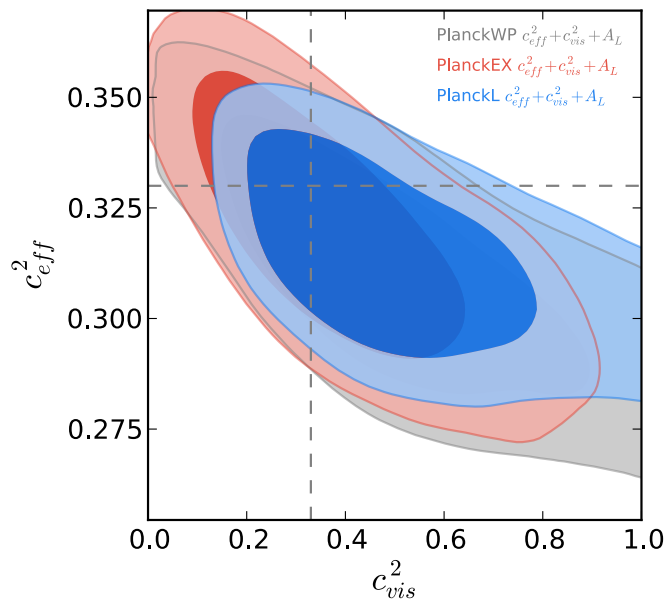
Figure 4.35. Two-dimensional posterior probabilities in the $c_{\mathrm{vis}}^2 - c_{\mathrm{eff}}^2$ plane for the indicated datasets and models. The dashed lines indicate the expected values in the standard model, [96].

of the CNB, finding that the Planck 2013 dataset hints at anomalous values for these parameters: $c_{\mathrm{vis}}^2 = 0.60 \pm 0.18$ at 68% c.l. and $c_{\mathrm{eff}}^2 = 0.304 \pm 0.013$ at 68% c.l.. When we allow A_{L} to vary we found a better consistency with the standard model with $c_{\mathrm{vis}}^2 = 0.51 \pm 0.22$, $c_{\mathrm{eff}}^2 = 0.311 \pm 0.019$, and $A_{\mathrm{L}} = 1.08 \pm 0.18$ at 68% c.l.. The anomalous large value of A_{L} measured by Planck could then be possibly connected to non-standard neutrino properties.

Chapter 5

Physical candidates for an extra "Dark Radiation" component

As already discussed in the previous chapter, the CMB measurements from the Planck satellite, combined with measurements of the Hubble constant H_0 from the Hubble Space Telescope (HST) from Ref. [6], gives the constraint $N_{\text{eff}} = 3.83 \pm 0.54$ at 95% c.l.. When low multipole polarization measurements from WMAP9 release, see Ref. [1], and high multipole CMB data from both the ACT, see Ref. [89], and the SPT, see Ref. [116], are added in the analysis, the constraint on N_{eff} is $3.62^{+0.50}_{-0.48}$ at 95% c.l., see Ref. [5], indicating the presence of an extra dark radiation component at the $\sim 2.4 - \sigma$ confidence level.

The simplest scenario to explain this extra dark radiation component includes extra sterile neutrino species, since there is no fundamental symmetry in nature forcing a definite number of right-handed (sterile) neutrino species, that are allowed in the Standard Model fermion content. In any way, there are other possibilities which are as well closely related to minimal extensions to the standard model of elementary particles, as thermal axions, or extended dark sectors with additional relativistic species.

In this chapter (but see also Ref. [20]) we further investigate, in light of the new observations made by Planck, most of these physical models that could possibly explain this dark radiation anomaly.

In particular, we focus on the so-called $(3 + 2)$, see Ref. [117], and $(3 + 1)$ neutrino mass models, see Ref. [118], analyzing the decoupling processes of the sterile neutrino states in the early Universe and presenting the constraints from a combined analysis of Planck plus galaxy clustering data from the CMASS sample data Release 9 (DR9) of the BOSS experiment, see Ref. [119], part of the Sloan Digital Sky Survey IIII program, see Ref. [120].

Also models containing a dark sector with light species that eventually decouples from the standard model could contribute to N_{eff}, as, for instance, asymmetric dark matter models (see e.g. Refs. [121, 122] and references therein), or extended weakly-interacting massive particle models (see the recent work presented in Ref. [123]). Here we follow the formalism from Ref. [122], in which the authors have used a general approach to describe the dark sector structure, including both light and heavy relativistic degrees of freedom in the dark sector at the time of decoupling.

While the light relativistic degrees of freedom correspond to the number of degrees of freedom that ultimately constitute the dark radiation sector, the heavy relativistic degrees of freedom correspond to relatively heavy degrees of freedom that will turn non-relativistic and heat the dark radiation fluid. Here we derive the constraints on the number of light and heavy degrees of freedom of the dark sector as a function of its decoupling temperature from the standard model sector.

5.1   Sterile neutrino constraints

A number of studies in the literature have been devoted to constrain the light sterile massive neutrino thermal abundances, see e.g. Refs. [124, 125, 126, 127, 128, 129, 106, 130]. However, the extra sterile neutrinos do not necessarily need to feature thermal abundances, depending dramatically their contribution on the mass-energy density of the Universe on the flavour mixing processes operating at the decoupling period, see Refs. [131, 132, 133]. The authors of Ref. [134] have shown that the constraints on N_{eff} from Planck data can set upper bounds on the sterile neutrino mixing angles.

The flavor neutrino eigenstates ν_α, $\alpha = e, \mu, \tau, s, p$ are related to the mass eigenstates ν_i, $i = 1, 2, 3, 4, 5$, through a 5×5 unitary matrix which we indicate as U:

$$\nu_\alpha = U_{\alpha i} \nu_i \ . \tag{5.1}$$

In the early Universe at temperatures above neutrino decoupling ($T > 1$ MeV), sterile neutrinos can result from the oscillations of active neutrinos, and their precise abundances at decoupling can be computed by means of the density matrix formalism. We follow Ref. [135], in which the kinetic equations for the density matrix read:

$$\dot{\rho} = i \left[H_{\mathrm{m}} + V_{\mathrm{eff}}, \rho \right] - \left\{ \Gamma, (\rho - \rho_{\mathrm{eq}}) \right\} \ , \tag{5.2}$$

where $H_{\mathrm{m}} = U H_0 U^\dagger$ is the free neutrino Hamiltonian in the flavor basis, being U is the unitary mixing matrix. The matrix

$$\rho_{\mathrm{eq}} = \mathrm{diag}(\rho_{eq}) = I(\exp(E/T) + 1)^{-1}, \tag{5.3}$$

with I the identity matrix, refers to the equilibrium value of the density matrix. The effective potential V_{eff} reads

$$V_{\mathrm{eff},a} = -C_a G_F^2 T^4 E / \alpha \ , \tag{5.4}$$

and refers to the interactions of neutrinos with the medium, being G_F the Fermi coupling constant, T the plasma temperature, E the neutrino energy and $\alpha = 1/137$ the fine structure constant. The constants C_a depend on the neutrino flavor and are $C_e \sim 0.61$ and $C_{\mu,\tau} \sim 0.17$ (for $T < m_\mu$), see Ref. [136]. In eq. (5.2) Γ refers to the coherence loss in the evolution of the non diagonal terms, and we followed Ref. [135] to describe this effect. The damping factor Γ is diagonal in the flavor basis, $\Gamma = \mathrm{diag}(\Gamma_e, \Gamma_\mu, \Gamma_\tau, 0, 0)$:

$$\Gamma_a = g_a \, \frac{90 \, \zeta(3)}{7 \, \pi^4} \, G_F^2 \, T^4 \, p \; , \tag{5.5}$$

with $a = e, \mu, \tau$. We computed the values of the g_a parameters numerically, $g_e \simeq 3.6$ and $g_\mu = g_\tau \simeq 2.5$, see Ref. [137].

In the range of temperatures for neutrino decoupling $\dot{T} \simeq -HT$, being H the Hubble expansion rate:

$$H(T) = \sqrt{\frac{4\pi^3 g_\star(T)}{45}} \frac{T^2}{m_{Pl}} \; , \tag{5.6}$$

where m_{Pl} is the Planck mass and $g_\star(T)$ is the number of relativistic degrees of freedom, which depends on the temperature. We neglect the sterile neutrino thermalization impact on $g_\star(T)$, being the temperature dependence of the former function the standard one with three active neutrinos. Therefore the equation we need to numerically solve to compute the sterile neutrino abundances at decoupling reads, see Ref. [131]:

$$\left(\frac{\partial \rho}{\partial T} \right) = -\frac{1}{HT} (i \, [H_{\rm m} + V_{\rm eff}, \rho] - \{\Gamma, (\rho - \rho_{\rm eq})\}) \; . \tag{5.7}$$

We integrate from $T \sim 100$ MeV, and follow the sterile neutrino abundance until $T = 1$ MeV. For numerical purposes, and accordingly to sterile neutrino searches, we have set all the fourth and fifth sterile neutrino mixing parameters to zero except for $U_{e4,e5}$ and $U_{\mu4,\mu5}$. Moreover, we fix the parameters for the three active neutrino mixing to their best fit values from Ref. [138]. Finally we assume for the active neutrinos a normal hierarchy scheme with $m_1 = 0$ and for the solar and atmospheric mass splittings the best fit values reported by Ref. [138]. Therefore we fix the sum of the active neutrino masses to 0.056 eV.

Figures 5.1 and 5.2 depict, respectively, the fourth and the fourth and fifth sterile neutrino abundances in the $(3+1)$ and in the $(3+2)$ models, normalized to the equilibrium distribution, as a function of the temperature for the following mixing parameters: $U_{e4} = 0.14$, $U_{\mu4} = 0.17$ and $\Delta m_{14}^2 = 0.93$ eV^2 ($U_{e4} = 0.13$, $U_{\mu4} = 0.15$, $\Delta m_{14}^2 = 0.47$ eV^2, $U_{e5} = 0.14$, $U_{\mu5} = 0.13$ and $\Delta m_{15}^2 = 0.87$ eV^2), which are the best-fit values obtained in Ref. [139] (see also Ref. [140]) from a global fit to neutrino oscillation data. Notice that the best-fit values from neutrino oscillation physics imply that the sterile states will have thermal abundances and therefore some tension will arise when comparing with the bounds from current cosmological measurements.

We now place bounds on the sterile neutrino mass using different cosmological observables. Since constraints on sterile neutrino masses are model dependent, we use the same procedure adopted by the Planck collaboration in Ref. [5], deriving constraints on an "effective" neutrino mass $m_{\nu,\rm sterile}^{\rm eff}$ that could then be translated in constraints on a specific sterile neutrino model. In this framework, we consider one active massive neutrino with mass of $m_\nu = 0.06$ eV, two active massless neutrino and a fourth sterile neutrino with a mass $m_{\nu,\rm sterile}^{\rm eff} \equiv (94.1\omega_{\nu,\rm sterile})$ eV and that, when is relativistic, will contribute to the relativistic energy density by increasing the effective neutrino number by a term $\Delta N_{\rm eff}$ that is however assumed as an extra free parameter. In few words, a specific model would connect $m_{\nu,\rm sterile}^{\rm eff}$ and $\Delta N_{\rm eff}$ but in our case the two parameters vary freely.
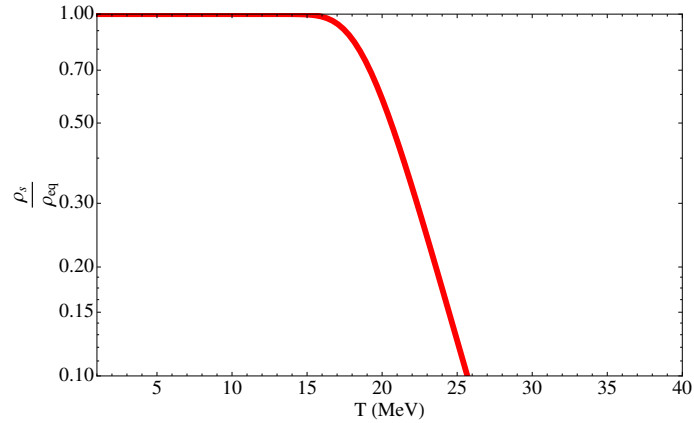
Figure 5.1. We show the sterile neutrino abundance relative to the equilibrium ones, as a function of the temperature, for the $(3+1)$ model, using the best fit values for the mixing angles and mass splittings from Ref. [139], arising from a global fit to neutrino oscillation data, [20].
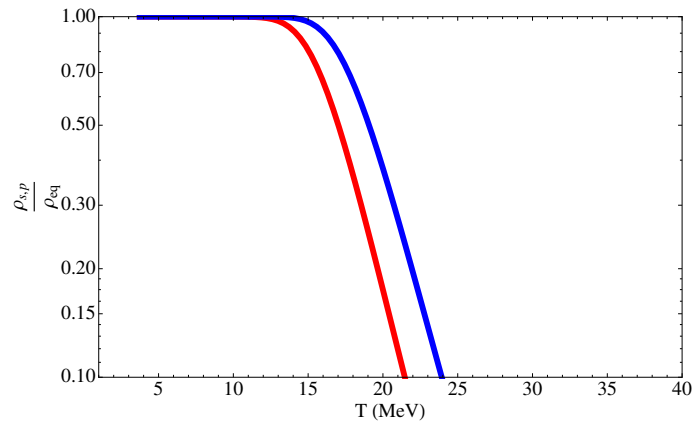
Figure 5.2. We show the sterile neutrino abundances relative to the equilibrium ones, as a function of the temperature, for the $(3+2)$ model, using the best fit values for the mixing angles and mass splittings from Ref. [139], arising from a global fit to neutrino oscillation data, [20].

Our analysis is therefore described by the following set of parameters:

$$\{\omega_b, \omega_c, \Theta_s, \tau, n_s, \log[10^{10}A_s], N_{\text{eff}}, m_{\nu,\text{sterile}}^{\text{eff}}\} \,, \tag{5.8}$$

$\omega_b \equiv \Omega_b h^2$ and $\omega_c \equiv \Omega_c h^2$ being the physical baryon and cold dark matter energy densities, Θ_s the ratio between the sound horizon and the angular diameter distance at decoupling, τ is the reionization optical depth, n_s the scalar spectral index, A_s the amplitude of the primordial spectrum and $N_{\text{eff}} = 3.046 + \Delta N_{\text{eff}}$. Notice that current cosmological data are sensitive to the total sum of neutrino masses $\sum m_\nu = \sum m_{\nu,\text{active}} + m_{\nu,\text{sterile}}^{\text{eff}}$.

The connection between the neutrino cosmological observables and the neutrino mixing parameters is non trivial, and only in some cases there exists a direct link between the two sets of parameters. Even future cosmological data will be unable to set the precise mixing pattern unless the survey sensitivity to neutrino masses is much better than the neutrino mass splittings, see Ref. [141].

The priors on these parameters are shown in Tab. 6.1. We used the Boltzmann CAMB code, Ref. [27] and a Monte Carlo Markov Chain (MCMC) analysis based on the MCMC package `cosmomc`, Ref. [97].

Parameter	Prior
$\Omega_b h^2$	$0.005 \rightarrow 0.1$
$\Omega_c h^2$	$0.01 \rightarrow 0.99$
Θ_s	$0.5 \rightarrow 10$
τ	$0.01 \rightarrow 0.8$
n_s	$0.9 \rightarrow 1.1$
$\ln(10^{10}A_s)$	$2.7 \rightarrow 4$
N_{eff} (eV)	$3.046 \rightarrow 7$
$m_{\nu,\text{sterile}}^{\text{eff}}$ (eV)	$0 \rightarrow 3$

Table 5.1. Uniform priors for the cosmological parameters for the MCMC analysis, [20].

For Plack data, we add the high-l and low-l TT likelihoods (including lensing) and we also add the low-l TE, EE, BB WMAP likelihood, see Ref. [5] for details. We marginalize over all foregrounds parameters, following Ref. [5]. We also consider high multipoles data from both SPT, see Refs. [90, 91], and ACT, see Ref. [89], experiments. We used firstly galaxy clustering data. When dealing with massive neutrinos, galaxy clustering measurements have large constraining power due to the clear signature induced by massive neutrinos on the matter power spectrum at scales larger than their free streaming scale, see Ref. [15]. We therefore also consider the DR9 CMASS sample of galaxies, Ref. [119], from the BOSS experiment with an effective redshift $z_{\text{eff}} = 0.57$, in the form of full shape power spectrum measurements (see Refs. [142, 143, 144] for previous studies with BOSS DR9 data but within the standard three neutrino picture scheme), which have been shown to provide competitive results to those obtained with geometrical information from Baryon Acoustic Oscillation measurements, see Ref. [144].

Figure 5.3, shows the results of our MCMC analyses in the ($m_{\nu,\text{sterile}}^{\text{eff}}$ (eV), $\Omega_c h^2$) plane, assuming one sterile neutrino mass state. We found $m_{\nu,\text{sterile}}^{\text{eff}} < 0.34$ eV at

95% c.l.. Even if the existence of one extra massive sterile neutrino is perfectly allowed by cosmological data, the squared mass difference required by neutrino oscillation within $(3+1)$ models ($\Delta m_{14}^2 = 0.93$ eV^2 in Ref. [139]) is much higher than the one obtained using the cosmological limit quoted above (setting $m_1 \simeq 0$). Figure 5.4 shows the results of our MCMC in the ($m_{\nu,\text{sterile}}^{\text{eff}}$ (eV), $3.046 + \Delta N_{\text{eff}}$) plane. Notice that the existence of two fully thermal sterile neutrino states is highly disfavoured by cosmological data. We found $3.30 < N_{\text{eff}} < 4.43$ and $\sum m_{\nu,\text{sterile}}^{\text{eff}} < 0.33$ eV both at 95% c.l.. Therefore, cosmological measurements compromise the viability of $(3+2)$ neutrino mass models for the mixing parameters preferred by oscillation neutrino data.
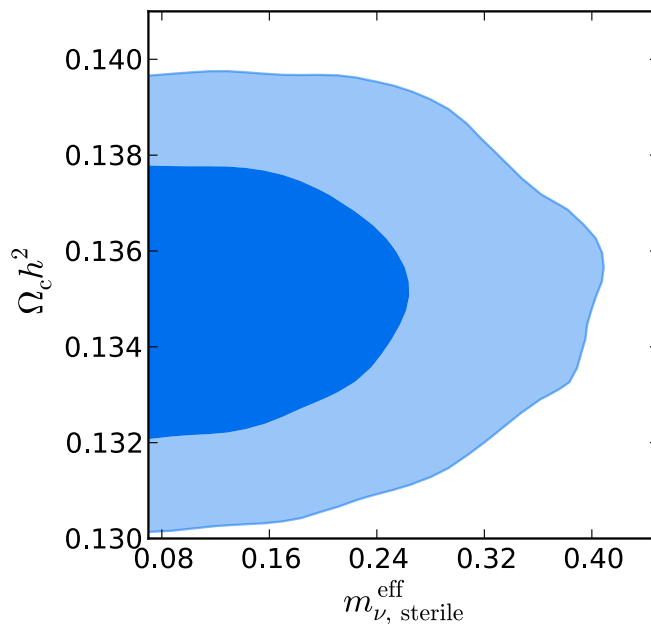
Figure 5.3. 68% and 95% confidence level contours in the $(3+1)$ massive sterile neutrino scenario and in the N_{eff} massive sterile neutrino case. The figure shows the results of our MCMC analyses in the ($m_{\nu,\text{sterile}}^{\text{eff}}$ (eV), $\Omega_c h^2$) plane, assuming one sterile neutrino mass state, [20].

We also place constraints on the $m_{\nu,\text{sterile}}^{\text{eff}}$ vs N_{eff} plane including HST data, considering a different choice of datasets respect to Ref. [5], namely Planck+HST and Planck+WP+HighL+HST. The effect of the Hubble constant prior was not considered in Ref. [5]. Figures 5.5 and 5.6 show the results of our MCMC analyses in the ($m_{\nu,\text{sterile}}^{\text{eff}}$ (eV), N_{eff}) plane. For Planck+HST (Fig. 5.5) we found $m_{\nu,\text{sterile}}^{\text{eff}} < 0.44$ eV and $3.25 < N_{\text{eff}} < 4.37$ at 95% CL. In the second case, Planck+WP+HST+HighL (Fig. 5.6) we found $m_{\nu,\text{sterile}}^{\text{eff}} < 0.36$ eV and $3.14 < N_{\text{eff}} < 4.15$ at 95% c.l..

In summary, in the context of $(3+N)$ neutrino mass models, the existence of one additional fully thermal sterile massive neutrino is perfectly allowed by Planck data combined either with galaxy clustering data or with a prior from HST on the Hubble constant. In this case, we obtained an upper bound on the mass of the fourth sterile neutrino $m_4 < 0.34$ eV at 95% c.l., which, for the normal hierarchy scheme and assuming the mass of the lightest neutrino state $m_1 = 0$, will imply $m_{14}^2 \sim 0.11$ eV^2
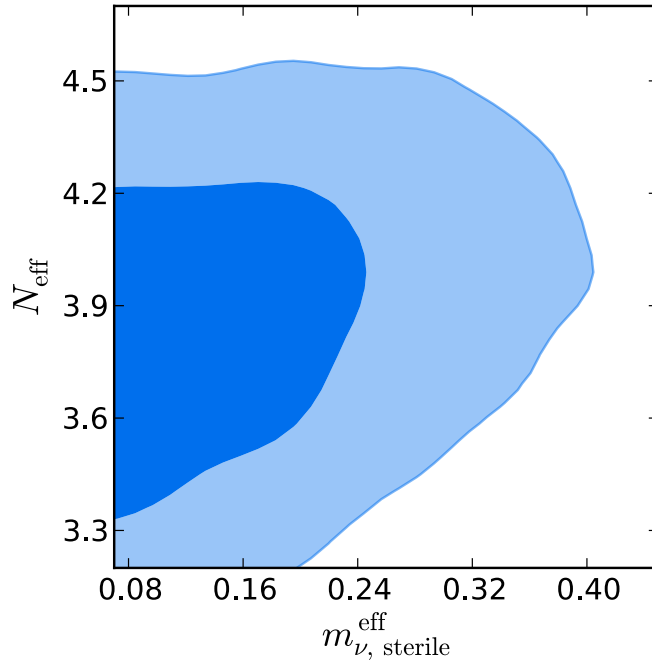
Figure 5.4. 68% and 95% confidence level contours in the $(3 + 1)$ massive sterile neutrino scenario and in the N_{eff} massive sterile neutrino case. The figure shows the results of our MCMC in the $(m_{\nu,\text{sterile}}^{\text{eff}}$ (eV), $3.046 + \Delta N_{\text{eff}})$ plane, [20].
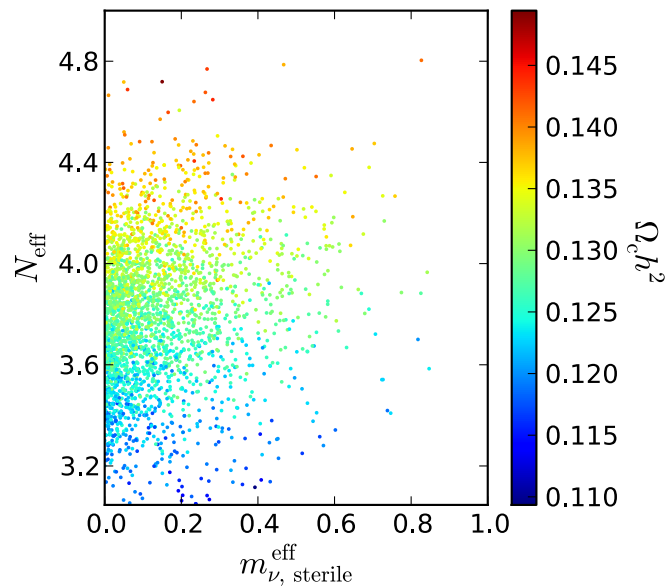
Figure 5.5. Samples in the $N_{\text{eff}} - m_{\nu,\text{sterile}}^{\text{eff}}$ plane, colour-coded by $\Omega_c h^2$. The figure shows the results obtained from the Plack data combined with HST, [20].
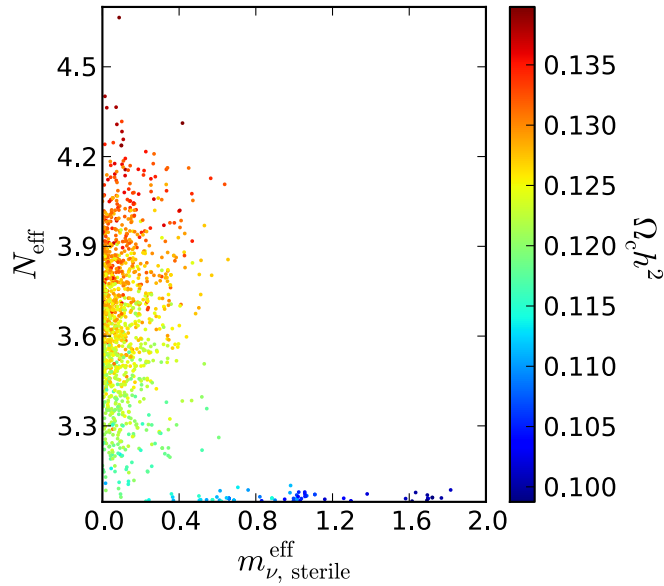
Figure 5.6. Samples in the $N_{\text{eff}} - m_{\nu,\text{sterile}}^{\text{eff}}$ plane, colour-coded by $\Omega_c h^2$. The figure shows the results obtained from the Planck data with WMAP9 polarization, SPT, ACT and HST, [20].

for sterile neutrino oscillation searches. The existence of two fully non thermal sterile neutrino massive states is however disfavoured for the cosmological datasets used in our analyses. This result agrees with the findings of Ref. [130], in which one of the two massive sterile states within $(3+2)$ models was required to be non fully thermal when including galaxy clustering data in the analyses.

5.2 Extended Dark sector models

Any model containing a dark sector with relativistic degrees of freedom that eventually decouples from the standard model sector will contribute to N_{eff}. An example of these models is the so-called asymmetric dark matter scenario, which, in general, contains extra radiation degrees of freedom produced by the annihilations of the thermal dark matter component. Here we follow the general approach of Ref. [122], in which the dark sector contains both light (g_l) and heavy (g_h) relativistic degrees of freedom at the temperature of decoupling T_D from the standard model. For high decoupling temperature, $T_D > \text{MeV}$, the contribution to the effective number of relativistic degrees of freedom reads, see Ref. [122]:

$$\Delta N_{\text{eff}} = \frac{13.56}{g_{\star S}(T_D)^{\frac{4}{3}}} \frac{(g_l + g_h)^{\frac{4}{3}}}{g_l^{\frac{1}{3}}} \,, \tag{5.9}$$

where $g_{\star S}(T_D)$ is calculated using the approximated expression given in Ref. [145].

If the dark sector decouples at lower temperatures ($T_D < \text{MeV}$), there are two possibilities for the couplings of the dark sector with the standard model: either the

dark sector couples to the electromagnetic plasma or it couples to neutrinos. In the second case, which is the one we consider here,

$$N_{\text{eff}} = (3 + \frac{4}{7} \frac{(g_h + g_l)^{\frac{4}{3}}}{g_l^{\frac{1}{3}}})(\frac{3 \times \frac{7}{4} + g_H + g_h + g_l}{3 \times \frac{7}{4} + g_h + g_l})^{\frac{4}{3}} , \qquad (5.10)$$

being g_H the number of degrees of freedom that become non relativistic between Big Bang Nucleosynthesis (BBN) and the dark sector decoupling period.

As firstly illustrated in Ref. [122], it is possible to use the measured value of N_{eff} to find the required heavy degrees of freedom heating the light dark sector plasma g_h as a function of the dark sector decoupling temperature T_D for a fixed value of g_l. Figures 5.7 and 5.8 illustrate the 2-σ required ranges for g_h using $N_{\text{eff}} = 3.62^{+0.50}_{-0.48}$ and $N_{\text{eff}} = 3.83 \pm 0.54$, respectively, for $g_H = 0$. Notice that at decoupling temperatures $T_D > \text{MeV}$, the standard model relativistic degrees of freedom will be heated, requiring therefore heating in the dark sector to enhance the value of ΔN_{eff}. On the other hand, at low decoupling temperatures, the number of the required heavy degrees of freedom g_h decreases as ΔN_{eff} does. Indeed, for the case of $N_{\text{eff}} = 3.62^{+0.50}_{-0.48}$ ($N_{\text{eff}} = 3.83 \pm 0.54$), having extra heavy degrees of freedom is highly (mildly) disfavoured. This is because at low temperatures, the photon background cannot get extra heating from standard model particles and therefore an extra heating in the dark sector will increase dramatically the value of N_{eff}.
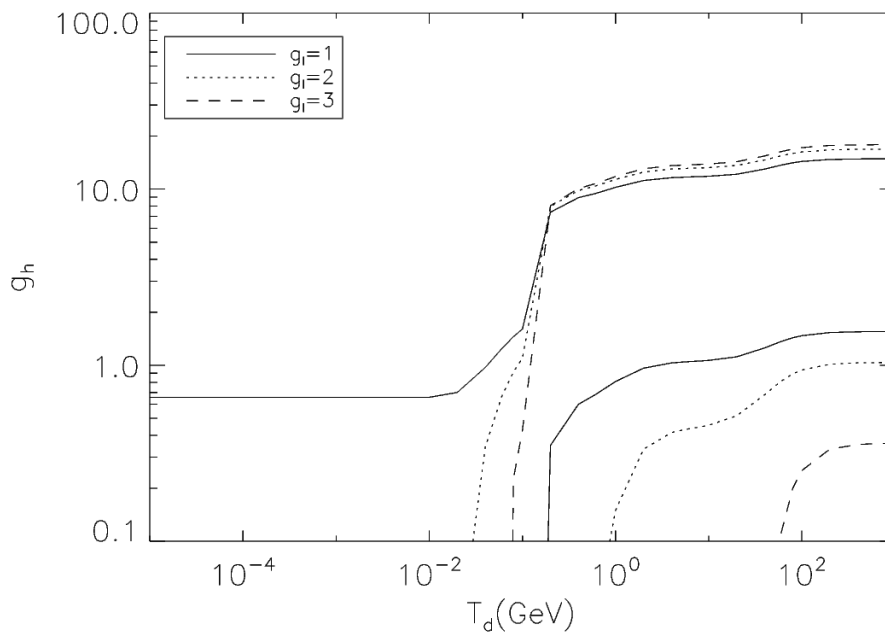
Figure 5.7. The figure shows the $2 - \sigma$ required ranges for the number of heavy degrees of freedom heating the dark sector g_h using $N_{\text{eff}} = 3.62^{+0.50}_{-0.48}$ for several values of g_l, the light degrees of freedom of the dark sector, [20].
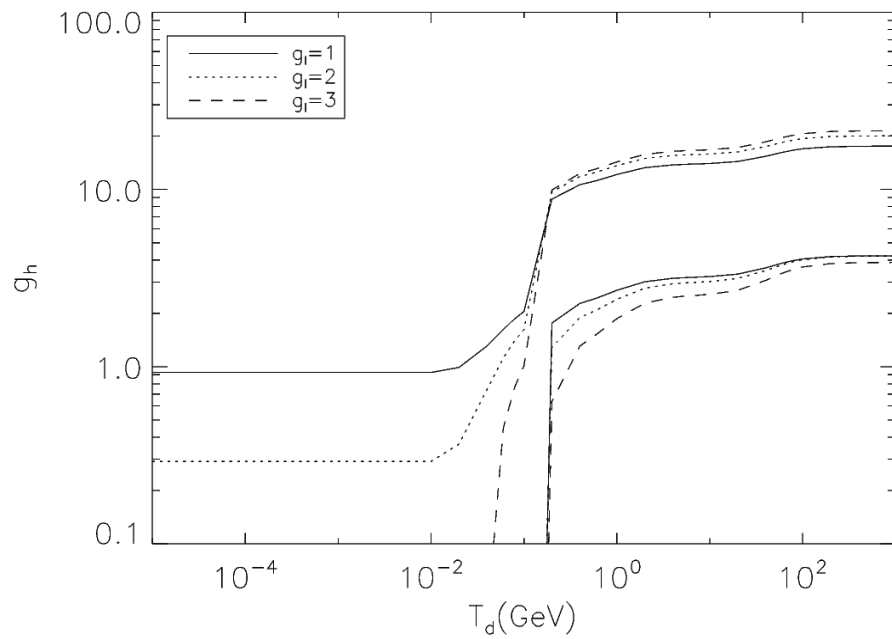
Figure 5.8. The figure shows the $2 - \sigma$ required ranges for the number of heavy degrees of freedom heating the dark sector g_h using $N_{\text{eff}} = 3.83 \pm 0.54$ for several values of g_l, the light degrees of freedom of the dark sector, [20].

Chapter 6

Constraints on the neutrino sector from Planck plus BOSS DR11

In standard cosmology, hot, thermal relics are identified with the three light, active neutrino flavours of the Standard Model of elementary particles. The masses of these three neutrino states have an impact in the different cosmological observables, see Refs. [146, 15] for a detailed description. Traditionally, the largest effect caused by neutrino masses on the Cosmic Microwave Background (CMB) anisotropies, is via the *Early Integrated Sachs Wolfe effect (ISW)*. Light active neutrino species may turn non-relativistic close to the decoupling period, affecting the gravitational potentials and leaving a signature which turns out to be maximal around the first acoustic oscillation peak in the photon temperature anisotropy spectrum.

More recently, the Planck satellite CMB data, Ref. [5], has opened the window to tackle the neutrino mass via gravitational lensing measurements: neutrino masses are expected to leave an imprint on the lensing potential (due to the higher expansion rate) at scales smaller than the horizon when neutrinos turn non relativistic states, see Ref. [147]. However, the largest effect of neutrino masses on the several cosmological observables comes from the suppression of galaxy clustering at small scales. Neutrinos, being hot thermal relics, possess large velocity dispersions. Consequently, the non-relativistic neutrino overdensities will only cluster at wavelengths larger than their free streaming scale, reducing the growth of matter density fluctuations at small scales, see e.g. Refs. [148, 149, 150, 129, 142, 1, 90, 89, 106, 144, 151, 143, 152].

Non degenerate neutrinos have different free streaming scales and in principle, with perfect measurements of the matter power spectrum, the individual values of the neutrino masses could be identified. In practice, the former is an extremely challenging task. Cosmological measurements are, for practical purposes, only sensitive to the total neutrino mass, i.e. to the sum of the three active neutrino masses.

CMB measurements from the Planck satellite, including the lensing likelihood and low-l polarization measurements from WMAP 9-year data, Ref. [102], provide a limit on the sum of the three active neutrino masses of $\sum m_\nu < 1.11$ eV at 95% c.l.. When a prior on the Hubble constant H_0 from the Hubble Space Telescope, Ref. [6],

is added in the analysis, the constraint is strongly tightened, being $\sum m_\nu < 0.21$ eV at 95% CL, due to the huge existing degeneracy between H_0 and $\sum m_\nu$, see Ref. [129]. The addition of Baryon Acoustic Oscillation (BAO) measurements from the Sloan Digital Sky Survey (SDSS)-II Data Release 7, see Ref. [153, 99], from the WiggleZ survey, see Ref. [154], from the Baryon Acoustic Spectroscopic Survey (BOSS), see Ref. [155], one of the four surveys of SDSS-III, see Ref. [120], Data Release 9, see Ref. [7], and from 6dF, see Ref. [115], to Planck CMB measurements also significantly improves the neutrino mass constraints, leading to $\sum m_\nu < 0.26$ eV at 95% c.l. (see also Ref. [156]).

However, the former bounds are obtained assuming that neutrinos are the only hot thermal relic component in the Universe. The existence of extra hot relic components, as sterile neutrino species and/or thermal axions will change the cosmological neutrino mass constraints, see Refs. [157, 124, 126, 125, 129, 106, 151, 158, 159, 160, 161, 162]. Massless, sterile neutrino-like particles, arise naturally in the context of models which contain a dark radiation sector that decouples from the Standard Model. A canonical example are asymmetric dark matter models, in which the extra radiation degrees of freedom are produced by the annihilations of the thermal dark matter component, see Ref. [122] and also Refs. [113, 123] for extended weakly-interacting massive particle models. On the other hand, extra sterile massive, light neutrino species, whose existence is not forbidden by any fundamental symmetry in nature, may help in resolving the so-called neutrino oscillation anomalies, see Ref. [163, 139] and also Refs. [131, 164, 130, 134, 20] for recent results on the preferred sterile neutrino masses and abundances considering both cosmological and neutrino oscillation constraints. Another candidate is the thermal axion, see Ref. [165], which constitutes the most elegant solution to the strong CP problem, i.e. why CP is a respected symmetry of Quantum Chromodynamics (QCD) despite the existence of a natural, four dimensional, Lorentz and gauge invariant operator which badly violates CP. Axions are Pseudo-Nambu-Goldstone bosons associated to a new global $U(1)_{PQ}$ symmetry, which is spontaneously broken at an energy scale f_a. The axion mass is inversely proportional to the axion coupling constant f_a :

$$m_a = \frac{f_\pi m_\pi}{f_a} \frac{\sqrt{R}}{1+R} = 0.6 \text{ eV } \frac{10^7 \text{ GeV}}{f_a} \ , \tag{6.1}$$

where $R = 0.553 \pm 0.043$ is the up-to-down quark masses ratio and $f_\pi = 93$ MeV is the pion decay constant. Axions may be copiously produced in the early Universe via thermal or non-thermal processes, providing therefore, a possible hot relic candidate in the thermal case, to be considered together with the standard relic neutrino background.

Both extra, sterile neutrino species and axions have an associated free streaming scale, reducing the growth of matter fluctuations at small scales. Indeed, it has been noticed by several authors, see Refs. [166, 167], that the inclusion of Planck galaxy cluster number counts data, see Ref. [168], in the cosmological data analyses, favours a non zero value for the sterile neutrino mass: the free streaming sterile neutrino nature will reduce the matter power at small (i.e. cluster) scales but will leave unaffected the scales probed by the CMB. A similar tendency for $\sum m_\nu > 0$ appears, albeit to a smaller extent, see Ref. [166], when considering CFHTLens weak lensing constraints on the clustering matter amplitude, see Ref. [169].

Extra dark radiation or light species as neutrinos and axions will also contribute to the effective number of relativistic degrees of freedom N_{eff}. The canonical value $N_{\text{eff}} = 3.046$ corresponds to the three active neutrino contribution. If there are extra light species at the Big Bang Nucleosynthesis (BBN) epoch, the expansion rate of the Universe will be higher, leading to a higher freeze out temperature for the weak interactions which translates into a higher primordial helium fraction. The measurements of deuterium, see Ref. [11], and helium, see Ref. [170], light element abundances provide the constraint $N_{\text{eff}} = 3.50 \pm 0.20$, see Ref. [11].

In this chapter (see also Ref. [21]) we analyse the constraints on the three active neutrino masses, extending the analyses to possible scenarios with additional hot thermal relics, as sterile neutrino species or axions, using the available cosmological data in the beginning of the year 2014. The data combination used in our study includes also the most precise distance BAO constraints from the BOSS Data Release 11 (DR11) results from Ref. [8], see also Refs. [171, 172, 173].

6.1   Cosmological data analyses

The baseline scenario we analyse here is the light active massive neutrino scheme with three degenerate massive neutrinos, described by the parameters:

$$\{\omega_b, \omega_c, \Theta_s, \tau, n_s, \log[10^{10}A_s], \sum m_\nu\} , \tag{6.2}$$

$\omega_b \equiv \Omega_b h^2$ and $\omega_c \equiv \Omega_c h^2$ being the physical baryon and cold dark matter energy densities, Θ_s the ratio between the sound horizon and the angular diameter distance at decoupling, τ is the reionization optical depth, n_s the scalar spectral index, A_s the amplitude of the primordial spectrum and $\sum m_\nu$ the sum of the masses of the three active neutrinos in eV. We then consider simultaneously the presence of two hot relics, both massive neutrinos and axions, enlarging the former scenario with one thermal axion of mass m_a. The other possibility is the existence of extra dark radiation species, that we firstly address by introducing a number of massless sterile neutrino-like species, parametrized via N_{eff} (together with the baseline three massive neutrino total mass $\sum m_\nu$). The extra additional sterile states, if massive, may help in resolving the so-called neutrino oscillation anomalies. Consequently, we also constrained simultaneously the N_{eff} massive sterile neutrino scenario and the sum of the three active neutrino masses $\sum m_\nu$. We recall that the effective number of massive sterile neutrino species is represented by $\Delta N_{\text{eff}} = N_{\text{eff}} - 3.046$, and its mass is m_s^{eff}, which is related to the physical sterile neutrino mass via the relation:

$$m_s^{\text{eff}} = (T_s/T_\nu)^3 m_s = (\Delta N_{\text{eff}})^{3/4} m_s , \tag{6.3}$$

being T_s (T_ν) the current temperature of the sterile (active) neutrino, and assuming that the sterile states are hot thermal relics with a phase space distribution similar to the active neutrino ones.

Table 6.1 specifies the priors considered on the different cosmological parameters. For our numerical analyses, we used the Boltzmann CAMB code, Ref. [27], and extracted cosmological parameters from current data using a Monte Carlo Markov Chain (MCMC) analysis based on the publicly available MCMC package `cosmomc`, Ref. [97].

Parameter	Prior
$\Omega_b h^2$	$0.005 \to 0.1$
$\Omega_c h^2$	$0.01 \to 0.99$
Θ_s	$0.5 \to 10$
τ	$0.01 \to 0.8$
n_s	$0.9 \to 1.1$
$\ln\left(10^{10} A_s\right)$	$2.7 \to 4$
$\sum m_\nu$ [eV]	$0.06 \to 3$
m_a [eV]	$0.1 \to 3$
$N_{\rm eff}$	$0(3.046) \to 10$
$m_s^{\rm eff}$ [eV]	$0 \to 3$

Table 6.1. Uniform priors for the cosmological parameters considered here. In the case of the extra relativistic degrees of freedom $N_{\rm eff}$, the numbers refer to the massless (massive) case.

In particular, we ran chains using the Metropolis-Hastings (MH) algorithm to obtain posterior distributions for the model parameters, given a certain dataset combination. The only exception is for the measurements of the power spectrum amplitude that are included in our analysis by post-processing the MH chains that were previously generated without accounting for these data. The post-processing is done using the technique of importance sampling; this technique is very reliable when the posterior distributions obtained after including new data are centered on the same values as the old distributions, and becomes on the contrary less reliable the more the new posteriors are shifted with respect to the old ones. The reason for this fact is that, in this case, one needs to sample from the low-probability tail of the old distribution, that is poorly explored by the MH algorithm (unless the chains run for a very long time). We stressed this fact since the inclusion of the data on the power spectrum amplitude shifts the posterior for some of the model parameters.

All the cases under consideration (additional massless species, massive sterile neutrinos, and axions) can be studied with none, or minimal, modifications to the CAMB code. In particular, the massive sterile and axion cases can be reproduced in the Boltzmann code by means of a suitable reparameterization and by treating, code-wise, the additional species as massive neutrinos. This relies on the fact that, for an equilibrium distribution function, the evolution equations only depend on the mass over temperature ratio m_i/T_i and on the total density Ω_i ($i =$ a, s). The equivalence is perfect for thermal sterile neutrinos, because they have a Fermi-Dirac distribution function like ordinary neutrinos; instead, this is not the case for thermal axions since they are described by a Bose-Einstein distribution function. We took into account in our study the bosonic nature of axions at the background level, but not in the perturbation equations. However we argue that the error that we committed in keeping the Fermi-Dirac distribution function in the perturbation equations for axions is negligible given the uncertainties on the model parameters.

CMB data

We consider the data on CMB temperature anisotropies measured by the Planck satellite (including information on the lensing potential) from Refs. [2, 9, 101] combined with 9-year polarization data from WMAP, Ref. [102], and with additional temperature data from high-resolution CMB experiments, namely the Atacama Cosmology Telescope (ACT) from Ref. [174] and the South Pole Telescope (SPT) from Refs. [116].

The likelihood functions associated to these datasets are estimated and combined using the likelihood code distributed by the Planck collaboration, described in Refs. [101] and [9], and publicly available at Planck Legacy Archive[1]. The Planck TT likelihood is constructed following a hybrid approach: the high-l ($l \geq 50$) part is based on a pseudo-C_l technique and uses power spectra estimated from the detectors of the 100, 143 and 217 GHz frequency channels, while the low-l ($l \leq 49$) part uses a Gibbs sampling-based approach and combines data from all frequencies from 30 to 353 GHz. We used Planck TT data up to a maximum multipole number of $l_{\mathrm{max}} = 2500$. These are supplemented by the low-l WMAP 9-year polarization likelihood, that includes multipoles up to $l = 23$, see Ref. [102]. For what concerns the small-scale observations, we followed the approach of the Planck collaboration, as implemented in their likelihood code, and include the ACT spectra presented in Ref. [174] and the SPT spectra presented in Ref. [116]. In particular, the likelihood uses the ACT 148×148 spectra in the range $1000 < l < 9440$, the ACT 148×218 and 218×218 spectra in the range $1500 < l < 9440$, and the SPT 95, 150 and 220 GHz spectra in the range $2000 < l < 10000$, as described in Sec. 4.1 of Ref. [5]. The primary purpose of considering these subsets of the ACT and SPT data is to improve the constraints on the unresolved foregrounds. Finally, we used the information on the gravitational lensing power spectrum estimated from the trispectrum of the Planck maps, as implemented in the Planck lensing likelihood described in Ref. [9].

We refer to the combination of all the above-mentioned data as the *CMB* dataset.

In our analysis of the CMB dataset, we compute the helium abundance following the BBN theoretical prediction, in which the helium mass fraction is a function of $\Omega_b h^2$ and N_{eff} (see the BBN section below) and fix the lensing spectrum normalization to $A_L = 1$. We marginalized over all foregrounds parameters as described in Ref. [5].

Large scale structure data

We consider several large scale structure datasets in different forms. First of all, we includ all the available galaxy survey measurements in the form of Baryon Acoustic Oscillation (BAO) data. As a novelty, we add to the existing BAO datasets (SDSS Data Release 7, Ref. [153, 99], WiggleZ survey, Ref. [154], 6dF, Ref. [115]) the most recent and most accurate BAO measurements to date, arising from the BOSS Data Release 11 (DR11) results, Ref. [8]. Using approximately a sample of one million galaxies and covering 8500 squared degrees, the DR11 results provide the

---

[1]http://pla.esac.esa.int/pla/aio/planckProducts.html

constraints on the spherically averaged distance D_V/r_d [2] to be 13.42 ± 0.13 and 8.25 ± 0.16 at redshifts $z = 0.57$ and $z = 0.32$, respectively. We present the results separately for DR11 BAO measurements, as well as the combination of the former results with other previous BAO measurements, referring to them as *DR11* and *BAO*, respectively.

We also exploit the WiggleZ survey large scale structure measurements in their full matter power spectrum form from Ref. [176], in order to quantify the benefits of using *shape* measurements of the matter power spectrum versus *geometrical* BAO information in extended cosmological scenarios with additional degeneracies among the different parameters, see the earlier work of Refs. [149, 129] where similar comparisons were performed. This dataset is referred as *WZ*, and whenever it is included, the BAO measurement from the WiggleZ survey is not considered in the BAO dataset.

Supernova luminosity distance and Hubble constant measurements

Supernova luminosity distance measurements from the first three years of the Supernova Legacy Survey from Ref. [177] are included in the hot thermal dark matter relic bounds presented here, referring to these data as *SNLS*.

Our cosmological data analyses also address the effect of a Gaussian prior on the Hubble constant $H_0 = 73.8 \pm 2.4$ km/s/Mpc, accordingly with the measurements from the Hubble Space Telescope, Ref. [6]. We refer to this prior as *HST*.

Additional datasets: σ_8 measurements

Measurements of the galaxy power shear spectra by tomographic weak lensing surveys provide a powerful tool to set constraints on the mass distribution in the Universe. The amplitude and the shape of the weak lensing signal are sensitive to the normalization of the power spectrum, the so-called σ_8 parameter (which is the standard deviation of the matter density perturbations in a sphere of radius $8 Mpc/h$), as well as to the overall matter energy density of the Universe, Ω_m. Using six tomographic redshift bins spanning from $z = 0.28$ to $z = 1.12$, the CFHTLens survey finds $\sigma_8(\Omega_m/0.27)^{0.46} = 0.774^{+0.032}_{-0.041}$, see Ref. [169]. We use this constraint in our analyses, applying this constraint to our Monte Carlo Markov chains.

A strong and independent measurement of the amplitude of the power spectrum arises from the abundance of clusters as a function of the redshift, being the cluster redshift distribution a powerful probe of both Ω_m and σ_8. The Planck Sunyaev-Zeldovich (SZ) selected clusters catalog, which consists of 189 galaxy clusters with measured redshift in the X range, is the largest SZ cluster sample to date and has provided the constraint $\sigma_8(\Omega_m/0.27)^{0.3} = 0.782 \pm 0.010$, see Ref. [168] via the cluster mass function. We address as well this constraint in our Monte Carlo Markov chain analyses. These measurements have been included in our analysis by post-processing the chains that were previously generated without accounting for these data.

---

[2]The value of the sound horizon r_d used for these values is obtained using the Eisenstein & Hu fitting formula, see Ref. [175].

Big Bang Nucleosynthesis

The light elements abundance is also sensitive to several cosmological parameters. The primordial abundance of deuterium is usually considered as an invaluable *baryometer*, since the higher the baryon abundance $\Omega_b h^2$, the less deuterium survives. On the other hand, while the mass fraction of helium-4 ^4He ($Y_{\rm p}$) is rather insensitive to $\Omega_b h^2$, it is directly related to the expansion rate at the BBN period, which strongly depends on the effective number of relativistic degrees of freedom $N_{\rm eff}$. As previously stated, if there are extra light species at the BBN epoch, the expansion rate of the Universe will be higher, leading to a higher freeze out temperature for the weak interactions which translates into a higher primordial helium fraction $Y_{\rm p}$. In our work, Ref. [21], we exploit the primordial deuterium values from Ref. [178] $(D/H)_p = (2.87 \pm 0.22) \times 10^{-5}$ as well as the most recent deuterium measurements $(D/H)_p = (2.53 \pm 0.04) \times 10^{-5}$, Ref. [11], to compare the cosmological constraints obtained with these two diferent primordial deuterium estimates, including also the measurements of the helium mass fraction $Y_{\rm p} = 0.254 \pm 0.003$, Ref. [170]. We use the former constraints in the scenarios in which extra relativistic degrees of freedom are expected to be present at the BBN period.

Notice that Planck CMB data are also sensitive to the value of $Y_{\rm p}$ via measurements of the CMB damping tail (high multipole region), and therefore we use the BBN consistency option of the MCMC software exploited here, `cosmomc` (Ref. [97]), assuming therefore that the value of the extra relativistic degrees of freedom remains unchanged between the BBN and the CMB epochs. Then, given a cosmological model, the theoretical primordial abundance of helium, which is a function of $\Omega_b h^2$ and $N_{\rm eff}$ [3] has been computed, using AlterBBN (Ref. [179]), a numerical code devoted to calculate the BBN abundances within non standard cosmologies. We perform a similar calculation for the deuterium primordial abundance, and then fit the theoretical expectations for the deuterium and helium primordial abundances (previously computed for the CMB data analyses in the latter case) to the measurements quoted above, adding the resulting likelihood in our MCMC analyses by means of a postprocessing of our chains.

Consistency of datasets

We derive our constraints on model parameters using different combinations of the datasets described in the previous sections. However, in a few cases there are tensions between datasets, that we describe in the following. We also briefly assess, at least qualitatively, the effect on parameters of adding these data.

We use the Planck lensing likelihood in all our analyses. The lensing likelihood is based on the information encoded in the 4-point correlation function (i.e., the trispectrum) of CMB temperature anisotropies. On the other hand, lensing also directly affects the CMB power spectrum. As explained in Sec. 5.1 of Ref. [5], there is a slight tension between the lensing amplitudes that are inferred from the trispectrum and from the power spectrum. In particular, while the former is consistent with the value expected in ΛCDM, the temperature power spectrum

---

[3]See for instance the fitting functions provided in Ref. [178], extracted from the numerical results of the PArthENoPE BBN code, Ref. [180].

shows a mild preference for a higher lensing power. Since the effect of increasing the neutrino mass is similar to that of a smaller lensing amplitude (as both result in a suppression of power at small scales), including the lensing likelihood tends to shift the value of the total neutrino mass to larger values, see Ref. [5]. Instead, the inclusion of the lensing likelihood does not change significantly the constraints on the effective number of relativistic degrees of freedom, at least for the ΛCDM model.

Another piece of information that is in tension with the corresponding Planck estimate is the value of the Hubble constant inferred from astrophysical measurements, as discussed in Sec. 5.3 of Ref. [5]. This includes the HST value used in our analysis, $H_0 = 73.8 \pm 2.4$ km/s/Mpc, that is discrepant with the Planck ΛCDM estimate $H_0 = 67.3 \pm 1.2$ km/s/Mpc at more than 2-σ, although it should always be remembered that CMB estimates are highly model dependent. The reasons for this discrepancy are not yet well understood and are a matter of intense debate in the community. It is however possible that this tension is relieved in some extensions of the standard ΛCDM model. For this reason, we decide to consider the HST data in some of our enlarged datasets.

Finally, we use the σ_8 measurements from the CHFTLens survey and from the Planck SZ cluster counts, as reported in Sec. 6.1. These values are however both discrepant with the value estimated from Planck CMB at the 2-σ level (see discussion in Sec. 5.5 of Ref. [5]). This tension has not yet been explained either, but it could be related to the difficulties in adequately modelling selection biases and calibrating cluster masses. As in the case of the Hubble constant, however, there is the possibility that the discrepancy is alleviated in some extended cosmological models (like for example those that include the neutrino mass as a free parameter). Following the same rationale as for the inclusion of the HST data, we derived constraints from enlarged datasets that include the σ_8 measurements. These should however be regarded as quite un-conservative.

6.2   Results

6.2.1   Massive neutrinos

We now present the results on our baseline scenario with three active neutrino degenerate species. Table 6.2 depicts the 95% c.l. constraints on the sum of the three active neutrino masses $\sum m_\nu$. Notice that, without the inclusion of the constraints on σ_8 and Ω_m the upper limits on the neutrino mass are mostly driven by the new BOSS DR11 BAO measurements, being the tightest limit $\sum m_\nu < 0.22$ eV at 95% c.l. from the combination of CMB data, BAO and HST measurements of the Hubble constant. However, since there exists a well known discrepancy on the measured value of H_0 from the Planck and the HST experiments, see Ref. [5], we also considered the combination of CMB and BAO data with SNLS Supernovae Ia luminosity distance measurements. Such a combination provided an upper 95% c.l. limit of $\sum m_\nu < 0.23$ eV, in perfect agreement with the findings of the recent BOSS results, see Ref. [172], using the full shape of the clustering correlation function. The addition of the constraints on σ_8 and Ω_m from the CFHTLens survey displaces the bounds on the neutrino mass to higher values, the reason for that being the lower σ_8 preferred by CFHTLens weak lensing measurements. Due the poor constraining

	CMB+DR11	CMB+DR11 +HST	CMB+DR11 +WZ	CMB+DR11 +WZ+HST	CMB+ DR11 +WZ+BAO+HST	CMB+DR11 +BAO	CMB+DR11 +BAO+HST	CMB+ DR11 +BAO+SNLS
$\sum m_\nu$ [eV]	< 0.25	< 0.22	< 0.25	< 0.23	< 0.24	< 0.26	< 0.22	< 0.23
SZ Clusters & CFHTLens								
$\sum m_\nu$ [eV]	$0.30^{+0.12}_{-0.14}$	$0.25^{+0.12}_{-0.13}$	$0.27^{+0.14}_{-0.13}$	$0.25^{+0.10}_{-0.11}$	$0.26^{+0.18}_{-0.13}$	$0.29^{+0.13}_{-0.12}$	$0.24^{+0.10}_{-0.12}$	$0.27^{+0.12}_{-0.13}$
SZ Clusters								
$\sum m_\nu$ [eV]	$0.30^{+0.12}_{-0.14}$	$0.25^{+0.13}_{-0.13}$	$0.27^{+0.12}_{-0.13}$	$0.24^{+0.10}_{-0.10}$	$0.25^{+0.17}_{-0.13}$	$0.29^{+0.13}_{-0.12}$	$0.23^{+0.10}_{-0.12}$	$0.27^{+0.11}_{-0.13}$
CFHTLens								
$\sum m_\nu$ [eV]	< 0.33	< 0.28	< 0.30	< 0.27	< 0.28	< 0.33	< 0.27	< 0.30

Table 6.2. 95% c.l. constraints on the sum of the neutrino masses, $\sum m_\nu$, from the different combinations of datasets explored in Ref. [21].

power of the weak lensing data the neutrino mass bounds are not significantly altered. On the other hand, when adding the constraint on σ_8 and Ω_m from the Planck-SZ cluster catalog on galaxy number counts, a non zero value for the sum of the three active neutrino masses of ~ 0.3 eV is favoured at 4-σ. In particular, the combination of CMB data with BAO measurements from BOSS DR11, WiggleZ power spectrum (full shape) data and a prior on H_0 from HST after considering the inclusion of Planck SZ clusters information leads to the value $\sum m_\nu = 0.24^{+0.10}_{-0.10}$ eV at 95% c.l.. The combination of weak lensing data and galaxy number counts data is mostly driven by the latter and therefore the constraints do not change significantly with respect to the case in which the analyses are performed with galaxy cluster counts information only. A similar effect, although in a slightly different scenario and different datasets, was found by Refs. [166, 167].

Figures 6.1 and 6.2 illustrate our findings for three possible data combinations: CMB data, combined with BOSS DR11 BAO measurements, additional BAO measurements and a prior on the Hubble constant from HST (depicted by the blue contours); and the same data combination but considering also the $\sigma_8 - \Omega_m$ weak lensing (galaxy number counts) constraint, depicted by the red (green) contours. The Figure 6.1 depicts the very well known degeneracy in the $(\sum m_\nu \ (\text{eV}), H_0)$ plane, showing the 68% and 95% c.l. allowed contours by the different datasets specified above. Considering CMB data only, a higher value of $\sum m_\nu$ can be compensated by a decrease on the Hubble constant H_0 since the shift induced in the distance to the last scattering surface caused by a larger $\sum m_\nu$ can be compensated by a lower H_0. Notice that when Planck SZ cluster information on the $\sigma_8 - \Omega_m$ relationship is added, the allowed neutrino mass regions are displaced and a non zero value for the sum of the three active neutrino masses is favoured at $\sim$4-σ. The Figure 6.2 shows the 68% and 95% c.l. allowed regions in the $(\sum m_\nu \ (\text{eV}), \sigma_8)$ plane. The allowed contours of both σ_8 and $\sum m_\nu$ are considerably displaced after considering Planck clusters data. The power spectrum normalization σ_8 has smaller values when neutrinos are massive (due to the neutrino free streaming nature), being precisely these smaller values of σ_8 those preferred by galaxy cluster number counts.

6.2.2   Massive neutrinos and thermal axions

We now present the constraints on a scenario including both massive neutrinos and a thermal axion.

For axion thermalization purposes, only the axion-pion interaction is relevant. To compute the axion decoupling temperature T_D we followed the usual freeze out condition

$$\Gamma(T_D) = H(T_D) \ . \tag{6.4}$$

The average rate $\pi + \pi \to \pi + a$ is given by, see Ref. [181]:

$$\Gamma = \frac{3}{1024\pi^5} \frac{1}{f_a^2 f_\pi^2} C_{a\pi}^2 I \ , \tag{6.5}$$

where
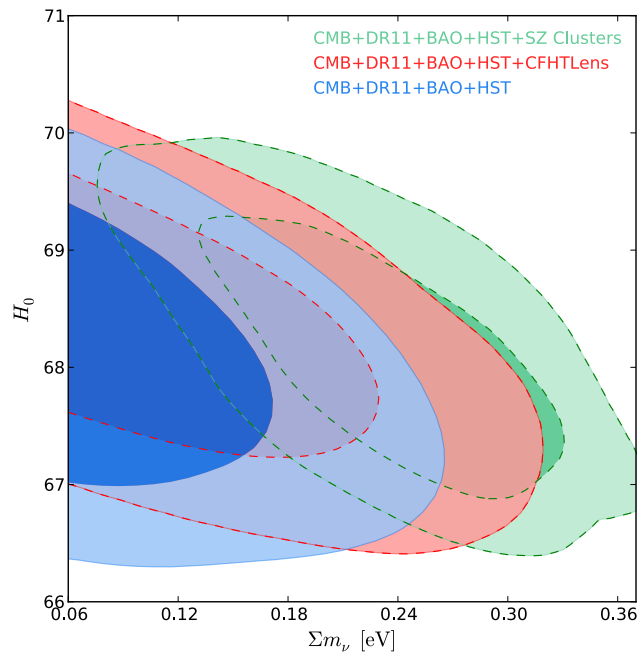
Figure 6.1. The blue contours show the 68% and 95% c.l. allowed regions from the combination of CMB data, BOSS DR11 BAO measurements, additional BAO measurements and a prior on the Hubble constant from HST in the $(\sum m_\nu \text{ (eV)}, H_0)$ plane. The red (green) contours depict the results when the $\sigma_8 - \Omega_m$ weak lensing (galaxy number counts) constraint is added in the analysis, [21].
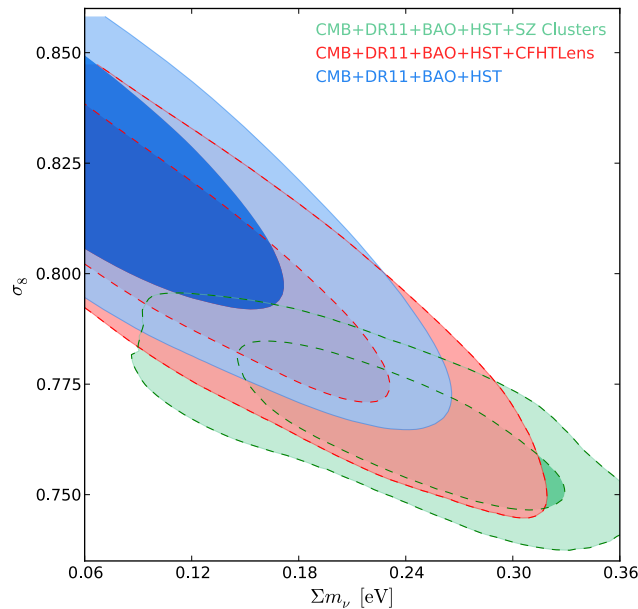
Figure 6.2. The blue contours show the 68% and 95% c.l. allowed regions from the combination of CMB data, BOSS DR11 BAO measurements, additional BAO measurements and a prior on the Hubble constant from HST in the $(\sum m_\nu \text{ (eV)}, \sigma_8)$ plane. The red (green) contours depict the results when the $\sigma_8 - \Omega_m$ weak lensing (galaxy number counts) constraint is added in the analysis, [21].

	CMB+DR11	CMB+DR11 +HST	CMB+DR11 +WZ	CMB+DR11 +WZ+HST	CMB+DR11 +WZ+BAO+HST	CMB+DR11 +BAO	CMB+DR11 +BAO+HST	CMB+DR11 +BAO+SNLS
$\sum m_\nu$ [eV]	< 0.24	< 0.21	< 0.24	< 0.22	< 0.21	< 0.23	< 0.20	< 0.22
m_a [eV]	< 0.79	< 0.77	< 0.65	< 0.62	< 0.59	< 0.74	< 0.75	< 0.76
SZ Clusters & CFHTLensing								
$\sum m_\nu$ [eV]	< 0.36	< 0.27	$0.21^{+0.013}_{-0.13}$	< 0.32	< 0.30	< 0.31	< 0.28	< 0.31
m_a [eV]	< 1.08	< 1.09	< 0.88	< 0.81	< 0.77	< 1.12	$0.63^{+0.47}_{-0.49}$	$0.58^{+0.50}_{-0.48}$
SZ Clusters								
$\sum m_\nu$ [eV]	< 0.36	< 0.27	$0.20^{+013}_{-0.14}$	< 0.32	< 0.30	< 0.31	< 0.27	< 0.31
m_a [eV]	< 1.07	< 1.07	< 0.87	< 0.81	< 0.77	< 1.10	$0.62^{+0.46}_{-0.48}$	$0.57^{+0.50}_{-0.47}$
CFHTLens								
$\sum m_\nu$ [eV]	< 0.29	< 0.24	< 0.28	< 0.25	< 0.25	< 0.27	< 0.24	< 0.26
m_a [eV]	< 0.94	< 0.95	< 0.74	< 0.68	< 0.67	< 0.96	< 0.94	< 0.98
BBN								
$\sum m_\nu$ [eV] $(D/H)_p$[11]	< 0.27	< 0.24	< 0.26	< 0.27	< 0.25	< 0.27	< 0.27	< 0.31
$\sum m_\nu$ [eV] $(D/H)_p$[178]	< 0.24	< 0.20	< 0.23	< 0.21	< 0.21	< 0.22	< 0.20	< 0.22
m_a [eV] $(D/H)_p$[11]	< 1.15	< 0.76	< 0.60	< 0.59	< 0.57	< 0.79	< 0.77	< 1.38
m_a [eV] $(D/H)_p$[178]	< 0.82	< 0.80	< 0.67	< 0.64	< 0.61	< 0.77	< 0.78	< 0.79

Table 6.3. 95% c.l. constraints on the sum of the neutrino masses, $\sum m_\nu$, and on the axion mass, m_a, both in eV, from the different combinations of datasets explored here. When BBN bounds are included, the first (second) raw refers to the constraints obtained combining the primordial deuterium values from Ref. [11] (Ref. [178]) $(D/H)_p = (2.53 \pm 0.04) \times 10^{-5}$ $((D/H)_p = (2.87 \pm 0.22) \times 10^{-5})$ with measurements of the helium mass fraction $Y_p = 0.254 \pm 0.003$ from Ref. [170], [21].

$$C_{a\pi} = \frac{1-R}{3(1+R)} \ ,$$

(6.6)

is the axion-pion coupling constant, see Ref. [181], and

$$I = n_a^{-1}T^8 \int dx_1 dx_2 \frac{x_1^2 x_2^2}{y_1 y_2} f(y_1)f(y_2) \times \int_{-1}^{1} d\omega \frac{(s-m_\pi^2)^3(5s-2m_\pi^2)}{s^2 T^4} \ ,$$

(6.7)

where $n_a = (\zeta_3/\pi^2)T^3$ is the number density for axions in thermal equilibrium, $f(y) = 1/(e^y - 1)$ denotes the pion distribution function, $x_i = |\vec{p}_i|/T$, $y_i = E_i/T$ $(i = 1,2)$, $s = 2(m_\pi^2 + T^2(y_1 y_2 - x_1 x_2 \omega))$, and we assumed a common mass for the charged and neutral pions, $m_\pi = 138$ MeV.

We numerically solved the freeze out equation (6.4), obtaining the axion decoupling temperature T_D versus the axion mass m_a (or, equivalently, versus the axion decay constant f_a). From the axion decoupling temperature, we can compute the current axion number density, related to the present photon density $n_\gamma = 410.5 \pm 0.5$ cm^{-3} via

$$n_a = \frac{g_{\star S}(T_0)}{g_{\star S}(T_D)} \times \frac{n_\gamma}{2} \ ,$$

(6.8)

where $g_{\star S}$ refers to the number of *entropic* degrees of freedom. At the current temperature, $g_{\star S}(T_0) = 3.91$.

Table 6.3 presents the constraints on the sum of the three active neutrino masses and on the axion mass (both in eV) for the different cosmological data combinations considered. Notice that BBN bounds are also quoted here since a thermal axion will also contribute to the extra radiation component at the BBN period, by an amount given by:

$$\Delta N_{\text{eff}} = \frac{4}{7} \left(\frac{3}{2} \frac{n_a}{n_\nu} \right)^{4/3} \ ,$$

(6.9)

being n_a the current axion number density and $n_\nu = 112$ cm^{-3}, the current number density of each active neutrino plus antineutrino flavour. We applied the BBN consistency relation in our MCMC analyses of Planck data, to compute the Helium mass fraction as a function of ΔN_{eff}. Nevertheless the bounds on neutrino and axion masses are not significantly affected if the Helium mass fraction is kept fixed for CMB purposes. Notice that, before applying constraints from Planck SZ Clusters or CHFTLens constraints on the $\sigma_8 - \Omega_m$ relationship, the most stringent 95% c.l. bounds, without including BBN bounds, are $\sum m_\nu < 0.21$ eV and $m_a < 0.59$ eV, considering CMB, BOSS BAO DR11, additional BAO measurements, WiggleZ power spectrum (full shape) information and the H_0 HST prior. These bounds are in perfect agreement with the findings of Ref. [162], albeit they are slightly tighter, mostly due to the more accurate new BOSS BAO measurements.

After considering BBN bounds with deuterium estimates from Ref. [11] (Ref. [178]) and helium constraints from Ref. [170], which constrain the contribution of the thermal axion to the relativistic degrees of freedom at the BBN epoch, the 95% c.l. bounds quoted above traslate into $\sum m_\nu < 0.25$ eV and $m_a < 0.57$ eV ($\sum m_\nu < 0.21$ eV and $m_a < 0.61$ eV).

The addition of weak lensing constraints on the $\sigma_8 - \Omega_m$ relationship from the CFHTLens experiment makes the neutrino and axion mass bounds weaker, due to the lower σ_8 preferred by the former dataset, which favours higher values for the thermal relic masses. If further information on the $\sigma_8 - \Omega_m$ relationship from the Planck SZ cluster number counts is considered in the MCMC analyses, there exists evidence for a neutrino mass of ~ 0.2 eV at the ~3-σ level exclusively for the case in which CMB data is combined with BOSS BAO DR11 measurements and full-shape power spectrum information from the WiggleZ galaxy survey. There exists as well a mild evidence (~2-σ) for an axion mass of 0.6 eV for two isolated cases in which either the HST H_0 prior or SNIa luminosity distance measurements are considered in combination with all the BAO measurements exploited in the paper. However, there is no evidence for neutrino and axions masses simultaneously.

Figure 6.3 depicts the 68% and 95% c.l. allowed regions arising from the combination of CMB data, BOSS DR11 BAO measurements, additional BAO measurements and a prior on the Hubble constant from HST in the ($\sum m_\nu$ (eV), m_a(eV)) plane. Once the Planck SZ cluster number counts information on the $\sigma_8 - \Omega_m$ relationship is added, a non zero value of the axion mass is favoured by data at the $\sim 2.2\sigma$. The Fig. 6.4 shows the 68% and 95% c.l. contours in the ($\sum m_\nu$ (eV), m_a(eV)) plane resulting from the analysis of CMB data, BOSS DR11 BAO measurements, additional BAO measurements - except for the WiggleZ galaxy survey information which is removed and considered in its full-shape form - and the HST H_0 prior. Notice that no evidence for non-zero neutrino masses nor for non-zero axion mass appears in this case.
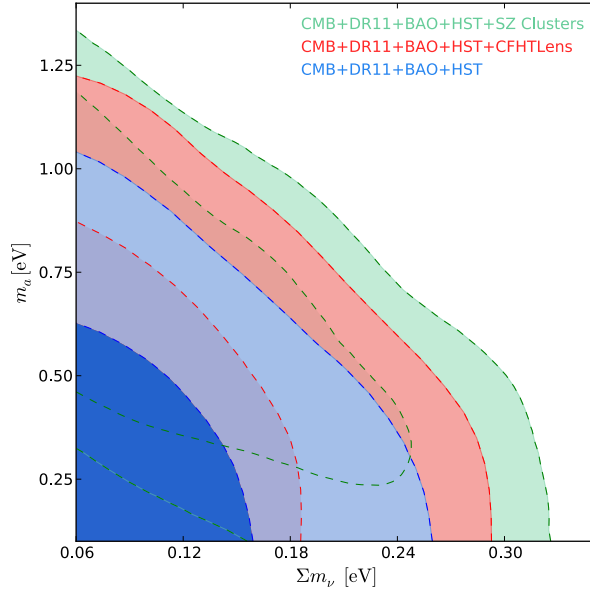
Figure 6.3. The blue contours show the 68% and 95% c.l. allowed regions from the combination of CMB data, BOSS DR11 BAO measurements, additional BAO measurements and a prior on the Hubble constant from HST (depicted by the blue contours) in the ($\sum m_\nu$ (eV), m_a (eV)) plane. The red (green) contours depict the results when the $\sigma_8 - \Omega_m$ weak lensing (galaxy number counts) constraint is added in the analysis, [21].
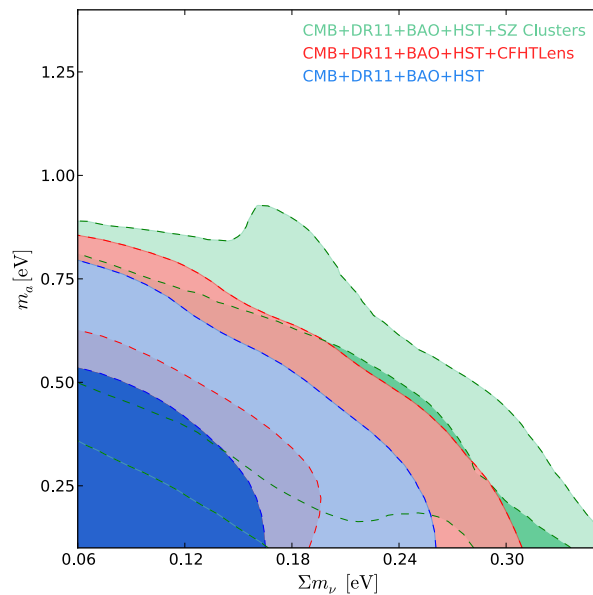
Figure 6.4. The blue contours show the 68% and 95% c.l. allowed regions from the combination of CMB data, WiggleZ full-shape matter power spectrum measurements, BOSS DR11 BAO measurements, additional BAO measurements and a prior on the Hubble constant from HST (depicted by the blue contours) in the ($\sum m_\nu$ (eV), m_a (eV)) plane. The red (green) contours depict the results when the $\sigma_8 - \Omega_m$ weak lensing (galaxy number counts) constraint is added in the analysis, [21].

6.2.3 Massive neutrinos and extra dark radiation species

We now report the constraints resulting when considering both massive neutrinos and ΔN_{eff} massless dark radiation species. These massless species may appear in extensions of the Standard Model of elementary particles containing a dark sector, as, for instance, in the so-called asymmetric dark matter scenarios. In all these models, when the value of N_{eff} is larger than the canonical 3.046, $\Delta N_{\mathrm{eff}} = N_{\mathrm{eff}} - 3.046$ is related to the extra density in massless hot relics. On the other hand, if the value of N_{eff} is smaller than the standard 3.046, the active neutrino temperature is reduced and there are no extra massless species.

Table 6.4 depicts the 95% c.l. constraints on the sum of the three active neutrino masses $\sum m_\nu$ and well as on the total number of dark radiation species N_{eff}, corresponding to the contribution from the three active neutrinos plus ΔN_{eff} massless dark radiation species, for the different data combinations explored here. The bounds on the neutrino mass are less stringent than in standard three neutrino massive case due to the large degeneracy between $\sum m_\nu$ and N_{eff}, since a larger number of massless sterile neutrino-like species will increase the radiation content of the Universe, and, in order to leave unchanged both the matter-to-radiation equality era and the location of the CMB acoustic peaks, the matter content of the Universe must also increase, allowing therefore for larger neutrino masses. We found $\sum m_\nu < 0.31$ eV and $N_{\mathrm{eff}} = 3.45^{+0.59}_{-0.54}$ at 95% c.l. from the combination of CMB data and BOSS DR11 BAO measurements. When the prior on the value of the Hubble constant from HST is included in the analyses, the mean value of N_{eff} and the bound

	CMB+DR11	CMB+DR11 +HST	CMB+DR11 +WZ	CMB+DR11 +WZ+HST	CMB+DR11 +WZ+BAO+HST	CMB+DR11 +BAO	CMB+DR11 +BAO+HST	CMB+DR11 +BAO+SNLS
$\sum m_\nu$ [eV]	< 0.31	< 0.31	< 0.32	< 0.34	< 0.34	< 0.31	< 0.31	< 0.29
$N_{\rm eff}$	$3.45^{+0.59}_{-0.54}$	$3.66^{+0.52}_{-0.49}$	$3.33^{+0.55}_{-0.62}$	$3.57^{+0.50}_{-0.48}$	$3.56^{+0.45}_{-0.49}$	$3.43^{+0.58}_{-0.59}$	$3.66^{+0.48}_{-0.47}$	$3.48^{+0.58}_{-0.56}$
SZ Clusters & CFHTLensing								
$\sum m_\nu$ [eV]&	$0.37^{+0.24}_{-0.18}$	$0.37^{+0.20}_{-0.20}$	$0.32^{+0.19}_{-0.19}$	$0.35^{+0.16}_{-0.17}$	$0.37^{+0.26}_{-0.17}$	$0.32^{+0.18}_{-0.21}$	$0.37^{+0.18}_{-0.20}$	$0.32^{+0.15}_{-0.17}$
$N_{\rm eff}$	$3.32^{+0.53}_{-0.55}$	$3.54^{+0.48}_{-0.54}$	$3.24^{+0.58}_{-0.70}$	$3.56^{+0.59}_{-0.59}$	$3.56^{+1.09}_{-0.60}$	$3.17^{+0.64}_{-0.59}$	$3.54^{+60}_{-0.62}$	$3.25^{+0.47}_{-0.43}$
SZ Clusters								
$\sum m_\nu$ [eV]	$0.37^{+0.24}_{-0.19}$	$0.36^{+0.18}_{-0.18}$	$0.32^{+0.19}_{-0.19}$	$0.35^{+0.17}_{-0.16}$	$0.36^{+0.26}_{-0.18}$	$0.32^{+0.18}_{-0.20}$	$0.37^{+0.18}_{-0.21}$	$0.32^{+0.15}_{-0.16}$
$N_{\rm eff}$	$3.33^{+0.55}_{-0.53}$	$3.55^{+0.51}_{-0.58}$	$3.25^{+0.57}_{-0.68}$	$3.56^{+0.59}_{-0.58}$	$3.55^{+0.65}_{-0.59}$	$3.54^{+0.63}_{-0.59}$	$3.54^{+0.62}_{-0.59}$	$3.25^{+0.49}_{-0.44}$
CFHTLens								
$\sum m_\nu$ [eV]	< 0.41	< 0.44	< 0.39	< 0.41	< 0.42	< 0.40	< 0.43	< 0.39
$N_{\rm eff}$	$3.39^{+0.57}_{-0.55}$	$3.59^{+0.52}_{-0.54}$	$3.28^{+0.58}_{-0.63}$	$3.55^{+0.53}_{-0.47}$	$3.54^{+0.52}_{-0.47}$	$3.33^{+0.61}_{-0.61}$	$3.58^{+0.50}_{-0.50}$	$3.37^{+0.58}_{-0.55}$
BBN								
$\sum m_\nu$ [eV] $(D/H)_p$[11]	< 0.27	< 0.29	< 0.29	< 0.24	< 0.25	< 0.28	< 0.32	< 0.32
$\sum m_\nu$ [eV] $(D/H)_p$[178]	< 0.30	< 0.28	< 0.32	< 0.31	< 0.32	< 0.31	< 0.28	< 0.28
$N_{\rm eff}$ $(D/H)_p$[11]	$3.17^{+0.26}_{-0.27}$	$3.24^{+0.26}_{-0.25}$	$3.13^{+0.30}_{-0.29}$	$3.25^{+0.25}_{-0.24}$	$3.22^{+0.27}_{-0.25}$	$3.11^{+0.31}_{-0.31}$	$3.23^{+0.27}_{-0.26}$	$3.18^{+0.29}_{-0.31}$
$N_{\rm eff}$ $(D/H)_p$[178]	$3.47^{+0.35}_{-0.34}$	$3.56^{+0.34}_{-0.33}$	$3.52^{+0.33}_{-0.31}$	$3.52^{+0.27}_{-0.26}$	$3.52^{+0.33}_{-0.32}$	$3.48^{+0.35}_{-0.36}$	$3.57^{+0.34}_{-0.33}$	$3.49^{+0.36}_{-0.35}$

Table 6.4. 95% c.l. constraints on the sum of the neutrino masses, $\sum m_\nu$, in eV, and on the relativistic degrees of freedom $N_{\rm eff}$ from the different combinations of datasets explored here. When BBN bounds are included, the first (second) raw refers to the constraints obtained combining the primordial deuterium values from Ref. [11] (Ref. [178]) $(D/H)_p = (2.53 \pm 0.04) \times 10^{-5}$ $((D/H)_p = (2.87 \pm 0.22) \times 10^{-5})$ with measurements of the helium mass fraction $Y_p = 0.254 \pm 0.003$ from Ref. [170], [21]

.

on the neutrino masses are both mildly larger accordingly to the larger value of H_0 preferred by HST data. The Hubble constant H_0 and N_{eff} are positively correlated through measurements of the CMB, see Ref. [109] for a complete description of the effects of N_{eff} on the CMB. If the value of N_{eff} is increased, in order to keep fixed both the angular location of the acoustic peaks and the matter-to-radiation equality epoch (to leave unchanged the first peak height via the early ISW effect), the expansion rate is also increased, implying therefore a larger H_0 and a shorter age of the Universe at recombination.

Since HST measurements point to a higher H_0 value, a larger value of N_{eff} will be favoured by data, which also implies a higher neutrino mass bound due to the strong $\sum m_\nu - N_{\text{eff}}$ degeneracy. The 95% c.l. constraints from the combination of CMB data, BOSS DR11 BAO measurements and the HST H_0 prior are $\sum m_\nu < 0.34$ eV and $N_{\text{eff}} = 3.57^{+0.45}_{-0.48}$. Once the Hubble constant prior from the HST experiment is added in the analyses, there exists a very mild preference (2-σ) for a value of N_{eff} larger than the canonical expectation of 3.046, agreeing as well with the results of Ref. [5].

The addition of the measurements of the deuterium (either from older estimates, see Ref. [178], or from the most recent measurements from Ref. [11]) and the helium from Ref. [170] light element abundances, reduce both the mean value and the errors of N_{eff} significantly. After the addition of BBN bounds the errors on N_{eff} are reduced by a half. Table 6.4 contains the BBN constraints obtained using the fitting functions for the theoretical deuterium and helium primordial abundances, as a function of $\Omega_b h^2$ and N_{eff}, of Ref. [178] (extracted from the numerical results of the PArthENopE BBN code, Ref. [180]). We reported in the table exclusively these constraints because they are the most conservative ones: we found $\sum m_\nu < 0.24$ eV and $N_{\text{eff}} = 3.25^{+0.25}_{-0.24}$ at 95% c.l. from the analysis of CMB data, WiggleZ power spectrum measurements, the HST H_0 prior and BBN light elements abundances information (with the deuterium measurements from Ref. [11]). Notice that there is no evidence for $N_{\text{eff}} > 3$ when considering the most recent estimates of primordial deuterium abundances. However, if we consider instead previous measurements of deuterium, as those from Ref. [178], there exists a $3.5 - 4\sigma$ preference for $N_{\text{eff}} > 3$ if HST data is included in the analyses. Without the inclusion of HST data the preference for $N_{\text{eff}} > 3$ still persists, albeit at the $2.5 - 3\sigma$ c.l.. As previously stated, the BBN bounds on N_{eff} and $\sum m_\nu$ quoted in Tab. 6.4 are the most conservative ones we found. Different bounds are obtained if an alternative fitting function is used in order to compute the theoretical deuterium and helium primordial abundances. We performed as well such an exercise, using the fitting functions from Refs. [182, 11] and, in general, the mean value obtained for N_{eff} is larger than the constraints quoted above. In the case in which recent deuterium measurements are considered in the analysis, the mean value of N_{eff} is displaced by $\sim$2-σ with respect to the mean values obtained when using the fitting function of Ref. [178]. If previous deuterium measurements from Ref. [178] are used for our numerical analyses, the mean value of N_{eff} is also mildly larger than the mean N_{eff} values obtained when applying the fitting functions from Ref. [178]. The upper bound on the sum of the three active neutrino masses is also larger for the two analyses (with recent and previous deuterium measurements), due to the degeneracy between N_{eff} and $\sum m_\nu$. As an example, from the analysis of CMB data, WiggleZ power spectrum

measurements, the HST H_0 prior and BBN light elements abundances information (with recent deuterium measurements from Ref. [11]), our analysis point to the following values: $N_{\mathrm{eff}} = 3.47^{+0.27}_{-0.27}$ and $\sum m_\nu < 0.30$ eV, both at 95% c.l.. If previous measurements of deuterium are instead considered, Ref. [178], the 95% c.l. limits are $N_{\mathrm{eff}} = 3.60^{+0.33}_{-0.32}$ and $\sum m_\nu < 0.32$ eV. Therefore, a preference for $N_{\mathrm{eff}} > 3$ at the $3.5 - 4\sigma$ $(2.5 - 3\sigma)$ c.l. with (without) the HST H_0 prior included in the analyses will always be present in the results obtained with the fitting functions of Refs. [182, 11], independently of the deuterium measurements exploited.

As in the standard three massive neutrino case, the addition of the constraints on the σ_8 and Ω_m cosmological parameters from the CFHTLens survey displaces the bounds on the neutrino mass to higher values. When adding the $\sigma_8 - \Omega_m$ relationship from the Planck-SZ cluster catalog on galaxy number counts, a non zero value for the sum of the three active neutrino masses of ~ 0.35 eV is favoured at 4-σ. Notice that in this case the preferred mean value for $\sum m_\nu$ is higher than in the three massive neutrino case due to the fact that N_{eff} is a free parameter and there exists a large degeneracy among N_{eff} and $\sum m_\nu$. The combination of CMB data with BAO measurements from BOSS DR11, WiggleZ power spectrum (full shape) data and a prior on H_0 from HST after considering the inclusion of Planck SZ clusters information leads to the values $\sum m_\nu = 0.35^{+0.17}_{-0.16}$ eV and $N_{\mathrm{eff}} = 3.56^{+0.59}_{-0.58}$ at 95% c.l..

The bounds quoted above have been obtained using the BBN theoretical prediction for helium in the CMB data analysis. However, it is also possible to fix the helium fraction Y_{p} in the Monte Carlo Markov Chain analyses of CMB data and assume that Y_{p} is an independent parameter constrained by BBN observations only. We also performed such an exercise, fixing $Y_{\mathrm{p}} = 0.24$, and we found, in general, larger values for both the mean value of N_{eff} and its errors, and, consequently, a slightly larger bound on the neutrino mass, due to the $\sum m_\nu - N_{\mathrm{eff}}$ degeneracy. In particular, we found $\sum m_\nu < 0.32$ eV and $N_{\mathrm{eff}} = 3.60^{+0.67}_{-0.65}$ at 95% c.l. from the combination of CMB data and BOSS DR11 BAO measurements, and $\sum m_\nu < 0.34$ eV and $N_{\mathrm{eff}} = 3.84^{+0.60}_{-0.56}$ at 95% c.l. if a prior from HST on the Hubble constant H_0 is added to the former data combination. These findings agree with the results of Ref. [151], where it is also found that the BBN consistency relation leads to a constraint on N_{eff} closer to the canonical value of 3.046 than in the case of fixing $Y_{\mathrm{p}} = 0.24$. Once BBN measurements are considered in the data analyses, the differences between the analyses with and without the BBN consistency relation included become irrelevant.

Figure 6.5 shows the degeneracy between the $\sum m_\nu$ and the total number of dark radiation species N_{eff} (which accounts for the contribution of the three active neutrino species plus ΔN_{eff} massless sterile neutrino-like species). The red contours depict the 68% and 95% c.l. allowed regions resulting from the combination of CMB, BOSS DR11 BAO measurements, and previous BAO measurements. As the value of N_{eff} increases, a larger neutrino mass is allowed, to leave unchanged both the matter-to-radiation equality era and the angular location of the acoustic peaks, as well as the height of the first acoustic peak via the early ISW effect. The blue region denotes the results considering the HST H_0 prior as well in the analysis: notice that the allowed regions are shifted towards higher values of N_{eff}. Figure 6.6 illustrates the degeneracy between N_{eff} and the Hubble constant H_0. The color coding is identical to the one used in the Figure 6.5, in which the red contours are related to
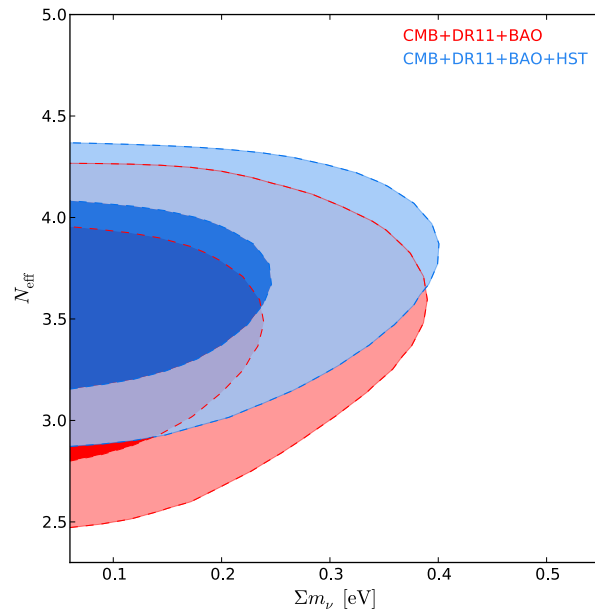
Figure 6.5. The red contours show the 68% and 95% c.l. allowed regions from the combination of CMB data, BOSS DR11 BAO measurements and additional BAO measurements in the ($\sum m_\nu$ (eV), N_{eff}) plane. The blue contours depict the constraints after a prior on the Hubble constant from HST is added in the analysis, [21].
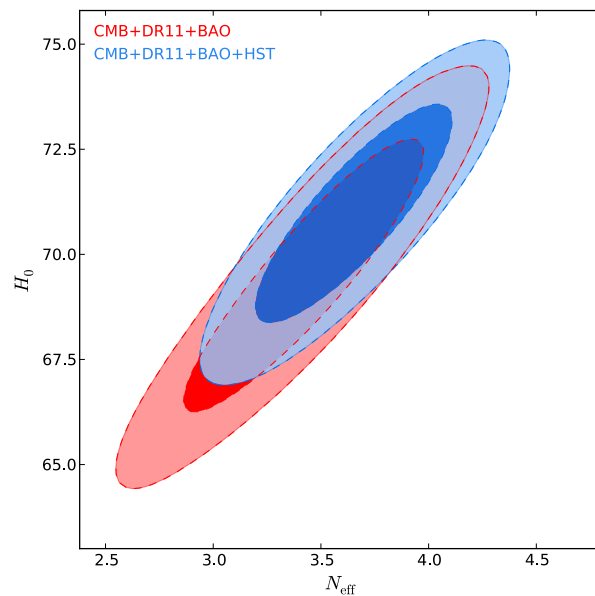
Figure 6.6. The red contours show the 68% and 95% c.l. allowed regions from the combination of CMB data, BOSS DR11 BAO measurements and additional BAO measurements in the (N_{eff}, H_0) plane. The blue contours depict the constraints after a prior on the Hubble constant from HST is added in the analysis, [21].

the 68% and 95% c.l. allowed regions from the combination of CMB data, BOSS DR11 BAO measurements and additional BAO measurements and the blue regions refer to the constraints after adding a prior on the Hubble constant from the HST experiment.

6.2.4   Massive neutrinos and extra massive sterile neutrino species

The latest possibility for thermal relics explored in our study is the case in which there exists three active light massive neutrinos plus one massive sterile neutrino species characterised by an effective mass m_s^{eff}, which reads, eq. (6.3):

$$m_s^{\text{eff}} = (T_s/T_\nu)^3 m_s = (\Delta N_{\text{eff}})^{3/4} m_s \ , \tag{6.10}$$

being T_s (T_ν) the current temperature of the sterile (active) neutrino species, $\Delta N_{\text{eff}} \equiv N_{\text{eff}} - 3.046 = (T_s/T_\nu)^3$ the effective number of degrees of freedom associated to the sterile, and m_s its real mass. We assumed an upper prior on the effective sterile neutrino mass m_s^{eff} of $3eV$, as specified in Table 6.1.

Table 6.5 depicts the 95% c.l. constraints on the active and sterile neutrino masses as well as on the total number of massive neutrinos N_{eff}. Notice that the mean value of N_{eff} is, in general, slightly larger than in the case in which the sterile neutrinos are considered as massless particles due to the fact that m_s^{eff} and N_{eff} are positively correlated. Indeed, there exists a physical lower prior for N_{eff} of 3.046 which is not needed in the case of three active neutrinos plus extra massless species. We quoted exclusively the 95% c.l. upper limit for the cases in which the 95% c.l. lower limit is set by the physical prior of 3.046. Concerning the bounds on the sum of the three active neutrinos, they are more stringent than in the massless sterile neutrino-like scenario because $\sum m_\nu$ and m_s^{eff} are also positively correlated. As in the massless sterile neutrino-like analyses, larger values of N_{eff} will be favoured by data when HST measurements are included. The addition of BBN bounds reduce the errors on N_{eff} significantly, alleviating the degeneracies between N_{eff} and the active/sterile neutrino masses. Table 6.5 contains the BBN constraints obtained using the fitting functions for the theoretical deuterium and helium primordial abundances from Ref. [178], which, as in the massless extra dark radiation case, are found to provide the most conservative bounds. We found $\sum m_\nu < 0.27$ eV, $m_s^{\text{eff}} < 0.14$ eV and $N_{\text{eff}} = 3.28^{+0.22}_{-0.21}$ at 95% c.l. from the analysis of CMB data, BOSS DR11 BAO, additional BAO measurements, WiggleZ full-shape large scale structure information, the HST H_0 prior and BBN light elements abundances information with the most recent measurements of the primordial deuterium abundances from Ref. [11], indicating no significant preference for $N_{\text{eff}} > 3$. However, when considering primordial deuterium measurements from Ref. [178], there exists a preference for $N_{\text{eff}} > 3$ at the 3-σ level (mildly stronger when HST data is also considered in the analyses). This preference is similar to that found in the extra massless case, although notice that in this case there exists a lower prior on $N_{\text{eff}} = 3.046$ and therefore the mean value of N_{eff} will always be larger than its standard prediction. If we instead use the theoretical functions for the helium and deuterium abundances from Refs. [182, 11], we got similar conclusions to those found in the massless dark radiation case: a $3 - 4\sigma$ preference for $N_{\text{eff}} > 3$ is always present. The bounds on the neutrino masses are, as in the massless case, mildly loosened. The constraints

	CMB+DR11	CMB+DR11 +HST	CMB+DR11 +WZ	CMB+DR11 +WZ+HST	CMB+DR11 +WZ+BAO+HST	CMB+DR11 +BAO	CMB+DR11 +BAO+HST	CMB+DR11 +BAO+SNLS
$\sum m_\nu$ [eV]	< 0.28	< 0.27	< 0.28	< 0.30	< 0.31	$< 0.30^{1}$	< 0.29	< 0.26
$m_s^{\rm eff}$ [eV]	< 0.29	< 0.28	< 0.60	< 0.28	< 0.25	$< 0.27^{1}$	< 0.28	< 0.31
$N_{\rm eff}$	< 4.01	$3.73^{+0.51}_{-0.51}$	< 3.89	< 4.06	$3.64^{+0.48}_{-0.48}$	$3.57^{+0.50\;1}_{-0.50}$	< 4.16	< 4.02
SZ Clusters& CFHTLens								
$\sum m_\nu$ [eV]	< 0.40	< 0.43	< 0.36	< 0.41	< 0.43	< 0.43	< 0.39	< 0.37
$m_s^{\rm eff}$ [eV]	< 0.50	< 0.48	< 1.37	< 0.39	< 0.34	< 0.49	< 0.59	< 0.59
$N_{\rm eff}$	< 3.90	$3.67^{+0.49}_{-0.55}$	< 3.77	< 4.08	$3.67^{+0.51}_{-0.45}$	$3.47^{+0.51}_{-0.39}$	< 4.01	< 3.85
SZ Clusters								
$\sum m_\nu$ [eV]	< 0.40	< 0.42	< 0.36	< 0.41	< 0.42	< 0.41	< 0.39	< 0.38
$m_s^{\rm eff}$ [eV]	< 0.49	< 0.48	< 1.36	< 0.39	< 0.34	< 0.49	< 0.53	< 0.59
$N_{\rm eff}$	< 3.90	$3.66^{+0.49}_{-0.55}$	< 3.77	< 4.06	$3.66^{+0.50}_{-0.45}$	$3.46^{+0.41}_{-0.38}$	< 4.02	< 3.85
CFHTLens								
$\sum m_\nu$ [eV]	< 0.35	< 0.33	< 0.32	< 0.35	< 0.35	< 0.39	< 0.34	< 0.31
$m_s^{\rm eff}$ [eV]	< 0.39	< 0.39	< 1.16	< 0.34	< 0.29	< 0.37	< 0.43	< 0.47
$N_{\rm eff}$	< 3.94	$3.68^{+0.51}_{-0.51}$	< 3.85	< 4.06	$3.63^{+0.49}_{-0.49}$	$3.50^{+0.48}_{-0.44}$	< 4.09	< 3.94
BBN								
$\sum m_\nu$ [eV] $(D/H)_p$[11]	< 0.28	< 0.23	< 0.25	< 0.24	< 0.27	< 0.39	< 0.24	< 0.23
$\sum m_\nu$ [eV] $(D/H)_p$[178]	< 0.27	< 0.25	< 0.28	< 0.28	< 0.28	< 0.29	< 0.26	< 0.25
$m_s^{\rm eff}$ [eV] $(D/H)_p$[11]	< 0.45	< 0.34	< 0.37	< 0.46	< 0.14	< 0.24	< 0.56	< 0.62
$m_s^{\rm eff}$ [eV] $(D/H)_p$[178]	< 0.27	< 0.25	< 0.29	< 0.24	< 0.23	< 0.27	< 0.26	< 0.27
$N_{\rm eff}$ $(D/H)_p$[11]	< 3.41	< 3.53	< 3.49	< 3.58	$3.28^{+0.22}_{-0.21}$	$3.25^{+0.17}_{-0.17}$	< 3.47	< 3.43
$N_{\rm eff}$ $(D/H)_p$[178]	$3.48^{+0.37}_{-0.35}$	$3.59^{+0.35}_{-0.34}$	$3.45^{+0.33}_{-0.38}$	$3.56^{+0.34}_{-0.34}$	$3.56^{+0.33}_{-0.32}$	$3.50^{+0.35}_{-0.36}$	$3.59^{+0.35}_{-0.45}$	$3.50^{+0.36}_{-0.37}$

Table 6.5. 95% c.l. constraints on the active (sterile) neutrino masses, $\sum m_\nu$ ($m_s^{\rm eff}$), in eV, and on the total number of massive neutrino species, $N_{\rm eff}$, from the different combinations of datasets explored here. When BBN bounds are included, the first (second) raw refers to the constraints obtained combining the primordial deuterium values from Ref. [11] (Ref. [178]) $(D/H)_p = (2.53 \pm 0.04) \times 10^{-5}$ $((D/H)_p = (2.87 \pm 0.22) \times 10^{-5})$ with measurements of the helium mass fraction $Y_p = 0.254 \pm 0.003$ from Ref. [170].

---

[a]These limits have been obtained by imposing an additional prior on the thermal velocity of sterile neutrinos. See discussion in the text for further details.

quoted above translate into $\sum m_\nu < 0.28$ eV, $m_s^{\text{eff}} < 0.22$ eV and $N_{\text{eff}} = 3.50^{+0.27}_{-0.28}$ ($\sum m_\nu < 0.30$ eV, $m_s^{\text{eff}} < 0.24$ eV and $N_{\text{eff}} = 3.64^{+0.33}_{-0.33}$) at 95% c.l. from the analysis of CMB data, BOSS DR11 BAO, additional BAO measurements, WiggleZ full-shape large scale structure information, the HST H_0 prior and BBN light elements abundances information with the most recent measurements of the primordial deuterium abundances from Ref. [11] (Ref. [178]).

We have also found that the posterior distribution obtained from the CMB+DR11+BAO dataset (without the addition of any BBN or σ_8 information) is multimodal. In fact, we found that the probability density is significantly different from zero, other than for $m_{\text{eff}} \lesssim 0.3$ eV (as for the other datasates), also for $m_{\text{eff}} \gtrsim 1$ eV. A further inspection of the chains has shown that these two regions roughly corresponds to the two cases of a hot/warm (at recombination) sterile neutrino, with a mass-to-temperature ratio at that time $m_s/T_{s,\text{rec}} \lesssim 10$, and of a cold sterile with $m_s/T_{s,\text{rec}} \gtrsim 100$. The limits quoted in Tab. 6.5 for the CMB+DR11+BAO dataset, in the basic case where no other information is considered, have been obtained by postprocessing the chains in order to keep only those models with $m_s/T_{s,\text{rec}} \lesssim 10$. This is consistent with the purpose of the paper [21] of costraining the presence of a hot component in addition to active neutrinos. We also verified that these limits are reasonably stable with respect to the choice of the value of the mass-to-temperature ratio at which to cut the distribution, as long as this value lies inside the low-probability region $10 \lesssim m_s/T_{s,\text{rec}} \lesssim 100$. It still has to be clarified which, if any in particular, of the BAO datasets is responsible for the appearance of the *cold sterile* region in the posterior probability, and to which feature in the data this is possibly related. A very preliminar analysis, performed using only one at a time among the DR7, 6dF and WiggleZ BAO datasets, seems to show that this effect is mainly driven by the first two datasets, while using only the WiggleZ BAO measurements yields naturally an upper limit for m_{eff} of about 0.3 eV, without any need to exclude a priori the cold region.

Contrarily to the massless dark radiation case (and similarly to the thermal axion scenario), the addition of the constraints on the σ_8 and Ω_m cosmological parameters from the Planck-SZ cluster catalog on galaxy number counts does not lead to a non zero value for the neutrino masses. However, the bounds on the neutrino masses are less stringent when adding the Planck-SZ or the CFHTLens constraints on the σ_8 and Ω_m cosmological parameters, due to the lower σ_8 preferred by the former datasets, which favours higher values for the thermal relic masses. After considering the inclusion of Planck SZ clusters and CFHTLens information to CMB data, BOSS DR11 BAO and additional BAO measurements and the HST H_0 prior, the 95% c.l. bounds on the active and the sterile neutrino parameters are $\sum m_\nu < 0.39$ eV, $m_s^{\text{eff}} < 0.59$ eV and $N_{\text{eff}} < 4.01$.

The bounds quoted in Tab. 6.5 have been obtained using the BBN theoretical prediction for helium in the CMB data analysis, as in the case of extra massless species. We also performed in this massive case the exercise of fixing the helium fraction Y_{p} in the Monte Carlo Markov Chain analyses of CMB data and assumed that Y_{p} is an independent parameter constrained by BBN observations only. Again, as in the massless case, we found larger values for the mean value of N_{eff} (and, consequently, slightly larger bounds on both the active and sterile neutrino masses) when neglecting the BBN consistency relation in the MCMC analyses.
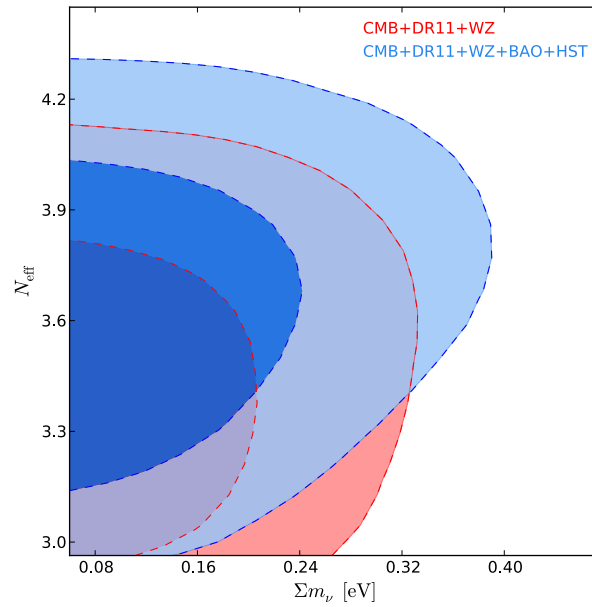
Figure 6.7. The red contours show the 68% and 95% c.l. allowed regions from the combination of CMB data, BOSS DR11 BAO measurements and WiggleZ full shape power spectrum measurements in the $(\sum m_\nu$ (eV)$, N_{\rm eff})$ plane. The blue contours depict the constraints after a prior on the Hubble constant from HST and the remaining BAO data are added in the analysis, [21].
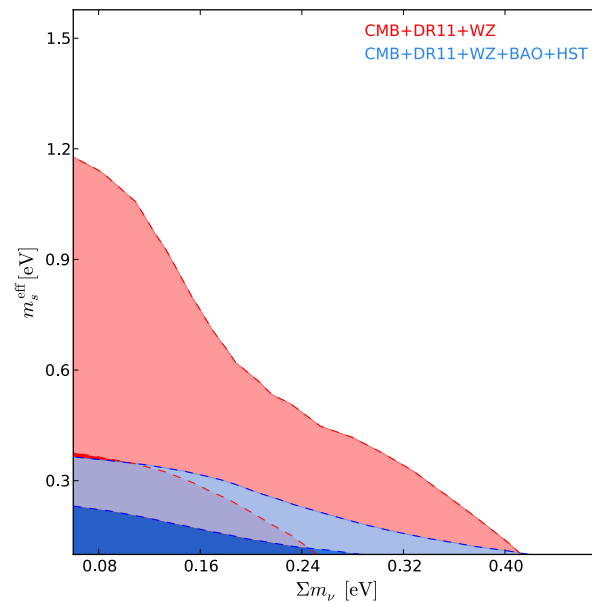
Figure 6.8. The red contours show the 68% and 95% c.l. allowed regions from the combination of CMB data, BOSS DR11 BAO measurements and WiggleZ full shape power spectrum measurements in the $(\sum m_\nu$ (eV)$, m_s^{\rm eff}$ (eV)$)$ plane. The blue contours depict the constraints after a prior on the Hubble constant from HST and the remaining BAO data are added in the analysis, [21].

Figure 6.7 shows the degeneracy between the $\sum m_\nu$ and the total number of neutrino species $N_{\rm eff}$ (which accounts for the contribution of the three active neutrino species plus $\Delta N_{\rm eff}$ massive sterile neutrinos). The red contours depict the 68% and 95% c.l. allowed regions resulting from the combination of CMB, BOSS DR11 BAO measurements, and full shape power spectrum measurements from the WiggleZ survey. Notice that the allowed values of $N_{\rm eff}$ are slightly larger than in the massless dark radiation scenario, since sub-eV massive sterile neutrinos are contributing to the matter energy density at the recombination period and therefore a larger value of $N_{\rm eff}$ will be required to leave unchanged both the angular location and the height of the first acoustic peak. The blue region depicts the results considering both the HST H_0 prior and the remaining BAO data as well in the analysis. The Figure 6.8, illustrates the degeneracy between the active and the sterile neutrino masses, since both active and sterile sub-eV massive neutrinos contribute to the matter energy density at decoupling, and both are free streaming relics which suppress structure formation at small scales, after they become non relativistic.

6.3   CMB constraints including the results from the BICEP2 experiment
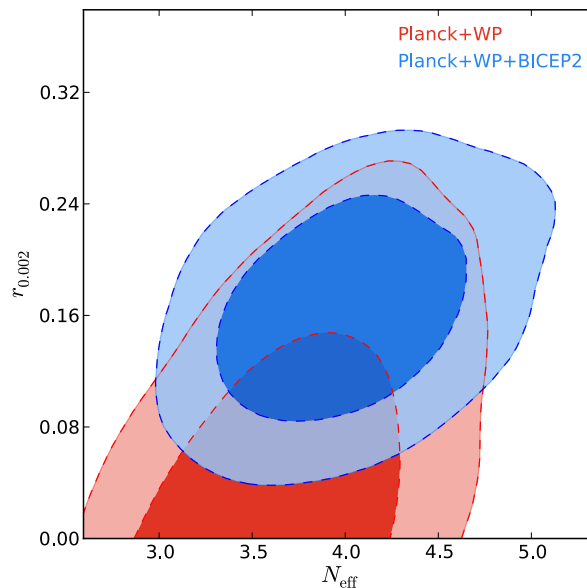
Figure 6.9. Constraints in the $N_{\rm eff}$ vs r plane from Planck+WP and Planck+WP+BICEP2 data. Notice how the inclusion of the BICEP2 constraint shifts the contours towards $N_{\rm eff} > 3$, [21].

The BICEP2 experiment, Ref. [10], claimed a detection at about $5.9 - \sigma$ for B-mode polarization on large angular scales[4], compatible with the presence of a tensor

---

[4]This claim has been recently questioned by the Planck collaboration, see Ref. [**?**], since this signal could be completely explained by a polarization signal from galactic dust. This point is discussed in the chapter 10.
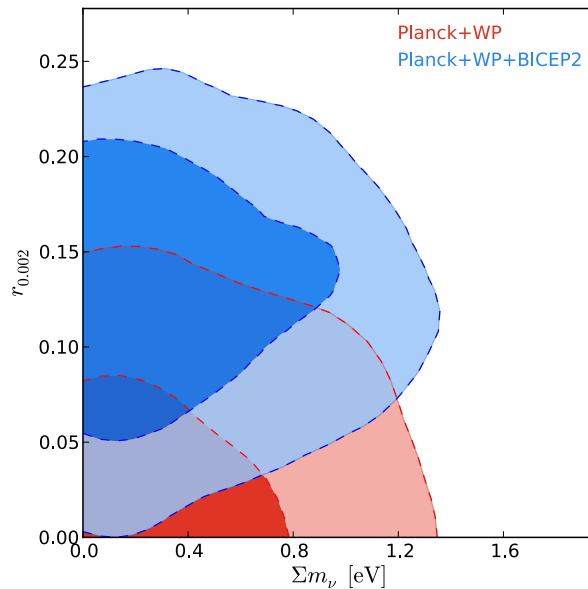
Figure 6.10.   Constraints in the Σm_ν vs r plane from Planck+WP and Planck+WP+BICEP2 data. In this case there is no indication for neutrino masses from the combination of CMB data, [21].

component with amplitude $r_{0.002} = 0.2^{+0.06}_{-0.05}$ at 68% c.l.. It is therefore interesting to evaluate the impact of this measurement for the effective number of relativistic species and neutrino masses. We therefore performed an analysis including a tensor component (with zero running). The results are presented in Figures 6.9 and 10.2. As we can see, when the BICEP2 data are included, an extra background of relativistic particle is preferred with $N_{\text{eff}} = 4.00 \pm 0.41$ at 68% c.l., where N_{eff} is the number of massless, dark radiation species. CMB data alone is therefore suggesting a value for $N_{\text{eff}} > 3$ at good significance. This result comes from the apparent tension between the Planck+WP limit of $r < 0.11$ at 95% c.l. and the recent BICEP2 result. This tension appears as less evident when extra relativistic particles are included. We imagine a further preference for $N_{\text{eff}} > 3$ if the HST data is included. The BICEP2 result does not affect the current constraints on neutrino masses as we can see from the Figure 10.2.

In conclusion, in this chapter (but see also Ref. [21]) we have reported the constraints on the masses of the different thermal relics in different scenarios using the available cosmological data in the beginning of year 2014. The tightest limit we found in the minimal three active massive neutrino scenario is $\sum m_\nu < 0.22$ eV at 95% CL from the combination of CMB data, BAO data and HST measurements of the Hubble constant. However, the constraint on σ_8 and Ω_m from the Planck-SZ cluster catalog on galaxy number counts favours a non zero value for the sum of the three active neutrino masses of ~ 0.3 eV at $4 - \sigma$, see also Refs. [166, 167].

Chapter 7

Constraining Neutrino Isocurvature Perturbations with CMB anisotropies

As briefly described in the previous chapter, the standard model of inflation postulates the existence of a single scalar field responsible for driving an accelerated expansion of the Universe and for generating a nearly scale invariant background of primordial perturbations. This class of inflationary models has only one degree of freedom, predicting that the ratio between the number densities of the different particle species is spatially homogeneous, which means adiabatic perturbations and excludes the presence of significant non-Gaussianities in the fluctuations.

Though the recent measurements of the Cosmic Microwave Background anisotropies provided by the Planck experiment (see e.g. Ref. [5]) are perfectly consistent with purely adiabatic and Gaussian primordial perturbations, the presence of a significant, sub-dominant, non-adiabatic perturbation component in the cosmological fluids (cold dark matter, baryons and neutrinos) cannot be completely excluded, see e.g. Refs. [183, 184, 185, 186, 187, 92]. This *isocurvature* component could be produced from some extra field other than the Inflaton ϕ, as in multifield inflationary models. It is indeed possible (see, for example, Refs. [188, 189]) that, while the Inflaton drives the exponential expansion, the primordial fluctuations could be generated by a different field named *Curvaton*. After the Inflaton decay, the isocurvature perturbation produced initially by the Curvaton is converted in an adiabatic component. After the Curvaton decay, some residual isocurvature perturbation is therefore expected in the energy density of the different cosmological components. In particular, in this chapter, we study the presence of isocurvature perturbations in the neutrino component. Indeed, if there are neutrino isocurvature perturbations, then we may have a non vanishing chemical potential for their background distribution in phase space. Probing neutrino isocurvature density perturbation (NID), in the Curvaton scenario is therefore complementary to constraining the lepton number in the neutrino sector.

The results presented in this chapter are mainly taken from two refereed papers. First of all, in Ref. [22] we have forecasted, using Fisher matrix techniques, the capability of present and future CMB experiments like Planck, see Refs. [190, 191], SPIDER, see Ref. [192], and CMBPol, see Ref. [193], to constrain simultaneously

the amplitude of isocurvature perturbations in the neutrino density component and the extra energy density associated to the neutrino chemical potential. These bounds can then be translated into constraints on the neutrino chemical potential to temperature ratio ξ_i ($i = e, \mu, \tau$) and the corresponding perturbation amplitudes, and can be compared to those on the ξ_i's which can be derived using Big Bang Nucleosynthesis (BBN).

On the other hand, we have presented in Ref. [23], for the first time, a combined analysis for N_{eff} and NID from the recent Planck data.

7.1 Neutrino isocurvature perturbations

We can describe the density perturbations in terms of the gauge-invariant quantity ζ, see Refs. [194, 195, 196] in this way:

$$\zeta = -\psi - H\frac{\delta\rho}{\dot{\rho}}, \tag{7.1}$$

where again ψ is the (gauge-dependent) curvature perturbation, H the Hubble parameter, ρ the total energy density, and the dot denotes derivatives with respect to the cosmological time t. The quantity ζ describes the curvature perturbation on slices of uniform total density.

In the case of multicomponent fluids it is possible to define the quantities ζ_i for each of the i-th energy component

$$\zeta_i = -\psi - H\frac{\delta\rho_i}{\dot{\rho}_i}. \tag{7.2}$$

We have an adiabatic fluctuation if the ratios $\delta\rho_i/\dot{\rho}_i$ are all the same, so that $\zeta_i = \zeta$ for all components. Otherwise, we can define an isocurvature fluctuation S_i in the i-th fluid component as the relative entropy fluctuation with respect to photons:

$$S_i \equiv 3(\zeta_i - \zeta_\gamma). \tag{7.3}$$

We remind that the equilibrium distribution function of neutrinos is:

$$f_i(E) = [\exp(E/T_\nu \mp \xi_i)]^{-1}, \tag{7.4}$$

where T_ν is their temperature, and $\xi_i = \mu_i/T_\nu$, μ_i being the chemical potential. Moreover, we considered the three standard model neutrino families, $i = e, \mu, \tau$, and the minus (plus) signs for neutrinos (antineutrinos). If there are neutrino isocurvature perturbations, necessarily we have a non zero lepton asymmetry in the neutrino sector, $n_L \equiv n_\nu - n_{\bar{\nu}}$, unless the asymmetries in the three flavours exactly cancel. At this stage, the three neutrino families can have different chemical potentials. As we said in the first chapter, the neutrino temperature is $T_\nu = T_\gamma$ until the time of electron-positron annihilation, $T_\gamma \simeq 1 MeV$ (shortly after neutrino decoupling), while at later times $T_\nu = (4/11)^{1/3}T_\gamma$, unless tiny corrections, see Ref. [19].

We can write the energy density $\rho_i \equiv \rho_{\nu_i} + \rho_{\bar{\nu}_i}$ in the high-temperature limit $T_\nu \gg m_\nu$, given the distribution function eq. 7.4, in this way, see Ref. [197]:

$$\rho_i = \frac{7\pi^2}{120} A_i T_\nu^4 = \frac{7}{8} A_i \left(\frac{T_\nu}{T_\gamma} \right)^4 \rho_\gamma \, , \tag{7.5}$$

where

$$A_i \equiv \left[1 + \frac{30}{7} \left(\frac{\xi_i}{\pi} \right)^2 + \frac{15}{7} \left(\frac{\xi_i}{\pi} \right)^4 \right] \, , \tag{7.6}$$

As we saw, we can define the effective number of neutrino families N_{eff} as the ratio between the total neutrino density and the density of a single non-degenerate ($\xi = 0$) neutrino species in thermal equilibrium at $T_\nu = (4/11)^{1/3} T_\gamma$. In the standard cosmological scenario we expect $N_{\text{eff}} = 3.046$, see Ref. [19], and any deviation ΔN_{eff} from this value means the presence of an extra energy density of relativistic particles in the early Universe (dark radiation). From our definition we have that $N_{\text{eff}} = \sum_i A_i + 0.046$. In this way, We can relate the isocurvature perturbation in the total neutrino density to the fluctuations $\delta N_{\text{eff}}^{(i)}$:

$$S_\nu = 3(\zeta_\nu - \zeta_\gamma) \simeq \frac{\sum_i \delta N_{\text{eff}}^{(i)}}{4 N_{\text{eff}}}. \tag{7.7}$$

7.2   CMB forecasts

We assume for semplicity that both the average values and the fluctuations in the chemical potentials are flavor blind, i.e. $\bar{\xi}_e = \bar{\xi}_\mu = \bar{\xi}_\tau = \bar{\xi}$, and similarly $\delta\xi_e = \delta\xi_\mu = \delta\xi_\tau = \delta\xi$. Moreover, we assume that fluctuations in the neutrino degeneracy parameter are Gaussian distributed with variance σ_ξ^2 around the mean $\bar{\xi}$, and in general, both can have a scale and epoch dependence.

Conventionally, in the CMB studies the "non-adiabaticity" of perturbations is parameterized from two quantities, α and β. In particular, we define, see Refs. [186, 92], the quantity α in the following:

$$\frac{\alpha(k_0)}{1 - \alpha(k_0)} \equiv \frac{P_S(k_0)}{P_\zeta(k_0)} \, , \tag{7.8}$$

where $P_S(k)$ is the power spectrum of isocurvature perturbations and $P_\zeta(k)$ the curvature perturbations spectrum, both evaluated at a fixed pivot wave number $k_0 = 0.002 \, \text{Mpc}^{-1}$. Then the cross-correlation coefficient β is defined as:

$$\beta = \frac{P_{\zeta S}(k_0)}{\sqrt{P_S(k_0) P_\zeta(k_0)}} \, . \tag{7.9}$$

where $P_{\zeta S}(k)$ is the cross-correlation power spectrum. This parameter takes into account the correlation between the adiabatic and isocurvature modes, see Refs. [198, 199, 200]. We choosed the sign convention for the curvature perturbation such that the temperature fluctuation at large scales is given by $\Delta T/T = \zeta/5 - 2S/5$. Given the above convention, the physically observable effect is that correlated perturbations, i.e. $\beta > 0$, reduce the temperature power spectrum at low multipoles,

and the adiabatic and isocurvature fluctuations in the Curvaton scenario are totally anticorrelated, see Refs. [201, 202, 203], i.e. $\beta = -1$.

Moreover, we assume that the two power spectra have the the same spectral tilt n_s:

$$\Delta^2_{\mathcal{R},S}(k) \equiv \frac{k^3 P_{\mathcal{R},S}}{2\pi^2} \propto k^{n_s-1}. \tag{7.10}$$

The CMB is sensitive to both α and the total ΔN_{eff} induced by the average value $\bar{\xi}$ for this scenario, and in principle also by the variance σ^2_ξ, if sufficiently large. For our analyses or forecasts, we considered the constraints in the $\Delta N_{\text{eff}} - \alpha$ plane.

The total CMB power spectrum is conventionally parameterized as the sum of the adiabatic, the neutrino isocurvature density and the totally anticorrelated spectra in this way:

$$C_l = (1 - \alpha)C_l^{ad} + \alpha C_l^{NID} - 2\sqrt{\alpha(1-\alpha)}C_l^{corr}, \tag{7.11}$$

with α defined in eq. 7.8, we considered $\beta = -1$.

In Ref. [22] we derived forecasts for the Planck, Ref. [190], SPIDER, Ref. [192], and the CMBPol, Ref. [193], experiments. The Planck satellite, Refs. [190, 191], launched in May 2009, measured the CMB temperature and polarization fluctuations with unprecedented precision ($\Delta T/T \sim 2 \times 10^{-6}$) over the whole sky and down to very small angular scales ($\sim$5'). Planck temperature measurements have been released to the scientific community in March 2013, and significantly improved the determination of cosmological parameters allowing to furher test the ΛCDM paradigm. However, we first present a forecast for this experiment, also to provide a test of method when comparing with the real data in the next section. SPIDER, Ref. [192], scheduled to flight in 2015, is a ballon-borne polarimeter design to accurately measure the B-mode of CMB polarization down to $l \sim 100$. Finally, CMBPol, Ref. [193], is a next-generation satellite currently in the concept study phase.

In order to derive forecasts for these experiments (see Ref. [22]), we used a Fisher matrix formalism, assuming three frequency channels for each experiment (the adopted experimental specifications are listed in Table 7.1).

Experiment	Channel[GHz]	FWHM	$\sigma_T[\mu K]$	$\sigma_P[\mu K]$
Planck	217	5.0'	13.1	18.5
$f_{sky} = 0.65$	143	7.0'	5.99	8.48
	100	9.5'	6.75	9.55
SPIDER	280	17'	0.20	0.29
$f_{sky} = 0.1$	150	30'	0.08	0.11
	90	49'	0.08	0.11
CMBPol	220	3.8'	0.66	0.93
$f_{sky} = 0.65$	150	5.6'	0.25	0.35
	100	8.4'	0.22	0.31

Table 7.1. Experimental specifications for Planck, Ref. [190], SPIDER, Ref. [192], and CMBPol, Ref. [193], used in our analysis. For each experiment, we listed the observed fraction f_{sky} of the sky, the channel frequency in GHz, the FWHM in arcminutes, the sensitivity per pixel for the Stokes I (σ_T), Q and U (σ_P) parameters in μK.

In general the Fisher matrix is defined as follows

$$F_{ij} \equiv \left\langle -\frac{\partial^2 \ln \mathcal{L}}{\partial p_i \partial p_j} \right\rangle_{p_0}, \tag{7.12}$$

where $\mathcal{L}(\text{data}|\mathbf{p})$ is the likelihood function of a set of parameters $\mathbf{p}$ given some data; the partial derivatives and the averaging are evaluated using the fiducial values of the parameters $\mathbf{p_0}$. Since the Cramér-Rao inequality implies that $(F^{-1})_{ii}$ is the smallest variance in the parameter p_i, we can think of F^{-1} as the best possible covariance matrix for estimates of the vector $\mathbf{p}$. The 1-σ error for each parameter is given by:

$$\sigma_{p_i} = \sqrt{(F^{-1})_{ii}}. \tag{7.13}$$

The Fisher matrix for a CMB experiment is then written as follows (see Ref. [204]):

$$F_{ij}^{\text{CMB}} = \sum_{l=2}^{l_{\max}} \frac{\partial C_l}{\partial p_i} (\text{Cov}_l)^{-1} \frac{\partial C_l}{\partial p_i}, \tag{7.14}$$

where Cov_l is the spectra covariance matrix. We used information in the power spectra up to $l_{\max} = 2500$.

We considered a detector noise of $(\theta\sigma)^2$ for each frequency channel, with θ the FWHM of the beam assuming a Gaussian profile and σ the sensitivity. We added to each fiducial spectrum C_l, calculated with CAMB, Ref. [27], the noise spectrum:

$$N_l = (\theta\sigma)^2 \, e^{l(l+1)/l_b^2}, \tag{7.15}$$

where $l_b \equiv \sqrt{8 \ln 2}/\theta$. In our analysis, we assumed that the statistical errors are greater than beam and foreground uncertainties.

In order to use the Fisher matrix formalism, we need to compute the partial derivative of the total power spectrum, eq. (7.11), $\frac{\partial C_l}{\partial \alpha}$, that diverges for $\alpha = 0$. This problem prevents the use of the Fisher matrix formalism for the fiducial value $\alpha = 0$. In order to solve them, we find convenient to introduce the auxiliary parameter $\gamma = \sqrt{\alpha}$, rewriting the total power spectrum, eq. (7.11), as:

$$C_l = (1 - \gamma^2)C_l^{ad} + \gamma^2 C_l^{NID} - 2\gamma\sqrt{(1-\gamma^2)}C_l^{corr}. \tag{7.16}$$

With our notation, the partial derivative $\frac{\partial C_l}{\partial \gamma}$ is analytical in $\gamma = 0$, as we can see in the following:

$$\frac{\partial C_l}{\partial \gamma} \equiv (-2\gamma)C_l^{ad} + 2\gamma C_l^{NID} - \frac{2(1-2\gamma^2)}{\sqrt{(1-\gamma^2)}}C_l^{corr}. \tag{7.17}$$

Then the parameterization in terms of γ, instead of $\alpha = \gamma^2$ as often seen in the literature, cancels the divergence of the partial derivative $\frac{\partial C_l}{\partial \alpha}$ in $\alpha = 0$, allowing us to use the Fisher matrix formalism for the fiducial value $\gamma = 0$.

In the analysis we fix as fiducial model a flat ΛCDM model with parameter values given by the WMAP7 measurements, Ref. [205], i.e. $\Omega_b h^2 = 0.02258$ and $\Omega_{dm} h^2 = 0.1109$, the optical depth to reionization $\tau = 0.088$, $H_0 = 71 \, \text{km/s/Mpc}$,

the spectral index $n_s = 0.963$, and the amplitude of the curvature perturbation $\Delta_{\mathcal{R}}^2(k_0) = 2.43 \times 10^{-9}$. We consider three families of massless neutrinos, but checking that to take massive neutrinos with total mass $M_\nu = 0.6 eV$ neutrinos did not affect the results. Moreover, we used the fiducial values $\Delta N_{\text{eff}} = 0$, $\gamma = 0$.

The results of our analysis are shown in Figure 11.20, where we draw the 2-dimensional likelihood in the ΔN_{eff}-γ plane for Planck, SPIDER and CMBPol. We report the corresponding 1-σ constraints for γ and ΔN_{eff} in Tab. 7.2.
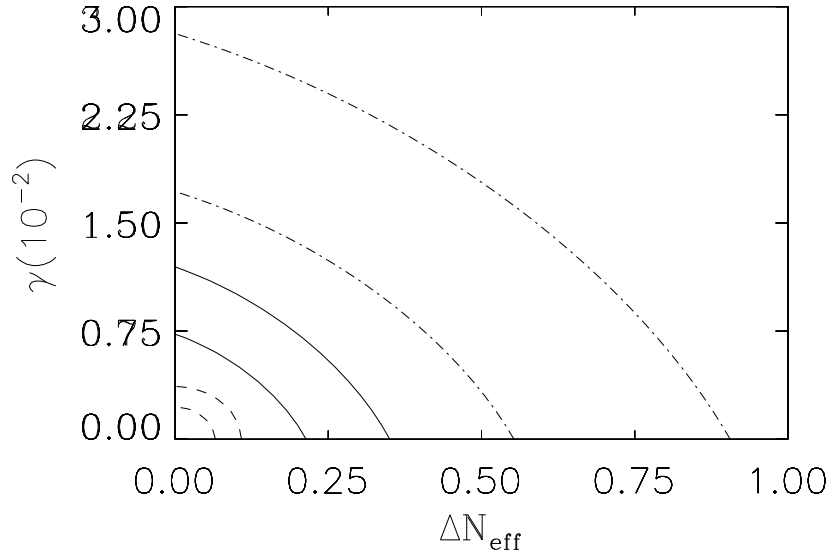
Figure 7.1. The 68% and 95% c.l. likelihood contours for Planck (solid line), SPIDER (dot-dashed line) CMBPol (dashed line), see also Ref. [22].

	fiducial value	$\sigma(\text{Planck})$	$\sigma(\text{SPIDER})$	$\sigma(\text{CMBPol})$
γ	0.0	$5.3 \cdot 10^{-3}$	$1.2 \cdot 10^{-2}$	$1.5 \cdot 10^{-3}$
ΔN_{eff}	0.0	0.16	0.40	0.043

Table 7.2. The 1-σ constraints for γ and ΔN_{eff}, for the Planck, SPIDER and CMBPol experiments,[22].

7.3 Comparison of forecasts with BBN constraints

Big Bang Nucleosynthesis, and in particular the primordial helium abundance Y_{p}, is recognized to be the most sensitive cosmic "leptometer" presently available, see for example Refs. [206, 207] or the review [178]. However, to compare BBN constraints to the CMB bounds is non-trivial, because the BBN is sensitive to different parameters than the CMB.

In this case, which assumes flavour-independent parameters and Gaussian distributions, the only two independent parameters are $\bar{\xi}$ and σ_ξ, with $\Delta N_{\rm eff}$ fully specified in terms of them, but essentially negligible for the values $\bar{\xi} \ll 1$ of interest here. Even assuming that the average value $\bar{\xi}$ is scale-independent, in any way we expect a slight dependence on the scale for the width of the distribution of fluctuations.

We fixed (arbitrarily) σ_ξ at a scale $\lambda_{\rm BBN}$, that roughly corresponds to the horizon size at the time of BBN, of the order of $\sim \mathcal{O}(100)$ comoving parsecs. This means to fix $\sigma_\xi^2 \sim \Delta_\xi^2(k_{\rm BBN})$ where $k_{\rm BBN} = 2\pi/\lambda_{\rm BBN} \equiv 6 \times 10^4 \, {\rm Mpc}^{-1}$. The CMB constraints can be expressed into σ_ξ^2 by just evaluating $\Delta_\zeta^2(k_{\rm BBN})$ (given that Δ_S^2 has the same scale-dependence). We used WMAP7 best fit values $\Delta_\zeta^2(k = 0.002 \, {\rm Mpc}^{-1}) = 2.42 \times 10^{-9}$ and $n_s = 0.966$ gives $\Delta_\zeta^2(k_{\rm BBN}) = 1.35 \times 10^{-9}$. A first important consequence of the CMB constraints on α is that their holds for BBN-relevant fluctuations, that means that σ_ξ is very small.

This allows us to use the predictions of the homogeneous, degenerate BBN to infer the results of an *inhomogeneous* degenerate BBN scenario (see Ref. [208] for an early study of this subject). Indeed, for a Gaussian probability distribution for ξ:

$$P(\xi) = (2\pi\sigma_\xi^2)^{-1/2} \exp\left[-(\xi - \bar{\xi})^2/(2\,\sigma_\xi^2)\right], \tag{7.18}$$

we can estimate, for a generic nuclide abundance X:

$$\langle X \rangle = \int P(\xi)[X(\bar{\xi}) + X'(\bar{\xi})(\xi - \bar{\xi}) + \mathcal{O}((\xi - \bar{\xi})^2)]d\xi = X(\bar{\xi}) + \mathcal{O}(\sigma_\xi^2). \tag{7.19}$$

Since $P(\xi)$ is an even function of $\xi - \bar{\xi}$, the integrand linear in ξ vanishes. We estimated that even for a value as large as $\sigma_\xi \simeq 0.1$, the error of the approximation with respect to a proper averaging is of order of about $\sim 0.6\%$ for deuterium, or of the order of 0.3% for helium-4, either well below the errors on the observations. Since σ_ξ scales as σ_ξ^2, smaller values become soon negligible. The result is that we can use the bounds computed in the homogeneous, degenerate BBN to an excellent approximation for the case at hand. Moreover, this also implies that, while BBN may give excellent constraints on $\bar{\xi}$, it is insensitive to physically relevant values of the fluctuation σ_ξ.

By using the same conservative input as in Ref. [209] (fourth line in their Table I), we obtain the following bounds:

$$\bar{\xi}^{\rm min} = -0.055, \tag{7.20}$$

$$\bar{\xi}^{\rm max} = 0.12\,, \tag{7.21}$$

corresponding respectively to the value below and above which only 5% of the area of the marginalized distribution of probability of ξ lies. The BBN values are obtained with the PArthENoPE code, Ref. [180].

In order to compare BBN and CMB, we expressed the CMB forecasts in the $\bar{\xi} - \sigma_\xi$ plane. We can write the relationship between variables in the assumptions of $\delta\xi \ll 1$ and $\delta\xi \ll \bar{\xi}$. The relation between the power spectrum of the isocurvature perturbation S_ν to that of ξ is

$$S_\nu = \frac{3}{\pi} \frac{\frac{\bar{\xi}}{\pi} + \frac{\bar{\xi}^3}{\pi^3}}{\frac{7}{15} + \frac{2\bar{\xi}^2}{\pi^2} + \frac{\bar{\xi}^4}{\pi^4}} \delta\xi \equiv F(\bar{\xi})\delta\xi \,. \tag{7.22}$$

This relation implies that $\Delta_S^2 = F(\bar{\xi})^2 \Delta_\xi^2$, so that

$$\Delta_S^2(k_{\mathrm{BBN}}) = F(\bar{\xi})^2 \sigma_\xi^2 \Rightarrow \alpha \simeq 7.4 \times 10^8 F(\bar{\xi})^2 \sigma_\xi^2 \,, \tag{7.23}$$

where we have taken into account that the data constrain on α is $\mathcal{O}(0.01)$ or less. Since $\gamma = \sqrt{\alpha}$, we found:

$$\gamma \simeq 2.7 \times 10^4 F(\bar{\xi})\sigma_\xi \,. \tag{7.24}$$
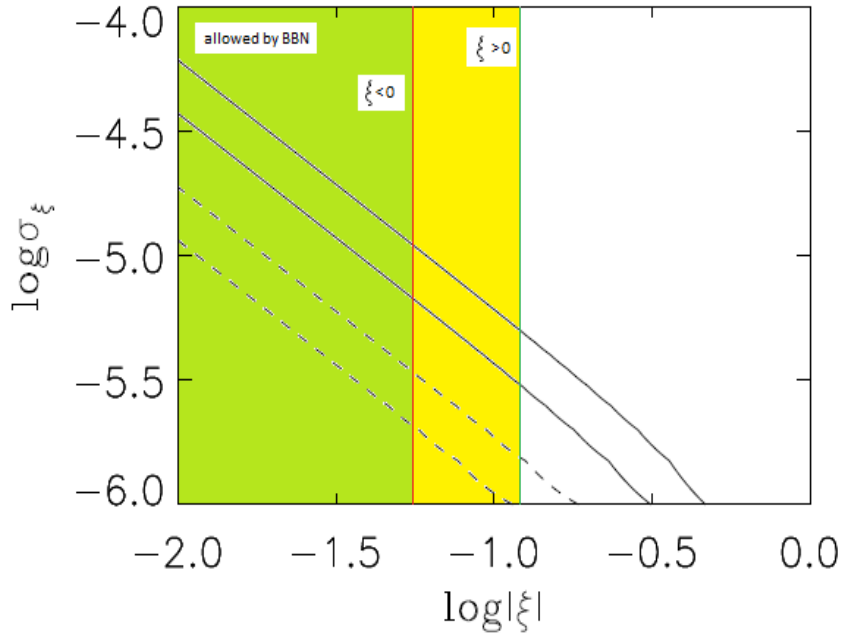
Figure 7.2. The 68% and 95% c.l. likelihood contours in the $(\log|\bar{\xi}|, \log\sigma_\xi)$ plane for Planck (solid line) and CMBPol (dashed line). The BBN allowed region, corresponding to the case considered in eq. (7.21), is that to left of vertical lines,[22].

On the other hand, because $N_{\mathrm{eff}} = \sum A_i$, with A_i given by eq. (7.6), we translated the bounds from the $(\gamma, \Delta N_{\mathrm{eff}})$ plane to the $(\bar{\xi}, \sigma_\xi)$ plane. In this case, we only considered Planck and CMBPol since they give the better constraints on the parameters. The two-dimensional 68% and 95% confidence regions for Planck and CMBPol are reported in Fig. 7.2, along with the present BBN constraints on $\bar{\xi}$ reported in eq. (7.21).

In conclusion, we found that, assuming a fiducial model with purely adiabatic primordial fluctuations, these experiments can sensibly improve the CMB constraints on the non-adiabaticity parameter γ and on the effective number of neutrino families ΔN_{eff}, but are still unable to compete with BBN in this respect, which is the only one sensitive to *the sign* of $\bar{\xi}$.

7.4   Planck data analysis

The recent Planck measurements of the Cosmic Microwave Background anisotropies have drastically improved our knowledge about the inflationary scenario (see e.g. Ref. [5]). In any case, their also show some interesting anomaly or tension that, albeit at small confidence level, is clearly worthwile of further investigation. One of these is the compatibility of the Planck data with a larger value for the number of relativistic degrees of freedom at recombination than what is commonly expected in the standard scenario (Ref. [5]). For example, as described in the next chapter,in our analysys Ref. [95], we found a value of $N_{\text{eff}} = 3.71 \pm 0.40$ at 68% c.l. from the Planck CMB data alone, that becomes, when the Planck data are combined with the measurements of the Hubble constant from Ref. [6], $N_{\text{eff}} = 3.63 \pm 0.27$ at 68% c.l., i.e. an indication for a non standard value at more than 95% c.l..

A deviation of N_{eff} from the standard value 3.046, could indicate not only the presence of additional relativistic species but also other different and unexpected neutrino properties, as a non-zero chemical potential, as we saw in the previous section. Here (and in our paper Ref. [23]) we investigate if this anomaly could be connected with a non-standard inflationary process as the Curvaton scenario, since in this model a non zero neutrino chemical potential, and, therefore, a larger value for N_{eff} could arise as we again saw in the previous section.

Since probing neutrino isocurvature density perturbation (NID), in the Curvaton scenario is complementary to constrain the lepton number in the neutrino sector, it is important to investigate the current CMB bounds on NID perturbation component, allowing at the same time a variation in the neutrino effective number N_{eff}. Bounds on neutrino isocurvature perturbations have been presented in Ref. [210] and Ref. [211], and also the Planck collaboration has provided new and stringent bounds on NID, see Ref. [223], but fixing N_{eff} to the standard value of 3.046. Here (see also Ref. [23]) we present a combined analysis for N_{eff} and NID from the Planck data, and considering also the combination with the recent Hubble constant measurements.

Our analysis method is based on the Boltzmann CAMB code, Ref. [27], and a Monte Carlo Markov Chain (MCMC) analysis based on the MCMC package `cosmomc`, Ref. [97].

We sample the set of parameters that follow:

$$\{\omega_b, \omega_c, \Theta_s, \tau, n_s, \log[10^{10}A_s], N_{\text{eff}}, \alpha^{NID}\} \,, \tag{7.25}$$

where $\omega_b \equiv \Omega_b h^2$ and $\omega_c \equiv \Omega_c h^2$ are respectively the physical baryon and cold dark matter energy densities, Θ_s the ratio between the sound horizon and the angular diameter distance at decoupling, τ is the reionization optical depth, n_s the scalar spectral index, A_s the amplitude of the primordial spectrum, N_{eff} the effective neutrino number and α^{NID} is the NID amplitude. For this analysis we parameterized the total CMB power spectrum as:

$$C_l = (1 - \alpha^{NID})C_l^{ad} + \alpha^{NID}C_l^{NID} + 2sign(\alpha^{NID})\sqrt{\alpha^{NID}(1 - \alpha^{NID})}C_l^{corr} \,, \tag{7.26}$$

where again C_l^{ad} is the adiabatic component, C_l^{NID} is the neutrino isocurvature density component and C_l^{corr} is the correlated spectrum. In this case, the quantity α^{NID}, that is defined in eq. (7.8) in this way:

Parameter	Planck+WP	Planck+WP+HST
$\Omega_b h^2$	0.02215 ± 0.00050	0.02260 ± 0.00033
$\Omega_c h^2$	0.1222 ± 0.0068	0.1273 ± 0.0056
θ	1.0405 ± 0.0010	1.0408 ± 0.0011
τ	0.094 ± 0.015	0.099 ± 0.015
n_s	0.966 ± 0.021	0.987 ± 0.012
$log[10^{10} A_s]$	3.115 ± 0.035	3.122 ± 0.037
$H_0 [\mathrm{km/s/Mpc}]$	68.7 ± 3.9	72.5 ± 2.2
N_{eff}	3.26 ± 0.48	3.70 ± 0.30
α^{NID}	-0.0031 ± 0.0053	0.0002 ± 0.0031

Table 7.3. Constraints at 68% c. l. on N_{eff}, α^{NID} and the main 6 cosmological parameters from the Planck+WP and Planck+WP+HST cases.

$$\frac{\alpha^{NID}(k_0)}{1 - \alpha^{NID}(k_0)} \equiv \frac{P_S^{NID}(k_0)}{P_\zeta(k_0)} \tag{7.27}$$

has the power spectra of isocurvature perturbations $P_S^{NID}(k)$ and of curvature perturbations $P_\zeta(k)$ evaluated at a fixed pivot wave number $k_0 = 0.05 \, \mathrm{Mpc}^{-1}$ and having the same spectral tilt n_S. Moreover, since we considered only totally correlated or anti-correlated spectra, in order to simplify the notation, we varied only one parameter α^{NID}, that is ever defined positive, replacing $\beta = \pm 1$ with the $sign(\alpha^{NID})$. In fact, considering, as usual, the parameter β, as defined in eq. (7.9), the adiabatic and isocurvature perturbations are totally anti-correlated taking $\beta = -1$ and totally correlated taking $\beta = 1$ in the curvaton scenario. Giving this convention, we have no longer the parameter β, but the spectra are totally anti-correlated, or totally correlated, when $\alpha^{NID} < 0$, or $\alpha^{NID} > 0$.

We compared these theoretical power spectra with the recent CMB measurements made by the Planck experiment. For the Planck data, we added both the high-l and low-l TT likelihoods and we also used the low-l TE, EE, BB WMAP likelihood, as in Ref. [5] : this combination corresponds to the Planck+WP case. Moreover, always as in Ref. [5] , we marginalized over all foregrounds parameters. Then we also considered the HST constraint on the Hubble constant from Ref. [6].

The results of our analysis, Ref. [23], are reported in Table 7.3 and Figure 7.3, for Planck+WP and Planck+WP+HST datasets.

As we can see, the Planck+WP data do not show any indication for NID or for a larger value for N_{eff}, though a cosmological degeneracy exists along the α^{NID}-N_{eff} direction. Are the models with smaller values for N_{eff} to be more consistent with the CMB observations when $\alpha^{NID} < 0$. The current Planck+WP data alone do not show any supporting evidence for NID by considering variations in N_{eff}, and are more consistent with the standard value of $N_{\mathrm{eff}} = 3.046$, due to its larger error when NID are considered.

On the contrary, the inclusion of HST measurements reduces the error bars on the NID component while providing an indication for a non-standard value for N_{eff} at more than two standard deviations, consistently with the anti-correlation between
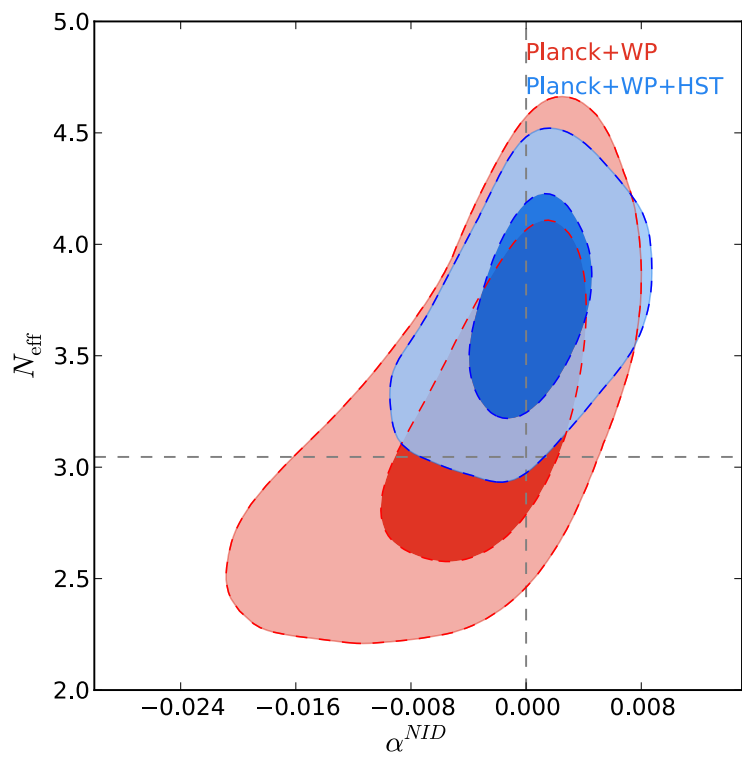
Figure 7.3. 68% and 95% c.l. likelihood contours for Planck+WP and Planck+WP+HST in the N_{eff} vs. α^{NID} plane. Note the small correlation between the two parameters, [23].

Parameter	Planck+WP $\alpha^{NID} > 0$	Planck+WP+HST $\alpha^{NID} > 0$
$\Omega_b h^2$	0.02260 ± 0.00043	0.02271 ± 0.00031
$\Omega_c h^2$	0.1287 ± 0.0059	0.1295 ± 0.0050
θ	1.04149 ± 0.00082	1.04149 ± 0.00082
τ	0.095 ± 0.014	0.096 ± 0.014
n_s	0.987 ± 0.017	0.992 ± 0.011
$log[10^{10}A_s]$	3.100 ± 0.033	3.104 ± 0.031
$H_0[\text{km/s/Mpc}]$	72.4 ± 3.4	73.3 ± 2.0
N_{eff}	3.71 ± 0.42	3.81 ± 0.27
α^{NID}	< 0.0023	< 0.0025

Table 7.4. Constraints at 68% c. l. on N_{eff}, $\alpha^{NID} > 0$ and the main 6 cosmological parameters from the Planck+WP and Planck+WP+HST cases, [23].

Parameter	Planck+WP $\alpha^{NID} < 0$	Planck+WP+HST $\alpha^{NID} < 0$
$\Omega_b h^2$	0.02198 ± 0.00043	0.02249 ± 0.00031
$\Omega_c h^2$	0.1196 ± 0.0056	0.1248 ± 0.0049
θ	1.04012 ± 0.00085	1.04003 ± 0.00080
τ	0.093 ± 0.014	0.102 ± 0.015
n_s	0.958 ± 0.018	0.982 ± 0.011
$log[10^{10}A_s]$	3.119 ± 0.034	3.145 ± 0.033
$H_0[\text{km/s/Mpc}]$	67.3 ± 3.3	71.8 ± 2.0
N_{eff}	3.08 ± 0.40	3.59 ± 0.27
α^{NID}	> -0.0056	> -0.0023

Table 7.5. Constraints at 68% c. l. on N_{eff}, $\alpha^{NID} < 0$ and the main 6 cosmological parameters from the Planck+WP and Planck+WP+HST cases, [23].

N_{eff} and α^{NID} evident in the Figure 7.3.

Since, for example, in the curvaton scenario the residual isocurvature components are either fully correlated or fully anti-correlated (see Ref. [189]), we repeated the analysis by imposing each time the $\alpha^{NID} > 0$ prior, as reported in Table 7.4, or $\alpha^{NID} < 0$ prior, as reported in Table 7.5, for the two datasets: Planck+WP and Planck+WP+HST. In this way, we can also better evaluate the impact of a weak prior on α^{NID} respect to specific correlated or anti-correlated models.

When we consider $\alpha^{NID} > 0$, the constraint on the NID component is practically left unaffected by the inclusion of a HST prior. This is evident from Figure 7.4, where we report the 2-D constraints on the H_0 vs $\alpha^{NID} > 0$ for the Planck+WP and Planck+WP+HST datasets.

The interesting aspect is that when we impose a $\alpha^{NID} < 0$ prior, the Planck+WP case provide a value for the Hubble constant that is in tension with current HST determinations, even if the N_{eff} parameter is allowed to vary. For this reason a
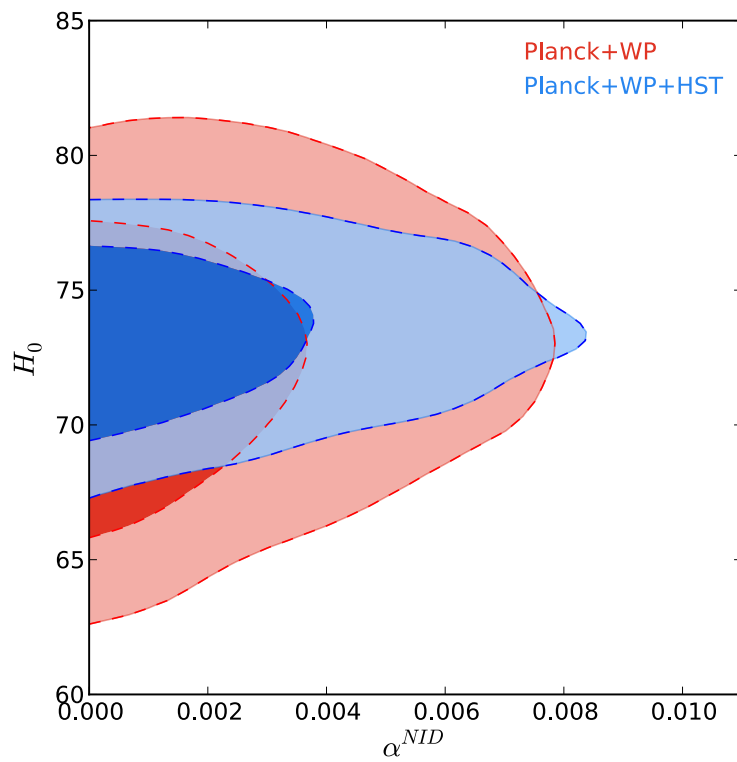
Figure 7.4. The 68% and 95% c.l. likelihood contours for Planck+WP and Planck+WP+HST combination of data, considering totally correlated spectra $\alpha^{NID} > 0$, [23].
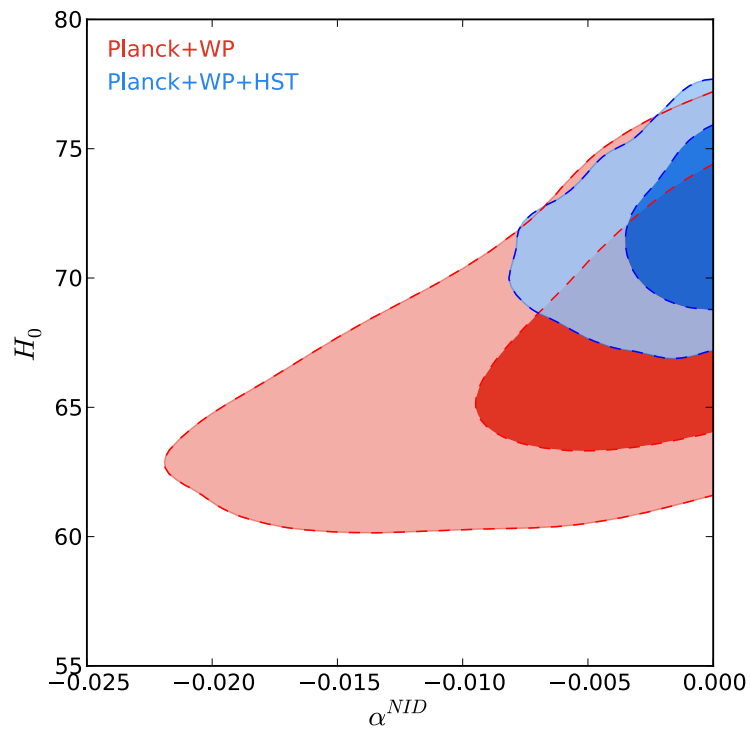
Figure 7.5. The 68% and 95% c.l. likelihood contours for Planck+WP and Planck+WP+HST combination of data, considering totally anti-correlated spectra $\alpha^{NID} < 0$, [23].

NID component with $\alpha^{NID} < 0$ cannot resolve the current tension on the values of H_0 between the Planck data and the HST constraint. Moreover, the HST prior is included, an anticorrelated, $\alpha^{NID} < 0$, neutrino isocurvature density component is severly constrained, as we can see in the Figure 7.5, where we reported the 2-D constraints on the H_0 vs $\alpha^{NID} < 0$ for the Planck+WP and Planck+WP+HST datasets. In this case, the combined analysis suggests a value for N_{eff} larger than the standard expectations at more than two standard deviations, as we can see in Table 7.5.

Chapter 8

Constraints on Axion Cold Dark Matter

One of the great puzzles related to the ΛCDM model is the nature of the dark matter (DM) component that, according to the Planck observations, Refs. [5, 2, 101], makes up roughly 27% of the total matter-energy content of the Universe. A well-motivated DM candidate is the axion, that was first proposed by Peccei and Quinn in Ref. [165] to explain the strong CP problem, i.e., the absence of CP violation in strong interactions.

In this chapter (but see also Ref. [212]) we consider the hypothesis that the axion accounts for all the DM present in the Universe. We have put this "axion dark matter" (ADM) scenario under scrutiny using the cosmological data, such as the observations of CMB temperature, Refs. [5, 2, 101], and polarization anisotropies (including BICEP2 claimed detection[1] of B-mode polarization, see Refs. [10, 213]) and of Baryon Acoustic Oscillations (BAO), Refs. [8, 153, 99, 154, 115]. The ADM model has also been revisited by other authors, Refs. [214, 215], in light of BICEP2 data, and our analyses in the minimal ΛCDM scenario agree with these previous works. However, in order to assess the robustness of the cosmological constraints presented in the literature, as well as the tension between BICEP2 and Planck measurements of the tensor-to scalar ratio, we also considered extensions of the simplest ADM model. The effects of additional relativistic degrees of freedom, of neutrino masses, of a dark energy equation-of-state parameter and of a free-tensor spectral index are carefully explored.

8.1 Axion cosmology

In order to solve the strong CP problem dynamically, Peccei and Quinn postulated the existence of a new global $U(1)$ (quasi-) symmetry, often denoted $U(1)_{PQ}$, that is spontaneously broken at the Peccei-Quinn (PQ) scale f_a. The spontaneous breaking of the PQ symmetry generates a pseudo Nambu-Goldstone boson, the axion, which can be copiously produced in the Universe's early stages, both via thermal and

---

[1]This claim has been recently questioned by the Planck collaboration, see Ref. [?], since this signal could be completely explained by a polarization signal from galactic dust. This point is discussed in the chapter 10.

non-thermal processes. Thermal axions with sub-eV masses contribute to the hot dark matter component of the Universe, as neutrinos, and the cosmological limits on their properties have been updated and presented in Refs. [162, 21].

Here we focus on axion-like particles produced non-thermally, as they were postulated as natural candidates for the cold dark matter component, see Refs. [216, 217, 218, 219, 220]. The history of axions starts at the PQ scale f_a. For temperatures between this scale and the QCD phase transition Λ_{QCD}, the axion is, for practical purposes, a massless particle. When the Universe's temperature approaches Λ_{QCD}, the axion acquires a mass via instanton effects. The effective potential V for the axion field $a(x)$ is generated through non-pertubative QCD effects, see Ref. [221], and, setting the color anomaly $N = 1$, it may be written as

$$V(a) = f_a^2 m_a^2(T) \left[1 - \cos\left(\frac{a}{f_a}\right) \right] , \tag{8.1}$$

where the axion mass is a function of temperature. Introducing the misalignment angle $\theta \equiv a/f_a$, the field evolves according to the Klein-Gordon equation on a flat Friedmann-Lemaître-Robertson-Walker background:

$$\ddot{\theta} + 3H\dot{\theta} + m_a^2(T)\theta = 0 , \tag{8.2}$$

where the axion temperature-dependent mass is, see Ref. [221]:

$$m_a(T) = \begin{cases} Cm_a(T=0)(\Lambda_{\text{QCD}}/T)^4 & T \gtrsim \Lambda_{\text{QCD}} \\ m_a(T=0) & T \lesssim \Lambda_{\text{QCD}} \end{cases} \tag{8.3}$$

where $C \simeq 0.018$ is a model dependent factor, see Refs. [221, 222], $\Lambda_{\text{QCD}} \simeq 200\,MeV$ and the zero-temperature mass $m_a(T=0)$ is related to the PQ scale:

$$m_a \simeq 6.2\,\mu eV \left(\frac{f_a}{10^{12}\,GeV}\right)^{-1} . \tag{8.4}$$

The axion is effectively massless at $T \gg \Lambda_{\text{QCD}}$, as it can be seen from eq. (8.3).

The PQ symmetry breaking can occur before or after inflation. If there was an inflationary period in the Universe after or during the PQ phase transition, there will exist, together with the standard adiabatic perturbations generated by the Inflaton field, axion isocurvature perturbations, associated to quantum fluctuations in the axion field. In this scenario, i.e. when the condition

$$f_a > \left(\frac{H_I}{2\pi}\right) , \tag{8.5}$$

is satisfied, the initial misalignment angle θ_i should be identical in the whole observable Universe, with a variance given by

$$\langle \sigma_\theta^2 \rangle = \left(\frac{H_I}{2\pi f_a}\right)^2 , \tag{8.6}$$

and corresponding to quantum fluctuations in the massless axion field

$$\langle \delta_a^2 \rangle = \left(\frac{H_I}{2\pi}\right)^2 , \tag{8.7}$$

where H_I is the value of the Hubble parameter during inflation. These quantum fluctuations generate an axion isocurvature power spectrum

$$\Delta_a(k) = k^3 |\delta_a^2|/2\pi^2 = \frac{H_I^2}{\pi^2} \theta_i^2 f_a^2 \ . \tag{8.8}$$

The Planck data, combined with the 9-year polarization data from WMAP, Ref. [102], constrained the primordial isocurvature fraction (defined as the ratio of the isocurvature perturbation spectrum to the sum of the adiabatic and isocurvature spectra) to be, see Ref. [223]:

$$\beta_{\rm iso} < 0.039 \ , \tag{8.9}$$

at 95% c.l. and at a scale $k = 0.05$ Mpc^{-1}. This limit can be used to exclude regions in the parameter space of the PQ scale and the scale of inflation H_I, since they are related via

$$H_I = 0.96 \times 10^7 \ {\rm GeV} \left(\frac{\beta_{\rm iso}}{0.04}\right)^{1/2} \left(\frac{\Omega_a}{0.120}\right)^{1/2} \left(\frac{f_a}{10^{11} \ {\rm GeV}}\right)^{0.408} \ , \tag{8.10}$$

where Ω_a is the axion mass-energy density. In this scenario, in which the PQ symmetry is not restored after inflation, and therefore the condition $f_a > \left(\frac{H_I}{2\pi}\right)$ holds, and assuming that the dark matter is made of axions produced by the misalignment mechanism [2], Planck data has set a 95% c.l. upper bound on the energy scale of inflation, see Ref. [223]:

$$H_I \leq 0.87 \times 10^7 \ {\rm GeV} \left(\frac{f_a}{10^{11} \ {\rm GeV}}\right)^{0.408} \ . \tag{8.11}$$

The BICEP2 collaboration has reported 6-σ evidence for the detection of primordial gravitational waves[3], with a tensor to scalar ratio $r = 0.2^{+0.07}_{-0.05}$, pointing to inflationary energy scales of $H_I \sim 10^{14}$ GeV, see Refs. [10, 213]. These scale would require a value for f_a which lies several orders of magnitude above the Planck scale and consequently nullifies the axion scenario in which the PQ is broken during inflation. We conclude that, if future CMB polarization experiments will confirm, even partially in light of the recent Planck collaboration work (see Ref. [**?**]), the BICEP2 findings, the axion scenario in which the PQ symmetry is broken during inflation will be ruled out, at least in its simplest form. This conclusion could be circumvented in a more complicated scenario (see e.g. Ref. [224] for a proposal in this direction) but we not consider here this possibility.

There exists however another possible scenario in which the PQ symmetry is broken after inflation, i.e.

---

[2]An additional relevant mechanism of axion production that we will shortly see is via the decay of axionic strings. However, in this particular scenario such contribution will be negligible, since strings and other defects are diluted after the inflationary stage.

[3]This claim has been recently questioned by the Planck collaboration, see Ref. [**?**], since this signal could be completely explained by a polarization signal from galactic dust. This point is discussed in the chapter 10.

$$f_a < \left(\frac{H_I}{2\pi}\right) \, , \tag{8.12}$$

In this second axion cold dark matter scheme, there are no axion isocurvature perturbations since there are not axion quantum fluctuations. On the other hand, there will exist a contribution to the total axion energy density from axionic string decays. We briefly summarize these two contributions (misalignment and axionic string decays) to $\Omega_a h^2$. The misalignment mechanism will produce an initial axion number density which reads

$$n_a(T_1) \simeq \frac{1}{2} m_a(T_1) f_a^2 \langle f(\theta_i)\theta_i^2 \rangle \tag{8.13}$$

where T_1 is defined as the temperature for which the condition $m_a(T_1) = 3H(T_1)$ is satisfied, and $f(\theta_i)$ is a function related to anharmonic effects, linked to the fact that eq. (8.2) has been obtained assuming that the potential, eq. (8.1), is harmonic. The value of $f(\theta_i)\theta_i^2$ is an average of a uniform distribution of all possible initial values:

$$\langle \theta_i^2 f(\theta_i) \rangle = \frac{1}{2\pi} \int_{-\pi}^{\pi} \theta_i^2 f(\theta_i) d\theta_i = 8.77 \, , \tag{8.14}$$

considering the analytic expression for $f(\theta_i)$ provided by Ref. [225]. If anharmonic effects are neglected (i.e. $f(\theta_i) = 1$), the factor quoted above should be replaced by the standard $\pi^2/3$, changing the cold dark matter axion population and consequently the cosmological constraints presented here.

The mass-energy density of axions today related to misalignment production is obtained via the product of the ratio of the initial axion number density to entropy density times the present entropy density, times the axion mass m_a, and reads, see Ref. [225]:

$$\Omega_{a,mis}h^2 = \begin{cases} 0.236\langle\theta_i^2 f(\theta_i)\rangle \left(\frac{f_a}{10^{12}\text{ GeV}}\right)^{7/6} & f \lesssim \hat{f}_a \\ 0.0051\langle\theta_i^2 f(\theta_i)\rangle \left(\frac{f_a}{10^{12}\text{ GeV}}\right)^{3/2} & f \gtrsim \hat{f}_a \end{cases} \tag{8.15}$$

where $\hat{f}_a = 9.91 \times 10^{16}$ GeV.

By considering the BICEP2 results, the value of f_a, which, in this second scenario, should be always smaller than the inflationary energy scale, will always be smaller than $\hat{f}_a$ and therefore, the misalignment axion cold dark matter energy density is

$$\Omega_{a,mis}h^2 = 2.07 \left(\frac{f_a}{10^{12}\text{ GeV}}\right)^{7/6} \, . \tag{8.16}$$

As previously stated, there will also be a contribution from axionic string decays and other axion topological-defect decays, as domain walls, $\Omega_{a,dec}h^2$. The total (axion) cold dark matter density $\Omega_a h^2$ is the sum of the misalignment and topological-defect decay contributions [4], see Ref. [214]:

---

[4]For the values of f_a considered here, and relevant for the axion cold dark matter scenario, $f_a \sim 10^{11}$ GeV, axions will decouple when the number of relativistic degrees of freedom includes all the standard model particles, being their current number density highly suppressed and their contribution to $\Delta N_{eff} \sim 0.03$, see Refs. [21, 227], deviation which is currently unobservable and may be at reach in future surveys as Euclid, see Ref. [228].

$$\Omega_{\mathrm{a}}h^2 = 2.07\,(1 + \alpha_{\mathrm{dec}}) \left(\frac{f_{\mathrm{a}}}{10^{12}\ \mathrm{GeV}}\right)^{7/6}, \tag{8.17}$$

where α_{dec} is the ratio $\alpha_{\mathrm{dec}} = \Omega_{\mathrm{a,dec}}/\Omega_{\mathrm{a,mis}}$ between the two contributions. Following Ref. [225], we considered $\alpha_{\mathrm{dec}} = 0.164$, see Ref. [226], so that[5]

$$\Omega_{\mathrm{a}}h^2 = 2.41 \left(\frac{f_{\mathrm{a}}}{10^{12}\mathrm{GeV}}\right)^{7/6}. \tag{8.18}$$

Here we quote our results on m_a for the case $\alpha_{\mathrm{dec}} = 0.164$. However, the CMB is actually only sensitive to $\Omega_{\mathrm{a}}h^2 \propto (1 + \alpha_{\mathrm{dec}})m_a^{-7/6}$, therefore limits on m_a for an arbitrary value of α_{dec} can be obtained from the ones reported in our analysis by means of the rescaling:

$$m_a \longrightarrow m_{\mathrm{a}}' = m_{\mathrm{a}} \left[\frac{(1 + \alpha_{\mathrm{dec}})}{(1 + 0.164)}\right]^{6/7}. \tag{8.19}$$

In a similar approach, the limits obtained on m_a when neglecting anharmonic effects can also be obtained from the values presented in the next section as

$$m_{\mathrm{a}}'' = m_{\mathrm{a}} \times \left(\frac{\pi^2/3}{8.77}\right)^{6/7} = m_{\mathrm{a}} \times\ 0.43. \tag{8.20}$$

8.2 Data analysis

The basic ADM scenario we analyze is described by the following set of parameters:

$$\{\omega_{\mathrm{b}},\, \theta_s,\, \tau,\, n_s, \log[10^{10}A_s],\, r,\, m_{\mathrm{a}}\}, \tag{8.21}$$

where $\omega_{\mathrm{b}} \equiv \Omega_{\mathrm{b}}h^2$ is the physical baryon density, θ_s the ratio of the sound horizon to the angular diameter distance at decoupling, τ is the reionization optical depth, A_s and n_s are, respectively, the amplitude and spectral index of the primordial spectrum of scalar perturbations, r is the ratio between the amplitude of the spectra of tensor and scalar perturbations, and finally m_{a} is the axion mass. The latter sets the density of cold dark matter $\Omega_{\mathrm{c}}h^2 \equiv \Omega_{\mathrm{a}}h^2$ through eq. (8.17). All the quantities characterising the primordial scalar and tensor spectra (amplitudes, spectral indices, possibly running) are evaluated at the pivot wave number $k_0 = 0.05\, Mpc^{-1}$. In the baseline model we assume flatness, purely adiabatic initial conditions, a total neutrino mass $\sum m_\nu = 0.06\, eV$ and a cosmological constant-like dark energy ($w = -1$). We also assume, unless otherwise noted, that the inflation consistency condition $n_T = -r/8$ between the tensor amplitude and spectral index holds.

Extensions to the baseline model described above are also explored. We start by considering the effective number of relativistic degrees of freedom and the sum of neutrino masses, first separately and then jointly, as additional parameters. A model with ΔN_{eff} sterile massive neutrino species, characterised by a sterile neutrino

---

[5]A value for the axionic string decays fractional contribution larger than the one used here has been reported in Ref. [229]. This value is obtained by combining the observed value of $\Omega_{\mathrm{c}}h^2$ with estimates of the axion mass based on the Josephson effect.

mass m_s^{eff}, has also been analysed. Then we proceeded to add the equation-of-state parameter w of dark energy to the baseline model. Finally, we also studied the effect of having more freedom in the inflationary sector, by letting the running of the scalar spectral index vary or by relaxing the assumption of the inflation consistency.

We use the CAMB Boltzmann code, Ref. [27], to evolve the background and perturbation equations, and derived posterior distributions for the model parameters from current data using a Monte Carlo Markov Chain (MCMC) analysis based on the publicly available MCMC package `cosmomc`, Ref. [97], that implements the Metropolis-Hastings algorithm.

We consider the data on CMB temperature anisotropies measured by the Planck satellite, see Refs. [2, 101], supplemented by the 9-year polarization data from WMAP, Ref. [102].

The likelihood functions associated to these datasets are estimated and combined using the likelihood code distributed by the Planck collaboration, described in Ref. [101], and publicly available at Planck Legacy Archive[6]. We used Planck TT data up to a maximum multipole number of $l_{\text{max}} = 2500$, and WMAP 9-year polarization data (WP) up to $l = 23$, see Ref. [102].

The BICEP2 collaboration has reported evidence for the detection of B-modes in the multipole range $30 < l < 150$ after three seasons of data taking in the South Pole, Refs. [10, 213], with $6 - \sigma$ significance. This B-mode excess is much higher than known systematics and expected foregrounds, being the spectrum well fitted with a tensor-to-scalar ratio $r = 0.2_{-0.05}^{+0.07}$. Notice however that when foregrounds are taken into account, subtraction of different foreground models makes the best-fit value for r move in the range $0.12 - 0.21$. Here we nevertheless assume that the BICEP2 signal was entirely of cosmological origin, but, recently this signal has been questioned by the Planck collaboration, see Ref. [**?**], since could be completely explained by a polarization signal from galactic dust. The likelihood data from the BICEP2 collaboration has been included in our MCMC analyses accordingly to the `cosmomc` package.

We also use BAO measurements, namely the SDSS Data Release 7 from Refs. [153, 99], WiggleZ survey from Ref. [154] and 6dF from Ref. [115] datasets, as well as the most recent and most accurate BAO measurements to date, arising from the BOSS Data Release 11 (DR11) results from Ref. [8].

We now present the results for the allowed axion mass ranges in the scenario which would survive once the BICEP2 findings concerning the tensor to scalar ratio and, consequently, the energy scale associated to inflation, are confirmed by ongoing and near future searches of primordial B modes. In this case, the PQ symmetry should be broken after inflation. We restricted ourselves to such scenario.

Tables 8.1 and 8.2 depict the results for the different cosmologies explored, for two possible data combinations: *(a)* Planck temperature data + WMAP polarization (WP) and *(b)* Planck temperature data, WP and BICEP2 measurements. The constraints on the tensor to scalar ratio are quoted for a reference scale of $k_0 = 0.05~\text{Mpc}^{-1}$. For the sake of simplicity, we do not show all the results with the BAO measurements included in the numerical analyses. We quote the values of the cosmological parameters resulting from the analyses with BAO data included only

---

[6]http://pla.esac.esa.int/pla/aio/planckProducts.html

Parameter	ADM+r	ADM+r $+N_{\mathrm{eff}}$	ADM+r $+\sum m_\nu$	ADM+r $+\sum m_\nu+N_{\mathrm{eff}}$	ADM+r $+ m_s^{\mathrm{eff}} + N_{\mathrm{eff}}$	ADM+r $+w$	ADM+r $+ n_t$	ADM+r $+ dn_s/d\ln k$
$\Omega_b h^2$	0.02204 ± 0.00028	0.02261 ± 0.00043	0.02189 ± 0.00033	0.02245 ± 0.00047	0.02246 ± 0.00039	0.02208 ± 0.00028	0.02211 ± 0.00029	0.02229 ± 0.00031
$\Omega_a h^2$	0.1194 ± 0.0027	0.1280 ± 0.0054	0.1203 ± 0.0029	0.1277 ± 0.0054	0.1275 ± 0.0055	0.1192 ± 0.0026	0.1206 ± 0.0030	0.1198 ± 0.0027
θ	1.04127 ± 0.00064	1.04053 ± 0.00072	1.04097 ± 0.00070	1.04039 ± 0.00073	1.04040 ± 0.00074	1.04132 ± 0.00063	1.04117 ± 0.00063	1.04133 ± 0.00064
τ	0.089 ± 0.013	0.097 ± 0.015	0.089 ± 0.013	0.096 ± 0.015	0.096 ± 0.014	0.089 ± 0.013	0.089 ± 0.013	0.100 ± 0.016
n_s	0.9614 ± 0.0075	0.991 ± 0.018	0.9576 ± 0.0088	0.985 ± 0.019	0.982 ± 0.018	0.9617 ± 0.0073	0.9615 ± 0.0074	0.9572 ± 0.0080
$log[10^{10}A_s]$	3.086 ± 0.025	3.122 ± 0.033	3.086 ± 0.025	3.119 ± 0.033	3.119 ± 0.032	3.087 ± 0.024	3.149 ± 0.026	3.114 ± 0.031
$H_0[\mathrm{km/s/Mpc}]$	67.4 ± 1.2	73.2 ± 3.5	64.5 ± 3.3	70.4 ± 4.7	70.2 ± 3.4	84 ± 10	67.0 ± 1.2	67.5 ± 1.2
r	< 0.12	< 0.19	< 0.13	< 0.19	< 0.18	< 0.13	< 0.93	< 0.23
$m_a(\mu eV)$	81.5 ± 1.6	76.8 ± 2.8	81.0 ± 1.6	77.0 ± 2.7	77.1 ± 2.9	81.6 ± 1.5	80.8 ± 1.7	81.3 ± 1.6
N_{eff}	(3.046)	3.79 ± 0.41	(3.046)	3.71 ± 0.41	3.72 ± 0.37	(3.046)	(3.046)	(3.046)
$\sum m_\nu(eV)$	(0.06)	(0.06)	< 0.97	< 0.83	(0.06)	(0.06)	(0.06)	(0.06)
w	(-1)	(-1)	(-1)	(-1)	(-1)	-1.50 ± 0.31	(-1)	(-1)
$m_s^{\mathrm{eff}}(eV)$	(0)	(0)	(0)	(0)	< 0.87	$< (0)$	(0)	(0)
n_t	(0)	(0)	(0)	(0)	(0)	(0)	2.19 ± 0.87	(0)
$dn_s/d\ln k$	(0)	(0)	(0)	(0)	(0)	(0)	(0)	-0.022 ± 0.011

Table 8.1. Constraints at 68% c.l. on cosmological parameters from our analysis for Planck+WP, except for the upper bounds on the neutrino mass and on the tensor-to-scalar ratio, which refer to 95% c.l. upper limits, [212].

Parameter	ADM+r	ADM+r +N_{eff}	ADM+r +$\sum m_\nu$	ADM+r +$\sum m_\nu$+N_{eff}	ADM+r + m_s^{eff} + N_{eff}	ADM+r +w	ADM+r + n_t	ADM+r + $dn_s/d\ln k$
$\Omega_b h^2$	0.02202 ± 0.00028	0.02285 ± 0.00043	0.02193 ± 0.00032	0.02276 ± 0.00046	0.02272 ± 0.0043	0.02207 ± 0.00028	0.02202 ± 0.00029	0.02234 ± 0.00031
$\Omega_a h^2$	0.1186 ± 0.0026	0.1313 ± 0.0057	0.1191 ± 0.0028	0.1312 ± 0.0059	0.1257 ± 0.0015	0.1183 ± 0.0025	0.1192 ± 0.0026	0.1193 ± 0.0027
θ	1.04138 ± 0.00063	1.04032 ± 0.00071	1.04118 ± 0.00067	1.04023 ± 0.00073	1.04020 ± 0.00075	1.04143 ± 0.00062	1.04129 ± 0.00065	1.04141 ± 0.00064
τ	0.089 ± 0.013	0.101 ± 0.015	0.090 ± 0.013	0.101 ± 0.015	0.104 ± 0.016	0.090 ± 0.013	0.089 ± 0.013	0.104 ± 0.016
n_s	0.9649 ± 0.0074	1.0057 ± 0.0173	0.9628 ± 0.0083	1.0032 ± 0.0184	1.004 ± 0.0175	0.9654 ± 0.0073	0.9611 ± 0.0074	1.0004 ± 0.0150
$log[10^{10}A_s]$	3.084 ± 0.025	3.136 ± 0.034	3.085 ± 0.025	3.135 ± 0.034	3.134 ± 0.033	3.085 ± 0.025	3.149 ± 0.025	3.123 ± 0.031
$H_0[\text{km/s/Mpc}]$	67.7 ± 1.2	76.0 ± 3.6	65.9 ± 2.8	74.5 ± 4.3	73.6 ± 3.9	87.1 ± 9.1	67.5 ± 1.2	67.7 ± 1.2
r	0.166 ± 0.036	0.180 ± 0.037	0.168 ± 0.035	0.183 ± 0.038	0.183 ± 0.038	0.168 ± 0.035	0.172 ± 0.047	0.194 ± 0.040
$m_a(\mu eV)$	82.0 ± 1.5	75.3 ± 2.8	81.6 ± 1.6	75.3 ± 2.8	75.3 ± 2.9	82.1 ± 1.5	81.6 ± 1.5	81.5 ± 1.6
N_{eff}	(3.046)	4.13 ± 0.43	(3.046)	4.08 ± 0.44	4.08 ± 0.42	(3.046)	(3.046)	(3.046)
$\sum m_\nu(eV)$	(0.06)	(0.06)	< 0.78	< 0.58	(0.06)	(0.06)	(0.06)	(0.06)
w	(-1)	(-1)	(-1)	(-1)	(-1)	-1.57 ± 0.26	(-1)	(-1)
$m_s^{\text{eff}}(eV)$	(0)	(0)	(0)	(0)	< 0.63	$< (0)$	(0)	(0)
n_t	(0)	(0)	(0)	(0)	(0)	(0)	1.66 ± 0.51	(0)
$dn_s/d\ln k$	(0)	(0)	(0)	(0)	(0)	(0)	(0)	-0.0278 ± 0.0099

Table 8.2. Constraints at 68% c.l. on cosmological parameters from our analysis for Planck+WP+BICEP2, except for the bounds on the neutrino mass, which refer to 95% c.l. upper limits, [212].

in the cases in which these values notably differ from the results obtained without considering BAO measurements.

Assuming a standard ADM model we obtain $m_a = 81.5 \pm 1.6 \, \mu$eV ($m_a = 82.0 \pm 1.5 \, \mu$eV) from Planck, WP (+BICEP2) data, corresponding to a cold dark matter energy density of $\Omega_a h^2 = 0.1194 \pm 0.0027$ ($\Omega_a h^2 = 0.1186 \pm 0.026$). Notice that the mean values obtained can be estimated by equating eq. (8.18) to the total dark matter energy density inferred from cosmological observations. Therefore, in mixed axion-cold dark matter schemes (see e.g Ref. [230] for an implementation of this possible scenario), the required axion cold dark matter will be smaller, implying higher mean values for m_a.

Neglecting anharmonic effects in the axion potential would shift the mean values roughly by a half. If we consider as well BAO measurements, the former value translates into $m_a = 82.2 \pm 1.0 \, \mu$eV. Therefore, the inclusion of BAO data reduces mildly the error on m_a. Notice that the value of m_a that we obtain in the standard ADM model after considering BICEP2 data, $m_a = 81.5 \pm 1.6 \, \mu$eV, is in perfect agreement with the value obtained by Ref. [214], where it is found that $m_a = 71 \pm 2 \, \mu$eV $(1 + \alpha_{dec})$, after applying eq. (8.19), which provides the correct rescaling of our bounds for an arbitrary α_{dec}.
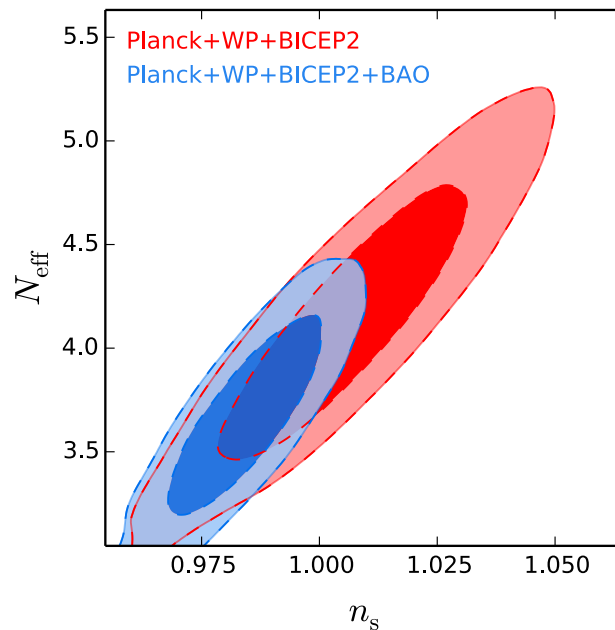
Figure 8.1. The red contours show the 68% and 95% c.l. allowed regions from the combination of Planck data, WP and BICEP2 measurements in the (n_s, N_{eff}) plane. The blue contours depict the constraints after the BAO datasets are added in the analysis, [212].

When allowing N_{eff} to be a free parameter to extend the minimal ADM scenario to scenarios in which additional relativistic species are present, we get $m_a = 76.8 \pm 2.8 \mu$eV and $N_{eff} = 3.79 \pm 0.41$ for Planck+WP, and $m_a = 75.3 \pm 2.8 \mu$eV and $N_{eff} = 4.13 \pm 0.43$ after combining Planck data with WP and BICEP2 measurements. When BAO datasets are included in the analysis, the former values are translated
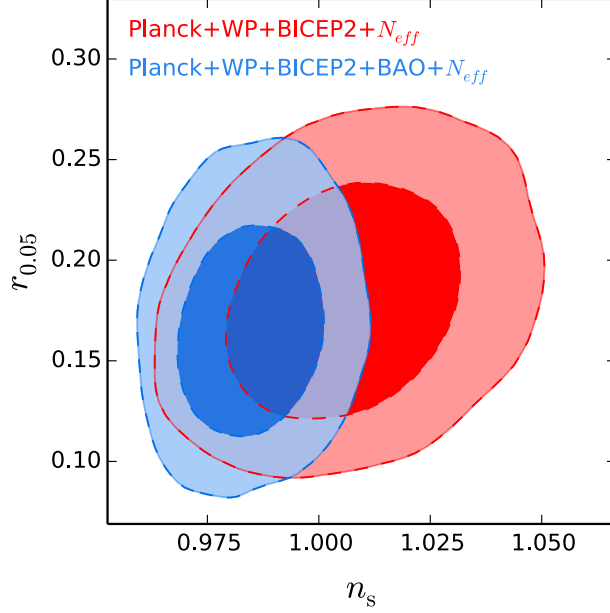
Figure 8.2. the red contours show the 68% and 95% c.l. allowed regions from the combination of Planck data, WP and BICEP2 measurements in the (n_s, r) plane. The blue contours depict the constraints after the BAO datasets are added in the analysis, [212].

into $m_a = 76.6 \pm 2.6 \mu$eV and $N_{eff} = 3.69 \pm 0.30$. Therefore, there exists from Planck+BICEP2 data a $2 - 3\sigma$ evidence for extra radiation species. The higher value of N_{eff} found when considering tensor modes and BICEP2 simultaneously was first found in Ref. [21] (see also previous chapter), where it was also pointed out that the tension between the tensor-to scalar ratio r extracted by Planck and WP data and the value of r found by BICEP2 data is less evident when $N_{eff} > 3$. The reason for this is because, if the value of $N_{eff} > 3$, the power in the CMB damping tail is suppressed. This can be compensated by a higher scalar spectral index n_s which in turn, will reduce the power at large scales. This power reduction at small multipoles can be compensated by increasing the tensor to scalar ratio r, and the overall result is a positive correlation between N_{eff} and r. This effect is illustrated in Fig. 8.1, where is depicted the strong positive correlation between N_{eff} and n_s and Fig. 8.2 shows the relation between n_s and r. Concerning exclusively CMB data, a larger value of N_{eff} can be compensated with a larger value of r (and viceversa), being the degeneracy among these two parameters mildly broken when considering as well BAO data in the MCMC analysis. Thus the preference for $N_{eff} > 3$, already present in the Planck data, is further increased by the inclusion of the BICEP2 likelihood that assigns a large probability to the $r \simeq 0.2$ region.

The larger value of N_{eff} results in a smaller axion mass (and in a larger associated error) due to the well-known existing correlation between N_{eff} and $\Omega_a h^2$ (that is, the cold dark matter energy density) when considering only CMB data, since it is possible to increase both to leave the redshift of matter-to-radiation equality unchanged. This effect can be clearly noticed from the results depicted in Tabs. 8.1

and 8.2, where the value of $\Omega_a h^2$ is about $\sim 2 - \sigma$ larger than the value found in the minimal scenario with no extra dark radiation species. The error on the $\Omega_a h^2$ cosmological parameter is also larger. Given that $\Omega_a h^2$ is inversely proportional to m_a, this results in an anticorrelation between N_{eff} and m_a. The large degeneracy between N_{eff} and $\Omega_c h^2 \equiv \Omega_a h^2$ also drives the large value of H_0 found in this case. The degeneracy is partly broken by the inclusion of BAO information: when the BAO datasets are considered, both H_0 and N_{eff} are closer to their ADM$+r$ values, being $H_0 = 71.7 \pm 1.9$ and $N_{\text{eff}} = 3.69 \pm 0.30$ respectively.

We also consider a model in which the active neutrino mass is a free parameter. In this case $m_a = 81.6 \pm 1.6 \mu$eV after combining Planck data with WP and BICEP2 measurements, while $m_a = 82.4 \pm 1.1 \mu$eV when BAO datasets are also considered. However, in this ΛCDM plus massive neutrino scenario, the neutrino mass bounds are unaffected when considering tensors and BICEP2 data. Indeed, the 95% c.l. bound on the total neutrino mass we got after considering all the data explored here, $\sum m_\nu < 0.25$ eV, agrees perfectly with the one found when neither tensors nor BICEP2 data are included in the analyses, see Ref. [21]. We also explored in Ref. [212] the case in which the three massive active neutrinos coexist with ΔN_{eff} massless species. The numerical results without BAO data are presented in the fifth column of Tabs. 8.1 and 8.2. The values obtained for the axion mass and for the number of relativistic degrees of freedom in this scenario are very close to the ones reported above for the N_{eff} cosmology, finding, from CMB data, evidence for extra dark radiation species at more than $2 - \sigma$. When considering the full dataset exploited in that paper, including BAO measurements, the bound on the neutrino mass becomes less stringent than in the three massive neutrino scenario due to the strong $\sum m_\nu$-N_{eff} degeneracy: we found a 95% c.l. bound of $\sum m_\nu < 0.47$ eV from the combination of Planck data with WP, BICEP2 and BAO measurements. Notice that, as in the case of the ADM plus N_{eff} relativistic degrees of freedom model, the mass of the axion is smaller and the value of the Hubble constant is larger than in the standard ADM scenario. The reason for that is due to the large existing degeneracy between $\Omega_a h^2$ and N_{eff} when considering CMB data only: notice the higher value of $\Omega_a h^2$ in Tabs. 8.1 and 8.2, when compared to its value in the standard ADM$+r$ scenario.

The last neutrino scenario we consider is the case in which there are ΔN_{eff} sterile massive neutrino species, characterised by a mass m_s^{eff}, which, for instance, in the case of a thermally-distributed sterile neutrino state, reads, eq. (6.3)

$$m_s^{\text{eff}} = (T_s/T_\nu)^3 m_s = (\Delta N_{\text{eff}})^{3/4} m_s \ , \tag{8.22}$$

where T_s, T_ν are the current temperature of the sterile and active neutrino species, respectively, and m_s is the true sterile neutrino mass. We recall however that the parameterization in terms of ΔN_{eff} and m_s^{eff} is more general, and also includes, among others, the case of a Dodelson-Widrow sterile neutrino (in which case $m_s^{\text{eff}} = \Delta N_{\text{eff}} m_s$). For this particular case we fixed the mass of the three light neutrino species $\sum m_\nu = 0.06$ eV, i.e. the minimum value indicated by neutrino oscillation data. In this case, we obtain an axion mass, a number of neutrino species and a effective sterile neutrino mass of $m_a = 75.3 \pm 2.9 \mu$eV, $N_{\text{eff}} = 4.08 \pm 0.42$ and $m_s^{\text{eff}} < 0.63$ eV at 95% c.l. ($m_a = 76.5 \pm 2.6 \mu$eV, $N_{\text{eff}} = 3.82 \pm 0.32$ and $m_s^{\text{eff}} < 0.51$ eV

at 95% c.l.) before (after) the combination of Planck, WP and BICEP2 measurements with BAO results. As previously explained and as expected, the mean values for N_{eff} are considerably larger than those found in the absence of BICEP2 data. Concerning the bounds on the effective sterile neutrino mass, the values are mildly shifted when the BICEP2 measurements are addressed due to the anticorrelation between N_{eff} and m_s^{eff}, being the 95% c.l. constraints on the neutrino mass constraints tighter when considering BICEP2 data. Our findings agree with the results presented in Refs. [231, 232, 233], which also included BICEP2 data. Note that the mean value of the cold dark matter density, made by axions, is, again, larger than what is found in the standard ADM+r scenario.

The next scenario we explore here is a wCDM model with a free, constant, dark energy equation-of-state parameter w. Both the values of the axion masses and the value of the tensor to scalar ratio r are very close to their values in the ADM model. However, when the BAO data are not considered, the equation-of-state parameter is different from -1 at $\sim 95\%$ c.l. ($w = -1.57 \pm 0.26$), and we also found a very large value for $H_0 = 87.1 \pm 9.1$ km/s/Mpc. The addition of BAO constraints make both the value of the Hubble constant H_0 and of the dark energy equation of state w much closer to their expected values within a minimal ΛCDM scenario, being the values of these two parameters $w = -1.12 \pm 0.12$ and $H_0 = 70.5 \pm 2.8$ km/s/Mpc, respectively. This illustrates the highly successful constraining power of BAO data concerning dark energy measurements.

In Ref. [234] we have extracted the tensor spectral index from the BICEP2 measurements. The standard inflationary paradigm predicts a small, negative, tensor spectral index. More concretely, the inflation consistency relation implies that $n_T \simeq -r/8$. We now relax this constrain leaving n_T as a free parameter. We rule out a scale invariant tensor spectrum with $3 - \sigma$ significance when considering CMB data only. The addition of BAO measurements does not change significantly these results, see Fig. 8.3. As expected, the axion mass constraints are unaffected by the presence of a free n_T. The value of the tensor-to-scalar ratio we found is $r = 0.172 \pm 0.047$ using the Planck+WP+BICEP2 dataset. The fact that the data support a non-zero spectral index for tensors also implies that r strongly depends on the scale k_0. The corresponding 95% c.l. limit on $r_{0.002} \equiv r(k = 0.002 \, Mpc^{-1})$ is $r_{0.002} < 0.055$ for the Planck+WP+BICEP2 datasets, see Fig. 8.4.

The latest extended scenario we consider is the one with a running of the scalar spectral index $n_{\text{run}} = dn_s/d\ln k$. This minimal extension was firstly addressed in the context of a ΛCDM scenario by the BICEP2 collaboration, in order to relax the discrepancy between their measurements of the tensor to scalar ratio r and the limits on the same quantity arising from Planck data, see Refs. [10, 213]. The reason for that is due to the degeneracy between the running and the scalar spectral index: a negative running of the spectral index can be compensated with a larger scalar spectral index, which will decrease the CMB temperature power spectra at large scales. This lowering effect at low multipoles can be compensated with a higher tensor contribution to the temperature fluctuations (by increasing r). The former degeneracies are depicted in Figures 8.5 and 8.6, respectively. The BICEP2 collaboration reports $dn_s/d\ln k = -0.022 \pm 0.010$ at 68% c.l., whose absolute value is smaller than what we found in the context of the ADM scenario, $dn_s/d\ln k = -0.028 \pm 0.010$ at 68% c.l..
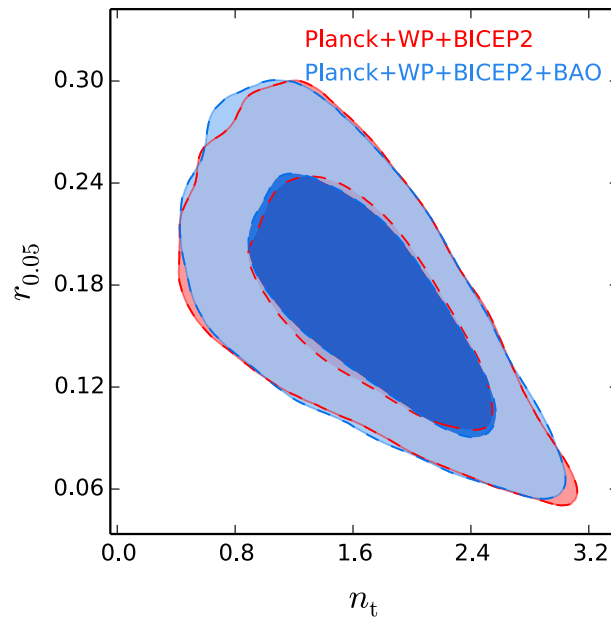
Figure 8.3. The red contours show the 68% and 95% c.l. allowed regions from the combination of Planck data, WP and BICEP2 measurements in the $(n_t, r_{0.05})$ plane, referring these limits to a scale of $k_0 = 0.05$ Mpc^{-1}. The blue contours depict the constraints after the BAO datasets are added in the analysis, [212].
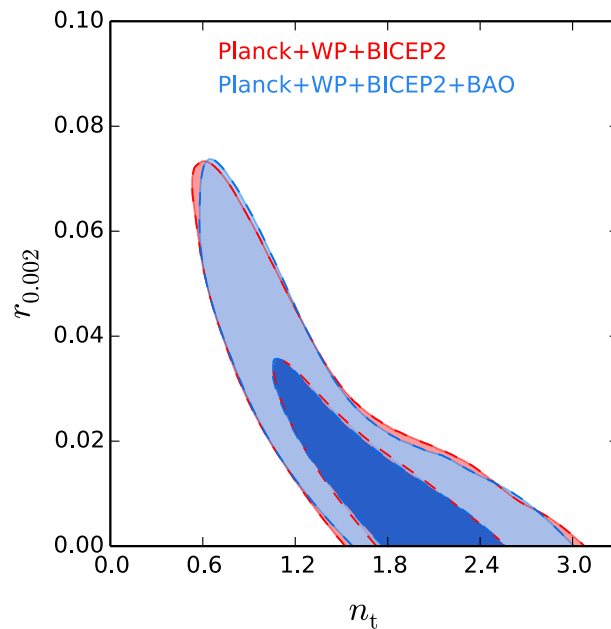
Figure 8.4. The red contours show the 68% and 95% c.l. allowed regions from the combination of Planck data, WP and BICEP2 measurements in the $(n_t, r_{0.05})$ plane, referring these limits to a scale of $k_0 = 0.002$ Mpc^{-1}. The blue contours depict the constraints after the BAO datasets are added in the analysis, [212].
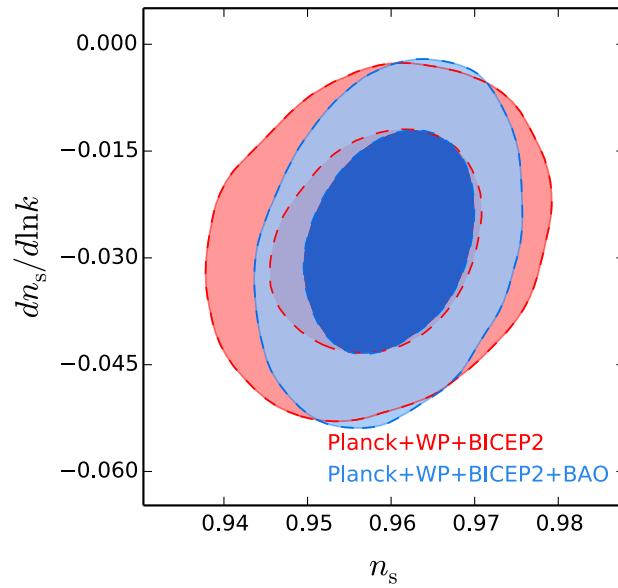
Figure 8.5. The red contours show the 68% and 95% c.l. allowed regions from the combination of Planck data, WP and BICEP2 measurements in the $(n_s, dn_s/d\ln k)$ plane. The blue contours depict the constraints after the BAO datasets are added in the analysis, [212].
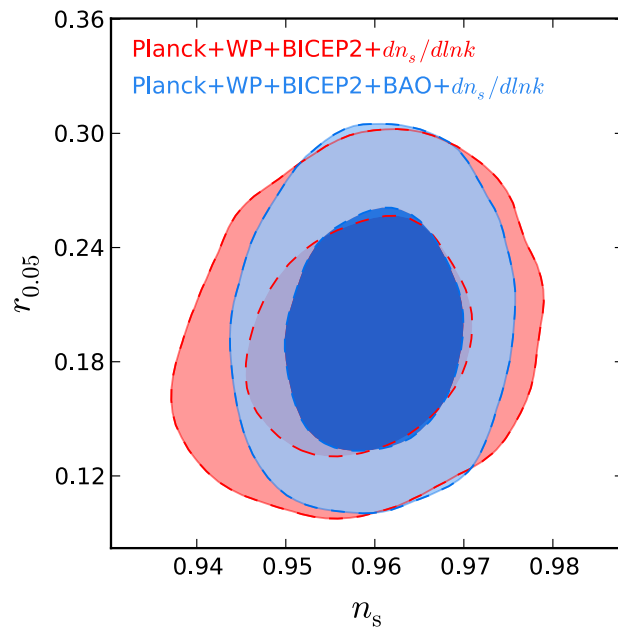
Figure 8.6. The red contours show the 68% and 95% c.l. allowed regions from the combination of Planck data, WP and BICEP2 measurements in the (n_s, r) plane. The blue contours depict the constraints after the BAO datasets are added in the analysis, [212].

Finally, we briefly comment on how the results reported are affected by theoretical uncertainties. These can be broadly divided into two classes: those due to the imprecise knowledge of the fraction of dark matter provided by misalignment-produced axions, and uncertainties in the $m_a - \Omega_{\mathrm{a,mis}}$ relation. Concerning the former, we have assumed so far that $\Omega_{\mathrm{dm}} = (1 + \alpha_{\mathrm{dec}}) \times \Omega_{\mathrm{a,mis}} = 1.164 \times \Omega_{\mathrm{a,mis}}$; however, we could consider the possibility that axions do not make up for the totality of dark matter, or that the contribution of axions produced by string decays (parameterised by α_{dec}) is larger than expected. In fact, there is still some controversy about the magnitude of the string radiation contribution to the total axion density, as some numerical studies find it to be the dominant mechanism (see e.g. Ref. [235]) while in other cases it is found to be comparable or subdominant with respect to the misalignment mechanism (like in Ref. [226], from which we took our reference value $\alpha_{\mathrm{dec}} = 0.164$). We have already commented on the effect of changing the ratio between misalignment- and string decay-produced axions. However, we could take a step further and take the very conservative view that we know nothing about the fraction of dark matter provided by misalignment-produced axions. In this case we can still note that

$$\Omega_{\mathrm{a,mis}} \leq \Omega_{\mathrm{a}} \leq \Omega_{\mathrm{dm}}, \tag{8.23}$$

from which it readily follows that the values reported in the tables (divided by a factor $1.164^{6/7} \simeq 1.14$ to consider only the misaligment contribution to the total Ω) can be considered as lower bounds on the axion mass. In other words, we can put conservative lower limits to the axion mass by requiring only that the density of misalignment-produced axions does not exceed the total dark matter density. For example, in the case of the minimal ADM+r scenario, using the value reported in Tab. 8.1 we get $m_a \geq 81.5\,\mu eV \times 1.164^{-6/7} = 71.5\,\mu eV$.

The second source of uncertainty is the $m_a - \Omega_{\mathrm{a,mis}}$ relation. The axion abundance depends, among others, on the details of the QCD phase transition through the temperature-dependent axion mass. Detailed calculations of the axion abundance, together with the relevant fitting formulas, have been presented e.g. in Refs. [236, 145]; in particular, the expressions derived there explicitly account for the dependence of $\Omega_{\mathrm{a,mis}}$ on the QCD scale Λ_{QCD}. We have run additional chains for the basic ADM+r scenario, substituting eq. (8.16) (that assumes $\Lambda_{\mathrm{QCD}} = 200$ MeV) with the $m_a - \Omega_{\mathrm{a,mis}}$ relation derived by Bae, Huh & Kim in Ref. [236] considering three different values for Λ_{QCD}, namely $\Lambda_{\mathrm{QCD}} = 320, 380, 440$ MeV [see. Eq (30) of Ref. [236]]. The results for the Planck+WP dataset are shown in Tab. 8.3. We see that the value of the axion mass require to explain the observed dark matter density decreases down to $63.7 \pm 1.2\,\mu eV$ when the QCD scale is increased up to 440 MeV. We got very similar shift for the Planck+WP+BICEP dataset. Another uncertain parameter that enters the $m_a - \Omega_{\mathrm{a,mis}}$ relation is the anharmonicity factor $f(\theta)$. As observed,the value of the axion mass scales as $\langle \theta_i^2 f(\theta_i) \rangle^{6/7}$.

In conclusion, the exact nature of dark matter is still an open issue, involving both particle physics and cosmology. As we discussed, a well-motivated candidate for the role of DM is the axion, the pseudo Nambu-Goldstone boson associated to the breaking of the PQ symmetry, proposed to explain the absence of CP violation in strong interactions. The axion can be created non-thermally in the early Universe

$\Lambda_{\text{QCD}}\,[MeV]$	$m_a\,[\mu eV]$
200	81.5 ± 1.6
320	75.6 ± 1.4
380	69.0 ± 1.3
440	63.7 ± 1.2

Table 8.3. 68% confidence level constraints on the axion mass considering differing values of the Λ_{QCD} scale, for the ADM+r scenario and the Planck+WP dataset. The first row correspond to our eq. (8.15) [eq. (34) of Ref. [225]] while the remaining rows correspond to eq. (30) of Ref. [236].

through the misalignment mechanism and the decay of axionic strings, and its mass is inversely proportional to the scale f_a at which the PQ symmetry is broken.

In this chapter, we presented the constraints on the "axion dark matter" scenario in which the PQ symmetry is broken after inflation, using the most precise CMB data available to date (including the BICEP2 on the spectrum of B-modes), as well as the recent and most precise distance BAO constraints to date from the BOSS Data Release 11 (DR11). We found that, in the minimal ADM scenario and for $\Lambda_{\text{QCD}} = 200 MeV$, the largest dataset implies $m_a = 82.2 \pm 1.1\,\mu eV$, corresponding to $f_a = (7.54 \pm 0.10) \times 10^{10}\,GeV$. We also studied the effect on our estimates of theoretical uncertainties, in particular the imprecise knowledge of the QCD scale Λ_{QCD}, in the calculation of the temperature-dependent axion mass. We found that in the simplest ADM scenario the Planck+WP dataset implies that the axion mass $m_a = 63.7 \pm 1.2\,\mu eV$ for $\Lambda_{\text{QCD}} = 440\,MeV$. We also commented on the possibility that axions do not make up for all the dark matter, or that the contribution of string-produced axions has been grossly underestimated; in that case, the values that we found for the mass can conservatively be considered as lower limits.

The search for axion dark matter is also the target of laboratory experiments like the Axion Dark Matter eXperiment (ADMX), Ref. [237], that uses a tunable microwave cavity positioned in a high magnetic field to detect the conversion of axions into photons. This is enhanced at a resonant frequency $\nu = m_a/2\pi$; for the typical masses found in our study, this corresponds to a frequency $\nu \simeq 15 - 20$ GHz. ADMX has been operating in the range $0.3 - 1$ GHz, thus being able to exclude DM axions in the mass range between 1.9 and 3.53 μeV, see Refs. [238, 239]. ADMX is currently undergoing an upgrade that will extend its frequency range up to a few GHzs (i.e., masses in the $10\,\mu eV$ range), see Ref. [240], which is unfortunately still not enough to detect DM axions in the mass range implied by cosmological observations[7], if the PQ symmetry is broken after inflation (as implied by the recent BICEP2 data). However, a second, smaller experiment called ADMX-HF is currently being built, that will allow to probe the $4 - 40$ Ghz range, see Ref. [240], thus

---

[7]This is still true even if one assumes $\alpha_{\text{dec}} \simeq 0$, that corresponds, for a given value of $\Omega_a h^2$, to the smallest value of the axion mass. We also note that it does not help either if axions only make up for part of the total DM content of the Universe. In fact, since $\Omega_a h^2 \propto m_a^{-6/7}$, having $\Omega_a h^2 < \Omega_c h^2$ would just shift the resonant frequency to even higher values.

being in principle sensitive to axion masses approximately in the $16 - 160\,\mu eV$ range, allowing to directly test the ADM scenario, at least in its simplest implementation.

Finally, we remark that the values of the axion mass found in our analysis correspond to an axion-photon coupling constant $G_{a\gamma\gamma}$ in the $10^{-14}\,GeV^{-1}$ range (or larger if we interpret our results on the mass as lower limits), the exact value depending on the electromagnetic and color anomalies associated of the axial current associated with the axion. Moreover, the BICEP collaboration claim of a detection of gravitational waves, see Ref. [10], has been recently questioned by the Planck collaboration, see Ref. [?], since the signal could be completely explained by a polarization signal from galactic dust. For this reason, we planned to analyze both the axion scenarios I and II, that was excluded from BICEP2, in order to constrain the axion mass, in light of the next polarization Planck data release.

Chapter 9

CMB Constraints on BBN Nuclear Rates

Big Bang Nucleosynthesis (BBN)) offers one of the most powerful methods to test the validity of the cosmological model around the MeV energy scale. Two key cosmological parameters enter BBN computations, the energy density in baryons, $\Omega_b h^2$, and the effective neutrino number, N_{eff}.

The measurements of CMB anisotropies obtained by the Planck satellite, see Ref. [5], are in very good agreement with the theoretical predictions of the minimal ΛCDM cosmological model. Assuming a given cosmological scenario and standard BBN dynamics, we can infer indirectly from Planck data the abundance of primordial nuclides with exquisite precision. For example, assuming ΛCDM, the Planck constraint on the baryon density, $\Omega_b h^2 = 0.02207 \pm 0.00027$, can be translated into a prediction for the primordial deuterium fraction, competitive with the most recent and precise direct observations, using the public BBN code `PArthENoPE`, Ref. [180]:

$$^{2}\text{H/H} = (2.65 \pm 0.07) \cdot 10^{-5} \quad (68\% \text{ C.L.}) , \tag{9.1}$$

The authors of Ref. [11] (see also Ref. [241]) presented an analysis of all known deuterium absorption-line systems, including some new data from very metal-poor Lyman-alpha systems at redshift $z = 3.06726$ (visible in the spectrum of the quasar QSO SDSS J1358+6522) and at redshift $z = 3.04984$ (seen in QSO SDSS J1419+0829). They obtained:

$$^{2}\text{H/ H} = (2.53 \pm 0.04) \cdot 10^{-5} \quad (68\% \text{ C.L.}) , \tag{9.2}$$

that is two standard deviations smaller than the (indirect, model-dependent) cosmological determination from CMB data, but with a comparable uncertainty.

This small tension could be the result of small experimental systematics, either in Planck or in astrophysical deuterium measurements. However, here we consider that current BBN calculations could also be plagued by systematics in the experimental determination of nuclear rates. In fact, the main uncertainty for standard BBN calculations of ^{2}H comes from the rate of the radiative capture reaction $d(p, \gamma)^{3}\text{He}$ (a recent review of the experimental status can be found in Ref. [242]). Its energy-dependent cross section $\sigma(E)$ is related to the energy-dependent astrophysical factor $S(E)$ through:

$$\sigma(E) = S(E)e^{-2\pi\eta}/E, \tag{9.3}$$

where η is the Sommerfeld factor. The low energy limit of $\sigma(E)$ is well-known thanks to the results of the underground experiment LUNA, Ref. [243], but, during BBN, the relevant energy range in the center of mass is rather around $E \simeq 30 - 300$ keV. For such energies, the uncertainty on the cross section is at the level of 6-10% when fitting $S(E)$ with a polynomial expression, and becomes a theoretical error on the primordial ^{2}H/H ratio of the order of 2% (for a fixed value of the baryon density and $N_{\rm eff}$), comparable to the experimental error in the above cosmological determination (9.1) or astrophysical determination (9.2).

Recently, a reliable *ab initio* nuclear theory calculation of this cross section has been performed in Refs. [244, 245, 246], and the uncertainty on this prediction can be conservatively estimated to be also of the order of 7%, see Ref. [247]. However, in the BBN energy range, the theoretical result is systematically larger than the best-fit value derived from the experimental data. By plugging the theoretical estimate of the cross section in a BBN code we find that more deuterium is destroyed for the same value of the cosmological baryon density, and thus the predicted primordial ^{2}H abundance results to be smaller, see Ref. [247]. The theory-indicated cross-section could be a a way to reconcile the slightly different values of ^{2}H/H measured in astrophysical data and predicted by Planck. Indeed, the result quoted in eq. (9.1) using the public BBN code `PArthENoPE`, Ref. [180], relies on a value of the cross section $d(p,\gamma)^3$He inferred from nuclear experimental data.

Further data on this crucial cross section in the relevant energy range are expected from experiments such as LUNA, but while waiting for such measurements, we found out to which extent the deuterium measurement of Ref. [11] can be made even more compatible with Planck predictions when the rate of the reaction $d(p,\gamma)^3$He was treated as a free input parameter. We addressed this issue assuming different cosmological models: the minimal ΛCDM model, ΛCDM plus extra radiation, a non spatially-flat Universe, etc. Moreover, here we use a version of `PArthENoPE` where the $d(p,\gamma)^3$He reaction rate is updated to the best fit experimental determination (see section 9.1). The deuterium fraction given by the public version of `PArthENoPE` is slightly different, but the change in the central value is at the level of 4 per mille, only.

In this chapter (see also Ref. [248] we point out that, remarkably, Planck CMB data are powerful enough to provide information on nuclear rates. Moreover, our results give independent support to the theoretical calculation of Ref. [246].

9.1   Dependence on cosmological parameters and nuclear rates

As well known, the theoretical value of the primordial ^{2}H/H abundance is a rapidly decreasing function of the baryon density parameter $\Omega_b h^2$, and, considering a slightly more general cosmological model with extra radiation, an increasing function of $N_{\rm eff}$. Finally, this value depends on the cross section of a few leading nuclear processes, that initially produce deuterium and subsequently process it into $A = 3$ nuclei. In particular, the calculation depends on the thermal rate of such processes,

Reaction	Rate Symbol	$\sigma_{2\mathrm{H/H}} \cdot 10^5$
$p(n,\gamma)^2\mathrm{H}$	R_1	± 0.002
$d(p,\gamma)^3\mathrm{He}$	R_2	± 0.062
$d(d,n)^3\mathrm{He}$	R_3	± 0.020
$d(d,p)^3\mathrm{H}$	R_4	± 0.013

Table 9.1. List of the four leading reactions and corresponding rate symbols controlling the deuterium abundance after BBN. The last column shows the error on the ratio $^2\mathrm{H/H}$ coming from experimental (or theoretical) uncertainties in the cross section of each reaction, for a fixed baryon density $\Omega_b h^2 = 0.02207$, [248].

obtained by convolving their energy-dependent cross section $\sigma(E)$ with the thermal energy distribution of incoming nuclei during BBN. The four leading reactions are listed in Table 9.1, and the uncertainties, like all other results quoted in this paper, are calculated with a version of `PArthENoPE` where the $d(p,\gamma)^3\mathrm{He}$ reaction rate is updated to the best fit determination of Ref. [242].

In the past, BBN calculations were based on the experimental determination of the cross section of nuclear processes, measured in laboratory experiments, but the situation has changed recently, since detailed theoretical calculations are now available. For example, for the cross section of the neutron-proton fusion reaction $p(n,\gamma)^2\mathrm{H}$, a very accurate result could be derived using pion-less effective field theory, with a theoretical error below the percent level, Refs. [249, 250] (see e.g. Ref. [251] for further details). Using `PArthENoPE`, one can propagate this error to the primordial deuterium abundance, obtaining an uncertainty very small, $\sigma_{2\mathrm{H/H}} = 0.002 \cdot 10^{-5}$, i.e. of the order of 0.1% (for $\Omega_b h^2$ fixed at the Planck best-fit value).

Instead, cross sections of $d-d$ fusion reactions, i.e. $d(d,n)^3\mathrm{He}$ and $d(d,p)^3\mathrm{H}$, are still determined using experimental data, and they have been measured in the 100 keV range with a 1-2% uncertainty, Ref. [252]. This produces uncertainty on the deuterium primordial abundance at most of the order of 1%, see Table 9.1, and the main source of uncertainty is due to the radiative capture process $d(p,\gamma)^3\mathrm{He}$ converting deuterium into helium.

As we already mentioned, when fitting a polynomial expression for $S(E)$ to the raw data, now dominated by the LUNA results, Ref. [243], we find that the uncertainty at 68% C.L. grows from 6% in the low energy limit to 19% around 1 MeV. This means that the uncertainty is in the range 6-10% in the energy range relevant for BBN, which gives an error on the primordial deuterium abundance of order $\sigma_{2\mathrm{H/H}} = 0.062 \cdot 10^{-5}$, as reported in Table 9.1, comparable to the experimental error estimated by Ref. [11] and dominant the error budget. In addition we have that the best fit value of $S(E)$ inferred from the data in the range 30 keV$\leq E \leq 300$ keV is lower than the theoretical result of Ref. [244, 246] by about 1-σ. So could be this difference to have an impact on the concordance of Planck results for the baryon density with the deuterium abundance measured by Ref. [11].

Using `PArthENoPE` with the best fit experimental cross section for the $d(p,\gamma)^3\mathrm{He}$ reaction, we can check that the best fit value of the astrophysical determination of the deuterium abundance, $^2\mathrm{H/H} = 2.53 \cdot 10^{-5}$ from Ref. [11], corresponds to

$\Omega_b h^2 = 0.02269$. However, in the case of the minimal cosmological model (i.e. the spatially flat ΛCDM model), we have seen that Planck data yield $\Omega_b h^2 = 0.02207 \pm 0.00027$ (68% C.L.). We can relax this moderate 2-σ tension, either by assuming a more complicated cosmological model compatible with higher values of the baryon density, or by adopting the theoretical value of the $d(p, \gamma)^3$He cross section, see Ref. [246]. In the latter case, for the ΛCDM model, the same range for the baryon density leads to

$$^2\text{H/H} = (2.58 \pm 0.07) \cdot 10^{-5} ,\qquad (9.4)$$

in nice agreement with the astrophysical determination at the 1-σ level. In other words, increasing the $d(p, \gamma)^3$He thermal rate has the same effect of increasing the cosmological baryon fraction.
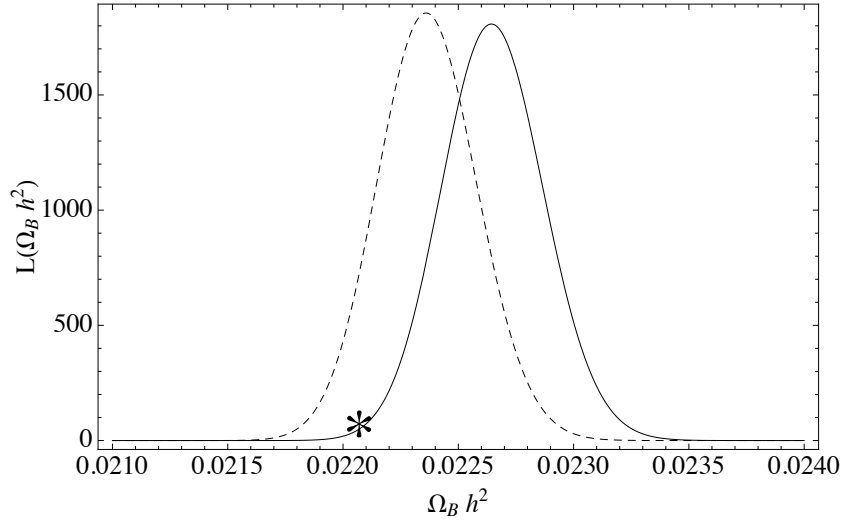
Figure 9.1. The likelihood $L(\Omega_b h^2)$, assuming the astrophysical determination of the primordial deuterium abundance ^{2}H/H by Cooke et al. in Ref. [11], adopting either the experimental best fit $R_2^{ex}(T)$ (solid) or *ab initio* calculation $R_2^{th}(T)$, (dashed), Ref. [246]. The star shows the Planck best fit value of $\Omega_b h^2$ in the minimal ΛCDM model, [248].

This is illustrated in Fig. 9.1 where the likelihood function $L(\Omega_b h^2, R_2)$

$$L(\Omega_b h^2, R_2) = \exp\left(-\frac{(^2\text{H/H}_{th}(\Omega_b h^2, R_2) - {}^2\text{H/H}_{ex})^2}{\sigma_{ex}^2}\right) ,\qquad (9.5)$$

is plotted versus baryon density in two different scenarios, using the theoretical value of ^{2}H/H (index th) or the experimental result of Ref. [11] (index ex). The solid line corresponds to $R_2^{ex}(T)$ obtained by using the best fit of experimental values for the $d(p, \gamma)^3$He cross section, while the dashed line to the theoretical prediction of the same cross section, Ref. [246], whose corresponding rate is denoted by $R_2^{th}(T)$. The theoretical rate brings the agreement with the Planck ΛCDM value of $\Omega_b h^2$ from the 2-σ to the 1-σ level. Note that, in calculating those likelihoods, we only included the experimental error on astrophysical measurements of the deuterium fraction, $\sigma_{ex} = 0.05$, because our purpose is to show what the baryon probablility could like after a future measurement campaign of the $d(p, \gamma)^3$He astrophysical factor. We

found that, if the theoretical calculation of Ref. [246] was experimentally confirmed, the likelihood profile would shift to the dashed curve.

The aim of this chapter is to see whether, by combining CMB and BBN data, we could grasp some robust information on the value of the thermal rate R_2 preferred by cosmology. To this end, we parameterized the generic $R_2(T)$ in terms of an overall rescaling factor A_2:

$$R_2(T) = A_2 \, R_2^{ex}(T), \tag{9.6}$$

and used it in `PArthENoPE`. This approximation can seem too simplistic, since the thermal rate is a function of the temperature. We notice that, for example, the ratio of the baseline fit of R_2 used in `PArthENoPE` and the one which is found starting from the calculation of Ref. [246] is not simply a constant as temperature varies in the BBN range and monotonically decreases. This variation is at level of 1%. The main point however, is the net effect on deuterium. Indeed, we have checked that the theoretical estimate R_2^{th} gives a primordial deuterium which is the same obtained by a constant rescaling of the experimental rate by a constant factor $R = 1.05$ *in the whole range for* $\Omega_b h^2$ of interest, from 0.021 up to 0.023, the difference between the two results for ^{2}H/H being at worst of order 0.1%. Hence, a constant rescaling factor A_2 was enough for our purpose, and offered the advantage of limiting the number of extra free parameters to one.

Assuming this ansatz, we introduce the baryon likelihood function, $L(\Omega_b h^2, A_2)$, through

$$L(\Omega_b h^2, A_2) = \exp\left(-\frac{(^2\mathrm{H}/\,\mathrm{H}_{th}(\Omega_b h^2, A_2) - {}^2\mathrm{H/H}_{ex})^2}{\sigma_{ex}^2 + \sigma_{th}^2}\right) \,, \tag{9.7}$$

where the theoretical value is a function of the baryon density and the $d(p,\gamma)^3$He thermal rate rescaling factor A_2. Again we used the experimental value of the primordial deuterium abundance and its squared uncertainty, see eq. (9.2). Finally, σ_{th}^2 is the squared propagated error on deuterium due to the present experimental uncertainty on R_2.

9.2 Data analysis

Our main dataset consist in the Planck public data release of March 2013, see Ref. [101], based on Planck temperature completed by WMAP9 polarization at low-l. We also considered the B modes polarization data from the BICEP2 experiment, Ref. [10]. In this respect, we include the 5 bandpowers of the BB spectrum and the window functions provided by the BICEP2 collaboration (http://bicepkeck.org/). We perform a likelihood analysis of this dataset following the method of Hamimeche and Lewis, see Ref. [253]. We combine these two CMB datasets (referred as Planck+WP and Planck+WP+BICEP2 respectively) with the deuterium abundance likelihood function $L(\Omega_b h^2, A_2)$ (referred as BBN).

Occasionally, we also include the direct measurement of the Hubble constant by Ref. [6] (HST), and information on Baryon Acoustic Oscillations by SDSS-DR7 at redshift $z = 0.35$ from Ref. [99], by SDSS-DR9 at $z = 0.57$ from Ref. [7], and by WiggleZ at $z = 0.44, 0.60, 0.73$ from Ref. [103] (referred alltogether as BAO).

For the data analysis method, we use indifferently the publicly available Monte Carlo Markov Chain packages CosMoMC, Ref. [97], and MONTE PYTHON, Ref. [254] (http://montepyhton.net), which rely on the Metropolis-Hastings algorithm for exploring the parameter space, and on a convergence diagnostic based on the Gelman and Rubin statistics. We use the April 2014 version of the two codes, which included the support for the Planck Likelihood Code v1.0 and implemented an efficient sampling of the parameter space using a fast/slow parameter decorrelation, see Ref. [104]. Obviously, we checked that the results from the two codes were identical. To evaluate the deuterium abundance produced during the Big Bang Nucleosynthesis, we used the `PArthENoPE` code, minimally modified in order to account for the global rescaling factor A_2.

We first consider the Planck+WP dataset assuming the minimal ΛCDM model with six free parameters: the density of baryons and cold dark matter $\Omega_b h^2$ and $\Omega_c h^2$, the ratio θ of the sound horizon to the angular diameter distance at decoupling, the optical depth to reionization τ, the amplitude A_S of the primordial scalar fluctuation spectrum at $k = 0.05 Mpc^{-1}$, and the spectral index n_S of this spectrum. Finally, we include the rescaling factor A_2, affecting only the determination of the primordial deuterium abundance. For this model, we consider purely adiabatic initial conditions, we imposed spatial flatness, we fix the effective number of neutrinos to its standard value $N_{\rm eff} = 3.046$, see Ref. [19], and we considered the sum of neutrino masses to be 0.06eV as in the Ref. [5].

Subsequently, we study several extensions of the minimal ΛCDM model, with extra free parameters: the neutrino effective number $N_{\rm eff}$, the spatial curvature of the Universe parametrised by $\Omega_k = 1 - \Omega_c - \Omega_b - \Omega_\Lambda$, and the amplitude of the lensing power spectrum $A_{\rm L}$, as defined in Ref. [88].

Finally, we consider a ΛCDM+r framework where we allow the possibility for a gravitational wave background with tensor to scalar amplitude ratio r. In this case we include the BICEP2 dataset, assuming the B mode signal claimed by this experiment to be the genuine signature of primordial inflationary tensor modes[1]. Since the amplitude of tensor modes measured by BICEP2 is in tension with the upper limit on r coming from the Planck experiment, we also consider two further extensions that could in principle solve the tension: an extra number of relativistic particles parametrized by $N_{\rm eff}$ (see e.g. Refs. [21, 231, 232]) and a running of the spectral index $dn_S/dlnk$, see Ref. [10].

In Table 9.2, we report our results for the parameters of the minimal ΛCDM model, plus the nuclear rate parameter A_2 and the derived cosmological parameter H_0, using the data combinations Planck+WP+BBN and PLANCK+WP+BBN+BAO.

As expected, we obtain that the data provides an indication for A_2 being greater than one, roughly at the level of two standard deviations, even when adding the BAO dataset. We can also check explicitly in Figure 9.2 that there is a clear anti-correlation between A_2 and $\Omega_b h^2$: in order to improve the agreement between Planck data and deuterium abundance measurements, we need either a value of the nuclear rate rescaling factor A_2 higher than one, or a value of the baryon density

---

[1]This detection of primordial inflationary tensor modes has been recently questioned by the Planck collaboration, see Ref. [**?**], since this signal could be completely explained by a polarization signal from galactic dust. This point is discussed in the chapter 8.

Parameter	Planck+WP +BBN	Planck+WP +BBN+BAO
$\Omega_b h^2$	0.02202 ± 0.00028	0.02209 ± 0.00025
$\Omega_c h^2$	0.1200 ± 0.0026	0.1188 ± 0.0017
θ	1.04129 ± 0.00063	1.04144 ± 0.00058
τ	0.089 ± 0.013	0.091 ± 0.013
n_s	0.9599 ± 0.0073	0.9625 ± 0.0058
$\log[10^{10} A_s]$	3.089 ± 0.025	3.089 ± 0.025
$H_0 [\text{km/s/Mpc}]$	67.2 ± 1.2	67.74 ± 0.78
A_2	1.155 ± 0.082	1.138 ± 0.076

Table 9.2. Constraints on cosmological parameters (at the 68% confidence level) in the case of the minimal ΛCDM model, [248].
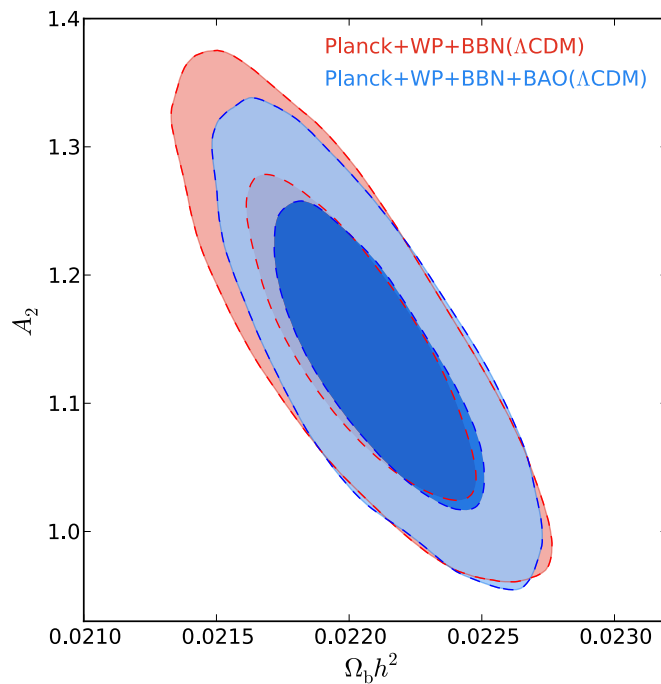
Figure 9.2. 2-D contour plots in the $\Omega_b h^2$ vs. A_2 plane, showing preferred parameter regions at the 68% and 95% confidence levels in the case of the minimal ΛCDM model, [248].
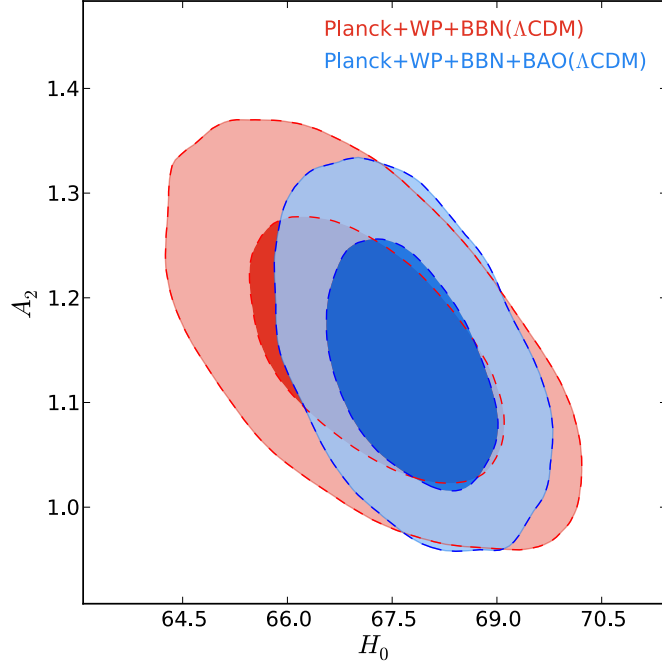
Figure 9.3. 2-D contour plots in the H_0 vs. A_2 plane, showing preferred parameter regions at the 68% and 95% confidence levels in the case of the minimal ΛCDM model, [248].

larger than the Planck mean value. In fact, deuterium is a decreasing function of both the R_2 rate and the baryon density Ω_b. The Figure 9.3 shows an interesting correlation between A_2 and the Hubble constant H_0. When A_2 is varied, yields a lower value for the Hubble constant in a combined Planck+WP+BBN analysis.

Given the fact that our results depend on the underlying cosmological model, it is interesting to investigate if some extensions of the standard ΛCDM model could bring the value of A_2 back in better agreement with the current experimental determination of $R_2(T)$ (corresponding by definition to $A_2 = 1$).

In Table 9.3, we report the constraints when a variation in the neutrino effective number N_{eff} is allowed. Even in this case, we can see that the combined Planck+WP+BBN and Planck+WP+BBN+BAO analyses show a preference for $A_2 > 1$ at roughly the 2-σ level, even if the central value and error bar for A_2 are almost doubled. When we include the direct measurement of the Hubble parameter (case Planck+WP+BBN+HST), the indication for $A_2 > 1$ is still stronger, at the 2.5-σ level. We can conclude that the preference for a large $d(p,\gamma)^3$He reaction rate is robust against the extension of the standard cosmological model to a free N_{eff}.

However, it is interesting to note (see Table 9.3) that the preferred value for the neutrino effective number N_{eff} is always larger than the standard value 3.046. As reported in section 6.4.4. of Ref. [5], the standard Planck+WP+BBN analysis (i.e. assuming $A_2 = 1$) gave $N_{\text{eff}} = 3.02 \pm 0.27$ (68% C.L.), while the CMB only result, including high-l data from ACT and SPT, was $N_{\text{eff}} = 3.36 \pm 0.34$. With our analysis, we obtained that this shift of N_{eff} towards its standard value was mostly driven by the low experimental value of R_2. In fact, when A_2 is let free, the preference for $N_{\text{eff}} > 3.046$ persists even when deuterium measurements are

Parameter	Planck+WP +BBN	Planck+WP +BBN+HST	Planck+WP +BBN+BAO
$\Omega_b h^2$	0.02241 ± 0.00042	0.02261 ± 0.00031	0.02233 ± 0.00029
$\Omega_c h^2$	0.1263 ± 0.0055	0.1281 ± 0.0049	0.1251 ± 0.0051
τ	0.096 ± 0.015	0.099 ± 0.014	0.094 ± 0.013
n_s	0.979 ± 0.017	0.988 ± 0.011	0.974 ± 0.010
$\log[10^{10} A_s]$	3.117 ± 0.034	3.128 ± 0.030	3.109 ± 0.029
$H_0 [\mathrm{km/s/Mpc}]$	71.0 ± 3.2	72.8 ± 2.0	70.1 ± 1.9
N_{eff}	3.56 ± 0.40	3.76 ± 0.27	3.43 ± 0.30
A_2	1.29 ± 0.15	1.33 ± 0.14	1.26 ± 0.14

Table 9.3. Constraints on cosmological parameters (at the 68% confidence level) in the case of the extended ΛCDM model with extra relativistic degrees of freedom, [248].
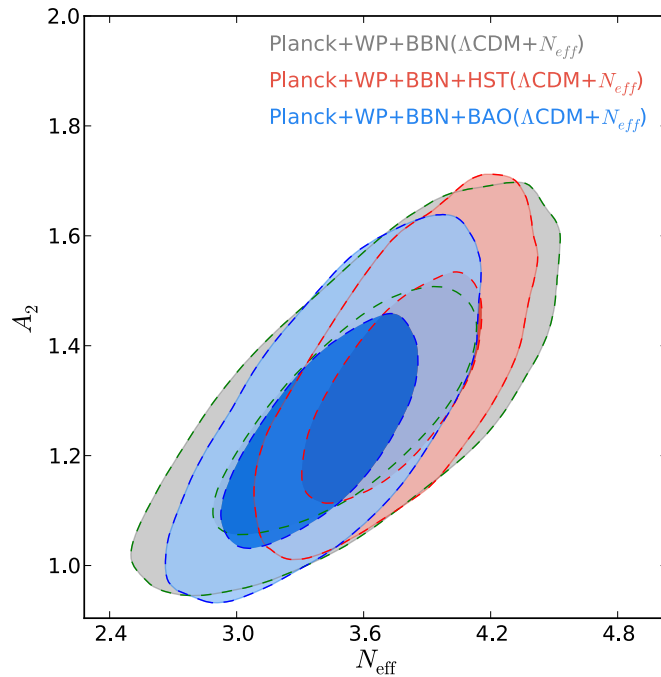
Figure 9.4. 2-D contour plots in the N_{eff} vs A_2 plane, showing preferred parameter regions at the 68% and 95% confidence levels in the case of the extended ΛCDM model with extra relativistic degrees of freedom, [248].

included, as we can see in Fig. 9.4, where we report the two dimensional likelihood contours in the $N_{\rm eff}$ vs. A_2 plane for the three different datasets: Planck+WP+BBN, Planck+WP+BBN+HST, and Planck+WP+BBN+BAO.

We can see a correlation between A_2 and $N_{\rm eff}$: large values of A_2 remain compatible with Planck+WP+BBN data, provided that at the same time $N_{\rm eff}$ is larger than three. Such considerations reinforce the motivations for future experimental campaign to collect further data in the few hundred keV range on the $d(p, \gamma)^3$He cross section. Notice that considering $A_2 = 1.05$, i.e. to the theoretical result of Ref. [246], a standard value of $N_{\rm eff}$ is allowed at 68% C.L., if the HST measurement of H_0 is not included in the analysis. If experiments would confirm the theoretical expectation for $R_2^{th}(T)$ in the BBN energy range, the overall agreement of CMB and BBN data for a standard number of relativistic degrees of freedom would improve with respect to the $A_2 = 1$ case.
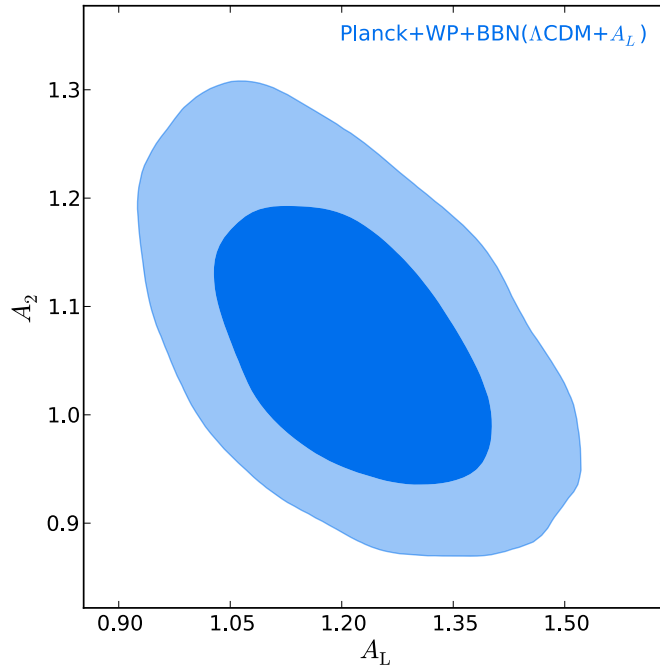
Figure 9.5. 2-D contour plots in the $A_{\rm L}$ vs A_2 plane showing probabilities at 68% and 95%, [248].

In Table 9.4 we find the constraints on A_2 for further extensions of the minimal ΛCDM model, using the Planck+WP+BBN. We vary the curvature parameter Ω_k, despite the fact that $\Omega_k \neq 0$ is difficult to explain from a theoretical point of view, and almost excluded when BAO data is also included: with free spatial curvature and without BAO data, the evidence for $A_2 > 1$ is slightly weaker. Finally, we consider the case of a free CMB lensing amplitude parameter $A_{\rm L}$, that is not a physical extension of the ΛCDM model. In fact, although Planck data prefer $A_{\rm L} > 1$, this result has no physical interpretation, but could be caused by a small and not yet identified systematic error affecting the Planck data (see the discussion in Ref. [5]), or alternatively, it may account in some approximate way for a non-standard growth rate of large scale structures after recombination. We can see in Table 9.4

Parameter	Planck+WP+BBN	Planck+WP+BBN	Planck+WP+BBN	Planck+WP+BBN
$\Omega_b h^2$	0.02242 ± 0.00035	0.02301 ± 0.00051	0.02227 ± 0.00032	0.02261 ± 0.00042
$\Omega_c h^2$	0.1169 ± 0.0030	0.1245 ± 0.0055	0.1185 ± 0.0027	0.1241 ± 0.0053
θ	1.04179 ± 0.00067	1.04112 ± 0.00078	1.04153 ± 0.00065	1.04104 ± 0.00079
τ	0.087 ± 0.013	0.094 ± 0.015	0.087 ± 0.013	0.092 ± 0.015
n_s	0.9687 ± 0.0085	0.996 ± 0.018	0.9640 ± 0.0075	0.981 ± 0.015
$\log[10^{10} A_s]$	3.078 ± 0.025	3.111 ± 0.034	3.081 ± 0.025	3.105 ± 0.033
$H_0[\mathrm{km/s/Mpc}]$	68.8 ± 1.4	74.3 ± 3.6	56.7 ± 5.4	5905 ± 6.4
N_{eff}	$[3.046]$	3.73 ± 0.40	$[3.046]$	3.50 ± 0.36
A_{L}	1.21 ± 0.12	1.25 ± 0.13	$[1]$	$[1]$
Ω_k	$[0]$	$[0]$	-0.035 ± 0.023	-0.035 ± 0.023
A_2	1.067 ± 0.086	1.21 ± 0.14	1.100 ± 0.084	1.21 ± 0.14

Table 9.4. Constraints on cosmological parameters (at the 68% confidence level) for several extensions of the ΛCDM model, with free parameters (N_{eff}, A_{L}, Ω_k). We vary at most two of these extra parameters at the same time, and fix the other ones to their standard model value, indicated above between squared brackets, [248].
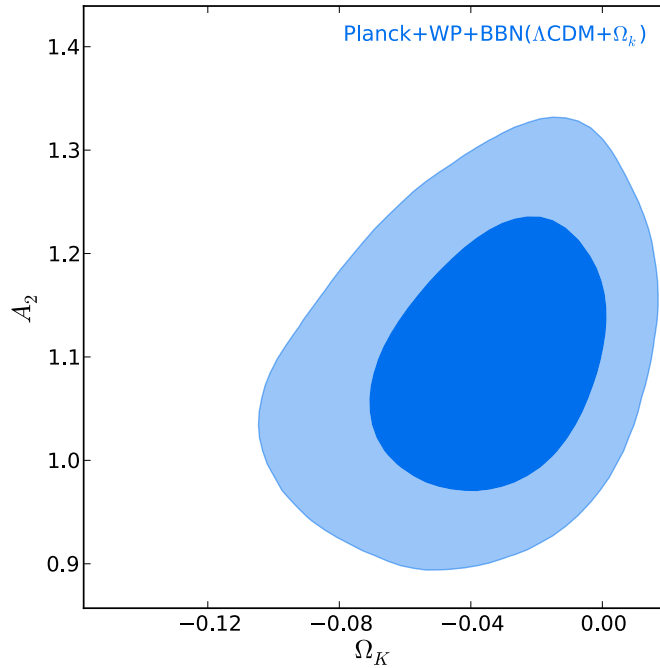
Figure 9.6. 2-D contour plots in the Ω_k vs A_2 plane showing probabilities at 68% and 95%, [248].

that when A_L is left free, the A_2 parameter becomes compatible with one. We show our results for the joint confidence limits on A_2 vs. Ω_k and A_2 vs. A_L in Figures 9.5 and 9.6.

In summary, Planck+WP+BBN data consistently indicate that $A_2 > 1$ (suggesting a $d(p, \gamma)^3$He reaction rate closer to theoretical predictions than to experimental results) in the minimal ΛCDM model, as well as in a model with free $N_{\rm eff}$. However, the evidence for $A_2 > 1$ goes away when either Ω_k or A_L are promoted as free parameters (with $N_{\rm eff} = 3.046$), but these scenarios are less theoretically motivated. Incidentally, we can see in Table 9.4 also that with a free Ω_k or A_L, and at the same time a free $N_{\rm eff}$, the evidence for $A_2 > 1$ persists.

Finally, we consider the Planck+WP+BICEP2+BBN dataset, and in Table 9.5 we report the constraints allowing for a gravitational wave background with tensor to scalar ratio $r_{0.05}$ at scales of $k = 0.05 \, \text{Mpc}^{-1}$. As we can see the indication for $A_2 > 1$ is still present. Moreover, allowing for a variation in $N_{\rm eff}$ provides even further evidence for $A_2 > 1$ at more than two standard deviations. It is however interesting that when we consider a running of the primordial spectral index A_2 becomes compatible with one in between one standard deviation. In Figure 9.7 we show the 2-D contour plots from the Planck+WP+BICEP2+BBN dataset in the $r_{0.05}$ vs A_2, in Figure 9.8 $N_{\rm eff}$ vs A_2 and in Figure 9.9 $dn_s/dlnk$ vs A_2 planes showing probabilities at 68% and 95%. As we can see, there is essentially no degeneracy between A_2 and $r_{0.05}$, but a degeneracy is clearly present between A_2 and $N_{\rm eff}$ and $dn_s/dlnk$.

The BICEP2 dataset, when combined with the Planck data, provides an evidence either for a larger $N_{\rm eff}$ either for a negative running of the spectral index $dn_s/dlnk$.

Parameter	Planck+WP+ BICEP2+BBN	Planck+WP+ BICEP2+BBN	Planck+WP+ BICEP2+BBN
$\Omega_b h^2$	0.02209 ± 0.00028	0.02286 ± 0.00044	0.02236 ± 0.00031
$\Omega_c h^2$	0.1184 ± 0.0027	0.1300 ± 0.0058	0.1195 ± 0.0027
θ	1.04146 ± 0.00063	1.04050 ± 0.00073	1.04144 ± 0.00063
τ	0.088 ± 0.012	0.100 ± 0.015	0.101 ± 0.015
n_s	0.9663 ± 0.0072	1.004 ± 0.018	0.9593 ± 0.0080
$log[10^{10}A_s]$	3.082 ± 0.024	3.131 ± 0.034	3.115 ± 0.031
$H_0[\text{km/s/Mpc}]$	67.9 ± 1.2	75.5 ± 3.7	67.7 ± 1.2
$r_{0.05}$	0.134 ± 0.045	0.153 ± 0.040	0.163 ± 0.040
N_{eff}	$[3.046]$	4.04 ± 0.44	$[3.046]$
$dn_s/dlnk$	$[0]$	$[0]$	-0.0256 ± 0.0097
A_2	1.145 ± 0.081	1.40 ± 0.17	1.080 ± 0.079

Table 9.5. Constraints on cosmological parameters (at the 68% confidence level) for the Planck+WP+BICEP2 dataset, with free parameters ($r_{0.05}$, N_{eff}, $dn_s/dlnk$). We vary at most two of these extra parameters at the same time, and fix the other ones to their standard model value, indicated above between squared brackets, [248].
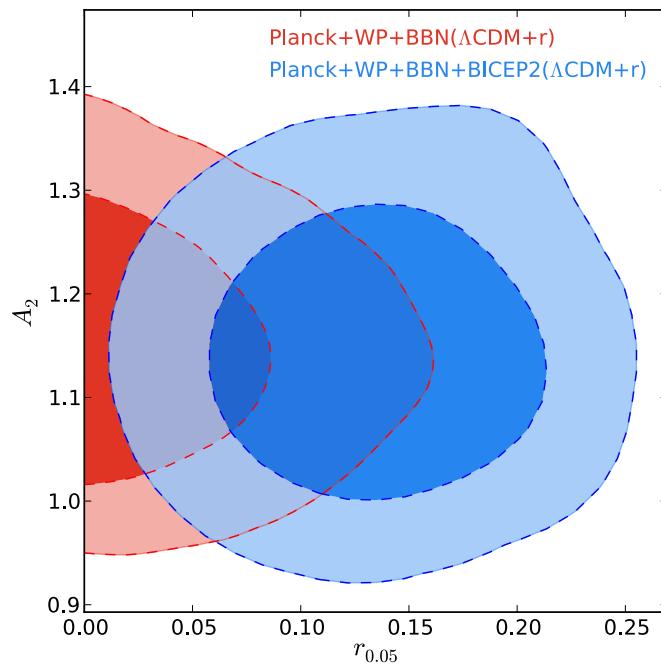
Figure 9.7. 2-D contour plots from the Planck+WP+BICEP2+BBN dataset in the r vs A_2 plane showing probabilities at 68% and 95%, [248].
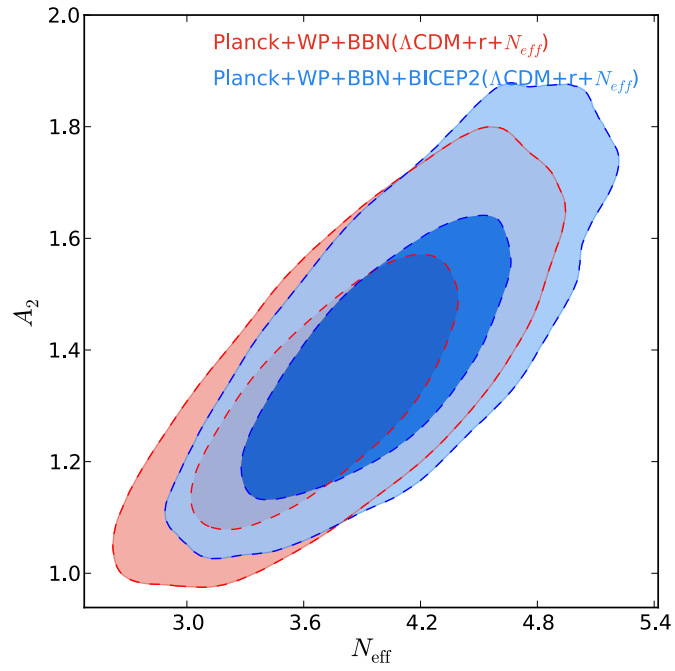
Figure 9.8. 2-D contour plots from the Planck+WP+BICEP2+BBN dataset in the N_{eff} vs A_2 plane showing probabilities at 68% and 95%, [248].
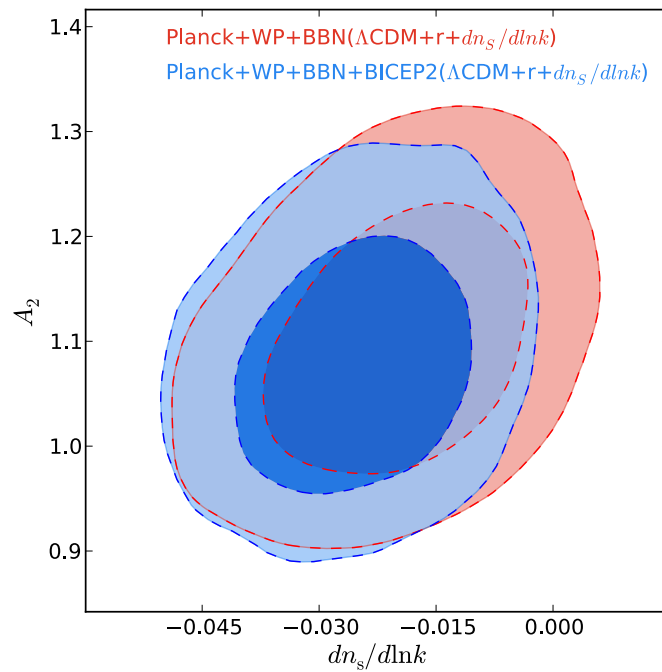
Figure 9.9. 2-D contour plots from the Planck+WP+BICEP2+BBN dataset in the $dn_s/dlnk$ vs A_2 plane showing probabilities at 68% and 95%, [248].

In the first case is needed a value of A_2 strictly larger than one in order to be in agreement with BBN, while in the second case, when running is considered, A_2 is well compatible with one. A precise measurement of A_2 from laboratory experiments could in principle help in discriminating between these two scenarios.

In conclusion, we have shown that a combined analysis of Planck CMB data and of recent deuterium abundance measurements in metal-poor damped Lyman-alpha systems provides some piece of information on the radiative capture reaction $d(p,\gamma)^3$He, converting deuterium into helium. The rate for this process represents the main source of uncertainty to date in the BBN computation of the primordial deuterium abundance within a given cosmological scenario, parameterized by the baryon density $\Omega_b h^2$ and effective neutrino number N_{eff}. The corresponding cross section has not been still measured with a sufficiently low uncertainty and normalization errors in the BBN center of mass energy range, 30 - 300 keV. Moreover, the best fit of available data appears to be systematically lower than the detailed theoretical calculation presented in Ref. [246].

An experiment such as LUNA at the underground Gran Sasso Laboratories may give an answer to this problem in a reasonably short time: with the present underground 400 kV LUNA accelerator, Ref. [255], is possible to measure the $d(p,\gamma)^3He$ cross section in the $20 < E_{cm}(keV) < 260$ energy range with an accuracy better than 3%, i.e. considerably better than the 9% systematic uncertainty estimated in Ref. [256]. This goal can be achieved by using the large BGO detector already used in Ref. [243], that ensures a detection efficiency of about 70% and a large angular coverage for the photons emitted by the $d(p,\gamma)^3He$ reaction.

Our study showed that, interestingly, the combined analysis of Planck and deuterium abundance data returns a larger rate A_2 for this reaction than the best fit computed in Ref. [242], where the authors exploit the available experimental information on $d(p,\gamma)^3$He cross section. On the other hand we found that Planck data result in better agreement with *ab initio* theoretical calculations, in the minimal ΛCDM cosmological model, as well as when allowing for a free effective neutrino number.

Chapter 10

The BICEP2 result and the spectral index of tensor modes

The detection of B-mode polarization made by the BICEP2 experiment, Ref. [10], could clearly represents one of the major discovery in cosmology in the past twenty years. While the BICEP2 result needs to be confirmed by future experiments, it is important to fully analyze the BICEP2 data and to identify all possible inconsistencies at the theoretical level. However, this detection has been recently questioned by the Planck collaboration, see Ref. [?], since this signal could be completely explained by a polarization signal from galactic dust.

In this chapter (but see also Ref. [234]) we focus our attention on the spectral index of tensor fluctuations n_T. Indeed, a crucial prediction of inflation is the production of a stochastic background of gravity waves (Ref. [257]) with a slightly tilted spectrum,

$$n_T = -2\epsilon \ , \tag{10.1}$$

where $\epsilon = -\dot{H}/H^2$ denotes a slow roll parameter from inflation (H is the Hubble rate during the inflationary stage).

In standard inflation ϵ is strictly positive, see Ref. [258], and in the usual parameter estimation routines, the tensor spectral index is assumed to be *red*, or negligible.

However, in recent years, a set of inflationary models has been elaborated where the spectral index of tensor modes could be positive, $n_T > 0$, i.e. *blue* (Refs. [259, 260]).

A first attempt to compare these models with observational data has been made in Refs. [261, 262].

The main theoretical problem for the production of a blue spectrum of gravitational waves (BGW) is that the stress-energy tensor must violate the so-called Null Energy Condition (NEC). In a spatially flat FRW metric, a violation of NEC indeed corresponds to the inequality $\dot{H} < 0$ and is ultimately the reason for the red tensor spectrum in standard inflation.

Models that violates NEC have been already presented. For example, in the so-called super-inflation models, see Ref. [263], where inflation is driven by a component violating the NEC a BGW spectrum is expected. Blue tensor spectra are also a

robust prediction of the pre-big bang scenario, Ref. [264]. Models based on string gas cosmology as in Ref. [265], where scalar metric perturbations are thought to originate from initial string thermodynamic fluctuations, see Ref. [266], also can explain a BGW background. A BGW spectrum is also a generic prediction of a class of four-dimensional models with a bouncing phase of the Universe, see Ref. [267]. To induce the bounce, the stress-energy tensor must violate the null energy condition (NEC). G-inflation, see Ref. [268], has a Galileon-like nonlinear derivative interaction in the Lagrangian with the resultant equations of motion being of second order. In this model, violation of the null energy condition can occur and the spectral index of tensor modes can be blue. BGW may also be present in scalar-tensor theories and $f(R)$ gravity theories.

It is therefore timely to investigate the constraints on the tensor spectral index n_T from the BICEP2 data. Strangely enough, no constraint on this parameter has been presented by the BICEP2 collaboration while, we find that the BICEP2 data could provide interesting results on this parameter.

10.1   Analysis method

Our analysis method is based on the Boltzmann CAMB code, Ref. [27], and a Monte Carlo Markov Chain (MCMC) analysis based on the MCMC package `cosmomc`, Ref. [97] (version December 2013). We have implemented in the MCMC package the likelihood code provided by the BICEP2 team (we just used BB data), and considered as free parameters the ratio of the tensor to scalar amplitude r at $0.01hMpc^{-1}$, defined as $r_{0.01}$, and the tensor spectral index n_T. We preferred to use the pivot scale at $k = 0.01hMpc^{-1}$ since the BICEP2 data is most sensitive to multipole $l \sim 150$ and using the approximate formula $l \sim 1.35 \times 10^4 k$.

All the remaining parameters have been kept fixed at the Planck+WP best fit values for the LCDM+r scenario (see Ref. [5]) with the running of the scalar spectral index fixed to zero.

Moreover, since the tensor amplitude should also be consistent with the upper limits on r coming from measurements of the temperature power spectrum, we have assumed a prior of $r_{0.002} < 0.11$ at 95% c.l. (see Ref. [223]). We referred to this prior as the "TT" prior.

Note that the TT prior is taken at much larger scales, $k = 0.002hMpc^{-1}$ than those sampled by the BICEP2 experiments. As we showed this prior is extremely important for the constraints on n_T.

The results of our analysis are reported in Table 10.1 and Figures fig:bicep21, fig:bicep22, fig:bicep23 and fig:bicep24. We consider four cases: n_T free, n_T free but with the TT prior, n_T assumed to be negative ($n_T < 0$) and n_T assumed to be negative plus the TT prior, respectively.

We can derive the following conclusions:

- The BICEP2 data alone slightly prefers a positive spectral index. The case $n_T = 0$ is consistent with the data in between two standard deviations.

- When a TT prior of $r_{0.002} < 0.11$ at 95% c.l.. has been assumed, the BICEP2 data strongly prefers a blue spectral index with $n_T \leq 0$ excluded at more than
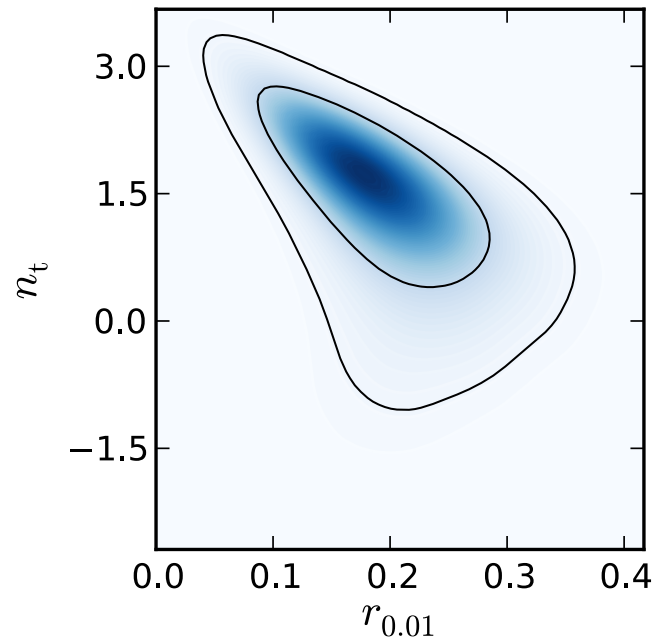
Figure 10.1. Constraints on the n_T vs $r_{0.01}$ plane with no prior on n_T, [234].
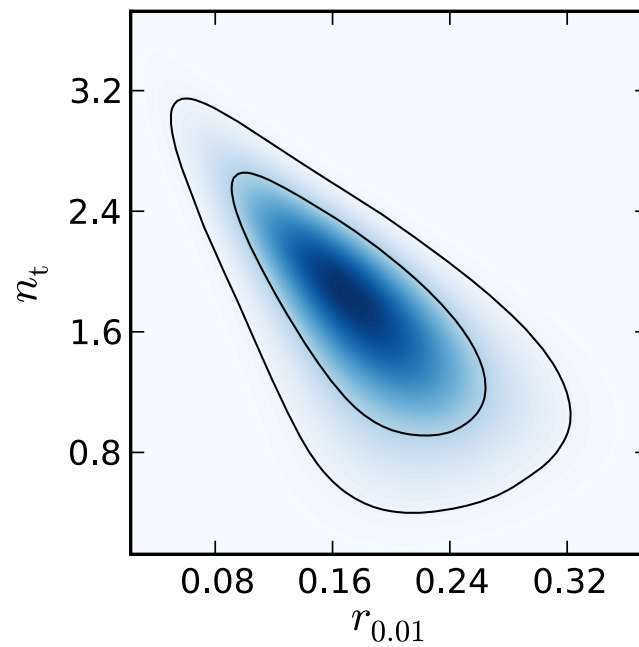
Figure 10.2. Constraints on the n_T vs $r_{0.01}$ plane with no prior on n_T but TT prior on $r_{0.002}$, [234].
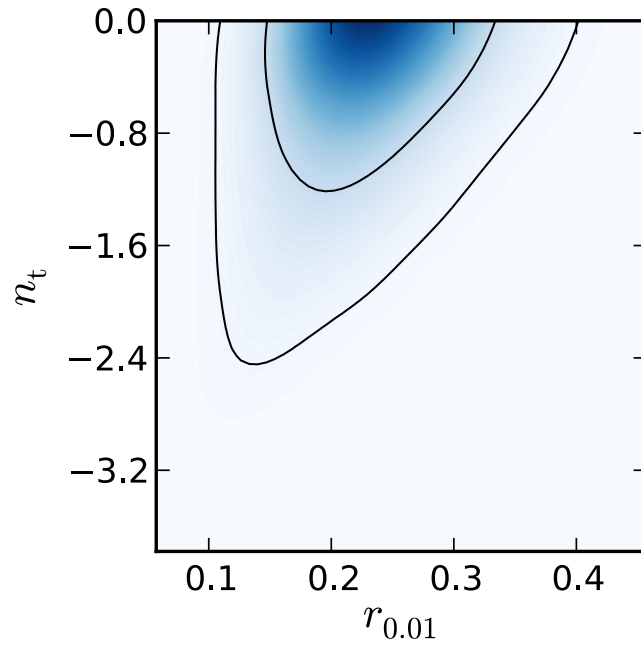
Figure 10.3. Constraints on the n_T vs $r_{0.01}$ plane with $n_T < 0$, [234].
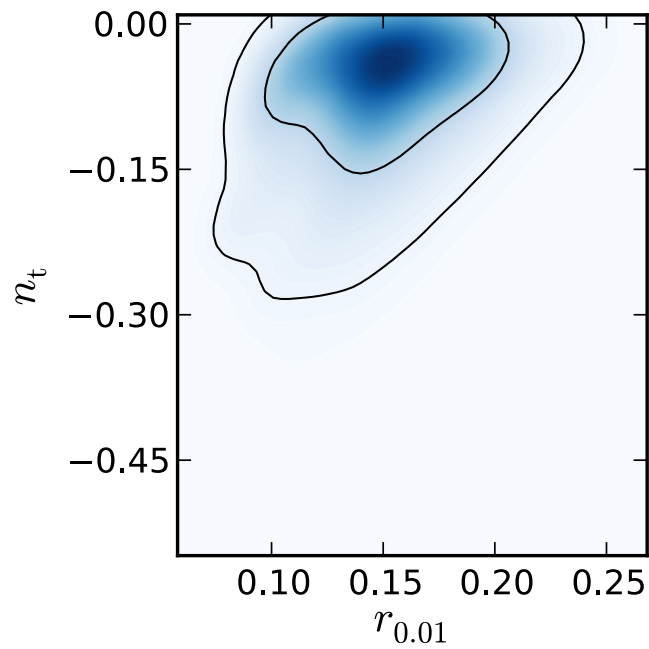
Figure 10.4. Constraints on the n_T vs $r_{0.01}$ plane with $n_T < 0$ and TT prior on $r_{0.002}$, [234].

Case	$r_{0.01}$	n_T
n_T free	0.19 ± 0.06	1.36 ± 0.83
TT prior+n_T free	0.18 ± 0.05	1.67 ± 0.53
$n_T < 0$	0.22 ± 0.06	$n_T > -0.76$
TT prior+$n_T < 0$	0.15 ± 0.03	$n_T > -0.09$

Table 10.1. Constraints at 68% c.l. on $r_{0.01}$ and n_T parameters for the cases described in the text. A blue spectral index ($n_T > 0$) is strongly suggested when a TT prior of $r_{0.002} < 0.11$ at 95% c.l. is included in the analysis.

three standard deviations.

- When we restricted the analysis to negative n_T we obtained a lower limit of $n_T > -0.76$ at 68% c.l. ($n_T > -0.09$ in case of the TT prior).

A crucial point in discussing the reliability of the BICEP2 result is the possible contamination from galactic dust. In Ref. [10] a galactic dust template was presented (named "DDM1") using the best available information on this component. However, since there is virtually no experimental constraint on the amplitude of the dust component, it is interesting to investigate the possible impact of dust on the conclusions presented here on the tensor index n_T.

In this respect, we repeated our analysis allowing the possibility of a dust component. We considered two possible cases: a dust component compatible with the DDM1 template and a component with an amplitude four times larger than the DDM1 template. This work is before the results from the Planck collaboration, see Ref. [**?**], for which the BICEP2 detection could be completely due to a polarization signal from galactic dust.

The results of this analysis, are reported in Figure 10.5. As we can see, allowing for a DDM1 component does not change significantly our results for the BICEP2 plus TT prior case, with $r_{0.01} = 0.13 \pm 0.05$ and $n_T = 1.79 \pm 0.77$ at 68% c.l.. I.e. if the real dust component is in agreement with the aestimates made by the BICEP2 team, the evidence for a blue tensor spectrum is still present. Viceversa, if the real dust component is larger by a factor four respect to the BICEP2 aestimates then we found $r_{0.01} < 0.044$ and n_T as unconstrained i.e. not only there is no evidence for a blue GW spectrum but also the BICEP2 indication for a GW background vanishes.

In this chapter we have presented the constraints on the spectral index n_T of tensor fluctuations from the recent data obtained by the BICEP2 experiment. We found that the BICEP2 data alone slightly prefers a positive, "blue", spectral index with $n_T = 1.36 \pm 0.83$ at 68% c.l.. However, when a TT prior on the tensor amplitude coming from temperature anisotropy measurements is assumed we got $n_T = 1.67 \pm 0.53$ at 68% c.l., ruling out a scale invariant $n_T = 0$ spectrum at more than three standard deviations. Considering only the possibility of a "red", $n_T < 0$ spectral index we obtained the lower limit $n_T > -0.76$ at 68% c.l. ($n_T > -0.09$ when a TT prior is included).

These results are at odds with current upper limits on the tensor spectral index coming from observations of pulsar timing, Big Bang Nucleosynthesis, and from
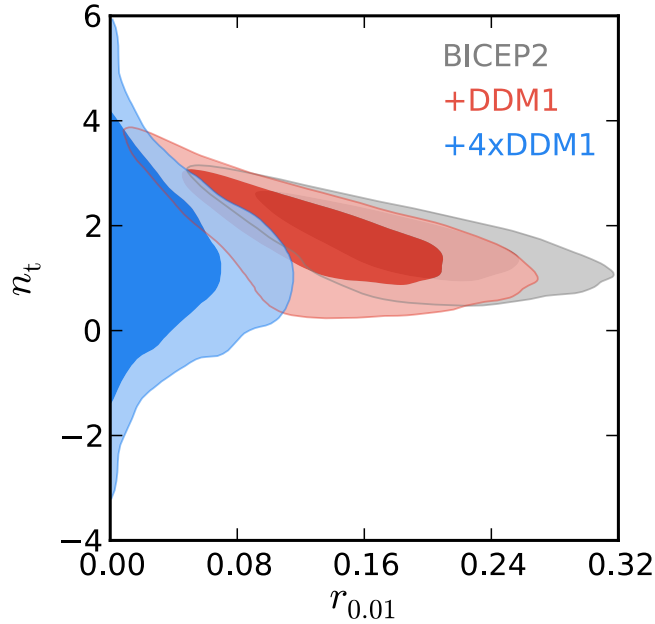
Figure 10.5. Constraints on the $r_{0.01}$ vs n_T plane for BICEP2 + TT prior case for three different dust components: no dust component, DDM1 template, and a component four times larger than the DDM1 aestimate, [234].

direct upper limits from the LIGO experiment (see e.g. Ref. [269]).

Considering $r_{0.01} = 0.2$ and using the method adopted in Ref. [269] we found the current upper limits on n_T: $n_T \leq 0.52$, $n_T \leq 0.28$ and $n_T \leq 0.12$ at 68% c.l. from pulsar timing, LIGO, Ref. [270] and BBN respectively. The LIGO and BBN limits are in strong tension with the BICEP2+CMB value. Therefore a positive spectral index does not provide an acceptable solution to the tension between the BICEP2 data and current upper limits on r from temperature anisotropies. While all these limits are on scales of significantly different order of magnitude, this may indicate either the need of further extensions to the LCDM model (as a running of the scalar spectral index, Ref. [10], or extra neutrino species, Ref. [21]) to relax the CMB temperature bound on $r_{0.002}$, or the presence of unresolved systematics. In this respect, we investigated the impact of a possible unaccounted, dust component. We have found that while a dust component compatible with the DDM1 template presented in Ref. [10] does not alter the conclusions presented in this paper, considering a component four times larger will drastically change our results. Since at the moment there is no experimental data available that can clarify the real amplitude of this component in the region sampled by BICEP2, the results presented here on the tensor spectral index need to be considered with great caution.

Chapter 11

The Lensing-ISW signal as a Cosmological Probe

While the CMB anisotropy distribution is generally expected to be Gaussian to high accuracy, small non-Gaussianities could be produced in the early Universe, during inflation (commonly referred to as primordial non-Gaussianities, see e.g. Ref. [271]) as well as be sourced, at a much later epoch, by the interaction of CMB photons with the local Universe. For instance, the lensing of CMB photons by dark matter structure produces a clear non-Gaussian signal in the CMB trispectrum (the Fourier transform of the four-point correlation function), which can be used to constrain the amplitude of the lensing potential. Such signal, already discovered by ACT, Ref. [3], and SPT, Ref. [4], experiments helps in further constraining cosmological models.

In this chapter (see also Ref. [272]) we study the implications of another non-Gaussian signal expected in the CMB, i.e. the one arising from cross-correlations between lensing and the Integrated Sachs-Wolfe effect (ISW), which affects the CMB bispectrum, i.e. the three-point correlation function. The signature of the lensing-ISW (L-ISW) correlations in the CMB bispectrum has been discussed by several authors (see e.g. Refs. [59, 273, 61, 274, 275, 276, 277, 278, 279, 280, 281]). Contrary to the primordial inflationary signal L-ISW bispectrum is a standard expectation of the standard model and is independent from the inflationary modelling.

In Refs. [61, 275, 276] the possibility of constraining cosmological parameters through the detection of the L-ISW bispectrum has been considered; in particular it has been shown that an accurate measurement of the L-ISW will help in constraining the equation of state and the fractional density of dark energy. In this chapter we analyze the potential of the L-ISW signal to constrain modified theories of gravity. In the latter, the evolution of the metric potentials can generally differ significantly from the ΛCDM prediction, therefore it is natural to expect that the L-ISW bispectrum would provide valuable constraints on these theories.

Here we focus on certain classes of modified gravity and adopted a parameterized approach to forecast the constraints achievable from measurements of the cosmic microwave background (CMB) bispectrum from future, at that time, experiments.

Cosmic acceleration is one of the major challenges faced by modern cosmology and understanding the very nature of what is sourcing it is the main focus of future cosmological experiments. Several approaches to the phenomenon of cosmic

acceleration have been proposed in the literature, including modifications of the laws of gravity on large scales in order to allow for self-accelerating solutions in matter-only Universes. Well-known examples of modified theories of gravity are $f(R)$ models, see Refs. [282, 283, 284, 285, 286], or the more general scalar-tensor theories, see Refs. [287, 288, 289, 290], the Dvali-Gabadadze-Porrati (DGP) model, see Refs. [291, 292], and its further extensions such as Degravitation, see Ref. [293]. In the past years several authors have analyzed constraints on modified gravity, or more generally departures from the cosmological standard model, both using current datasets as well as doing forecasts for future surveys, see Refs. [294, 295, 296, 297, 298, 299, 300, 301, 302, 303, 304, 305, 306, 307, 308, 309].

Moreover, (see Ref. [310]) we will investigate the implications of different values for the number of relativistic degrees of freedom N_{eff}, the total neutrino mass Σm_ν, and the neutrino perturbation viscosity c_{vis} on the L-ISW bispectrum. There are two reasons to do this: first, it is important to discuss what kind of information a measurement of L-ISW bispectrum could bring in the determination of these parameters. Secondly, since the L-ISW signal is an important contaminant in the determination of the primordial inflationary bispectrum, it is useful to understand the possible bias that different values for neutrino background parameters could introduce.

11.1 The lensing-ISW bispectrum

As we already saw in Chapter 2, see eq. (2.84), if the expansion of the Universe is not matter dominated (i.e. $\Omega_m \neq 1$), the time variation of the gravitational potential provides an additional source of CMB anisotropies; restricting to the linear regime, this effect is known as the Integrated Sachs Wolfe (ISW) effect, from Ref. [41], given by:

$$\frac{\Delta T}{T}(\hat{\mathbf{n}})|_{ISW} = \int d\chi (\Phi - \Psi)_{,\tau}(\hat{\mathbf{n}}, \chi) \ , \tag{11.1}$$

where $\hat{\mathbf{n}}$ is the direction of the line of sight, ψ is the newtonian potential, ϕ is the perturbation induced in spatial curvature, τ is the conformal time and χ is the comoving distance (see e.g. Ref. [311]). Temperature fluctuations of the CMB due to the ISW effect can be expanded in spherical harmonics

$$\frac{\Delta T}{T}(\hat{\mathbf{n}})|_{ISW} = \sum_{l=0}^{\infty} \sum_{m=-l}^{l} a_{lm}^{ISW} Y_{lm}(\hat{\mathbf{n}}) \ , \tag{11.2}$$

On the other hand, the paths of CMB photons are deflected by the gravitational lensing induced by the fluctuations of matter density while traveling from the recombination to the observer

$$\delta\tilde{T}(\hat{\mathbf{n}}) = \Delta T(\hat{\mathbf{n}} + \partial\phi) \simeq \Delta T(\hat{\mathbf{n}}) + \left[(\partial\phi) \cdot (\partial\Delta T)\right](\hat{\mathbf{n}}) \ , \tag{11.3}$$

where the lensing potential is defined as

$$\phi(\hat{\mathbf{n}}) = -\int_0^{\chi_*} d\chi \frac{\chi_* - \chi}{\chi_* \chi} \Big(\Phi - \Psi\Big)(\hat{\mathbf{n}}, \chi) \ . \tag{11.4}$$

From eq. (11.1) and (11.3), we can see that Weyl potential $(\Phi - \Psi)$ sources both ISW and weak lensing (WL), so the long-wavelength mode from ISW couples with the short-wavelength mode from WL.

As usual, it is convenient to consider an expansion in spherical harmonics of the temperature field:

$$\frac{\Delta T}{T}(\mathbf{n}) = \sum_{l=2}^{\infty} \sum_{m=-l}^{l} a_{lm} Y_{lm}(\mathbf{n}) \tag{11.5}$$

as well as of the lensing potential, $\phi(\mathbf{n}) = \sum_{l,m} \phi_{lm} Y_{lm}(\mathbf{n})$. Taylor expanding eq. (11.3) in the lensing potential, and applying the above harmonic expansions, we obtain the following relation between the lensed and unlensed multipole coefficients, (to first order in the lensing multipoles):

$$\tilde{a}_{l_1 m_1} \approx a_{l_1 m_1} + \sum_{l_2 m_2 l m} f_{l_1 l_2 l} \, a_{l_2 m_2}^* \phi_{lm}^* \begin{pmatrix} l_1 & l_2 & l \\ m_1 & m_2 & m \end{pmatrix} \tag{11.6}$$

where the coefficient $f_{l_1 l_2 l}$ is given by

$$f_{l_1 l_2 l} = \left(\frac{-l_1(l_1 + 1) + l_2(l_2 + 1) + l(l + 1)}{2} \right) \Upsilon_{l_1 l_2 l} \tag{11.7}$$

with

$$\Upsilon_{l_1 l_2 l_3} \equiv \sqrt{\frac{(2l_1 + 1)(2l_2 + 1)(2l_3 + 1)}{4\pi}} \begin{pmatrix} l_1 & l_2 & l_3 \\ 0 & 0 & 0 \end{pmatrix} . \tag{11.8}$$

Then in harmonic space, the theoretical angular averaged CMB bispectrum generated by the lensing-ISW correlation is given by

$$B_{l_1 l_2 l_3} = \sum_{m_1 m_2 m_3} \begin{pmatrix} l_1 & l_2 & l_3 \\ m_1 & m_2 & m_3 \end{pmatrix} \langle \tilde{a}_{l_1 m_1} \tilde{a}_{l_2 m_2} \tilde{a}_{l_3 m_3} \rangle = f_{l_1 l_2 l_3} C_{l_2}^{T\phi} C_{l_3}^{TT} + 5 \text{ perm.}. \tag{11.9}$$

where $\langle ... \rangle$ is the ensemble average, C_l^{TT} is the temperature (primordial plus ISW) power spectrum and $C_l^{T\phi}$ is the cross temperature-lensing angular power spectrum, $C_l^{T\phi} = \langle \phi_{lm}^* a_{lm} \rangle$, which depends on the Weyl potential and its first time-derivative (see e.g. Ref. [61]). In deriving (11.9) we have implicitly assumed the statistical isotropy of the Universe and have averaged the three-point correlation function (in harmonic space) over the orientation of triangles by mean of rotational invariance. Numerical codes evolving perturbations typically work with the reduced bispectrum, defined via

$$B_{l_1 l_2 l_3} = \Upsilon_{l_1 l_2 l_3} b_{l_1 l_2 l_3} . \tag{11.10}$$

As we can see clearly, if $C_\ell^{T\phi} = 0$ the bispectrum signal is zero, i.e. thanks to the correlations between lensing and ISW the bispectrum that give $C_\ell^{T\phi} \neq 0$ of the CMB anisotropies is different from zero even if the original anisotropies are expected to perfectly Gaussian.

11.2 Forecast method

In order to estimate parameters form the L-ISW bispectrum measurements from CMB Planck-like experiments, we assumed a fiducial model and we compared the simulate observations with several theoretical models, built varying the parameters of interest.

Assuming that the bispectrum is well approximated by Gaussian variables, we can forecast the constraints on cosmological parameters building a simple χ^2 function (see, for example, the same procedure adopted in Refs. [61, 275, 274, 54, 312, 276, 272, 311]):

$$\chi_b^2 = \sum_{l_1,l_2,l_3=2}^{l_{\max}} f_{sky} \left[\frac{B_{l_1 l_2 l_3}^{th} - B_{l_1 l_2 l_3}^{fid}}{\sigma_{l_1 l_2 l_3}} \right]^2 \tag{11.11}$$

where $B_{l_1 l_2 l_3}^{fid}$ is the fiducial temperature bispectrum, $B_{l_1 l_2 l_3}^{th}$ is the bispectrum with non-standard parameters to constrain. The sum is over all possible combinations of l_1, l_2, l_3 with $(l_1 < l_2 < l_3)$, $l_1 + l_2 + l_3$ even and we have set $l_{\max} = 1000$, which roughly corresponds to the maximum multipole sensibility for Planck-like experiments, (since at higher multipoles the contamination from foreground point sources starts to be dominant).

The uncertainty $\sigma_{l_1 l_2 l_3}$ is given by Ref. [313]:

$$(\sigma_{l_1 l_2 l_3})^2 = \bar{C}_{l_1}^{TT} \bar{C}_{l_2}^{TT} \bar{C}_{l_3}^{TT} \ , \tag{11.12}$$

where the $\bar{C}_l^{TT}$ are defined by

$$\bar{C}_l^{TT} = C_l^{TT} + \mathcal{N}_l. \tag{11.13}$$

and $\mathcal{N}_l$ is the experimental noise given by

$$\mathcal{N}_l = w^{-1} \mathcal{B}_l^{-2} \tag{11.14}$$

with

$$w \equiv (\sigma_{pix} \theta_{pix})^{-2}, \quad \mathcal{B}_l^2 \approx e^{-l(l+1)/l_s^2}, \tag{11.15}$$

where we assumed that the experimental beam profile $\mathcal{B}$ is Gaussian with width $l_s \equiv \sqrt{8\ln 2} \theta_{fwhm}^{-1}$. We have adopted $f_{sky} = 0.65$, a resolution $\theta_{fwhm} = 8'$, a sensitivity $\sigma_{pix} = 2.0 \times 10^{-6} \mu K$ and a noise power parameter $w^{-1} = 0.022 \times 10^{-15} \mu K^2$ as roughly we expected for the 150 GHz frequency channel of the Planck experiment (see Ref. [314]).

Once the χ^2 function was computed, we have built a likelihood from the bispectrum data given by:

$$\mathcal{L}_b = \exp\left(-\frac{\chi_b^2}{2}\right) \tag{11.16}$$

Since we modelled the (primordial plus ISW) spectrum as a Gaussian variable, we effectively neglected any inflationary non-Gaussian signal; furthermore, we ignored

contributions to the bispectrum from the lensing-Sunyaev-Zel'dovich correlation. Both signals could anyway be removed exploiting their different angular dependence (see e.g. Ref. [315]).

11.3 Constraining modified gravity theories with the L-ISW Bispectrum

Several models of modified gravity have been proposed as alternatives to ΛCDM, and analysing them one by one is impractical. The idea behind parametrised versions of modified gravity is exactly that of encompassing several models into a single framework. The parametrisations that we considered for our analysis cover a fairly large sample of theories and allowed us to draw quite general conclusions about the constraining power of the data considered.

In our analysis we fixed the background to that of the ΛCDM model of cosmology. The latter is currently in very good agreement with all observables constraining the expansion history, and many models of modified gravity can mimic it while introducing significant modifications at the level of perturbations. Therefore, fixing the background to ΛCDM, allows us to isolate the effects of departures at the level of growth of structure, where we expect the most significant deviations.

11.3.1 Overview: some modified gravity models

Linder model

In Ref. [316] Linder introduced a simple parametrisation of the growth of density perturbations in the linear regime, via a single parameter, the growth index γ (which we will denote with γ_L), defined through

$$g(a) = e^{\int_0^a dlna[\Omega_m(a)^{\gamma_L}-1]} \tag{11.17}$$

The idea is that of capturing independently the information from the expansion and the growth history, respectively in Ω_m and γ_L. Since in our analysis we fixed the background to ΛCDM, $\Omega_m(a)$ has been determined by that and the only parameter of interest was γ_L.

In the cosmological concordance model, ΛCDM, as well as in vanilla-type dark energy models, γ_L is to good approximation constant and equal to $\gamma_L \approx 6/11$. While it can generally be a function of time and scale, in several models of modified gravity it can still be approximated by a number, which often differs significantly from the ΛCDM value. For instance in the braneworld gravity of the DGP model, $\gamma_L \approx 0.68$ to good approximation over the whole history, see Ref. [316]. Things are more complicated for scalar-tensor models where often the time- and scale-dependence of γ_L cannot be neglected. However, γ_L remains a powerful *trigger* parameter, since any deviation of it from $\approx 6/11$ would indicate a breakdown of the cosmological concordance model.

As a starting point for our analysis, we assume $\gamma_L \approx const.$ and forecast constraints on this simple one parameter model.

Chameleon-type models

Chameleon-type theories correspond to gravity plus a scalar degree of freedom which is conformally coupled to matter fields, and has therefore a profile and a mass which depends on the local density of matter. The common action for such theories is

$$
S = \int d^4x \sqrt{-g} \left[\frac{M_P^2}{2} R - \frac{1}{2} g^{\mu\nu} \left(\nabla_\mu \phi \right) \left(\nabla_\nu \phi \right) - V(\phi) \right] + S_i \left(\chi_i, e^{-\alpha_i(\phi)/M_P} g_{\mu\nu} \right)
$$
(11.18)

where ϕ is the scalar d.o.f., χ_i is the ith matter field and $\alpha_i(\phi)$ is the coupling of χ_i to ϕ. We limited ourselves to cases in which the coupling was a linear function of the scalar field, i.e. $\alpha_i(\phi) \propto \beta_i \phi$. A well known example of the latter are $f(R)$ theories.

The free parameters of these theories are the mass scale of the scalar field and the couplings β_i. Since we considered constraints from late time cosmology, we have been interested only in the coupling to dark matter, and therefore drop the index i.

While the modifications enter through the coupling of the scalar field to matter, and therefore change the energy-momentum conservation equations, it is possible to keep the latter unchanged and effectively absorb the modifications of the evolution of perturbations in the Poisson and anisotropy equation. The latter are commonly parametrised with two functions μ and γ, as follows

$$
k^2 \Psi = -\frac{a^2}{2M_P^2} \mu(a,k) \rho\Delta,
$$
(11.19)

$$
\frac{\Phi}{\Psi} = \gamma(a,k),
$$
(11.20)

where $\rho\Delta \equiv \rho\delta + 3\frac{aH}{k}(\rho + P)v$ is the comoving density perturbation. Furthermore, for Chameleon-type theories μ and γ are well represented by the parametrisation introduced in Ref. [317]

$$
\mu(a,k) = \frac{1 + \beta_1 \lambda_1^2 k^2 a^s}{1 + \lambda_1^2 k^2 a^s},
$$
(11.21)

$$
\gamma(a,k) = \frac{1 + \beta_2 \lambda_2^2 k^2 a^s}{1 + \lambda_2^2 k^2 a^s},
$$
(11.22)

where the parameters β_i can be thought of as dimensionless couplings, λ_i as dimensional length-scales and s is determined by the time evolution of the characteristic lengthscale of the theory, i.e. the mass of the scalar d.o.f.. As shown in Ref. [298], in the case of Chameleon-type theories the parameters $\{\beta_i, \lambda_i^2\}$ are related in the following way

$$
\beta_1 = \frac{\lambda_2^2}{\lambda_1^2} = 2 - \beta_2 \frac{\lambda_2^2}{\lambda_1^2}
$$
(11.23)

and $1 \lesssim s \lesssim 4$, so that effectively the degrees of freedom are one coupling and a time-evolving lengthscale.

$f(R)$ theories

As it becomes clear in the Einstein frame, $f(R)$ theories are a subclass of the models described by action (11.18), corresponding to a universal fixed coupling $\alpha_i = \sqrt{2/3}\,\phi$. Therefore they can also be described by the parametrisation in (11.21). It can be easily seen that the fixed coupling $\alpha_i = \sqrt{2/3}\,\phi$ gives $\beta_1 = 4/3$ and $\beta_2 = 1/2$. Viable $f(R)$ models that closely mimic ΛCDM have $s \sim 4$, see Ref. [298], therefore the number of free parameters in Eqs. (11.21) can be effectively reduced to one lengthscale (using (11.23) e.g. the lengthscale λ_1.

The latter is directly related to the mass scale of the scalar degree of freedom introduced by these theories and represented by $f_R \equiv df/dR$, known as the *scalaron*. Specifically, λ_1 sets the inverse mass scale of the scalaron today, i.e. $\lambda_1 = 1/m_{f_R}^0$. The results in the literature are usually presented in terms of a parameter B_0 which is related to λ_1 as follows, see Ref. [294]:

$$B_0 = \frac{2H_0^2\lambda_1^2}{c^2} \tag{11.24}$$

Studying this particular subclass is interesting because some models belonging to this category have been shown to be cosmologically viable and pass local tests of gravity, see Ref. [318].

11.3.2 Analysis method

In Figures 11.1 and 11.2 we plotted different theoretical predictions for $C_l^{T\phi}$ and the reduced bispectrum $b_{l_1 l_2 l_3}$ computed with the publicly available code MGCAMB (`http://www.sfu.ca/~aha25/MGCAMB.html`). As it can be noticed, the L-ISW bispectrum is clearly sensitive to modifications of gravity and in principle can be used to put constraints on models of modified gravity.

We now estimate the potential of upcoming L-ISW bispectrum measurements from CMB Planck-like experiments to constrain the seen modified gravity theories. We perform a likelihood analysis from the spectrum, L-ISW bispectrum (see Sec. 11.2) and their combination in order to compare the parametrised models of Sec. 11.3.1 to a fiducial model, chosen to reproduce a ΛCDM cosmology. We fixed the cosmological parameters according to the WMAP 7-year data best fit, Ref. [92], and vary only the parameters entering the parametrisations described in the previous modified gravity theories. Spanning over the parameter space, we calculated the spectrum and L-ISW bispectrum using MGCAMB and build the likelihoods as described in the following.

Each theoretical model is then compared to the fiducial model with a simple χ^2 function which assumes that the spectrum and bispectrum can be safely described as Gaussian variables, see Refs. [61, 276]. For the standard C_l^{TT} temperature anisotropy spectrum we have

$$\chi_s^2 = \sum_l^{1000}\left[\frac{C_l^{TT,th} - C_l^{TT,fid}}{\sigma_l^s}\right]^2 \tag{11.25}$$

where the uncertainty σ^s is given by
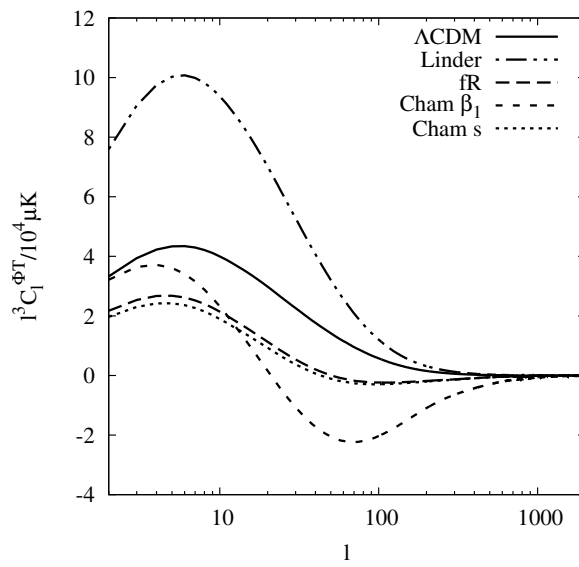
Figure 11.1. Dependence of the cross temperature-lensing $C_l^{T\phi}$ angular spectra on modified gravity parameters for the different models considered in the analysis. The solid curves correspond to ΛCDM, the dotted and dashed curves to the Linder parametrisation with $\gamma_L = 0.645$, the long-dashed curves to an f(R) model with $B_0 = 0.42$, the short-dashed curves to a Chameleon model (Chamβ_1) with $\beta_1 = 1.3$, $B_0 = 0.50$ $s = 2.0$, while the dotted line to a Chameleon model (Cham s) with $\beta_1 = 1.3$, $B_0 = 0.50$, $s = 3.3$, [272].
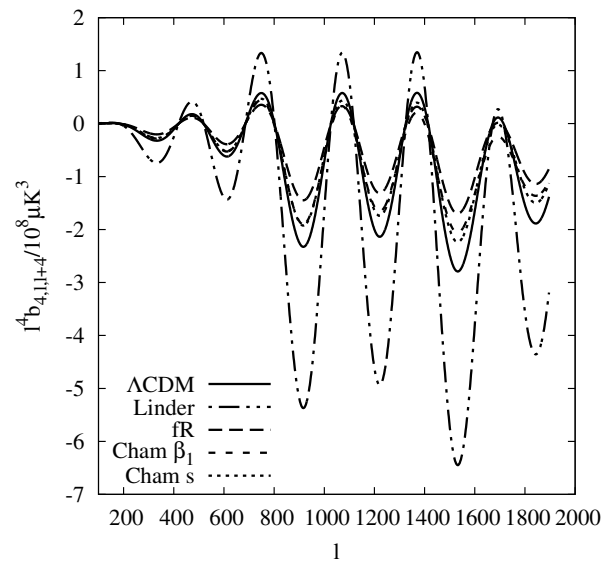
Figure 11.2. Dependence of the reduced bispectrum on modified gravity parameters for the different models considered in the analysis. The solid curves correspond to ΛCDM, the dotted and dashed curves to the Linder parametrisation with $\gamma_L = 0.645$, the long-dashed curves to an f(R) model with $B_0 = 0.42$, the short-dashed curves to a Chameleon model (Chamβ_1) with $\beta_1 = 1.3$, $B_0 = 0.50$ $s = 2.0$, while the dotted line to a Chameleon model (Cham s) with $\beta_1 = 1.3$, $B_0 = 0.50$, $s = 3.3$, [272].

$$\sigma_l^s = \sqrt{\frac{2}{(2l+1)}} C_l^{TT} \,, \tag{11.26}$$

We did not include any covariance noise matrix in eq. (11.26), effectively assuming σ^s to be cosmic-variance limited up to $l = 1000$, which is a good approximation for Planck-like experiments.

For the bispectrum we have eq. (11.11)

$$\chi_b^2 = \sum_{l_1,l_2,l_3=2}^{l_{\max}} \left[\frac{B_{l_1l_2l_3}^{th} - B_{l_1l_2l_3}^{fid}}{\sigma_{l_1l_2l_3}^b} \right]^2 \tag{11.27}$$

where the sum is over all possible combinations of l_1, l_2, l_3 with $(l_1 \leq l_2 \leq l_3)$, $l_1 + l_2 + l_3$ even and we have set $l_{\max} = 1000$, which roughly corresponds to the maximum multipole sensibility for Planck-like experiments, (since at higher multipoles the contamination from foreground point sources starts to be dominant).

The uncertainty $\sigma_{l_1l_2l_3}^b$ is given by

$$\left(\sigma_{l_1l_2l_3}^b \right)^2 = n_{l_1l_2l_3} C_{l_1}^{TT} C_{l_2}^{TT} C_{l_3}^{TT} \,, \tag{11.28}$$

where $n_{l_1l_2l_3}$ is 6 for equilateral configurations $(l_1 = l_2 = l_3)$, 2 for isoscele ones (with two multipoles equal) and 1 for the scalene ones (when all the multipoles are different). There is no noise covariance matrix in the C_l^{TT}.

Once the χ^2 functions are computed, we can build the separate likelihoods for the spectrum and bispectrum data respectively:

$$\mathcal{L}_{s,b} = \exp\left(-\frac{\chi_{s,b}^2}{2} \right) \tag{11.29}$$

Neglecting the correlation between spectrum and bispectrum, we can further combine them in a total likelihood as follows:

$$\mathcal{L}_c = \mathcal{L}_s \mathcal{L}_b = \exp\left(-\frac{\chi_b^2 + \chi_s^2}{2} \right) \tag{11.30}$$

In the calculation of the likelihood from the CMB angular power spectrum we did not include the lensing term that is clearly correlated with L-ISW bispectrum. Furthermore, when combining the two likelihoods like in (11.30), we are neglecting correlations between spectrum and bispectrum data that could arise from the large scale ISW term. This is a good approximation since the bispectrum will constrain modified gravity parameters with a much stronger significance than spectrum data alone. When computing the bispectrum we did not include the non-linear Rees-Sciama term, since that would require a modeling of non-linearities in modified gravity. The exclusion of the RS term is expected to affect our results at most by $\sim 17\%$, and therefore should not change our conclusions to a significant level.

Finally, since we have modeled the (primordial plus ISW) spectrum as a Gaussian variable, we have effectively neglected any inflationary non-Gaussian signal;

furthermore, we ignored contributions to the bispectrum from the lensing-Sunyaev-Zel'dovich correlation. Both signals could anyway be removed exploiting their different angular dependence (see e.g. Ref. [315]).

For each theoretical model considered, while keeping the cosmological parameters fixed to their WMAP 7-year values, we varied the modified gravity parameter(s) (one at a time for the models that have more than one parameter), and computed the spectrum and the L-ISW reduced bispectrum with MGCAMB ; we then used eq. (11.10) to compute the L-ISW bispectrum from the reduced one. We also chose a fiducial model and computed the corresponding spectrum and bispectrum. Once a sufficient number of spectra has been calculated, we computed the likelihood profiles and extract the confidence levels on the parameter of interest.

For each parametrisation, we chose a fiducial model based on a set of parameters that were, for most of the cases, the parameters that would have reduced the cosmology to the ΛCDM one. In the case of the Linder model this is achieved by setting $\gamma_L = 0.555$, see Ref. [316]. For $f(R)$ theories, $B_0 = 0$ is the value giving $\mu = 1 = \gamma$ which are the values of these functions in ΛCDM. For chameleon theories the choice of the fiducial model is more complicated. We started employing the dimensionless parameter B_0 (11.24) in place of the lengthscale λ_1, so that the parameters for these models become (B_0, s, β_1). As a matter of fact, we had three free parameters, no strong theoretical reasons to fix two of them and a complete degeneracy among the parameters when trying to reproduce ΛCDM, i.e. if we fixed either $B_0 = 0$ or $\beta_1 = 1$. We therefore proceeded by making a somewhat arbitrary choice on the fiducial model, fixing $\beta_1 = 1$, $B_0 = 0.5$, and $s = 2$ when studying the constraints on β_1 and $\beta_1 = 1.3$, $B_0 = 0.5$, $s = 2$ when studying the constraints at varying s.

In the case of Linder's model we evaluated the likelihoods in the range $0.475 \leq \gamma_L \leq 0.635$, at steps of 0.002 for values near the fiducial one and at steps of 0.01 for values near the boundaries. In the case of $f(R)$ we explored the likelihood function in the range $0 \leq B_0 \leq 0.7$, varying B_0 at steps of 0.1. In the chameleon case we used a step of 0.01 for β_1 and of 0.2 for s.

11.3.3   Results and Constraints

Linder model

In Table 11.1 and Figure 11.3 we report the constraints on γ_L from the spectrum, the L-ISW bispectrum and the combined analyses. As we can see the spectrum and bispectrum data are somewhat complementary: the CMB bispectrum is more powerful in constraining the γ_L parameter in the region of values lower than those of the fiducial one; on the contrary the temperature anisotropy spectrum is more efficient for larger values. The non-Gaussian shape of the likelihood from the temperature spectrum can be easily understood by the fact that even in the case of small ISW signal (when $\gamma_L \to 0$) the angular spectrum is different from zero and still provides a reasonable fit to the data. The bispectrum is, on the contrary, not null only if the ISW is different from zero and it therefore provides a much more reliable way to detect it.

As we can see, spectrum data provides solely an upper limit for γ_L, leaving it

	fiducial	**S** 95% c.l.	**B** 95% c.l.	**C** 95% c.l.
γ_L	0.555	$+0.044$ $-$	$+0.060$ -0.056	$+0.034$ -0.042

Table 11.1. Constraints on γ_L of Linder model from the spectrum (**S**) and bispectrum (**B**) and combined (**C**) analyses, [272].

practically unconstrained on the lower tail. On the contrary, bispectrum data give a $\sim 5\%$ error on γ_L. When spectrum and bispectrum data are combined there is a substantial improvement in the measurement.

Chameleon models

	fiducial	**S** 68% c.l.	**B** 68% c.l.	**C** 68% c.l.
β_1	1.00	$+0.25$ -0.17	$+0.10$ -0.13	$+0.09$ -0.10
s	2.00	$+0.55$ -0.17	$+0.42$ -0.28	$+0.30$ -0.15

Table 11.2. Constraints at 1 standard deviation on the Chameleon models parameters β_1 and s coming from the analysis of spectrum (**S**), bispectrum (**B**) and combined (**C**) datasets, [272].

The constraints on Chameleon models from the spectrum, L-ISW bispectrum and combined analyses are reported in Table 11.2 and Figures 11.4 and 11.5.

As for the Linder model, the two datasets are complementary in constraining the Chameleon parameters. The simple temperature power spectrum is more powerful in constraining values of $\beta_1 \leq 0.75$, *i.e.* the lower tail, while the bispectrum data provide stronger constraints on the higher tail, where the spectrum data leave the parameter practically unconstrained. The same behaviour is seen for the likelihood distribution of the s parameter. Small values of s ($s < 2$) can be better constrained by temperature spectrum data. However large values of s are left unconstrained from the temperature spectrum and, on the contrary, are significantly constrained when using the bispectrum. This is related to the entity of the ISW signal in the two tails; namely, the spectrum looses constraining power in the parameter range where the ISW is suppressed and tends to zero.
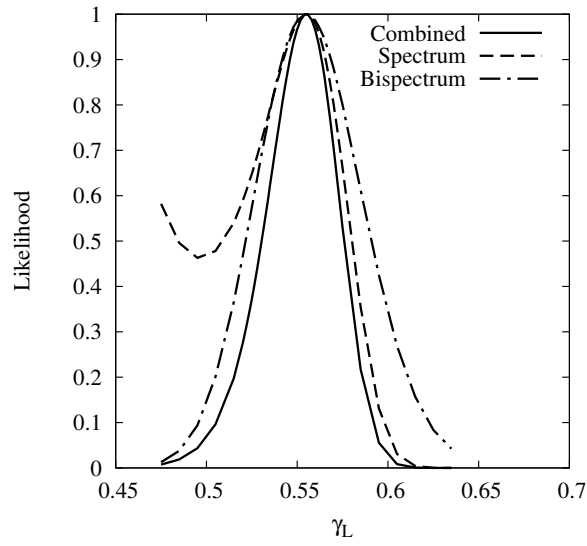
Figure 11.3. Likelihood distribution function for the growth index γ_L (11.17) from the analysis of spectrum, bispectrum and combined data, [272].
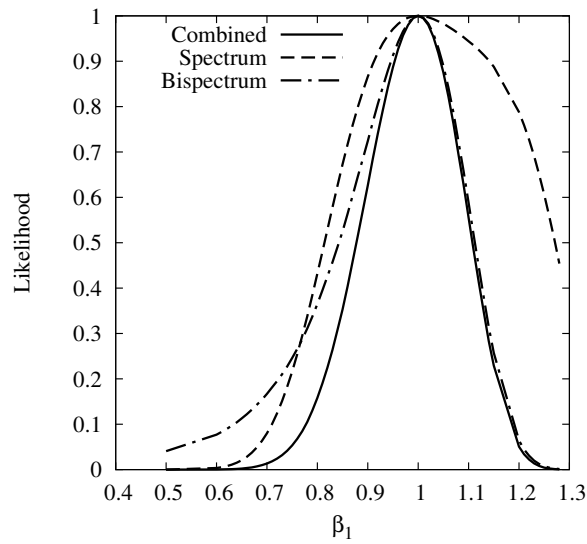
Figure 11.4. Likelihood distribution function for Chameleon models from the spectrum, bispectrum and the combined analyses. The figure gives the likelihood of the parameter β_1 when B_0 and s are fixed to $B_0 = 0.5$ $s = 2$,[272].
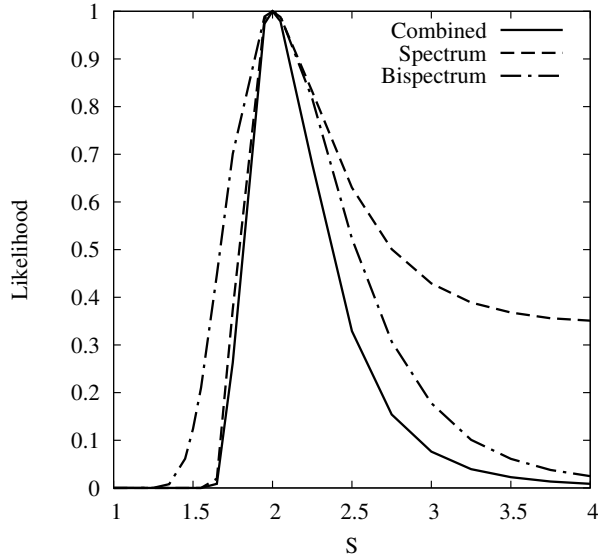
Figure 11.5. Likelihood distribution function for Chameleon models from the spectrum, bispectrum and the combined analyses. The figure gives the likelihood for s when B_0 and β_1 are fixed to $B_0 = 0.5$ and $\beta_1 = 1.3$,[272].

$f(R)$ theories

In Table 11.3 and Figure 11.6 we report the constraints on $f(R)$ models from the spectrum, L-ISW bispectrum and combined analyses. In this case the constraints coming from the bispectrum are definitely tighter than the ones from the temperature spectrum. Once again, this is related to the ISW signal which is suppressed w.r.t. ΛCDM one for all the values of B_0 in the range $0 < B_0 < 3/2$ (becoming null at $B_0 = 3/2$), see Ref. [319]. Current constraints from ISW data from CMB-galaxy correlations are of the order of $B_0 < 0.4$, see Ref. [307]. As we show, the L-ISW bispectrum can clearly improve CMB constraints on these theories, tightening the bounds by a factor of six.

	fiducial	**S** 68% c.l.	**B** 68% c.l.	**C** 68% c.l.
B_0	0	< 0.61	< 0.14	< 0.10

Table 11.3. Constraints at 1 standard deviation on $f(R)$ theory parameter B_0 coming from the analysis of spectrum (**S**), bispectrum (**B**) and combined (**C**) datasets, [272].

In conclusion, while some of the signal could be primordial, a clear non-Gaussian signal is expected from the correlation of lensing and the Integrated Sachs-Wolfe
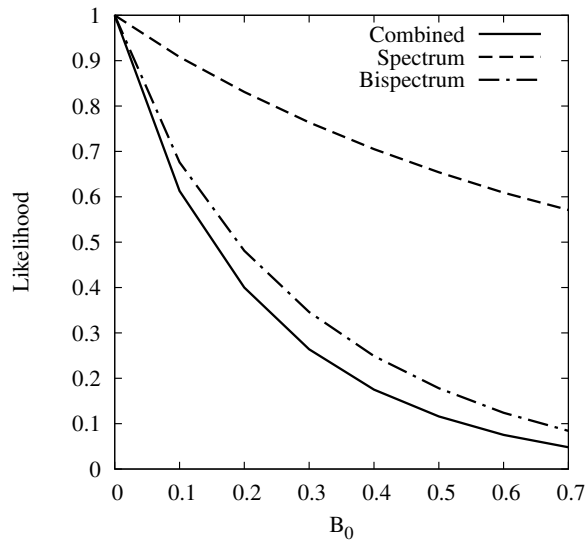
Figure 11.6. Likelihood distribution function for the parameter B_0 describing $f(R)$ theories from the analysis of spectrum, bispectrum and combined data, [272].

effect. This signal provides a new test of the cosmological scenario per se, and could further be used to test alternatives to the cosmological constant in the context of cosmic acceleration. In this chapter we have shown that in the case when all the cosmological parameters are fixed, the bispectrum signal is extremely useful providing a significant improvement in the constraints on modified theories of gravity. While the forecasted constraints have been obtained with the assumption of the cosmological concordance model as the fiducial one, we believe that our results have little dependence on this choice, since current data accepts only relatively small deviations from the standard picture.

11.4 Constraining Dark Radiation with the Lensing-ISW Bispectrum

In this section we are interested in checking the sensitivity of the CMB bispectrum from neutrino physics. We therefore consider three neutrino parameters: the number of relativistic degrees of freedom N_{eff}, the total neutrino mass Σm_ν, and the neutrino perturbation viscosity c_{vis}. In the case of three, massless, neutrinos these parameters are $N_{\text{eff}} = 3.046$, $\Sigma m_\nu = 0$, $c_{vis}^2 = 1/3$.

In Figures 11.7, 11.8 and 11.9 we plot different theoretical predictions for $C_l^{T\phi}$, and in Figures 11.10, 11.11, and 11.10 the reduced bispectrum $b_{l_1 l_2 l_3}$ in function of these previous parameters. As it can be noticed, the L-ISW reduced bispectrum is mildly sensitive to changes in Σm_ν and c_{vis} while there are larger differences in the

variation of N_{eff}.
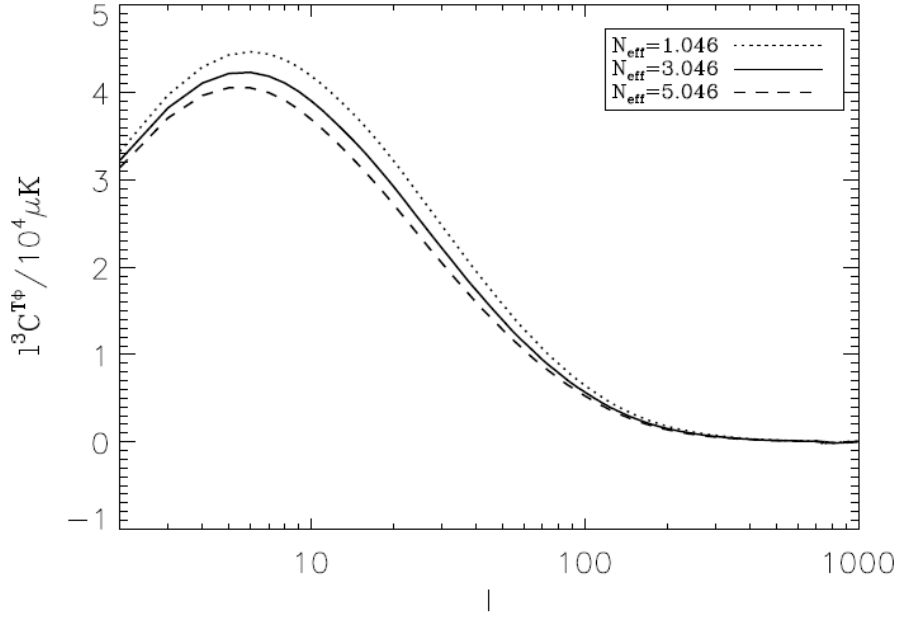
Figure 11.7. Theoretical predictions for $C_l^{T\phi}$ for the relativistic degrees of freedom N_{eff}, [310].

This different dependence can be explained as follows. As we can see from eq. (11.9) the bispectrum signal is given by the contribution of three terms: a geometrical factor arising from the Wigner 3J symbol selection rules, the power spectrum C_l^{TT} evaluated at the last scattering surface and the cross-correlation spectrum $C_l^{T\phi}$. The first term is responsible for the high frequency oscillations in the total (not reduced) bispectrum slice shape. The third term produces a smooth re-projection of the acoustic peaks over the angular scales, determining a low frequency modulation of the bispectrum signal. As a result, modifications affecting the primordial power spectrum via different choices of fiducial models must also affect the bispectrum shape. In particular, an increase in radiation density (i.e. an increase in N_{eff}) changes the Hubble rate at decoupling, it reduces the size of the acoustic horizon and shifts the acoustic peaks towards small angular scales. This effect is clearly seen also in the bispectrum. In Figure 11.13 we have plot the percentage difference between a model with $N_{\text{eff}} = 3.046$ and a model with $N_{\text{eff}} = 5.046$ for the C_l^{TT} and the $C_l^{T\phi}$. As we can see the percentage variation in the spectra is of the same order, around $\sim 10\%$. This indicates that the bispectrum signal is affected by a change in N_{eff} not only from of a change in the temperature spectrum but also from a change in the $C_l^{T\phi}$ term, due mainly to a variation in the matter clustering that affects CMB lensing.

The neutrino mass, on the contrary, mainly affects the lensing spectrum while leaves the primary anisotropy spectrum (for $\Sigma m_\nu < 2eV$) as practically unaffected. The variation in the bispectrum are therefore less pronounced. The viscosity parameter c_{vis} produces just mild variations both in the primary anisotropy spectrum and in the lensing spectrum. We can therefore expect that the L-ISW bispectrum will
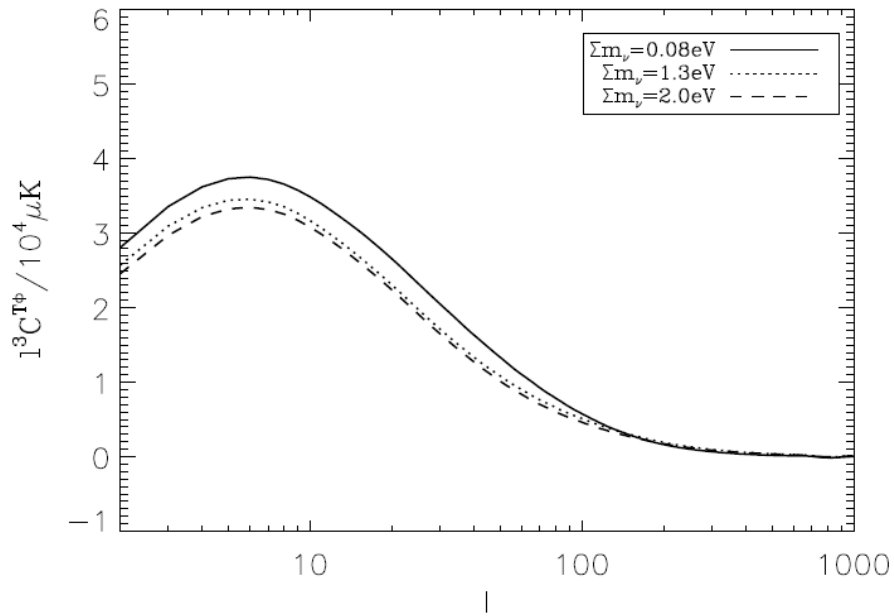
Figure 11.8. Theoretical predictions for $C_l^{T\phi}$ for the total neutrino mass Σm_ν, [310].
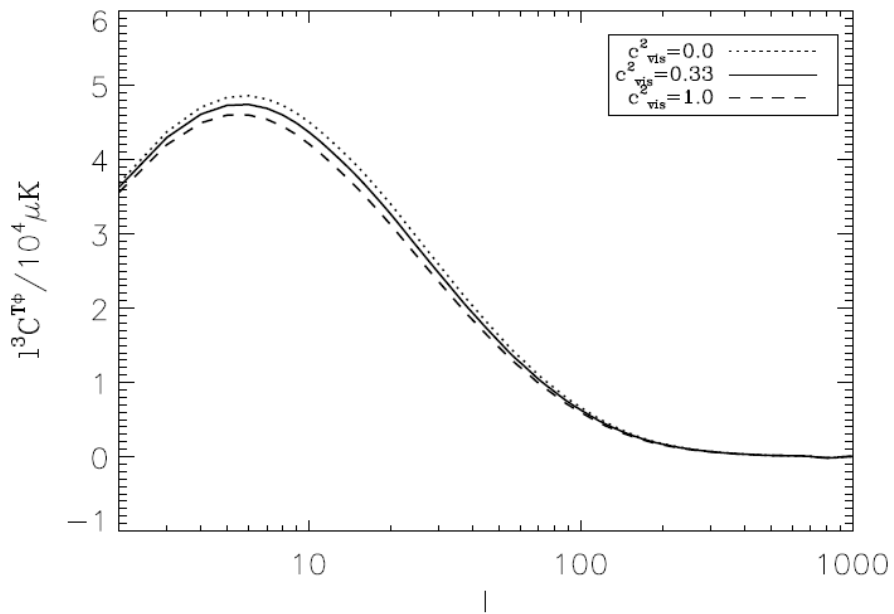
Figure 11.9. Theoretical predictions for $C_l^{T\phi}$ for the viscosity sound speed c_{vis}^2, [310].
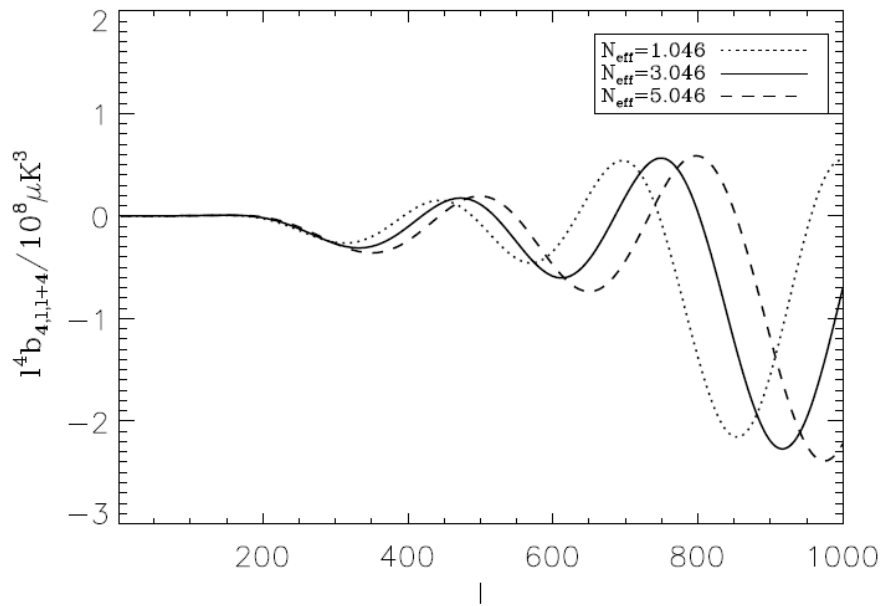
Figure 11.10. Theoretical predictions for the reduced bispectrum for the relativistic degrees of freedom N_{eff}, [310].
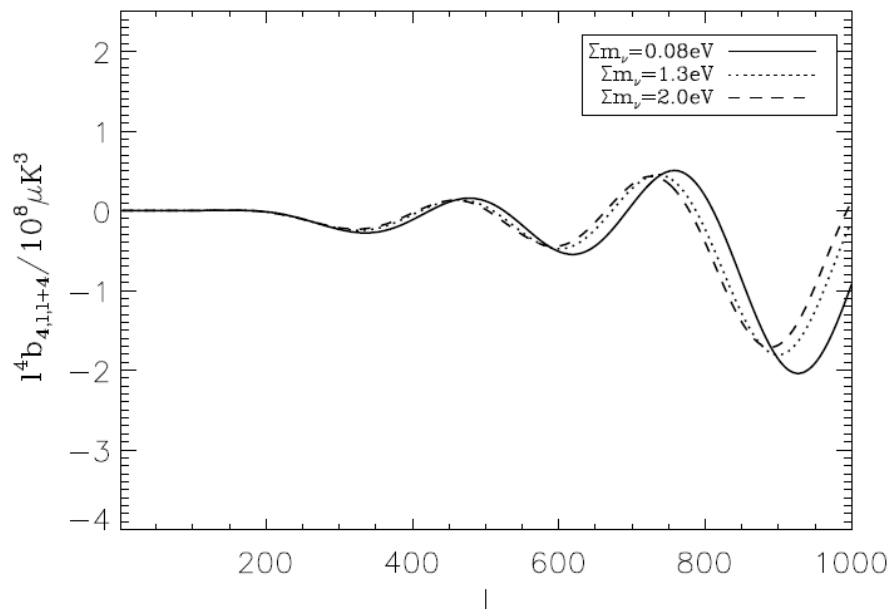
Figure 11.11. Theoretical predictions for the reduced bispectrum for the total neutrino mass Σm_ν, [310].
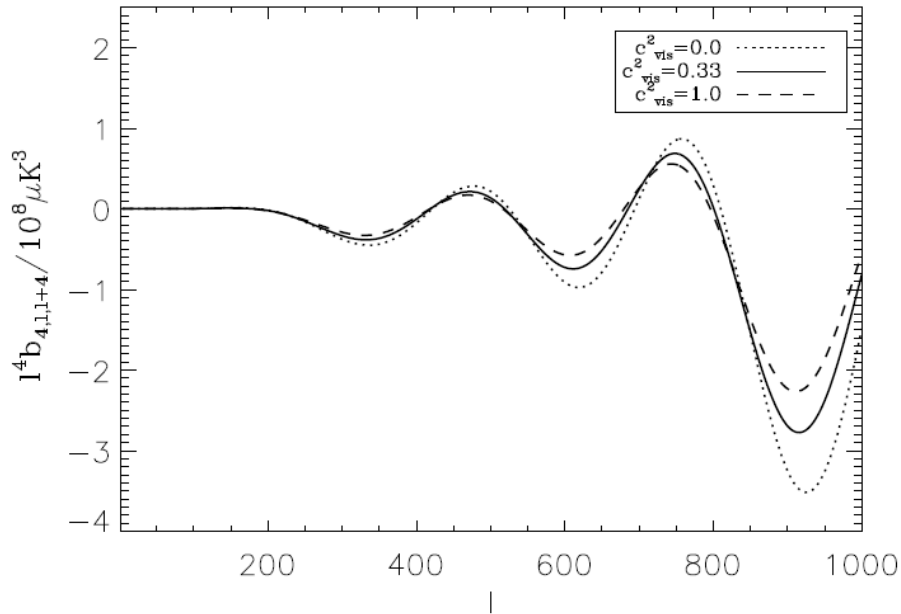
Figure 11.12. Theoretical predictions for the reduced bispectrum for the viscosity sound speed c_{vis}^2, [310].
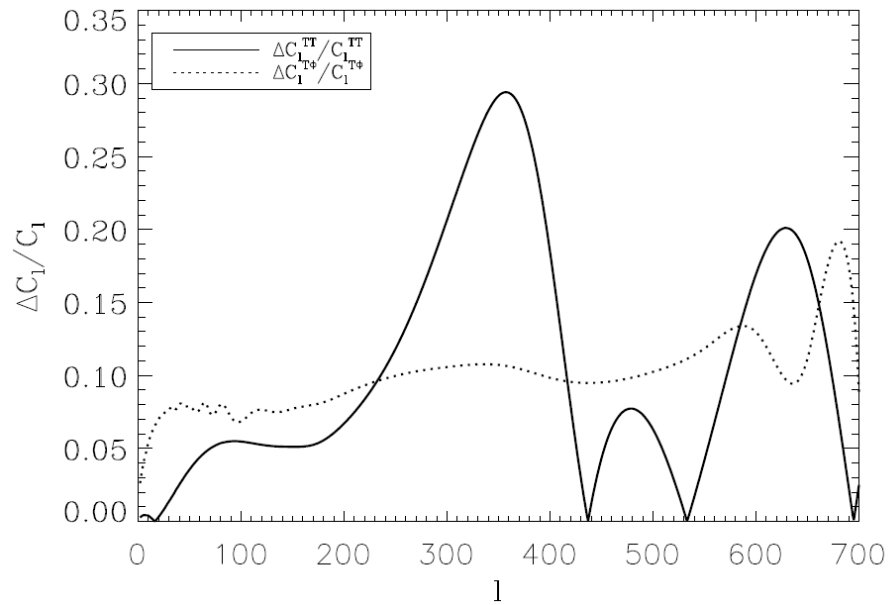
Figure 11.13. Percentage difference between a model with $N_{\text{eff}} = 3.046$ and a model with $N_{\text{eff}} = 5.046$ for the C_l^{TT} and the $C_l^{T\phi}$. As we can see the percentage variation in the spectra is of the same order, around $\sim 10\%$, [310].

be more powerful in constraining N_{eff} than the absolute neutrino mass scale or the viscosity parameter c_{vis}.

11.4.1   Analysis method

We now estimate the potential of upcoming L-ISW bispectrum measurements from CMB Planck-like experiments to constrain the neutrino parameters. We performed an analysis following the forecast method presented in Sec. 11.2 and also adopted in Ref. [311]. Namely, we assumed a fiducial model with parameters given by the WMAP 7-year data best fit, Ref. [92], in the case of three, active, neutrinos and quantify how well the L-ISW data could discriminate any deviation in the neutrino parameters.

We forecasted the parameters building a simple χ^2 function eq. (11.11):

$$\chi_b^2 = \sum_{l_1,l_2,l_3=2}^{l_{\max}} f_{sky} \left[\frac{B_{l_1l_2l_3}^{th} - B_{l_1l_2l_3}^{fid}}{\sigma_{l_1l_2l_3}} \right]^2 \qquad (11.31)$$

where $B_{l_1l_2l_3}^{fid}$ is the fiducial temperature bispectrum, $B_{l_1l_2l_3}^{th}$ is the bispectrum with non-standard neutrino parameters. The uncertainty $\sigma_{l_1l_2l_3}$ is given by eq. (11.12).

11.5   Results and constraints
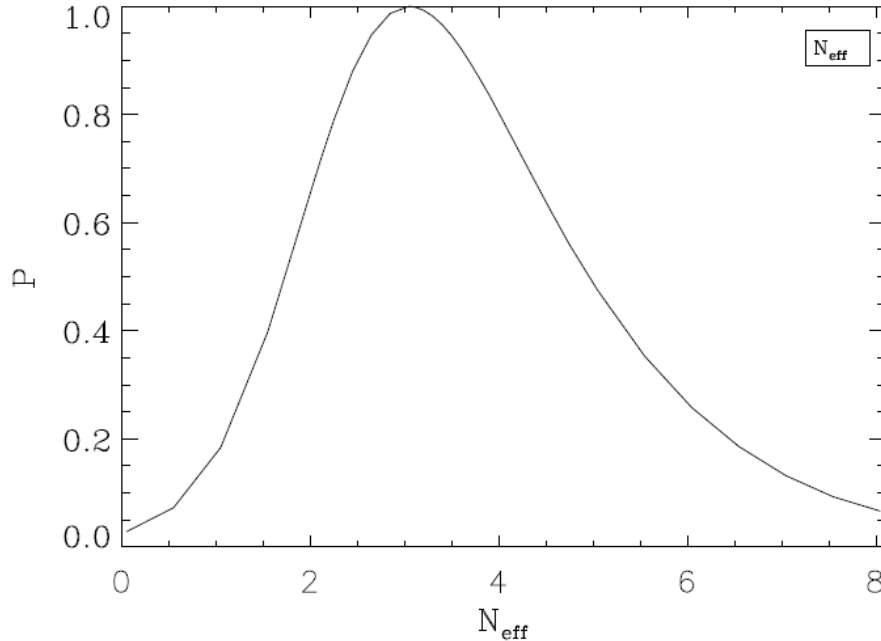
Figure 11.14. Likelihood functions from the bispectrum data for the effective neutrino number N_{eff}, [310].

In Figures 11.14, 11.15 and 11.16 we present the likelihood distribution functions when a single neutrino parameter is let to vary. In case of massless neutrinos,
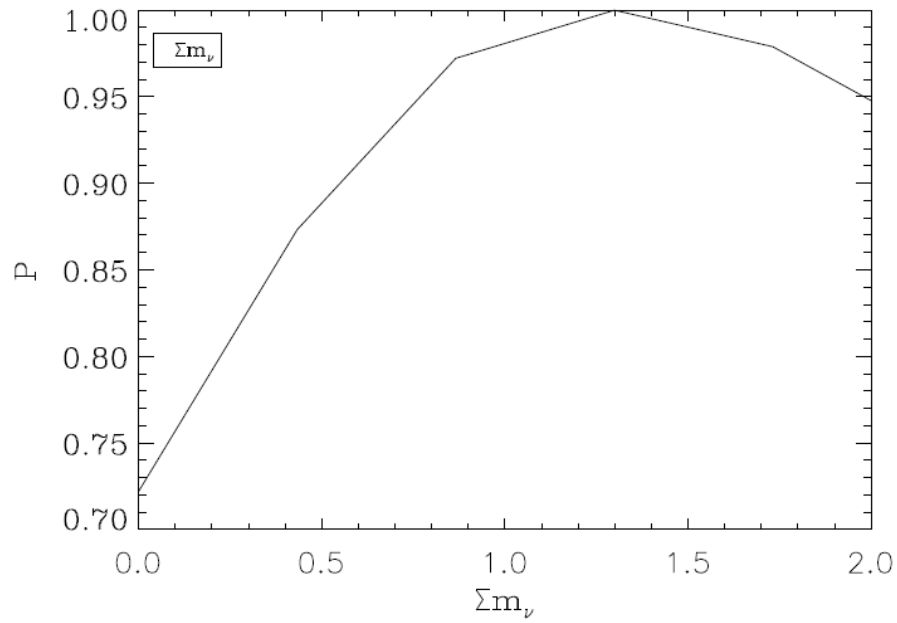
Figure 11.15. Likelihood functions from the bispectrum data for the total neutrino mass Σm_ν, [310].
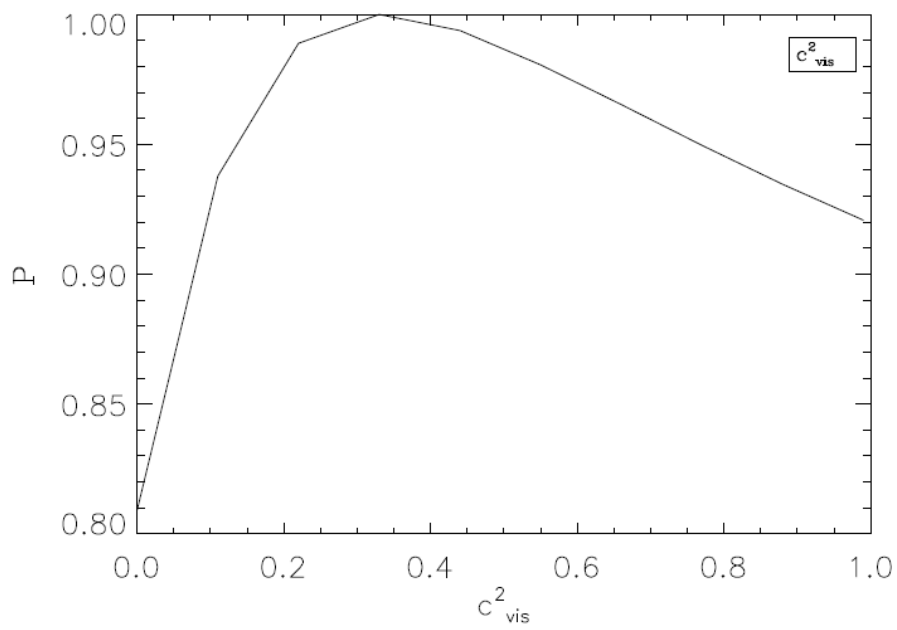
Figure 11.16. Likelihood functions from the bispectrum data for the viscosity sound speed c_{vis}^2, [310].

the fiducial model is taken as the WMAP7 best fit model with baryon density $\omega_b = 0.02258$, cold dark matter density $\omega_{cdm} = 0.1109$, Hubble parameter $h = 0.71$, and the standard neutrino parameters ($N_{\text{eff}} = 3.046$, $c_{vis}^2 = 1/3$). In case of massive neutrinos the fiducial model is taken with baryon density $\omega_b = 0.02219$, cold dark matter density $\omega_{cdm} = 0.1122$, Hubble parameter $h = 0.65$, a neutrino density of $\omega_\nu = 0.014$ (corresponding to a neutrino mass of $m_\nu = 1.3$ eV), and standard neutrino parameters ($N_{\text{eff}} = 3.046$, $c_{vis}^2 = 1/3$).

As we can see from the likelihoods functions, even if the very optimistic case of complete knowledge of all cosmological parameters, the bispectrum can provide an interesting constraint only on the neutrino effective number N_{eff}, with $2.0 < N_{\text{eff}} < 4.6$ at 68% c.l.. This constraint is significant weaker respect to those that could be achieved from the temperature spectrum (around $\Delta N_{\text{eff}} \sim 0.4$) but clearly provide an useful cross-check of the theory. The viscosity sound speed is practically left as unconstrained. The neutrino mass is also very weakly constrained as well. These constraints have been obtained under the optimistic assumption of neglecting correlations with other parameters. However we expect strong correlations, for example, between N_{eff} and the Hubble constant H_0 since they both change the expansion rate at decoupling and affect in a similar way the size of the acoustic horizon and the angular displacement of the acoustic peaks.

We have therefore performed an analysis letting the Hubble constant to vary with a Gaussian prior of $H_0 = 71 \pm 5$ that is conservative considering the current bounds on this parameter. We have found that also in this case the bispectrum can provide useful constraints with $1.8 < N_{\text{eff}} < 4.7$ at 68% c.l..

11.5.1 Bias on f_{NL}

We consider the important aspect of evaluating the bias produced by a wrong assumption in the neutrino parameters in constraining the primordial f_{NL} arising during inflation.

We remind that the optimal estimator for f_{NL} in case of small levels of non-Gaussianity is given by Ref. [281]

$$\langle \hat{f}_{\text{NL}} \rangle_{\text{lens}} = \frac{F_0(B^{\text{lens}}, B^{\text{prim}})}{F_0(B^{\text{prim}}, B^{\text{prim}})} \tag{11.32}$$

where F_0 is the Fisher Matrix for bispectra with expected null f_{NL} signal, B^{lens} is the lensing bispectrum and B^{prim} is the primordial bispectrum. $F_0 = F_0(B^a, B^b)$ (where a and b refer to $lens$ and $prim$) is given by:

$$F_0(B^a, B^b) = \frac{1}{6} \sum_{l_1 l_2 l_3} (B^a_{l_1 l_2 l_3})^* \times (\tilde{\bar{C}}^{TT}_{l_1} \tilde{\bar{C}}^{TT}_{l_2} \tilde{\bar{C}}^{TT}_{l_3})^{-1} B^b_{l_1 l_2 l_3}. \tag{11.33}$$

where $\tilde{\bar{C}}^{TT}_l$ is the lensed power spectrum $\bar{C}^{TT}_l = C^{TT}_l + \mathcal{N}_l$ that includes noise.

In Table 11.4 we report, for several choices of neutrino parameters, the Fisher errors σ_{fnl} and σ_{lens} on the amplitudes of the corresponding bispectrum templates, the correlation between the two bispectrum shapes and the systematic error, i.e. the bias, on f_{NL} if the CMB lensing contribution is neglected. $\sigma_{fnl}^{\text{marge}}$ is the Fisher

Model	σ_{fnl}	σ_{lens}	correlation	bias on f_{NL}	$\sigma_{fnl}^{\mathrm{marge}}$
$N_{\mathrm{eff}}^{rel} = 3.046$ $\sum m_\nu = 0$	4.33	0.18	0.24	9.7	4.47
$N_{\mathrm{eff}}^{rel} = 0.046$ $\sum m_\nu = 0$	4.40	0.16	0.24	12.5	4.54
$N_{\mathrm{eff}}^{rel} = 5.046$ $\sum m_\nu = 0$	4.30	0.19	0.25	9.3	4.44
$N_{\mathrm{eff}}^{rel} = 0.046$ $N_{\mathrm{eff}}^{mass} = 3$ $\sum m_\nu = 1eV$	4.17	0.22	0.23	7.5	4.29
$N_{\mathrm{eff}}^{rel} = 0.046$ $N_{\mathrm{eff}}^{mass} = 4$ $\sum m_\nu = 2eV$	4.13	0.24	0.24	7.1	4.26
$N_{\mathrm{eff}}^{rel} = 3.046$ $\sum m_\nu = 0$ $A_L = 1.7$	4.35	0.19	0.26	9.63	4.51

Table 11.4. Fisher errors σ_{fnl} and σ_{lens} on the amplitudes of the corresponding bispectrum templates, the correlation between the two bispectrum shapes and the systematic error, i.e. the bias, on f_{NL} if the CMB lensing contribution is neglected. $\sigma_{fnl}^{\mathrm{marge}}$ is the Fisher error on f_{NL} if the amplitude of the lensing contribution is marginalized over, [310].

error on f_{NL} if the amplitude of the lensing contribution is marginalized over. We assumed that the signal is cosmic variance limited up to $l \sim 2000$.

As we can see, there is a non-negligible variation in the reported values. It is therefore important to consider the possibility of non standard neutrino background when removing the ISW-lensing contribution. Otherwise the determination of the primordial f_{NL} value could be substantially biased.

Chapter 12

Conclusions

The goal of this thesis was to constrain fundamental physics with current cosmological data, in order to identify possible hints for new physics studiyng the tensions between the several experiments.

In particular, the first research subject of this thesis was to analyze the tension between the values of the neutrino effective number N_{eff} arising from the two ground based experiments ACT and SPT combined with WMAP7, and to compare these results with the Planck satellite bounds. Obviously this discrepancy could be due to the presence of systematics in at least one of the experiments, but could be due also to the degeneracy with other parameters that affect the damping tail of the CMB power spectrum, as the lensing amplitude A_{L}. In fact, the ACT results, while compatible with the standard expectation of three neutrino families $N_{\text{eff}} = 3.046$, indicate a level of CMB lensing, parametrized by the lensing amplitude parameter A_L, that is about 70% higher than expected. If not a systematic, an anomalous lensing amplitude could be produced by modifications of general relativity or coupled dark energy. Vice-versa, the SPT experiment, while compatible with a standard level of CMB lensing $A_L = 1$, prefers an excess of dark radiation, parametrized by the effective number of relativistic degrees of freedom N_{eff}. An excess of dark radiation could be due to the presence of relic relativistic unknown particles, beyond the standard model of particle physics (as axions, sterile neutrinos, etc.), at recombination epoch, or a non-vanishing neutrino chemical potential. In order to test the possible correlation, we analyzed these experiments combining them with WMAP9, varying at the same time both N_{eff} and A_L, and including information from BAO and HST experiments. We found that ACT gives $N_{\text{eff}} = 3.54 \pm 0.41$ and $A_L = 1.64 \pm 0.32$ at 68% c.l., while SPT gives $N_{\text{eff}} = 3.78 \pm 0.33$ and $A_L = 0.79 \pm 0.11$ at 68% c.l.. Both the tensions persist and, in particular, the A_L estimates from the two experiments, even when a variation in N_{eff} is allowed, are in tension at more than 95% c.l.. Moreover, we have shown that the inclusion of a neutrino mass exacerbates the lensing problem for the ACT data with the A_L even more discrepant with the $A_L = 1$ case. In order to solve this puzzle, we analyzed the Planck data in the same way. We have shown that the Planck+WP dataset is hinting new physics for both a presence of dark radiation and for an anomalous amplitude for the lensing parameter, finding $N_{\text{eff}} = 3.71 \pm 0.40$ and $A_{\text{L}} = 1.25 \pm 0.13$ at 68% c.l.. The anomalous lensing amplitude from Planck+WP is more consistent with the results obtained from the WMAP9+ACT dataset, while the

constraints on N_{eff} and other parameters, such as the Hubble constant and the matter density, are in very good agreement with those obtained from the WMAP9+SPT dataset. However, since the same signal of an anomalous lensing amplitude is not found in the trispectrum analysis, we decided to further investigate it considering the possibility of a correlation with the non-standard clustering neutrino properties, as the rest-frame sound speed c_{eff}^2, and the viscosity parameter c_{vis}^2. In fact, the Planck dataset hints at anomalous values for also these parameters, at a higher value of the viscosity parameter, with $c_{\text{vis}}^2 = 0.60 \pm 0.18$ at 68% c.l., and a lower value of the sound speed, with $c_{\text{eff}}^2 = 0.304 \pm 0.013$ at 68% c.l.. When we jointly analyzed the three parameters, we found a better consistency with the standard model with $c_{\text{vis}}^2 = 0.51 \pm 0.22$, $c_{\text{eff}}^2 = 0.311 \pm 0.019$ and $A_{\text{L}} = 1.08 \pm 0.18$ at 68% c.l..

The second aim of my thesis has been to investigate in more detail the current hints for dark radiation, by considering some viable candidates and constraining their properties. First of all, we have computed the expected abundances for the sterile neutrino states within the $(3 + 1)$ and $(3 + 2)$ sterile neutrino models using the best fit oscillation parameters from a global fit to neutrino oscillation data. Our results showed that in both $(3 + 1)$ and $(3 + 2)$ models the extra sterile states have thermal abundances. Then we have fitted massive sterile neutrino models, combining the Planck data with the high-l experiments ACT and SPT, and with the galaxy clustering informations coming from the full shape of the galaxy power spectrum from the Baryon Oscillation Spectroscopic Survey (BOSS) Data Release 9 measurements. Varying at the same time the neutrino effective number N_{eff} and the effective mass of the sterile neutrino $m_{\nu,\text{sterile}}^{\text{eff}}$, we found that $3.30 < N_{\text{eff}} < 4.43$ and $m_{\nu,\text{sterile}}^{\text{eff}} < 0.33$ eV both at 95% c.l., with the three active neutrinos having the minimum mass allowed in the normal hierarchy scheme, i.e. $\sum m_\nu \sim 0.06$ eV. Afterwards, we have considered Planck+WP+high-l dataset in combination with the HST measurements, finding $m_{\nu,\text{sterile}}^{\text{eff}} < 0.36$ eV and $3.14 < N_{\text{eff}} < 4.15$ at 95% c.l.. These values compromise the viability of the $(3 + 2)$ massive sterile neutrino models for the parameter region indicated by global fits of neutrino oscillation data, while the existence of one additional fully thermal sterile massive neutrino is perfectly allowed by these datasets.

Concerning models with a dark sector with light species that eventually decouples from the standard model, as, for instance, asymmetric dark matter models, having extra heavy degrees of freedom in the dark sector is highly disfavoured considering $N_{\text{eff}} = 3.62_{-0.48}^{+0.50}$ (Planck+WP+high-l), and mildly disfavoured considering $N_{\text{eff}} = 3.83 \pm 0.54$ (Planck+WP+high-l+HST).

Moreover, we constrained the extended cosmological scenarios with additional thermal relics, as thermal axions or sterile neutrino species, varying simultaneously the sum of active neutrino masses $\sum m_\nu$ and considering all the current available cosmological data in the beginning of year 2014, including the recent and most precise Baryon Acoustic Oscillation (BAO) measurements from the BOSS Data Release 11. The largest effect of neutrino masses on the different cosmological observables arises from their free streamig nature: the non-relativistic neutrino overdensities will contribute to clustering only at scales larger than their free streaming scale, suppressing the growth of matter density fluctuations at small scales. In the minimal three active neutrino scenario, we found $\sum m_\nu < 0.22$ eV at 95% c.l. from the

combination of CMB, BAO and Hubble Space Telescope measurements of the Hubble constant. A non zero value for the sum of the three active neutrino masses of ~ 0.3 eV is significantly favoured at more than 3 standard deviations when adding the constraints on σ_8 and Ω_m from the Planck Cluster catalog on galaxy number counts. This preference for non zero thermal relic masses disappears almost completely in both the thermal axion and massive sterile neutrino schemes. The existence of extra massive species is well motivated by either the so-called neutrino oscillation anomalies (in the case of sterile neutrino species) or by the strong CP problem (in the case of thermal axions). Both extra, sterile neutrino species and axions have an associated free streaming scale, reducing the growth of matter fluctuations at small scales. When considering simultaneously thermal axions and active massive neutrino species, and including CMB, BOSS BAO DR11, additional BAO measurements, WiggleZ power spectrum (full shape) information, the H_0 HST prior and BBN light element abundances, the 95% c.l. bounds are $\sum m_\nu < 0.25$ eV and $m_a < 0.57$ eV. When considering Planck SZ clusters and CFHTLens information added to CMB data, BOSS DR11 BAO, additional BAO measurements and the HST H_0 prior, the 95% c.l. bounds on the active and the sterile neutrino parameters are $\sum m_\nu < 0.39$ eV, $m_{\nu,\text{sterile}}^{\text{eff}}$ eV and $N_{\text{eff}} < 4.01$. Finally, we have considered the recent B-mode polarization measurements made by the BICEP2 experiment, finding that in a LCDM+r scenario the presence of extra relativistic particles is significantly suggested by current Planck+WP+BICEP2 data with $N_{eff} = 4.00 \pm 0.41$ at 68% c.l., solving the current tension between the Planck and BICEP2 experiments on the amplitude of tensor modes.

Another way to explain the excess in the neutrino effective number N_{eff} is to consider a non-vanishing neutrino chemical potential. We investigated this possibility in the Curvaton scenario, because after the decay of the Curvaton field are expected residual isocurvature fluctuations in the neutrino density component, that correspond to a non-zero chemical potential. We have forecasted the capability of future CMB experiment, in particular Planck-like, CMBpol (PRISM) and SPIDER, to constrain at the same time the amplitude of the neutrino isocurvature density α^{NID} and N_{eff}, and traslated this bounds on the average value of the degeneracy neutrino parameter $\bar{\xi}$ and its spatial variance σ_ξ^2, in order to compare them with the constraints from the BBN. We found that if $\Delta N_{\text{eff}} = N_{\text{eff}} - 3.046 = 0$, Planck, Spider and CMBPol will be able to bound $\Delta N_{\text{eff}} \lesssim 0.3, 0.8, 0.08$ at the 95% c.l.., respectively, corresponding to $\bar{\xi} < 0.5, 0.8, 0.24$. Afterwards, with the coming of the temperature data from Planck, we constrained jointly the amplitude of the neutrino isocurvature density α^{NID} and N_{eff}. We found that the Planck+WP dataset does not show any indication for a NID component, severely constraining its amplitude, and that current indications for a non-standard N_{eff} are further relaxed. When the HST prior on the Hubble constant is included, an anticorrelated neutrino isocurvature density component is severly constrained, while the combined analysis suggests a value for N_{eff} larger than the standard expectations at more than two standard deviations.

After having considered the axion particle, the pseudo Nambu-Goldstone boson associated to the breaking of the PQ symmetry, as hot dark matter to account for the excess of dark radiation, we investigated, in light of the recent B-mode polarization measurements made by the BICEP2 experiment, the possibility that the axion account fot the total amount of cold dark matter in the Universe. We

found that, in the minimal ADM scenario and for $\Lambda_{\rm QCD} = 200\,MeV$, the full dataset (Planck + WP + BOSS DR11 + BICEP2) implies that the axion mass $m_{\rm a} = 82.2 \pm 1.1\,\mu eV$ (corresponding to the Peccei-Quinn symmetry being broken at a scale $f_{\rm a} = (7.54 \pm 0.10) \times 10^{10}\,GeV$), or $m_{\rm a} = 76.6 \pm 2.6\,\mu eV$ ($f_{\rm a} = (8.08 \pm 0.27) \times 10^{10}\,GeV$) when we allow for a non-standard effective number of relativistic species $N_{\rm eff}$. We also found a 2-σ preference for $N_{\rm eff} > 3.046$. The limit on the sum of neutrino masses is $\sum m_\nu < 0.25\,eV$ at 95% c.l. for $N_{\rm eff} = 3.046$, or $\sum m_\nu < 0.47\,eV$ when $N_{\rm eff}$ is a free parameter. We also studied the effect on our estimates of theoretical uncertainties, in particular the imprecise knowledge of the QCD scale $\Lambda_{\rm QCD}$, in the calculation of the temperature-dependent axion mass. We found that in the simplest ADM scenario the Planck+WP dataset implies that the axion mass $m_{\rm a} = 63.7 \pm 1.2\,\mu eV$ for $\Lambda_{\rm QCD} = 400\,MeV$. Dark matter axions with mass in the $60 - 80\,\mu eV$ (corresponding to an axion-photon coupling $G_{\rm a\gamma\gamma} \sim 10^{-14}\,GeV^{-1}$) range can, in principle, be detected by looking for axion-to-photon conversion occurring inside a tunable microwave cavity permeated by a high-intensity magnetic field, and operating at a frequency $\nu \simeq 15 - 20$ GHz. This is out of the reach of current laboratory experiments like Axion Dark Matter eXperiment (ADMX, limited to a maximum frequency of a few GHzs), but is, on the other hand, within the reach of the upcoming ADMX-HF experiment, that will explore the $4 - 40$ GHz frequency range and then being sensitive to axions masses up to $\sim 160\,\mu eV$.

A further research subject has been the tension between the abundance of primordial deuterium obtained from the Lyman-alpha absorption-line system and the abundance computed by the Planck data. This discrepancy is the result of the uncertainty in the BBN computation on the rate A_2 of the capture radiative reaction $d(p, \gamma)^3He$ that converts deuterium into helium. Assuming the standard cosmological model, we performed a combined analysis of Planck data and of recent deuterium abundance measurements in metal-poor damped Lyman-alpha systems providing independent information on the cross section of this reaction. Interestingly, the result that we obtained is higher than the values suggested by a fit of present experimental data in the BBN energy range ($10 - 300$ keV), whereas it is in better agreement with *ab initio* theoretical calculations, based on models for the nuclear electromagnetic current derived from realistic interactions. Due to the correlation between the rate of the above nuclear process and the effective number of neutrinos $N_{\rm eff}$, the same analysis points out a $N_{\rm eff} > 3$ as well. We think that an experiment such as LUNA at the underground Gran Sasso Laboratories may give an answer to this problem in a reasonably short time. In fact, with the present underground $400\,kV$ LUNA accelerator is possible to measure the $d(p, \gamma)^3He$ cross section in the $20 < E_{cm}(keV) < 260$ energy range with an accuracy better than 3%.

Finally, we have used the Bispectrum signal, the three point correlation function of the CMB temperature anisotropies, due to the cross-correlation between the Weak Lensing and the Integrated Sachs-Wolfe effect to constrain the cosmological parameter. First of all, we investigated the possibility to constrain with this L-ISW Bispectrum three different classes of modified gravity models: Linder's growth index, Chameleon-type models and $f(R)$ theories. We have found that in the case when all the cosmological parameters are fixed, the bispectrum signal will be extremely useful providing a significant improvement in the constraints on modified theories of gravity. Afterwards, we have found that while a measurement of the CMB bispectrum can

provide only very weak constraints on the neutrino mass $\sum m_\nu$ and on the viscosity speed c_{vis}^2, it can achieve interesting constraints on the effective number of relativistic degrees of freedom N_{eff}: weaker respect to those that could be achieved from the temperature spectrum but clearly an useful cross-check of the theory. We have also investigated the bias introduced by current uncertainties in neutrino parameters in the determination of the primordial f_{NL} parameter that could arise in some inflationary model. We have found that the bias varies in a significant way between model with different neutrino parameters.

Bibliography

[1] G. Hinshaw, D. Larson, E. Komatsu, D. N. Spergel, C. L. Bennett, J. Dunkley, M. R. Nolta and M. Halpern *et al.*, arXiv:1212.5226 [astro-ph.CO].

[2] P. A. R. Ade et al. [Planck Collaboration], arXiv:1303.5062 [astro-ph.CO].

[3] S. Das, B. D. Sherwin, P. Aguirre, J. W. Appel, J. R. Bond, C. S. Carvalho, M. J. Devlin and J. Dunkley *et al.*, Phys. Rev. Lett. **107** (2011) 021301 [arXiv:1103.2124 [astro-ph.CO]].

[4] A. van Engelen, R. Keisler, O. Zahn, K. A. Aird, B. A. Benson, L. E. Bleem, J. E. Carlstrom and C. L. Chang *et al.*, arXiv:1202.0546 [astro-ph.CO].

[5] P. A. R. Ade *et al.* [Planck Collaboration], arXiv:1303.5076 [astro-ph.CO].

[6] A. G. Riess, L. Macri, S. Casertano, H. Lampeitl, H. C. Ferguson, A. V. Filippenko, S. W. Jha and W. Li *et al.*, Astrophys. J. **730**, 119 (2011) [Erratum-ibid. **732**, 129 (2011)] [arXiv:1103.2976 [astro-ph.CO]].

[7] L. Anderson, E. Aubourg, S. Bailey, D. Bizyaev, M. Blanton, A. S. Bolton, J. Brinkmann and J. R. Brownstein *et al.*, Mon. Not. Roy. Astron. Soc. **428**, 1036 (2013) [arXiv:1203.6594 [astro-ph.CO]].

[8] L. Anderson, E. Aubourg, S. Bailey, F. Beutler, V. Bhardwaj, M. Blanton, A. S. Bolton and J. Brinkmann *et al.*, arXiv:1312.4877 [astro-ph.CO].

[9] P. A. R. Ade *et al.* [Planck Collaboration], arXiv:1303.5077 [astro-ph.CO].

[10] P. A. R. Ade *et al.* [BICEP2 Collaboration], arXiv:1403.3985 [astro-ph.CO].

[11] R. Cooke, M. Pettini, R. A. Jorgenson, M. T. Murphy and C. C. Steidel, arXiv:1308.3240 [astro-ph.CO].

[12] B. Ryden, "Introduction to cosmology", Addison Wesley, 2004

[13] S.Dodelson, Modern Cosmology, Academic Press.

[14] J.Lesgourgues, An overview of Cosmology, arXiv:astro-ph/0409426.

[15] J. Lesgourgues and S. Pastor, Phys. Rept. **429**, 307 (2006) [astro-ph/0603494].

[16] A. D. Dolgov, S. H. Hansen, S. Pastor, S. T. Petcov, G. G. Raffelt and D. V. Semikoz, Nucl. Phys. B **632**, 363 (2002) [hep-ph/0201287].

[17] Y. Y. Y. Wong, Phys. Rev. D **66**, 025015 (2002) [hep-ph/0203180].

[18] K. N. Abazajian, J. F. Beacom and N. F. Bell, Phys. Rev. D **66**, 013008 (2002) [astro-ph/0203442].

[19] G. Mangano, G. Miele, S. Pastor, T. Pinto, O. Pisanti and P. D. Serpico, Nucl. Phys. B **729**, 221 (2005) [hep-ph/0506164].

[20] E. Di Valentino, A. Melchiorri and O. Mena, JCAP **1311**, 018 (2013) [arXiv:1304.5981].

[21] E. Giusarma, E. Di Valentino, M. Lattanzi, A. Melchiorri and O. Mena, Phys. Rev. D **90**, 043507 (2014) [arXiv:1403.4852 [astro-ph.CO]].

[22] E. Di Valentino, M. Lattanzi, G. Mangano, A. Melchiorri and P. Serpico, Phys. Rev. D **85**, 043511 (2012) [arXiv:1111.3810 [astro-ph.CO]].

[23] E. Di Valentino and A. Melchiorri, Phys. Rev. D **90**, no. 8, 083531 (2014) [arXiv:1405.5418 [astro-ph.CO]].

[24] J. C. Mather, E. S. Cheng, D. A. Cottingham, R. E. Eplee, D. J. Fixsen, T. Hewagama, R. B. Isaacman and K. A. Jesnsen *et al.*, Astrophys. J. **420**, 439 (1994).

[25] C. L. Bennett, A. Kogut, G. Hinshaw, A. J. Banday, E. L. Wright, K. Gorski, D. T. Wilkinson and R. Weiss *et al.*, Astrophys. J. **436**, 423 (1994) [astro-ph/9401012].

[26] C. -P. Ma and E. Bertschinger, Astrophys. J. **455**, 7 (1995) [astro-ph/9506072].

[27] A. Lewis, A. Challinor and A. Lasenby, Astrophys. J. **538**, 473 (2000) [astro-ph/9911177].

[28] McGraw Hill Encyclopaedia of Physics (2nd edition), C. B. Parker, 1994.

[29] http://www.thphys.uni-heidelberg.de/~amendola/teaching/introduction.pdf

[30] A. H. Guth, Phys. Rev. D, 23:347, 1981.

[31] D. Baumann, arXiv:0907.5424 [hep-th].

[32] G. Aad *et al.* [ATLAS Collaboration], Phys. Lett. B **716**, 1 (2012) [arXiv:1207.7214 [hep-ex]].

[33] S. Chatrchyan *et al.* [CMS Collaboration], Phys. Lett. B **716**, 30 (2012) [arXiv:1207.7235 [hep-ex]].

[34] P. Coles and P. Lucchin, *Cosmology: The Origin And The Evolution Of Cosmic Structures.* Secon edition, 2002

[35] E. W. Kolb and M. S. Turner, *The Early Universe*, 1990.

[36] D. H. Lyth and A. R. Liddle, *The Primordial Density Perturbation*, Cambridge University Press, 2009.

[37] A. Kosowsky, Annals Phys. **246**, 49 (1996) [astro-ph/9501045].

[38] U. Seljak and M. Zaldarriaga, Phys. Rev. Lett. **78**, 2054 (1997) [astro-ph/9609169].

[39] A. Riotto, CERN Yellow Report CERN-2010-001, 315-362 [arXiv:1010.2642 [hep-ph]].

[40] W. Hu and S. Dodelson, Ann. Rev. Astron. Astrophys. **40**, 171 (2002) [astro-ph/0110414].

[41] R.K. Sachs and A.M. Wolfe, Astrophysical Journal 147: 73 (1967)

[42] J. Silk, "Cosmic Black-Body Radiation and Galaxy Formation", ApJ, 151:459-+, February 1968

[43] Y.B. Zel'dovich and R.A. Sunyaev, AP&SS, 4:301-316, July 1969

[44] http://ned.ipac.caltech.edu/level5/March05/Scott/Scott4.html

[45] W. Hu, Lect. Notes Phys. **470**, 207 (1996) [astro-ph/9511130].

[46] http://background.uchicago.edu/ whu/araa/node20.htm

[47] C. P. Ma and J. N. Fry, Phys. Rev. Lett. **88**, 211301 (2002) [astro-ph/0106342].

[48] M.J. Rees and D.W. Sciama, Nature 217 511 (1968)

[49] U. Seljak, Astrophysical Journal 463:1-+, May 1996

[50] J.P. Ostriker and E.T. Vishniac, Astrophysical Journal 306:L51-L54, July 1986

[51] G. Tormen, Dispense per il corso di Cosmologia, (2002)

[52] D. J. Eisenstein and W. Hu, 1998, ApJ 496 (1998)

[53] N. Bartolo, S. Matarrese and A. Riotto, Phys. Rev. D **65**, 103505 (2002) [hep-ph/0112261].

[54] E. Komatsu and D. N. Spergel, Phys. Rev. D **63**, 063002 (2001) [astro-ph/0005036].

[55] M. Liguori, F. K. Hansen, E. Komatsu, S. Matarrese and A. Riotto, Phys. Rev. D **73**, 043505 (2006) [astro-ph/0509098].

[56] A. Gangui, F. Lucchin, S. Matarrese and S. Mollerach, Astrophys. J. **430**, 447 (1994) [astro-ph/9312033].

[57] L. M. Wang and M. Kamionkowski, Phys. Rev. D **61**, 063504 (2000) [astro-ph/9907431].

[58] A. Gangui and J. Martin, [astro-ph/9908009].

[59] S. Mollerach, A. Gangui, F. Lucchin and S. Matarrese, Astrophys. J. **453** (1995) 1 [astro-ph/9503115].

[60] D. N. Spergel and D. M. Goldberg, Phys. Rev. D **59**, 103001 (1999) [astro-ph/9811252].

[61] D. M. Goldberg and D. N. Spergel, Phys. Rev. D **59** (1999) 103002 [astro-ph/9811251].

[62] W. Hu, D. Scott, N. Sugiyama and M. J. White, 1, Phys. Rev. D **52**, 5498 (1995) [astro-ph/9505043].

[63] S. Seager, D. D. Sasselov and D. Scott, Astrophys. J. Suppl. **128**, 407 (2000) [astro-ph/9912182].

[64] W. Y. Wong, A. Moss and D. Scott, Mon. Not. Roy. Astron. Soc. **386**, 1023 (2008) [arXiv:0711.1357 [astro-ph]].

[65] E. R. Switzer and C. M. Hirata, Phys. Rev. D **77**, 083006 (2008) [astro-ph/0702143 [ASTRO-PH]].

[66] C. M. Hirata and E. R. Switzer, Phys. Rev. D **77**, 083007 (2008) [astro-ph/0702144 [ASTRO-PH]].

[67] C. M. Hirata, Phys. Rev. D **78**, 023001 (2008) [arXiv:0803.0808 [astro-ph]].

[68] J. A. Rubino-Martin, J. Chluba, W. A. Fendt and B. D. Wandelt, arXiv:0910.4383 [astro-ph.CO].

[69] D. Grin and C. M. Hirata, Phys. Rev. D **81**, 083005 (2010) [arXiv:0911.1359 [astro-ph.CO]].

[70] J. Chluba and R. M. Thomas, arXiv:1010.3631 [astro-ph.CO].

[71] J. Chluba, G. M. Vasil and L. J. Dursi, arXiv:1003.4928 [astro-ph.CO].

[72] Y. Ali-Haimoud and C. M. Hirata, Phys. Rev. D **83**, 043513 (2011) [arXiv:1011.3758 [astro-ph.CO]].

[73] J. R. Shaw and J. Chluba, arXiv:1102.3683 [astro-ph.CO].

[74] P. J. E. Peebles, S. Seager and W. Hu, Astrophys. J. **539**, L1 (2000) [astro-ph/0004389].

[75] X. L. Chen and M. Kamionkowski, Phys. Rev. D **70**, 043502 (2004) [astro-ph/0310473].

[76] N. Padmanabhan and D. P. Finkbeiner, Phys. Rev. D **72**, 023508 (2005) [astro-ph/0503486].

[77] L. Zhang, X. Chen, M. Kamionkowski, Z. g. Si and Z. Zheng, Phys. Rev. D **76**, 061301 (2007) [arXiv:0704.2444 [astro-ph]].

[78] T. R. Slatyer, N. Padmanabhan and D. P. Finkbeiner, Phys. Rev. D **80**, 043526 (2009) [arXiv:0906.1197 [astro-ph.CO]].

[79] S. Galli, F. Iocco, G. Bertone and A. Melchiorri, Phys. Rev. D **80**, 023505 (2009) [arXiv:0905.0003 [astro-ph.CO]].

[80] S. Galli, F. Iocco, G. Bertone and A. Melchiorri, Phys. Rev. D **84**, 027302 (2011) [arXiv:1106.1528 [astro-ph.CO]].

[81] G. Hutsi, J. Chluba, A. Hektor and M. Raidal, Astron. Astrophys. **535**, A26 (2011) [arXiv:1103.2766 [astro-ph.CO]].

[82] S. Galli, T. R. Slatyer, M. Valdes and F. Iocco, Phys. Rev. D **88**, 063502 (2013) [arXiv:1306.0563 [astro-ph.CO]].

[83] M. Kaplinghat, R. J. Scherrer and M. S. Turner, Phys. Rev. D **60**, 023516 (1999) [astro-ph/9810133].

[84] S. Galli, A. Melchiorri, G. F. Smoot and O. Zahn, Phys. Rev. D **80**, 023508 (2009) [arXiv:0905.1808 [astro-ph.CO]].

[85] E. Menegoni, M. Archidiacono, E. Calabrese, S. Galli, C. J. A. P. Martins and A. Melchiorri, Phys. Rev. D **85**, 107301 (2012) [arXiv:1202.1476 [astro-ph.CO]].

[86] M. Farhang, J. R. Bond and J. Chluba, Astrophys. J. **752**, 88 (2012) [arXiv:1110.4608 [astro-ph.CO]].

[87] M. Farhang, J. R. Bond, J. Chluba and E. R. Switzer, Astrophys. J. **764**, 137 (2013) [arXiv:1211.4634 [astro-ph.CO]].

[88] E. Calabrese, A. Slosar, A. Melchiorri, G. F. Smoot and O. Zahn, Phys. Rev. D **77** (2008) 123531 [arXiv:0803.2309 [astro-ph]].

[89] J. L. Sievers, R. A. Hlozek, M. R. Nolta, V. Acquaviva, G. E. Addison, P. A. R. Ade, P. Aguirre and M. Amiri *et al.*, arXiv:1301.0824 [astro-ph.CO].

[90] Z. Hou, C. L. Reichardt, K. T. Story, B. Follin, R. Keisler, K. A. Aird, B. A. Benson and L. E. Bleem *et al.*, arXiv:1212.6267 [astro-ph.CO].

[91] K. T. Story, C. L. Reichardt, Z. Hou, R. Keisler, K. A. Aird, B. A. Benson, L. E. Bleem and J. E. Carlstrom *et al.*, arXiv:1210.7231 [astro-ph.CO].

[92] E. Komatsu *et al.* [WMAP Collaboration], "Seven-Year Wilkinson Microwave Anisotropy Probe (WMAP) Observations: Cosmological Interpretation," Astrophys. J. Suppl. **192**, 18 (2011). [arXiv:1001.4538 [astro-ph.CO]].

[93] G. Hinshaw *et al.* [WMAP Collaboration], Astrophys. J. Suppl. **180**, 225 (2009) [arXiv:0803.0732 [astro-ph]].

[94] E. Di Valentino, S. Galli, M. Lattanzi, A. Melchiorri, P. Natoli, L. Pagano and N. Said, Phys. Rev. D **88**, no. 2, 023501 (2013) [arXiv:1301.7343 [astro-ph.CO], arXiv:1301.7343 [astro-ph.CO]].

[95] N. Said, E. Di Valentino and M. Gerbino, Phys. Rev. D **88** (2013) 023513 [arXiv:1304.6217 [astro-ph.CO]].

[96] M. Gerbino, E. Di Valentino and N. Said, Phys. Rev. D **88**, no. 6, 063538 (2013) [arXiv:1304.7400 [astro-ph.CO]].

[97] A. Lewis and S. Bridle, Phys. Rev. D **66**, 103511 (2002) [arXiv:astro-ph/0205436].

[98] Beutler, F., et al., Montly Notices of the Royal Astronomical Society, 416, 3017, 2011

[99] Padmanabhan, N., Xu, X., Eisenstein, D. J., Scalzo, R., Cuesta, A. J., Mehta, K. T., & Kazin, E. 2012, ArXiv e-prints, arXiv:1202.0090

[100] C. Blake et al., Montly Notices of the Royal Astronomical Society, 425, 405, 2012

[101] P. A. R. Ade *et al.* [Planck Collaboration], arXiv:1303.5075 [astro-ph.CO].

[102] C. L. Bennett, D. Larson, J. L. Weiland, N. Jarosik, G. Hinshaw, N. Odegard, K. M. Smith and R. S. Hill *et al.*, arXiv:1212.5225 [astro-ph.CO].

[103] C. Blake, T. Davis, G. Poole, D. Parkinson, S. Brough, M. Colless, C. Contreras and W. Couch *et al.*, Mon. Not. Roy. Astron. Soc. **415** (2011) 2892 [arXiv:1105.2862 [astro-ph.CO]].

[104] A. Lewis, Phys. Rev. D87, **103529** (2013) [arXiv:1304.4473 [astro-ph.CO]].

[105] Talk given by John Carlstrom at the 47 ESLAB Planck conference. `http://www.rssd.esa.int/SA/PLANCK/docs/eslab47/Session13_Wrap-up_and_Conclusions/47ESLAB_April_05_2013_15_10_Carlstrom.pdf`

[106] M. Archidiacono, E. Giusarma, A. Melchiorri and O. Mena, arXiv:1303.0143 [astro-ph.CO].

[107] M. Archidiacono, E. Calabrese and A. Melchiorri, Phys. Rev. D **84**, 123008 (2011) [arXiv:1109.2767 [astro-ph.CO]].

[108] T. L. Smith, S. Das and O. Zahn, Phys. Rev. D **85** (2012) 023001 [arXiv:1105.3246 [astro-ph.CO]].

[109] Z. Hou, R. Keisler, L. Knox, M. Millea and C. Reichardt, arXiv:1104.2333 [astro-ph.CO].

[110] W. Hu, D. J. Eisenstein, M. Tegmark and M. J. White, Phys. Rev. D **59**, 023512 (1999) [astro-ph/9806362].

[111] W. Hu, Astrophys. J. **506**, 485 (1998) [astro-ph/9801234].

[112] R. Trotta and A. Melchiorri, Phys. Rev. Lett. **95** (2005) 011305 [astro-ph/0412066].

[113] R. Diamanti, E. Giusarma, O. Mena, M. Archidiacono and A. Melchiorri, arXiv:1212.6007 [astro-ph.CO].

[114] L. Anderson, E. Aubourg, S. Bailey, F. Beutler, A. S. Bolton, J. Brinkmann, J. R. Brownstein and C. -H. Chuang *et al.*, arXiv:1303.4666 [astro-ph.CO].

[115] F. Beutler, C. Blake, M. Colless, D. H. Jones, L. Staveley-Smith, L. Campbell, Q. Parker and W. Saunders *et al.*, Mon. Not. Roy. Astron. Soc. **416**, 3017 (2011) [arXiv:1106.3366 [astro-ph.CO]].

[116] C. L. Reichardt, L. Shaw, O. Zahn, K. A. Aird, B. A. Benson, L. E. Bleem, J. E. Carlstrom and C. L. Chang *et al.*, Astrophys. J. **755**, 70 (2012) [arXiv:1111.0932 [astro-ph.CO]].

[117] M. Sorel, J. M. Conrad and M. Shaevitz, Phys. Rev. D **70**, 073004 (2004) [hep-ph/0305255].

[118] S. M. Bilenky, C. Giunti and W. Grimus Eur. Phys. J. C **1**, 247 (1998) [hep-ph/9607372]. V. D. Barger, T. J. Weiler and K. Whisnant Phys. Lett. B **427**, 97 (1998) [hep-ph/9712495].

[119] C. P. Ahn *et al.* [SDSS Collaboration], Astrophys. J. Suppl. **203**, 21 (2012) [arXiv:1207.7137 [astro-ph.IM]].

[120] D. J. Eisenstein *et al.* [SDSS Collaboration], Astron. J. **142**, 72 (2011) [arXiv:1101.1529 [astro-ph.IM]].

[121] M. Blennow, B. Dasgupta, E. Fernandez-Martinez, N. Rius and , JHEP **1103**, 014 (2011) [arXiv:1009.3159 [hep-ph]].

[122] M. Blennow, E. Fernandez-Martinez, O. Mena, J. Redondo and P. Serra, JCAP **1207**, 022 (2012) [arXiv:1203.5803 [hep-ph]].

[123] U. Franca, R. A. Lineros, J. Palacio and S. Pastor, arXiv:1303.1776 [astro-ph.CO].

[124] E. Giusarma, M. Corsi, M. Archidiacono, R. de Putter, A. Melchiorri, O. Mena, S. Pandolfi, Phys. Rev. **D83**, 115023 (2011). [arXiv:1102.4774 [astro-ph.CO]].

[125] J. Hamann, S. Hannestad, G. G. Raffelt, Y. Y. Y. Wong, JCAP **1109**, 034 (2011). [arXiv:1108.4136 [astro-ph.CO]].

[126] E. Giusarma, M. Archidiacono, R. de Putter, A. Melchiorri and O. Mena, Phys. Rev. D **85**, 083522 (2012) [arXiv:1112.4661 [astro-ph.CO]].

[127] S. Joudaki, K. N. Abazajian and M. Kaplinghat, Phys. Rev. D **87**, 065003 (2013) [arXiv:1208.4354 [astro-ph.CO]].

[128] S. Riemer-Sorensen, D. Parkinson, T. M. Davis and C. Blake, Astrophys. J. **763**, 89 (2013)

[129] E. Giusarma, R. de Putter and O. Mena, arXiv:1211.2154 [astro-ph.CO].

[130] M. Archidiacono, N. Fornengo, C. Giunti, S. Hannestad and A. Melchiorri, arXiv:1302.6720 [astro-ph.CO].

[131] A. Melchiorri, O. Mena, S. Palomares-Ruiz, S. Pascoli, A. Slosar and M. Sorel, JCAP **0901**, 036 (2009) [arXiv:0810.5133 [hep-ph]].

[132] S. Hannestad, I. Tamborra and T. Tram, JCAP **1207**, 025 (2012) [arXiv:1204.5861 [astro-ph.CO]].

[133] A. Mirizzi, N. Saviano, G. Miele and P. D. Serpico, Phys. Rev. D **86**, 053009 (2012) [arXiv:1206.1046 [hep-ph]].

[134] A. Mirizzi, G. Mangano, N. Saviano, E. Borriello, C. Giunti, G. Miele, O. Pisanti and , arXiv:1303.5368 [astro-ph.CO].

[135] A. D. Dolgov, Phys. Rept. **370**, 333 (2002) [hep-ph/0202122].

[136] D. Notzold and G. Raffelt, Nucl. Phys. B **307**, 924 (1988).

[137] A. D. Dolgov, S. H. Hansen, S. Pastor and D. V. Semikoz, Astropart. Phys. **14**, 79 (2000) [hep-ph/9910444].

[138] M. C. Gonzalez-Garcia, M. Maltoni, J. Salvado and T. Schwetz, JHEP **1212**, 123 (2012) [arXiv:1209.3023 [hep-ph]].

[139] J. Kopp, P. A. N. Machado, M. Maltoni and T. Schwetz, JHEP **1305**, 050 (2013) [arXiv:1303.3011 [hep-ph]].

[140] J. M. Conrad, C. M. Ignarra, G. Karagiorgi, M. H. Shaevitz and J. Spitz, Adv. High Energy Phys. **2013**, 163897 (2013) [arXiv:1207.4765 [hep-ex]].

[141] J. Hamann, S. Hannestad and Y. Y. Y. Wong, JCAP **1211**, 052 (2012) [arXiv:1209.1043 [astro-ph.CO]].

[142] G. -B. Zhao, S. Saito, W. J. Percival, A. J. Ross, F. Montesano, M. Viel, D. P. Schneider and M. Manera *et al.*, arXiv:1211.3741 [astro-ph.CO].

[143] S. Riemer-SÃÿrensen, D. Parkinson and T. M. Davis, arXiv:1306.4153 [astro-ph.CO].

[144] E. Giusarma, R. de Putter, S. Ho and O. Mena, arXiv:1306.5544 [astro-ph.CO].

[145] O. Wantz and E. P. S. Shellard, Phys. Rev. D **82**, 123508 (2010) [arXiv:0910.1066 [astro-ph.CO]].

[146] J. Lesgourgues and S. Pastor, Adv. High Energy Phys. **2012**, 608515 (2012) [arXiv:1212.6154 [hep-ph]].

[147] J. Lesgourgues, L. Perotto, S. Pastor and M. Piat, Phys. Rev. D **73**, 045021 (2006) [astro-ph/0511735].

[148] B. A. Reid, L. Verde, R. Jimenez and O. Mena, JCAP **1001**, 003 (2010) [arXiv:0910.0008 [astro-ph.CO]].

[149] J. Hamann, S. Hannestad, J. Lesgourgues, C. Rampf and Y. Y. Y. Wong, JCAP **1007**, 022 (2010) [arXiv:1003.3999 [astro-ph.CO]].

[150] R. de Putter, O. Mena, E. Giusarma, S. Ho, A. Cuesta, H. -J. Seo, A. J. Ross and M. White *et al.*, Astrophys. J. **761**, 12 (2012) [arXiv:1201.1909 [astro-ph.CO]].

[151] M. Archidiacono, E. Giusarma, S. Hannestad and O. Mena, arXiv:1307.0637 [astro-ph.CO].

[152] J. -W. Hu, R. -G. Cai, Z. -K. Guo and B. Hu, arXiv:1401.0717 [astro-ph.CO].

[153] W. J. Percival *et al.* [SDSS Collaboration], Mon. Not. Roy. Astron. Soc. **401**, 2148 (2010) [arXiv:0907.1660 [astro-ph.CO]].

[154] C. Blake, E. Kazin, F. Beutler, T. Davis, D. Parkinson, S. Brough, M. Colless and C. Contreras *et al.*, Mon. Not. Roy. Astron. Soc. **418**, 1707 (2011) [arXiv:1108.2635 [astro-ph.CO]].

[155] K. S. Dawson *et al.* [BOSS Collaboration], arXiv:1208.0022 [astro-ph.CO].

[156] R. de Putter, E. V. Linder and A. Mishra, arXiv:1401.7022 [astro-ph.CO].

[157] J. Hamann, S. Hannestad, G. G. Raffelt, I. Tamborra and Y. Y. Y. Wong, Phys. Rev. Lett. **105**, 181301 (2010) [arXiv:1006.5276 [hep-ph]].

[158] A. Melchiorri, O. Mena and A. Slosar, Phys. Rev. D **76**, 041303 (2007) [arXiv:0705.2695 [astro-ph]].

[159] S. Hannestad, A. Mirizzi, G. G. Raffelt and Y. Y. Y. Wong, JCAP **0708**, 015 (2007) [arXiv:0706.4198 [astro-ph]].

[160] S. Hannestad, A. Mirizzi, G. G. Raffelt and Y. Y. Y. Wong, JCAP **0804**, 019 (2008) [arXiv:0803.1585 [astro-ph]].

[161] S. Hannestad, A. Mirizzi, G. G. Raffelt and Y. Y. Y. Wong, JCAP **1008**, 001 (2010) [arXiv:1004.0695 [astro-ph.CO]].

[162] M. Archidiacono, S. Hannestad, A. Mirizzi, G. Raffelt and Y. Y. Y. Wong, JCAP **1310**, 020 (2013) [arXiv:1307.0615 [astro-ph.CO]].

[163] K. N. Abazajian, M. A. Acero, S. K. Agarwalla, A. A. Aguilar-Arevalo, C. H. Albright, S. Antusch, C. A. Arguelles and A. B. Balantekin *et al.*, arXiv:1204.5379 [hep-ph].

[164] M. Archidiacono, N. Fornengo, C. Giunti and A. Melchiorri, Phys. Rev. D **86**, 065028 (2012) [arXiv:1207.6515 [astro-ph.CO]].

[165] R.D. Peccei and H.R. Quinn, Phys. Rev. Lett. **38**, 1440 (1977); Phys. Rev. D **16**, 1791 (1977).

[166] J. Hamann and J. Hasenkamp, JCAP **1310**, 044 (2013) [arXiv:1308.3255 [astro-ph.CO]].

[167] M. Wyman, D. H. Rudd, R. A. Vanderveld and W. Hu, arXiv:1307.7715 [astro-ph.CO].

[168] P. A. R. Ade *et al.* [Planck Collaboration], arXiv:1303.5080 [astro-ph.CO].

[169] C. Heymans, E. Grocutt, A. Heavens, M. Kilbinger, T. D. Kitching, F. Simpson, J. Benjamin and T. Erben *et al.*, arXiv:1303.1808 [astro-ph.CO].

[170] Y. I. Izotov, G. Stasinska and N. G. Guseva, arXiv:1308.2100 [astro-ph.CO].

[171] L. Samushia, B. A. Reid, M. White, W. J. Percival, A. J. Cuesta, G. -B. Zhao, A. J. Ross and M. Manera *et al.*, arXiv:1312.4899 [astro-ph.CO].

[172] A. G. Sanchez, F. Montesano, E. A. Kazin, E. Aubourg, F. Beutler, J. Brinkmann, J. R. Brownstein and A. J. Cuesta *et al.*, arXiv:1312.4854 [astro-ph.CO].

[173] C. -H. Chuang, F. Prada, F. Beutler, D. J. Eisenstein, S. Escoffier, S. Ho, J. -P. Kneib and M. Manera *et al.*, arXiv:1312.4889 [astro-ph.CO].

[174] S. Das, T. Louis, M. R. Nolta, G. E. Addison, E. S. Battistelli, J R. Bond, E. Calabrese and D. C. M. J. Devlin *et al.*, arXiv:1301.1037 [astro-ph.CO].

[175] D. J. Eisenstein and W. Hu, Astrophys. J. **496**, 605 (1998) [astro-ph/9709112].

[176] D. Parkinson, S. Riemer-Sorensen, C. Blake, G. B. Poole, T. M. Davis, S. Brough, M. Colless and C. Contreras *et al.*, Phys. Rev. D **86**, 103518 (2012) [arXiv:1210.2130 [astro-ph.CO]].

[177] A. Conley, J. Guy, M. Sullivan, N. Regnault, P. Astier, C. Balland, S. Basa and R. G. Carlberg *et al.*, Astrophys. J. Suppl. **192**, 1 (2011) [arXiv:1104.1443 [astro-ph.CO]].

[178] F. Iocco, G. Mangano, G. Miele, O. Pisanti and P. D. Serpico, "Primordial Nucleosynthesis: from precision cosmology to fundamental physics," Phys. Rept. **472**, 1 (2009). [arXiv:0809.0631 [astro-ph]].

[179] A. Arbey, Comput. Phys. Commun. **183**, 1822 (2012) [arXiv:1106.1363 [astro-ph.CO]].

[180] O. Pisanti, A. Cirillo, S. Esposito, F. Iocco, G. Mangano, G. Miele, P. D. Serpico, "PArthENoPE: Public Algorithm Evaluating the Nucleosynthesis of Primordial Elements," Comput. Phys. Commun. **178**, 956-971 (2008). [arXiv:0705.0290 [astro-ph]]. URL http://parthenope.na.infn.it/

[181] S. Chang and K. Choi, "Hadronic axion window and the big bang nucleosynthesis," Phys. Lett. B **316**, 51 (1993) [arXiv:hep-ph/9306216].

[182] G. Steigman, Adv. High Energy Phys. **2012**, 268321 (2012) [arXiv:1208.0032 [hep-ph]].

[183] P. Crotty, J. Garcia-Bellido, J. Lesgourgues and A. Riazuelo, Phys. Rev. Lett. **91**, 171301 (2003) [astro-ph/0306286].

[184] M. Beltran, J. Garcia-Bellido, J. Lesgourgues and A. Riazuelo, Phys. Rev. D **70**, 103530 (2004) [astro-ph/0409326].

[185] K. Moodley, M. Bucher, J. Dunkley, P. G. Ferreira and C. Skordis, Phys. Rev. D **70**, 103520 (2004) [astro-ph/0407304].

[186] R. Bean, J. Dunkley and E. Pierpaoli, Phys. Rev. D **74**, 063503 (2006).

[187] R. Trotta, Mon. Not. Roy. Astron. Soc. **375**, L26 (2007) [astro-ph/0608116].

[188] D. H. Lyth, D. Wands, Phys. Lett. **B524**, 5-14 (2002).

[189] D. H. Lyth, C. Ungarelli and D. Wands, Phys. Rev. D **67**, 023503 (2003).

[190] The Planck Collaboration, arXiv:astro-ph/0604069.

[191] J. A. Tauber et al. (The Planck Collaboration), Astr. Astrophys. **520**, A1 (2010).

[192] A. A. Fraisse, P. A. R. Ade, M. Amiri, S. J. Benton, J. J. Bock, J. R. Bond, J. A. Bonetti and S. Bryan *et al.*, arXiv:1106.3087 [astro-ph.CO].

[193] J. Bock *et al.* [EPIC Collaboration], arXiv:0906.1188 [astro-ph.CO].

[194] J. M. Bardeen, P. J. Steinhardt and M. S. Turner, Phys. Rev. D **28**, 679 (1983).

[195] V. F. Mukhanov, H. A. Feldman and R. H. Brandenberger, Phys. Rept. **215**, 203 (1992).

[196] D. Wands, K. A. Malik, D. H. Lyth and A. R. Liddle, Phys. Rev. D **62**, 043527 (2000) [astro-ph/0003278].

[197] J. Lesgourgues and S. Pastor, Phys. Rev. D **60**, 103521 (1999) [hep-ph/9904411].

[198] D. Langlois, Phys. Rev. D **59**, 123512 (1999) [astro-ph/9906080].

[199] D. Langlois and A. Riazuelo, Phys. Rev. D **62**, 043504 (2000) [astro-ph/9912497].

[200] C. Gordon, D. Wands, B. A. Bassett and R. Maartens, Phys. Rev. D **63**, 023506 (2001) [astro-ph/0009131].

[201] D. H. Lyth and D. Wands, Phys. Rev. D **68**, 103516 (2003) [astro-ph/0306500].

[202] T. Moroi and T. Takahashi, Phys. Lett. B **522**, 215 (2001) [Erratum-ibid. B **539**, 303 (2002)] [hep-ph/0110096].

[203] N. Bartolo and A. R. Liddle, Phys. Rev. D **65**, 121301 (2002) [astro-ph/0203076].

[204] J. R. Bond, G. Efstathiou, M. Tegmark, Mon. Not. Roy. Astron. Soc. **291**, L33-L41 (1997).

[205] http://lambda.gsfc.nasa.gov/product/map/current/params/lcdm_sz_lens_wmap7.cfm

[206] P. D. Serpico and G. G. Raffelt, Phys. Rev. D **71**, 127301 (2005).

[207] V. Simha and G. Steigman, JCAP **0808**, 011 (2008) [arXiv:0806.0179 [hep-ph]].

[208] S. D. Stirling, R. J. Scherrer, Phys. Rev. **D66**, 043531 (2002).

[209] G. Mangano and P. D. Serpico, Phys. Lett. B **701**, 296 (2011).

[210] C. Gordon, K. A. Malik, Phys. Rev. **D69**, 063508 (2004).

[211] M. Savelainen, J. Valiviita, P. Walia, S. Rusak and H. Kurki-Suonio, Phys. Rev. D **88**, 063010 (2013) [arXiv:1307.4398 [astro-ph.CO]].

[212] E. Di Valentino, E. Giusarma, M. Lattanzi, A. Melchiorri and O. Mena, Phys. Rev. D **90**, 043534 (2014) [arXiv:1405.1860 [astro-ph.CO]].

[213] P. A. R Ade *et al.* [BICEP2 Collaboration], arXiv:1403.4302 [astro-ph.CO].

[214] L. Visinelli and P. Gondolo, arXiv:1403.4594 [hep-ph].

[215] D. J. E. Marsh, D. Grin, R. Hlozek and P. G. Ferreira, arXiv:1403.4216 [astro-ph.CO].

[216] J. Preskill, M. B. Wise and F. Wilczek, "Cosmology of the Invisible Axion," Phys. Lett. B **120**, 127 (1983).

[217] L. F. Abbott and P. Sikivie, Phys. Lett. B **120**, 133 (1983).

[218] M. Dine and W. Fischler, Phys. Lett. B **120**, 137 (1983).

[219] M. S. Turner and F. Wilczek, Phys. Rev. Lett. **66**, 5 (1991).

[220] D. H. Lyth and E. D. Stewart, Phys. Rev. D **46**, 532 (1992).

[221] D.J. Gross, R.D. Pisarski, and L.G. Yaffe, Rev. Mod. Phys. **53**, 43 (1981).

[222] P. Fox, A. Pierce and S. D. Thomas, hep-th/0409059.

[223] P. A. R. Ade *et al.* [Planck Collaboration], arXiv:1303.5082 [astro-ph.CO].

[224] T. Higaki, K. S. Jeong and F. Takahashi, arXiv:1403.4186 [hep-ph].

[225] L. Visinelli and P. Gondolo, Phys. Rev. D **80**, 035024 (2009) [arXiv:0903.4377 [astro-ph.CO]].

[226] P. Sikivie, Lect. Notes Phys. **741**, 19 (2008) [astro-ph/0610440].

[227] A. Salvio, A. Strumia and W. Xue, JCAP **1401**, 011 (2014) [arXiv:1310.6982 [hep-ph]].

[228] T. Basse, O. E. Bjaelde, J. Hamann, S. Hannestad and Y. Y. Y. Wong, JCAP **1405**, 021 (2014) [arXiv:1304.2321 [astro-ph.CO]].

[229] C. Beck, arXiv:1403.5676 [hep-ph].

[230] H. Baer, A. Lessa, S. Rajagopalan and W. Sreethawong, JCAP **1106**, 031 (2011) [arXiv:1103.5413 [hep-ph]].

[231] J. -F. Zhang, Y. -H. Li and X. Zhang, arXiv:1403.7028 [astro-ph.CO].

[232] C. Dvorkin, M. Wyman, D. H. Rudd and W. Hu, arXiv:1403.8049 [astro-ph.CO].

[233] M. Archidiacono, N. Fornengo, S. Gariazzo, C. Giunti, S. Hannestad and M. Laveder, arXiv:1404.1794 [astro-ph.CO].

[234] M. Gerbino, A. Marchini, L. Pagano, L. Salvati, E. Di Valentino and A. Melchiorri, Phys. Rev. D **90**, 047301 (2014) [arXiv:1403.5732 [astro-ph.CO]].

[235] R. A. Battye and E. P. S. Shellard, Phys. Rev. Lett. **73**, 2954 (1994) [Erratum-ibid. **76**, 2203 (1996)] [astro-ph/9403018].

[236] K. J. Bae, J. -H. Huh and J. E. Kim, JCAP **0809**, 005 (2008) [arXiv:0806.0497 [hep-ph]].

[237] S. J. Asztalos, G. Carosi, C. Hagmann, D. Kinion, K. van Bibber, M. Hotz, L. J. Rosenberg and G. Rybka *et al.*, Nucl. Instrum. Meth. A **656**, 39 (2011) [arXiv:1105.4203 [physics.ins-det]].

[238] S. J. Asztalos, R. F. Bradley, L. Duffy, C. Hagmann, D. Kinion, D. M. Moltz, L. JRosenberg and P. Sikivie *et al.*, Phys. Rev. D **69**, 011101 (2004) [astro-ph/0310042].

[239] S. J. Asztalos *et al.* [ADMX Collaboration], Phys. Rev. Lett. **104**, 041301 (2010) [arXiv:0910.5914 [astro-ph.CO]].

[240] K. van Bibber and G. Carosi, arXiv:1304.7803 [physics.ins-det].

[241] M. Pettini and R. Cooke, Mon. Not. Roy. Astron. Soc. **425**, 2477 (2012) [arXiv:1205.3785 [astro-ph.CO]].

[242] E. G. Adelberger, A. B. Balantekin, D. Bemmerer, C. A. Bertulani, J. -W. Chen, H. Costantini, M. Couder and R. Cyburt *et al.*, Rev. Mod. Phys. **83**, 195 (2011) [arXiv:1004.2318 [nucl-ex]].

[243] C. Casella *et al.* [LUNA Collaboration] Nucl. Phys. A **706**, 203 (2002)

[244] M. Viviani, A. Kievsky, L. E. Marcucci, S. Rosati and R. Schiavilla, Phys. Rev. C **61**, 064001 (2000) [nucl-th/9911051].

[245] L. E. Marcucci, K. M. Nollett, R. Schiavilla and R. B. Wiringa, Nucl. Phys. A **777**, 111 (2006) [nucl-th/0402078].

[246] L. E. Marcucci, M. Viviani, R. Schiavilla, A. Kievsky and S. Rosati, Phys. Rev. C **72**, 014001 (2005) [nucl-th/0502048].

[247] K. M. Nollett and G. P. Holder, arXiv:1112.2683 [astro-ph.CO].

[248] E. Di Valentino, C. Gustavino, J. Lesgourgues, G. Mangano, A. Melchiorri, G. Miele and O. Pisanti, Phys. Rev. D **90**, 023543 (2014) [arXiv:1404.7848 [astro-ph.CO]].

[249] G. Rupak, Nucl. Phys. A **678**, 409 (2000)

[250] J. W. Chen and M.J. Savage, Phys. Rev. C **60**, 60205 (1999)

[251] P. D. Serpico, S. Esposito, F. Iocco, G. Mangano, G. Miele and O. Pisanti, JCAP **0412**, 010 (2004) [astro-ph/0408076].

[252] D. S. Leonard *et al.*, Phys. Rev. C **73**, 045801 (2006) [nucl-ex/0601035]

[253] S. Hamimeche and A. Lewis, Phys. Rev. D **77**, 103013 (2008) [arXiv:0801.0554 [astro-ph]].

[254] B. Audren, J. Lesgourgues, K. Benabed and S. Prunet, JCAP **1302**, 001 (2013) [arXiv:1210.7183 [astro-ph.CO]].

[255] A. Formicola et al. (LUNA collaboration), Nucl. Instr. and Meth. A 507 (2003) 609.

[256] L. Ma et al., Phys. Rev. C 55, 588 (1997).

[257] L. F. Abbott and M. B. Wise, Nucl. Phys. B **244**, 541 (1984); A. A. Starobinsky, JETP Lett. **30**, 682 (1979) [Pisma Zh. Eksp. Teor. Fiz. **30**, 719 (1979)]. V. A. Rubakov, M. V. Sazhin and A. V. Veryaskin, Phys. Lett. B **115**, 189 (1982). R. Fabbri and M. d. Pollock, Phys. Lett. B **125**, 445 (1983).

[258] D. H. Lyth and A. Riotto, Phys. Rept. **314**, 1 (1999) [arXiv:hep-ph/9807278].

[259] F. Lucchin and S. Matarrese, Phys. Lett. B **164**, 282 (1985).

[260] S. Mollerach, S. Matarrese and F. Lucchin, Phys. Rev. D **50**, 4835 (1994) [astro-ph/9309054].

[261] R. Camerini, R. Durrer, A. Melchiorri and A. Riotto, Phys. Rev. D **77**, 101301 (2008) [arXiv:0802.1442 [astro-ph]];

[262] E. Di Valentino, A. Melchiorri and L. Pagano, Int. J. Mod. Phys. D **20** (2011) 1183.

[263] M. Baldi, F. Finelli and S. Matarrese, Phys. Rev. D **72**, 083504 (2005) [arXiv:astro-ph/0505552].

[264] R. Brustein, M. Gasperini, M. Giovannini and G. Veneziano, Phys. Lett. B **361**, 45 (1995) [hep-th/9507017].

[265] R. H. Brandenberger and C. Vafa, Nucl. Phys. B **316**, 391 (1989).

[266] A. Nayeri, R. H. Brandenberger and C. Vafa, Phys. Rev. Lett. **97**, 021302 (2006) [arXiv:hep-th/0511140].

[267] P. Creminelli, M. A. Luty, A. Nicolis and L. Senatore, JHEP **0612**, 080 (2006) [arXiv:hep-th/0606090]; E. I. Buchbinder, J. Khoury and B. A. Ovrut, Phys. Rev. D **76**, 123503 (2007) [arXiv:hep-th/0702154]; E. I. Buchbinder, J. Khoury and B. A. Ovrut, JHEP **0711**, 076 (2007) [arXiv:0706.3903 [hep-th]]; Creminelli and L. Senatore, JCAP **0711**, 010 (2007) [arXiv:hep-th/0702165].

[268] T. Kobayashi, M. Yamaguchi and J. Yokoyama, Phys. Rev. Lett. **105** (2010) 231302 [arXiv:1008.0603 [hep-th]]; K. Kamada, T. Kobayashi, M. Yamaguchi and J. Yokoyama, arXiv:1012.4238 [astro-ph.CO].

[269] A. Stewart and R. Brandenberger, JCAP **0808** (2008) 012 [arXiv:0711.4602 [astro-ph]].

[270] B. P. Abbott *et al.* [LIGO Scientific and VIRGO Collaborations], Nature **460**, 990 (2009) [arXiv:0910.5772 [astro-ph.CO]].

[271] N. Bartolo, E. Komatsu, S. Matarrese and A. Riotto, Phys. Rept. **402** (2004) 103 [astro-ph/0406398].

[272] E. Di Valentino, A. Melchiorri, V. Salvatelli and A. Silvestri, Phys. Rev. D **86**, 063517 (2012) [arXiv:1204.5352 [astro-ph.CO]].

[273] S. Mollerach and S. Matarrese, Phys. Rev. D **56** (1997) 4494 [astro-ph/9702234].

[274] L. Verde and D. N. Spergel, Phys. Rev. D **65** (2002) 043007 [astro-ph/0108179].

[275] B. Gold, Phys. Rev. D **71** (2005) 063522 [astro-ph/0411376].

[276] F. Giovi, C. Baccigalupi and F. Perrotta, Phys. Rev. D **71** (2005) 103009 [astro-ph/0411702].

[277] K. M. Smith and M. Zaldarriaga, Mon. Not. Roy. Astron. Soc. **417** (2011) 2 [astro-ph/0612571].

[278] P. Serra and A. Cooray, Phys. Rev. D **77** (2008) 107305 [arXiv:0801.3276 [astro-ph]].

[279] A. Mangilli and L. Verde, Phys. Rev. D **80**, 123007 (2009) [arXiv:0906.2317 [astro-ph.CO]].

[280] D. Hanson, K. M. Smith, A. Challinor and M. Liguori, Phys. Rev. D **80** (2009) 083004 [arXiv:0905.4732 [astro-ph.CO]].

[281] A. Lewis, A. Challinor and D. Hanson, JCAP **1103**, 018 (2011) [arXiv:1101.2234 [astro-ph.CO]].

[282] A. A. Starobinsky, Phys. Lett. B91, 99 (1980).

[283] S. Capozziello, S. Carloni and A. Troisi, Recent Res. Dev. Astron. Astrophys. **1**, 625 (2003) [astro-ph/0303041].

[284] S. M. Carroll, V. Duvvuri, M. Trodden and M. S. Turner, Phys. Rev. D **70**, 043528 (2004) [astro-ph/0306438].

[285] A. A. Starobinsky, JETP Lett. **86**, 157 (2007) [arXiv:0706.2041 [astro-ph]].

[286] S. Nojiri and S. D. Odintsov, arXiv:0801.4843 [astro-ph].

[287] G. Esposito-Farese and D. Polarski, Phys. Rev. D **63**, 063504 (2001) [gr-qc/0009034].

[288] N. Bartolo and M. Pietroni, Phys. Rev. D **61**, 023518 (2000) [hep-ph/9908521].

[289] E. Elizalde, S. Nojiri and S. D. Odintsov, Phys. Rev. D **70**, 043539 (2004) [hep-th/0405034].

[290] T. Chiba, Phys. Lett. B **575**, 1 (2003) [astro-ph/0307338].

[291] G. R. Dvali, G. Gabadadze and M. Porrati, Phys. Lett. B **485**, 208 (2000) [hep-th/0005016].

[292] C. Deffayet, Phys. Lett. B **502**, 199 (2001) [hep-th/0010186].

[293] G. Dvali, S. Hofmann and J. Khoury, Phys. Rev. D **76**, 084006 (2007) [hep-th/0703027 [HEP-TH]].

[294] Y. S. Song, W. Hu and I. Sawicki, Phys. Rev. D **75**, 044004 (2007) [astro-ph/0610532].

[295] R. Bean, D. Bernat, L. Pogosian, A. Silvestri and M. Trodden, Phys. Rev. D **75**, 064020 (2007) [astro-ph/0611321].

[296] L. Pogosian and A. Silvestri, Phys. Rev. D **77**, 023503 (2008) [Erratum-ibid. D **81**, 049901 (2010)] [arXiv:0709.0296 [astro-ph]].

[297] S. Tsujikawa, Phys. Rev. D **77**, 023507 (2008) [arXiv:0709.1391 [astro-ph]].

[298] G. B. Zhao, L. Pogosian, A. Silvestri and J. Zylberberg, Phys. Rev. D **79**, 083513 (2009) [arXiv:0809.3791 [astro-ph]].

[299] A. Lue, R. Scoccimarro and G. Starkman, Phys. Rev. D **69**, 044005 (2004) [astro-ph/0307034].

[300] K. Koyama and R. Maartens, JCAP **0601**, 016 (2006) [astro-ph/0511634].

[301] Y. S. Song, I. Sawicki and W. Hu, Phys. Rev. D **75**, 064003 (2007) [astro-ph/0606286].

[302] Y. S. Song, Phys. Rev. D **77**, 124031 (2008) [arXiv:0711.2513 [astro-ph]].

[303] A. Cardoso, K. Koyama, S. S. Seahra and F. P. Silva, Phys. Rev. D **77**, 083512 (2008) [arXiv:0711.2563 [astro-ph]].

[304] T. Giannantonio, Y. S. Song and K. Koyama, Phys. Rev. D **78**, 044017 (2008) [arXiv:0803.2238 [astro-ph]].

[305] R. Caldwell, A. Cooray and A. Melchiorri, Phys. Rev. D **76** (2007) 023507 [astro-ph/0703375 [ASTRO-PH]].

[306] S. F. Daniel, R. R. Caldwell, A. Cooray and A. Melchiorri, Phys. Rev. D **77** (2008) 103513 [arXiv:0802.1068 [astro-ph]].

[307] T. Giannantonio, M. Martinelli, A. Silvestri and A. Melchiorri, JCAP **1004** (2010) 030 [arXiv:0909.2045 [astro-ph.CO]].

[308] M. Martinelli, E. Calabrese, F. De Bernardis, A. Melchiorri, L. Pagano and R. Scaramella, Phys. Rev. D **83** (2011) 023012 [arXiv:1010.5755 [astro-ph.CO]].

[309] S. F. Daniel, E. V. Linder, T. L. Smith, R. R. Caldwell, A. Cooray, A. Leauthaud and L. Lombriser, Phys. Rev. D **81** (2010) 123508 [arXiv:1002.1962 [astro-ph.CO]].

[310] E. Di Valentino, M. Gerbino and A. Melchiorri, Phys. Rev. D **87**, no. 10, 103523 (2013).

[311] B. Hu, M. Liguori, N. Bartolo and S. Matarrese, Phys. Rev. D **88**, no. 2, 024012 (2013) [arXiv:1211.5032 [astro-ph.CO]].

[312] E. Komatsu, Class. Quant. Grav. **27**, 124010 (2010) [arXiv:1003.6097 [astro-ph.CO]].

[313] W. Hu, Phys. Rev. D **62**, 043007 (2000) [astro-ph/0001303].

[314] G. Efstathiou and J. R. Bond, Mon. Not. Roy. Astron. Soc. **304**, 75 (1999) [astro-ph/9807103].

[315] E. Calabrese, J. Smidt, A. Amblard, A. Cooray, A. Melchiorri, P. Serra, A. Heavens and D. Munshi, Phys. Rev. D **81** (2010) 043529 [arXiv:0909.1837 [astro-ph.CO]].

[316] E. V. Linder and R. N. Cahn, Astropart. Phys. **28** (2007) 481 [astro-ph/0701317].

[317] E. Bertschinger and P. Zukin, Phys. Rev. D **78** (2008) 024015 [arXiv:0801.2431 [astro-ph]].

[318] W. Hu and I. Sawicki, Phys. Rev. D **76** (2007) 064004 [arXiv:0705.1158 [astro-ph]].

[319] Y. -S. Song, H. Peiris and W. Hu, Phys. Rev. D **76**, 063517 (2007) [arXiv:0706.2399 [astro-ph]].